E-ISSN: 1687-6167
NUMBER 55
DECEMBER 2023

JSR A

JOURNAL OF SCIENTIFIC REPORTS A

Journal of Scientific Reports-A, December 2023, Number 55

Kutahya Dumlupinar University Journal of Reports A
Kutahya Civelek Campus Tavsanli Road 10 KM. 43270 Kutahya
Phone: (0274) 443 11 62
E-mail: journal@gmail.com
gsjpra.com

Dumlupinar University Press

gate of science

Kütahya Dumlupınar University
Institute of Graduate Studies

Journal of Scientific
Reports-A
E-ISSN: 2687-6167
Number 55, December 2023

Journal of Scientific Reports-A started its publication life in 2000 as name of Journal of Science and Technology of Dumlupınar University and is a national peer-reviewed journal published regularly twice a year in June and December. The language of the journal is English. Articles submitted to the journal are evaluated by at least two referees who are experts in the subject and selected by the editorial board. All articles submitted to the journal are evaluated by the double-blind method. Articles submitted to our journal for review should not be previously published, accepted for publication and in the process of being evaluated for publication in another journal. All responsibility for the articles published in the journal belongs to the author(s).

The journal aims to share scientific studies carried out in the fields of science and engineering at national and international level with scientists and the public. Original research articles, review articles and short notes in science and engineering disciplines are accepted for the journal. Original research articles are expected to contain theoretical and experimental results and should not be published in other journals. In the review articles, it is expected that scientific, technological and current developments on a specific subject are reflected by using an extensive bibliography and made a satisfying evaluation of these. Short notes should be brief writings prepared to announce the first findings of an original study.

Editorial Policy

The journal is open access and the article evaluation period is between 1-2 months.

Correspondence Address: Kütahya Dumlupınar Üniversitesi Evliya Çelebi Yerleşkesi Fen Bilimleri Enstitüsü 43270 KÜTAHYA
E-mail: joursra@gmail.com
Webpage: gsjsra.com
Phone: 0 274 443 19 42
Fax: 0 274 265 20 60

JSR A
Journal of Scientific Reports

JSR A
Journal of Scientific Reports

Journal of Scientific Reports-A, Number 55, December 2023

JSR A
Journal of Scientific Reports

JOURNAL OF SCIENTIFIC REPORTS-A
E-ISSN: 2687-6167

CONTENTS

RESEARCH ARTICLES

JSR A
Journal of Scientific Reports

JSR A
Journal of Scientific Reports

Journal of Scientific Reports-A, Number 55, December 2023

Contents lists available at *Dergipark*

Journal of Scientific Reports-A

journal homepage: *https://dergipark.org.tr/tr/pub/jsr-a*

E-ISSN: 2687-6167 ***Number 55, December 2023***

RESEARCH ARTICLE

Receive Date: 09.04.2023 *Accepted Date: 23.05.2023*

Silver nanoparticle synthesis by biogenic reduction method and investigation of antimicrobial, antibiofilm, anticancer activities

Funda Karakaya[1], Ali Savas Bülbül[2], Muhammed Bekmezci[3], Fatih Şen[4*]

[1]*Bayburt University, Faculty of Applied Sciences, Emergency and Disaster Management Division Bayburt, Türkiye, ORCID:* 0000-0003-4328-9062
[2]*Bayburt University, Faculty of Applied Sciences, Emergency and Disaster Management Division Bayburt, Türkiye, ORCID:* 0000-0002-2200-7348
[3]*Departmen of Material Science and Engineering, Faculty of Engineering, Dumlupinar University, 43000 Kutahya, Türkiye, ORCID:* 0000-0003-3965-6333
[4]*Sen Research Group, Department of Biochemistry, Dumlupinar University, 43000 Kutahya, Türkiye, ORCID:* 0000-0001-6843-9026

Abstract

In this study, R. aculeatus plant extract and biogenically formed AgNPs were investigated for their potential antibacterial, antibiofilm and anticancer abilities. AgNPs were characterised using scanning electron microscopy (SEM), Fourier transform infrared spectroscopy (FT-IR), X-ray diffraction (XRD) and UV-vis spectroscopy (UV-VIS). According to the Debye Scherrer formula, the particle size was found to be 32.56 nm. Disc diffusion and microdilution methods were used to investigate the antibacterial activity. In the disc diffusion study, the best results were obtained from the extract and AgNP. In the tests using plant extracts, Staphylococcus aureus ATCC 25923 showed the lowest antibiofilm activity, while Bacillus subtilis and Enterobacter aerogenes ATCC 13048 showed the highest activity. Salmonella infantis was most affected by AgNP, while Escherichia coli CFAI ATCC 25922 was least affected. Biogenically synthesised AgNPs were also investigated in cytotoxic activity studies. It was found to have the lowest concentration value on MCF-7 and HUVEC cell lines at the determined concentrations. The extract did not have any cytotoxic effect on MCF-7 cell line. HUVEC cell line showed the lowest cytotoxic activity of 10^{-3} g/mL. The antibacterial, antibiofilm and anticancer properties of R. aculeatus plant extract and biogenically produced AgNPs have been the subject of an important study. Furthermore, the comparison of the effects of plant extract and AgNPs on breast cancer cell lines and healthy cell lines provides a rich scientific material.

Keywords: Antimicrobial activity, Antibiofilm activity, Anticancer activity, Biogenic agent.

Corresponding Authors:
e-mail: fatihsen1980@gmail.com

1. Introduction

Treatment of diseases is a major economic concern for both individuals and countries. At the same time, finding appropriate treatment methods for the disease is also very important and is another important cause of individual concern. To eliminate these concerns, both plant sources and nanoparticles (NP), in which plants are used as biological reducing agents, are used in the treatment of many diseases [1].

Since ancient times, people have used plants both as nutrients and for therapeutic purposes to eliminate health problems. Today, plants have begun to be used for medicinal purposes all over the world and in our country [2]. Many of the drugs that are used extensively in the field of medicine are also obtained from plants [3]. Herbal medicines are prepared by obtaining active substances from plants that are generally included in the group of medicinal plants. Herbal products are often used in the treatment of diseases with chronic medical conditions, including breast cancer (2%), liver diseases (21%), HIV (22%), asthma (24%), and rheumatological disorders (26%) [4].

Ruscus aculeatus L. plant is notable among the medicinally important species. This species, which belongs to the Ruscaceae family, is found in maquis forests and its dimensions are around 20-50 cm. [5]. The active components of the plant are steroid saponins. These active ingredients have beneficial and anti-inflammatory effects on the veins, such as increasing blood circulation [6]. In addition, the main phenolics in the leaves and stems of the plant have been identified as quercetin and p-coumaric acid [7]. These identified phenolic compounds can be used as reducing agents [8]. The method, which includes these and similar biological compounds and is also known as green synthesis, allows the synthesis of nanoparticles with economical and relatively easy methods without the use of heavy chemicals [9–11].

The produced new age drugs are polymer, metal, or ceramic nanoparticles that can fight diseases such as cancer and human pathogens such as bacteria [12]. With nanotechnology applications, significant acceleration has been gained in drug release systems, sensor systems, innovative energy production systems, and antibacterial research [13–16]. Cancer is undoubtedly one of the most important of these diseases.

In addition, cancer, a complex and deadly disease, continues to pose major challenges to world health. Despite advances in treatment alternatives, the creation of effective anticancer drugs remains an important subject of study. Recently, nanotechnology has become a suitable field for the creation of new and focused methods in cancer treatment [17]. One of the nanotechnological applications is AgNPs. The anticancer effects of Ag NPs are due to their capacity to precisely target and destroy cancer cells while leaving healthy cells unharmed. The different size-dependent properties of AgNPs are responsible for this selectivity, making them more effective than conventional therapeutic agents in penetrating malignant tissues. AgNPs can also be functionalized with ligands or antibodies to directly target cancer cells, increasing their selectivity, and minimizing side effects [18–20]. AgNPs are important in the field of nanotechnology due to their unique properties such as chemical stability, good conductivity, catalytic, and most importantly antibacterial, antiviral, and antifungal properties [21,22]. Therefore, silver shows the best activity against bacteria, viruses, and other eukaryotic microorganisms [23,24]. Silver nanoparticles (AgNP), which draw attention with their antimicrobial properties, have many advantages such as the fact that silver is a very broad-spectrum antibiotic, almost no bacterial resistance in silver, and non-toxicity at low concentrations [25]. There are also different studies in the literature on obtaining AgNPs by green synthesis and their applications. One of these studies was performed with jujube seed extract. It was reported that the plant and silver structure used in the synthesis showed good antibacterial properties [26]. In a similar study, AgNPs were obtained with Diospyros malabarica Fruit Extract. According to the results, it was found to inhibit bacterial growth against *Staphylococcus aureus,* and *Escherichia coli* pathogenic microorganism strains at concentrations of 500 µg/ml as 8.4 ± 0.3 mm and 6.1 ± 0.7 mm, respectively [27]. In the study conducted with Moringa Oleifera biological agent, it was reported that an active NP was obtained against carcinoma cells and this NP was also used in different applications [28].

According to the research, it is important to select the right herbal agent and to put forward a suitable antibacterial-anticancer molecule by considering economic concerns.

For this reason, silver, which has remarkable biological activities compared to other metals, and the green synthesis method, which has been used frequently in recent years, were preferred in this study. In this study, AgNPs were synthesized for the first time using the R. aculeatus plant, and their antibacterial, antibiofilm, and anticancer activities were investigated.

2. MATERIAL AND METHOD

2.1. Preparation of Biogenic Agent

The plant sample used in the study was collected from the Balamba location in the center of Bartin province, located between 41° 53' north latitude and 32° 45' east longitude on the northwest coast of the Black Sea. After the identification of the species, the plant part to be used was washed, dried in a cool and non-humid environment, and made ready for grinding. Then, the leaf part of the plant was crushed in a mortar with the help of liquid nitrogen. This mixture was extracted for 4 hours in a magnetic heater set at 80 ºC. At the end of the period, the mixture was filtered through filter paper, and the extract obtained was stored at +4ºC to be used in the analyses [29,30].

2.2. Synthesis of Silver Nanoparticles

1 mM silver nitrate ($AgNO_3$) solution was added to 50 ml of the obtained biological agent and diluted. The liquid was stirred at 100 ^oC in a magnetic heater for 1 hour. The mixture was washed 3 times in a centrifuge with H_2O. Characterization processes were started by drying in an oven at 35 ^oC for 24 hours [31]. Figure 1 briefly summarizes the synthesis phase and the implementation step.

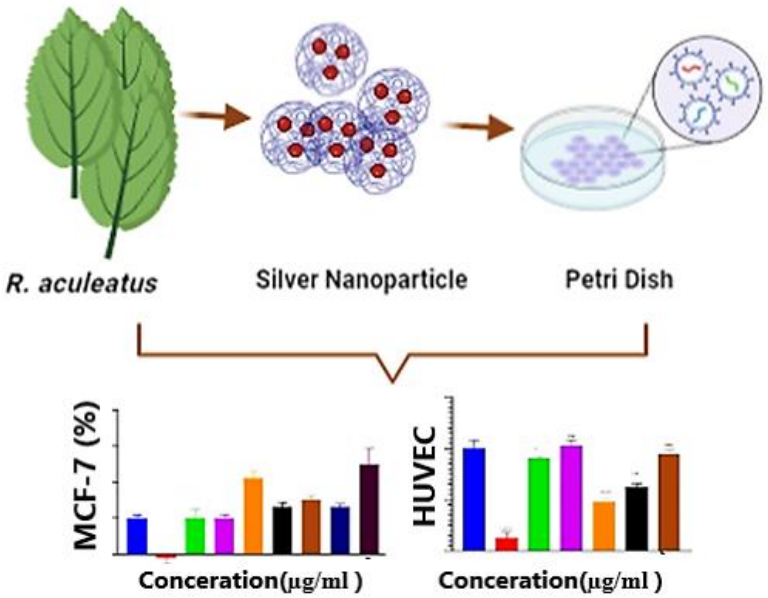

Fig. 1. Graphical representation of synthesis step and application method.

2.3. Characterization of AgNPs

Thermo Scientific Multiskan GO was used to take spectroscopic measurements in UV-vis analysis and measurements were made in the 300-800 nm range. Nanoparticles obtained by green synthesis were analyzed in 1, 24, and 48-hour working samples. X-ray diffraction (XRD) was used for the analysis of the crystal structure. A scanning electron microscope (SEM) was used for morphological analysis. In the FT-IR analysis, the presence of various functional groups in the molecules responsible for the biological reduction and stabilization of AgNPs, whether the structure is aromatic or aliphatic, the state of the bonds in the structure, and their binding sites were determined.

2.4. Concentration Preparation

0.2 g of dried AgNP was weighed and dissolved in 10 ml dH_2O in an ultrasonicated bath. The plant extract was taken into a 50 ml falcon tube and used as the initial concentration. Working concentrations were prepared by making 1/10 dilutions.

2.5. Disk Diffusion Method

Strains from stock microorganisms were suspended in Luria Bertoni (LB) broth and kept in a shaking incubator for 16-18 hours. After this period was completed, a 0.5 cell/ml McFarland turbidity test was performed on the microorganism strains and a dilution containing 1.5x106 cells/ml microorganism was prepared. Mueller Hinton Agar (MHA) solid medium was prepared for bacterial dilutions. Then, bacteria were planted on the surface of the petri dishes with the help of disposable sterile swabs.

Antimicrobial activity trials of AgNPs and plant extract were first analyzed by the disk diffusion method [32]. Fifteen microorganisms were used in the study. 6 were gram-positive and 9 were gram-negative. The solutions produced were impregnated on sterilized discs. Antibiotic discs containing the active substance Tetracycline (TE: 10 mg/ml) prepared from antibiotic drugs were used for positive control. Discs containing AgNP and plant extract were placed in Petri dishes appropriately. Bacteria were left in the incubator at 37^{o}C for 16-18 hours and the inhibition zone diameters around the discs were measured at the end of the period. The study was performed in triplicate for AgNP and plant extract, and the arithmetic mean and standard deviation of the results were calculated.

2.6. Minimum Inhibition Concentration (MIC)

The MIC of the plant extract and AgNP were determined using sterile 96-well microplates. After mixing 100 µL of LB Broth and 100 µL of AgNP and plant extract into the first wells of the microplates, 100 µL was taken and pipetted into the next well, and these dilutions were continued until the last well, and the concentration in each well was adjusted to be half of the previous one. Finally, 10 µL of microorganisms was added to all wells except for the negative control well. After these steps were completed, the microplates were left to incubate at 37ºC for 16-18 hours. At the end of the period, measurements were made in the spectrophotometer device at 600 nm.

2.7. Minimum Bactericidal Concentration (MBC)

After determining the MIC of the plant extracts and AgNPs used in the study against bacteria, the MBC were investigated. After determining the MIC, samples were taken from the wells where bacteria did not grow and inoculated into MHA medium using sterile rings. Then they were incubated at 37ºC for 16-18 hours. After this period was completed, 99.9% of the bacteria inoculated into the media The minimum antimicrobial agent concentration that kills was accepted as the MBC value.

2.8. Determination of Antibiofilm Activities

The MBC were investigated after the MIC of the plant extract and AgNPs used in the study against bacteria had been determined. After determining the MIC values, samples were taken from the wells where bacteria did not grow and injected onto an MHA medium using sterile loops. The impact of the plant extract and AgNP on the antibiofilm was compared to the data from the positive control, and the percentage decrease value of biofilm inhibition was computed using the following formula (Eq. 1):

$$\%\text{Reduction} = ((A_0 - A_1)/A_0) \times 100 \quad (1)$$

A_0: *positive control well*
A_1: *test wells*

2.9. Determination of Anticancer Activities

Cytotoxic effect of plant extract and green synthesized AgNP on breast cancer (MCF-7) and human umbilical vein endothelial cells (HUVEC) cell lines MTT (3-(4,5-dimethyltriazol-2-yl)-2,5-diphenyltetrazolium bromide) was determined by the method [33,34]. The mitochondrial dehydrogenase enzyme reduces MTT salt, which is a yellow, water-soluble salt, to water-insoluble formazan, resulting in purple-colored crystals. Formazan crystals dissolved because of treatment with dimethyl sulfoxide (DMSO) can be calculated quantitatively as a measure of viability by the calorimetric method in an ELISA reader [35].

Enough MCF-7 and HUVEC cells obtained by the passage in this study were each treated separately. First, the cells were suspended with trypan blue at a ratio of 1:1, and cell counts were made under the microscope with the help of a Thoma slide. Then, 105 cells/mL were added to each well of 96-well microplates and incubated for 24 hours at 37 °C in an incubator containing 5% CO_2. After incubation, plant extract and green synthesized AgNP concentrations of 10, 20, 30, 40, and 50 µg/mL were suspended and added to the wells. They were left to incubate again for 24 hours and the changes that occurred afterward were examined under the microscope and compared with the control groups. After this step, 10 µL of MTT solution was added to each well and incubated for 3 hours. At the end of the time, the microplates were read by ELISA at 630 nm and the results were calculated.

3. Results and Discussion

3.1. Analyzing the synthesized AgNPs

After the addition of silver nitrate, a color change was observed over time. The reason for the color change here is the stimulation of the surface plasmon resonance with silver nanoparticles [36]. The UV-VIS spectra recorded at 1 hour, 24 hours, and 48 hours after the start of the reaction are shown in Figure 2. As soon as the plant leaf extract and silver nitrate solution were mixed, the reduction of pure Ag^+ ions to Ag^0 was monitored by measuring the UV-vis spectrum at certain time intervals [37].

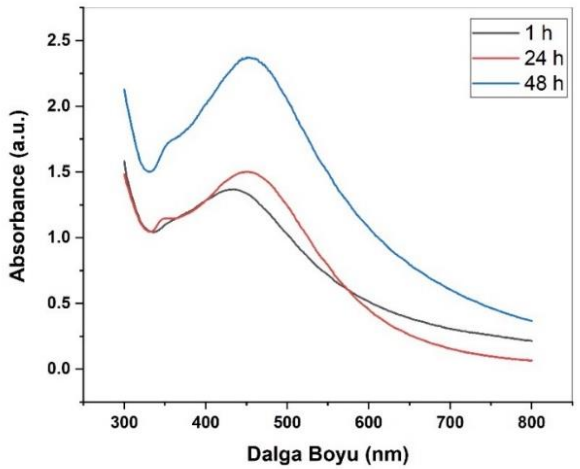

Fig. 2. UV-vis spectra of *R. aculeatus L.* recorded as a function of leaf extract and aqueous silver nitrate solution over time [38].

In the production of silver nanoparticles, it was observed that the plasmon resonance occurred at 426nm after 1 hour and the peak length increased steadily as the reaction time was extended to 24 (444nm) and 48 (444nm) hours.

The crystal structure of the particles was confirmed by analyzing them by X-ray diffraction (XRD). The analysis revealed a significant number of Braggs reflections that can be indexed. The peaks with a value of 2θ in our XRD spectrum were compared with the literature and showed that the AgNPs produced were nanocrystals. The XRD graph is given in Figure 3a. The XRD spectrum of the prepared AgNPs showed four diffraction bands at 2θ= 38.35, 46.46, 64.75, and 77.62, which are the characteristic Bragg diffraction plans of the face-centered cube (111), (200), (220) and (311). Through the biological agent, the reduction of Ag+ ions resulted in the formation of AgNPs with a crystalline structure by XRD. According to this result, it was determined that there is metallic silver in the face-centered cubic (FMC) structure. The Debye-Scherrer equation can be used to determine the typical particle size of AgNPs produced using the present green technique. The average nanoparticle size of AgNPs was calculated as 32.56 nm according to the Debye-Scherrer formula (Eq. 2):

$$d(\text{Å}) = k\lambda / \beta\cos\theta \quad (2)$$

d=Average size of NPs,
k= Factor (0,9),
λ= X-Wavelenght (1,54056Å),
β=Half-maximum point of the full width of the corresponding refractive peak (rad),
θ= Represents the maximum height angle (rad) of the peak.

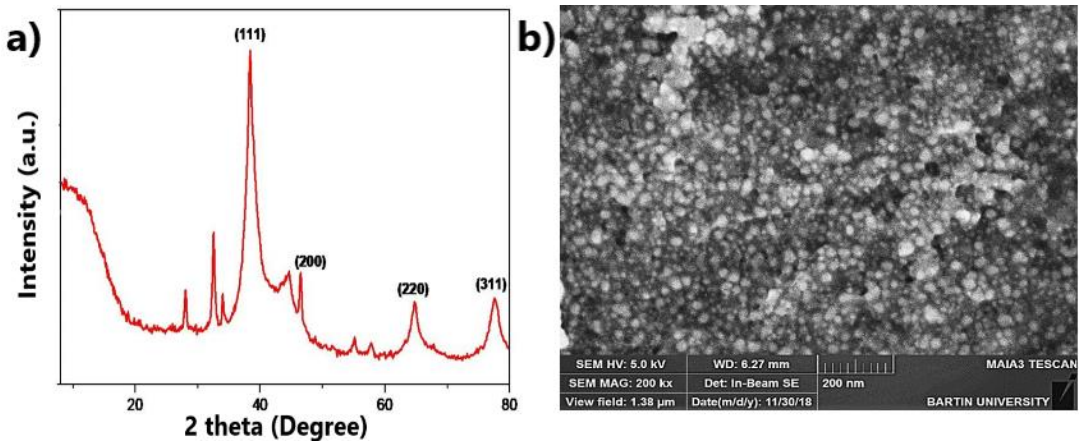

Fig. 3. a) AgNP XRD image b) AgNP SEM image at 200 nm [38].

Surface morphologies and dimensions of AgNPs obtained by the green synthesis method were analyzed by SEM. As a result of the imaging, it was determined that the biological AgNP was spherical in size and approximately 32.56 nm in size. The SEM image of AgNP is shown in Figure 3b. According to the FTIR spectrum results of the plant, the peak at wave number 3302 cm^{-1} is the O-H vibration from hydroxyl groups and similar peaks are hydroxyl groups at wave number 1616 cm^{-1}. C-C stretching vibration was observed due to the high phenyl levels in the polyphenolic components (Figure 4) [39]. The peak, which corresponds to a wave number of approximately 1443 cm^{-1}, corresponds to the -C-O bond vibration, which is composed of carbohydrates, glycogen, and oligosaccharides [40]. By comparing both spectra, it was determined that the peaks corresponding to 2917 cm^{-1} wave number were caused by saturated alkane (-C-H) stretching [41]. It was observed that the peaks observed at approximately 1022 cm^{-1} and 1029 cm^{-1} wave numbers are the maximum band absorption of glucose [42,43]. The presence of small shift-like peaks in the spectra reveals that the synthesized AgNPs contain natural compounds originating from the plant extract [44].

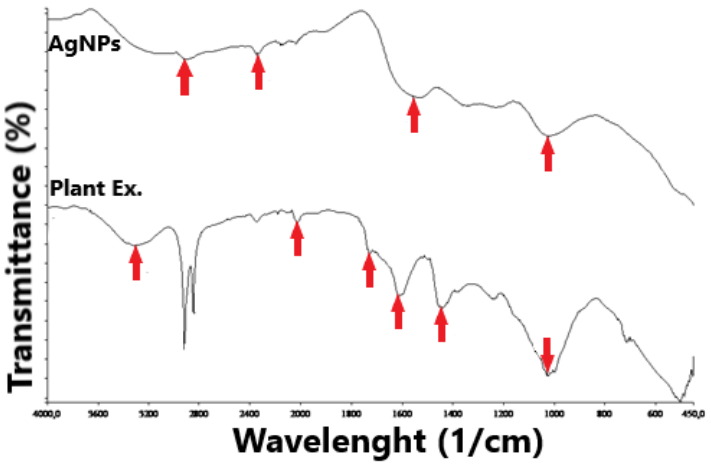

Fig. 4. a) Green synthesis AgNP b) FT-IR spectra of *Ruscus aculeatus* leaf extract [38].

3.2. Disk Diffusion Results

Table 1 presents the antimicrobial activity results of the plant extract and synthesis AgNP by disk diffusion method. When the data obtained were examined, it was observed that the plant extract showed inhibition zones on other species except for *S. marcescent* ATCC 13048 bacterial strain. AgNPs obtained as a result of synthesis showed an inhibition zone against *S. kebtucky*, *S. enteriditis* ATCC 13075, *E.durs*, and *S. typhimurium* microorganisms, but did not show an inhibition zone against other microorganisms.

Table 1. Measurements of zones of inhibition of plant extract and green synthesis AgNP against test microorganisms (mm) [38].

Microorganisms	**Extract**	**AgNP**	**TE 10**
Pseudomonas aeruginosa DSMZ 50071	8±0.00	-	17.5
Klebs iella pneumoniae	7±0.00	-	19.5
Salmonella infantis	8.3±1.52	-	15
Enterobacter aerogenes ATCC 13048	7±0.00	-	14
Salmonella enteritidis ATCC 13075	9.6±0.57	7±0.00	17.5
Salmonella typhimurium	7.3±0.57	7±0.00	18.5
Enterococcusfaecalis ATCC 29212	7±0.00	-	16.5
Bacillus subtilis DSMZ 1971	7.3±0.57	-	14
Listeria innocua	7.3±0.57	-	15.5
Staphylococcus aureus ATCC 25923	-	-	14.5
Saratia marrescens ATCC 13048	6.6±0.57	-	9
Salmonella kentucky	7.6±0.57	7.6±1.15	17.5
Staphylococcus epidermidis DSMZ 20044	7±0.00	-	11
Escherichia coli CFAI ATCC 25922	6±0.00	-	16

(-): There is no zone of inhibition. **(TE 10)**: Tetrasiklin (10 mg/ml) [38].

3.3. Minimum Inhibition Concentration (MIC) Results

MIC values of the plant extract and synthesized AgNP are shown in Table 2. Accordingly, it has been shown that the prepared 100% plant extract has no inhibitory effect against all microorganisms. On the other hand, the synthesized AgNP showed a minimum inhibitory effect against *Salmonella infantis*, one of the microorganisms tested, at a concentration of 0.12 mg/ml. While AgNP showed a minimum inhibitory effect at a concentration of 0.06 mg/ml against the tested microorganisms, *Pseudomonas* aeruginosa DSMZ 50071 and *Listeria innocua* strains, it showed a minimum inhibitory effect at a concentration of 0.03 mg/ml against the other 12 bacterial strains.

Table 2. MIC results of green synthesis AgNP against test microorganisms [38].

Microorganism Name	**AgNP- mg/mL**
Staphylococcus epidermidis DSMZ 20044	0.03
Salmonella kentucky	0.03
Enterococcus faecais ATCC 29212	0.03
Salmonella enteritidis ATCC 13075	0.03
Salmonella infantis	0.12
Bacillus subtilis DSMZ 1971	0.03
Enterobacter aerogenes ATCC 13048	0.03
Klebsiella pneumoniae	0.03
Enterococcus durans	0.03
Salmonella Typhimurium	0.03
Listeria innocua	0.06
Escherichia coli CFAI ATCC 25922	0.03
Pseudomonas aeruginosa DSMZ 50071	0.06
Staphylococcus aureus ATCC 25923	0.03
Saratia marrescens ATCC 13048	0.03

3.4. Minimum Bactericidal Concentration (MBC) Results

Table 3 shows the lowest bactericidal concentrations (MBC) that inhibit the growth of the plant extract and biosynthesized AgNP up to 99.9%. Accordingly, it was determined that the prepared 100% plant extract did not have an inhibitory effect of 99.9% against all microorganisms (Figure 5). The lowest bactericidal concentration of biologically synthesized AgNP, which inhibited 99.9% against *S. infantis*, was determined as 0.25 mg/ml. The lowest bactericidal concentration of biologically synthesized AgNP, which inhibited 99.9% of S. enteritidis ATCC 13075 bacteria, was determined as 0.06 mg/ml, while 0.12 mg against *P. aeruginosa* DSMZ 50071 and *Listeria innocua* bacterial strains. It was determined as /ml. In addition, the lowest bactericidal concentration, which inhibited 99.9% against 11 other bacterial strains, was determined as 0.03 mg/ml. Compared to our study, Kaviya et al. (2011) found that because of the silver nanoparticle synthesis and the use of fewer types of bacteria, the antimicrobial effect on *E. coli* and *P. aeruginosa* bacteria showed higher antibacterial activity against *S. aureus* bacteria, as in our study. Concentration (A1=A2=A3: %100, B1=B2=B3: %50 concentration - MBC) AgNP concentrations (A1: 1 mg/ml, B1: 0.5 mg/ml, C1: 0.25 mg/ml, D1: 0.12 mg/ml, E1: 0.06 mg/ml, F1: 0.03 mg/ml).

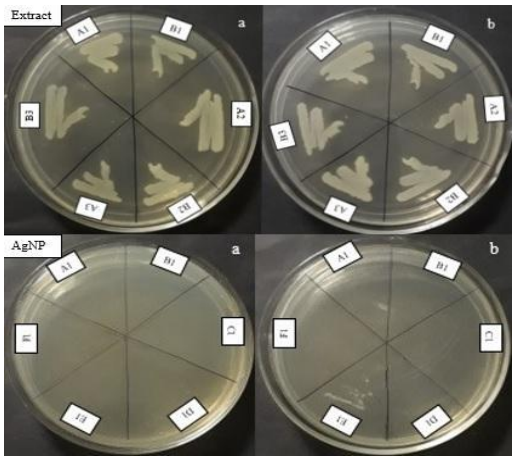

Fig. 5. Plant extract a: *P. aeruginosa* (A1,B1), *E. faecalis* (A3,B3), *S. kentucky* (A2,B2). b: *L. innocua* (A1,B1), *E. durans* (A3,B3), *S. enteritidis* (A2,B2), and MBC Results of AgNP [38].

Table 3. Minimum bactericidal concentrations of the green synthesis AgNP studied [38].

Microorganism Name	**AgNP- mg/mL**
Enterobacter aerogenes ATCC 13048	0.03
Klebsiella pneumoniae	0.03
PPseudomonas aeruginosa DSMZ 50071	0.12
Salmonella infantis	0.25
Listeria innocua	0.12
Salmonella enteritidis ATCC 13075	0.06
Salmonella Typhimurium	0.03
Staphylococcus aureus ATCC 25923	0.03
Escherichia coli CFAI ATCC 25922	0.03
Saratia marrescens ATCC 13048	0.03
Salmonella Kentucky	0.03
Enterococcusfaecalis ATCC 29212	0.03
Bacillus subtilis DSMZ 1971	0.03
Enterococcus durans	0.03
Staphylococcus epidermidis DSMZ 20044	0.03

3.5. Antibiofilm Results

When the antibiofilm effect results of the plant extract and AgNP against the test microorganisms at different concentrations in Table 4 and Table 5 are examined, it is seen that the extract did not inhibit biofilm formation at the lowest concentration (3.13%) and that the *S. infantis* strain did not inhibit the biofilm formation at the lowest concentration of AgNP (0.03 mg/ml) did not inhibit biofilm formation of *E. coli* CFAI ATCC 25922 strain. In addition, it was determined that all the test microorganisms at different concentrations inhibited biofilm formation. Based on the antibiofilm study, Mohanty et al. (2012) showed that they reduced the nanoparticles they synthesized by using starch material at 1-2 µM concentrations on *P. aeruginosa* and *S. aureus* bacterial species by 65% and 88%, respectively.

Table 4. Biofilm inhibition values of the plant extract at different concentrations (%) [38].

Microorganism Name	100	50	25	12.5	6.25	3.13
Enterobacter aerogenes ATCC 13048	43.8	39.4	48.9	48.3	43.2	9
Escherichia coli CFAI ATCC 25922	30.9	44.5	32	44.2	44.8	40.7
Salmonella infantis	45.8	41.4	37.5	30.5	12.4	-
Staphylococcus epidermidis DSMZ 20044	25	19.6	24.7	21.9	9.4	15
Staphylococcus aureus ATCC 25923	6	12.2	10.1	2.7	1.3	6.8
Bacillus subtilis DSMZ 1971	46.5	44.2	41.1	38	24	13.3

Table 5. Biofilm inhibition values of AgNP at different concentrations (mg/ml) [38].

Microorganism Name	1	0.5	0.25	0.12	0.06	0.03
Enterobacter aerogenes ATCC 13048	15	29.7	31.1	31.9	26.8	10.7
Staphylococcus aureus ATCC 25923	25.2	36.3	34.3	33.8	17.2	8.6
Salmonella infantis	60	65.5	62.6	63.4	55.8	53.2
Escherichia coli CFAI ATCC 25922	1 1.1	10.7	1 1 .1	11.7	7.9	-
Staphylococcus epidermidis DSMZ 20044	17.2	18	24.6	22.8	8.4	1.1
Bacillus subtilis DSMZ 1971	38	36.9	38.4	34.7	25	28.4

3.6. Anticancer Activity Results

Figure 6a shows the cell viability rates of AgNP and plant extract applied to the MCF-7 cell line at different concentrations (10^{-3}, 10^{-5}, $10^{-7,}$ and 10^{-9} µg/ml). Compared to the control group, the lowest value determined in the applied AgNP concentrations is 10^{-3} µg/ml. Other concentrations applied were found to have less cytotoxic effects. This result indicates that the cytotoxic effect of biosynthesized AgNPs against MCF-7 is stronger. The IC50 value of the green synthesized AgNP is 0.06 µg/ml for the MCF-7 cell line, while the IC50 value of the plant extract is 6.91 µg/ml.

Figure 6b shows the cell viability rates at different concentrations (10^{-3}, $10^{-4,}$ and 10^{-5} µg/ml) of AgNP and plant extract applied to the HUVEC cell line. In comparison to the control group, the lowest value determined in the applied AgNP concentrations is 10^{-3} g/ml. It was observed that the cytotoxic effect was less at other applied concentrations. In plant extract, the lowest value determined when compared to the control group is 10^{-3} µg/ml, and concentration values of 10^{-4} and 10^{-5} µg/ml have less cytotoxic effect compared to this value. The IC50 value of the green synthesized AgNP is 0.04 µg/ml for the HUVEC cell line, while the IC50 value of the plant extract is 18.4 µg/ml. In this context, Suman et al. (2013) reported that they exhibited a significant cytotoxic effect compared to other chemical-based synthetic drugs in their study on the HeLa cell line with the AgNPs they synthesized [45]. In this context, our study contributed by examining the effect of AgNP not only on a cancer cell line but also on a healthy cell line. A wider spectrum can be contributed to the literature with studies that can be performed on various cancer cell lines and on healthy cell lines that can be obtained from other tissues.

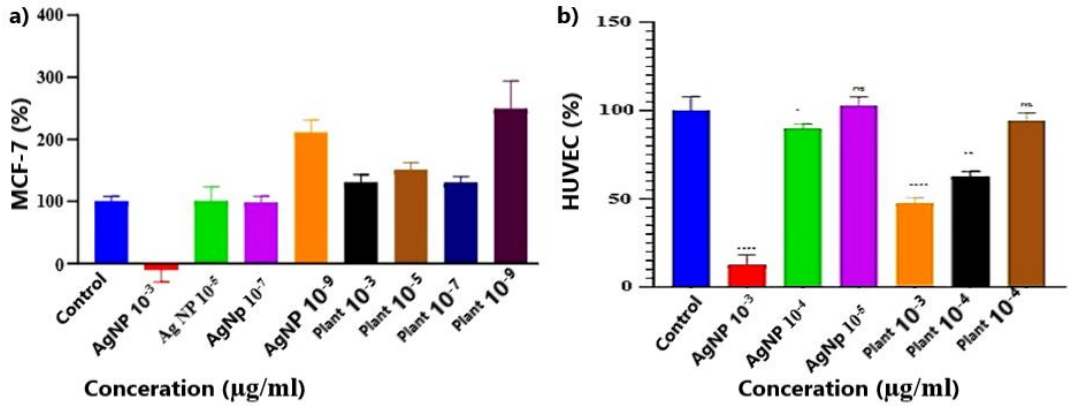

Fig. 6. a: Cytotoxic effects of. *Biogenic agent* extract and green synthesized AgNP on MCF-7 cell line b: Cytotoxic effects of *biogenic agent* extract and green synthesized AgNP on HUVEC cell line [38].

4. Conclusion

In this study, AgNP synthesis was carried out from grass wastes of the R. aculeatus plant by the green synthesis method. The synthesis result was calculated according to the Debye Scherer formula, in which 32.56 nm structures were seen. Antimicrobial and anticancer studies of the obtained AgNPs were investigated. The results calculated that the AgNPs had a MIC value of approximately 3 µg/ml *against Pseudomonas aeruginosa* and *Acinetobacter baumannii*. This value was calculated as the highest inhibitory effect against *Fusarium solani* 20 µg/ml. They determined that it is close to 90% in ml AgNP concentration. They showed that an inhibitory effect on cancer cell growth was achieved by increasing the AgNP concentration to 5 µg/ml, thus reducing the survival of cancer cells by about 30%. According to our study, the MIC values of AgNP synthesized against 15 different test microorganisms were observed between 0.03 and 0.12 mg/ml, while MBK values differed between 0.03-0.25 mg/ml. It has been observed that 100% plant extract has no inhibitory effect against all microorganisms. In the plant extract, it was observed that the cytotoxic effect of the applied concentrations was low. This result shows that the cytotoxic effect of biosynthesized AgNPs against MCF-7 is stronger. The IC50 value of the green synthesized AgNP is 0.06 µg/ml for the MCF-7 cell line, while the IC50 value of the plant extract is 6.91 µg/ ml. At the same time, tests were made against different bacterial species in our study. It was determined that all microorganisms except the E. coli bacterial strain inhibited biofilm formation at the lowest concentration of AgNP (0.03 mg/ml).

It was observed that the antimicrobial, anti-biophilic, and anticancer activity of the *R. aculeatus* plant was quite high with AgNP synthesis. With the study we have done, a source is presented to the literature for possible future studies. However, it may enable the use of new therapeutic agents and show promise for effective antibiofilm, and antimicrobial agent designs in the biomedical field.

Author Contribution

F.K., A.S.B., M.B., R.B., E.K., and F. S. organized all experiments and wrote the manuscript. F.K., and F.S. performed all experiments and characterizations.

Acknowledge

This study is derived from Funda Karakaya's master's thesis.

The information contained in this study was presented in summary at the Congress of Engineering and Natural Sciences (ICENSS-2021).

References

[1] Patra, J.K., Das, G., Fraceto, L.F., Campos, E.V.R., Rodriguez-Torres, M.D.P., Acosta-Torres, L.S., Diaz-Torres, L.a., Grillo, R., Mallappa, K.S., Sharma, S., Habtemariam S., and Han-Seung, S., (2018). Nano based drug delivery systems: recent developments and future prospects. Journal of Nanobiotechnology,16, 1–33.

[2] Faydalıoğlu, E., and Sürüoğlu, M., (2014). Tıbbi ve aromatik bitkilerin antimikrobiyal, antoksidan aktivitelerinin tayini ve kullanım olanakları. Erzincan University Journal of Science and Technology, 6, 233–265.

[3] Öztürk, A., and Özbek, H., (2005). The anti-Inflammatory activity of eugenia caryophllata essential oil: An animal model of anti-inflammatory activity. Electronic Journal of General Medicine, 2, 159–163.

[4] Sarışen, Ö., and Çalşkan, D., (2005). Fitoterapi: bitkilerle tedaviye dikkat (!). STED- Sürekli Tıp Eğitimi Dergisi, 14, 182–187.

[5] Çelikboyun, P., (2015). Ruscus aculeatus L. ve punica granatum L. bitkilerinin ekstrelerinin ve boyanmış kumaş örneklerinin antimikrobiyal özelliklerinin belirlenmesi. Balıkesir Üniversitesi Fen Bilimleri Enstitüsü.

[6] Vieira, A., (2010). A comparison of traditional anti-inflammation and anti-infection medicinal plants with current evidence from biomedical research. Results from a regional study. Pharmacognosy Research, 2, 293.

[7] Luís, Â., Domingues, F., and Duarte, A.P. (2011). Bioactive compounds, RP-HPLC analysis of phenolics, and antioxidant activity of some portuguese shrub species extracts. Natural Product Communications, 6, 1863-72.

[8] Salgado, P., Márquez, K., Rubilar, O., Contreras, D., and Vidal, G., (2019). The effect of phenolic compounds on the green synthesis of iron nanoparticles (FexOy-NPs) with photocatalytic activity. Applied Nanoscience (Switzerland), 9, 371–385.

[9] Devi, H.S., Boda, M.A., Shah, M.A., Parveen, S., and Wani, A.H. (2019). Green synthesis of iron oxide nanoparticles using Platanus orientalis leaf extract for antifungal activity. Green Processing and Synthesis, 8, 38–45.

[10] Can, M., (2020). Green gold nanoparticles from plant-derived materials: An overview of the reaction synthesis types, conditions, and applications. Reviews in Chemical Engineering, 36, 859–877.

[11] Ying, S., Guan, Z., Ofoegbu, P.C., Clubb, P., Rico, C., He, F., and Hong, J., (2022). Green synthesis of nanoparticles: Current developments and limitations. Environmental Technology & Innovation. 26, 102336.

[12] Singh, A., Jain, D., Upadhyay, M.K., Khandelwal, N., and Verma, H.N., (2010). Green synthesis of silver nanoparticles using argemone mexicana leaf extract and evaluation of their antimicrobial activities. Article in Digest Journal of Nanomaterials and Biostructures, 5, 483–489.

[13] Gur, T., Meydan, I., Seckin, H., Bekmezci, M., and Sen, F. (2021). Green synthesis, characterization and bioactivity of biogenic zinc oxide nanoparticles. Environmental Research, 111897.

[14] Erduran, V., Bekmezci, M., Bayat, R., and Sen, F. (2022). Functionalized carbon material-based electrochemical sensors for day-to-day applications. Functionalized Nanomaterial-Based. Electrochemical Sensors, 97–111.

[15] Goksu, H., Bekmezci, M., Bayat, R., Altuner, E.E., and Şen, F. (2021). The synthesis and characterization of size-controlled bimetallic nanoparticles. Nanomaterials for Direct Alcohol Fuel Cells, 433–447.

[16] Akin, M., Bayat, R., Erduran, V., Bekmezci, M., Isik, I., and Şen, F. (2021). Carbon-based nanomaterials for alcohol fuel cells. Nanomaterials for Direct Alcohol Fuel Cells, 319–336.

[17] Dessale, M., Mengistu, G., and Mengist, H.M. (2022). Nanotechnology: a promising approach for cancer diagnosis, therapeutics and theragnosis. International Journal of Nanomedicine, 17, 3735.

[18] Takáč, P., Michalková, R., Čižmáriková, M., Bedlovičová, Z., Balážová, Ľ., and Takáčová, G. (2023). The role of silver nanoparticles in the diagnosis and treatment of cancer: are there any perspectives for the future?. Life, 13(2), 466.

[19] Sanati, M., Afshari, A.R., Kesharwani, P., Sukhorukov, V.N., and Sahebkar, A. (2022). Recent trends in the application of nanoparticles in cancer therapy: The involvement of oxidative stress. Journal of Controlled Release, 348, 287–304.

[20] Artiukh, L., Povnitsa, O., Zahorodnia, S., Pop, C. V., and Rizun, N. (2022). Effect of coated silver nanoparticles on cancerous vs. healthy cells. Journal of Toxicology, 2022

[21] Klaus-Joerger, T., Joerger, R., Olsson, E., and Granqvist, C.G., (2001). Bacteria as workers in the living factory: Metal-accumulating bacteria and their potential for materials science. Trends in Biotechnology, 19, 15–20.

[22] Ahmad, A., Mukherjee, P., Senapati, S., Mandal, D., Khan, M.I., Kumar, R., and Murali, S., (2003). Extracellular biosynthesis of silver nanoparticles using the fungus fusarium oxysporum. Colloids and Surfaces B: Biointerfaces, 28, 313–318.

[23] Duncan, T. V., (2011). Applications of nanotechnology in food packaging and food safety: Barrier materials, antimicrobials and sensors. Journal of Colloid and Interface Science, 363, 1–24.

[24] Beykaya, M., and Çağlar, A., (2016). Bitkisel özütler kullanılarak gümüş-nanopartikül (agnp) sentezlenmesi ve antimikrobiyal etkinlikleri üzerine bir araştırma. Afyon Kocatepe University Journal of Sciences and Engineering, 16, 631–641.

[25] Rai, M., Yadav, A., and Gade, A., (2009). Silver nanoparticles as a new generation of antimicrobials. Biotechnology Advances, 27, 76–83.

[26] Naghizadeh, A., Mizwari, Z.M., Ghoreishi, S.M., Lashgari, S., Mortazavi-Derazkola, S., and Rezaie, B., (2021). Biogenic and eco-benign synthesis of silver nanoparticles using jujube core extract and its performance in catalytic and pharmaceutical applications: Removal of industrial contaminants and in-vitro antibacterial and anticancer activities. Environmental Technology & Innovation, 23, 101560.

[27] Bharadwaj, K.K., Rabha, B., Pati, S., Choudhury, B.K., Sarkar, T., Gogoi, S.K., Nayanjyoti, K., Debabrat, B., Zulhisyam, A.K., and Hisham A.E., (2021). Green synthesis of silver nanoparticles using diospyros malabarica fruit extract and assessments of their antimicrobial, anticancer and catalytic reduction of 4-nitrophenol (4-np). Nanomaterials, 11, 1999.

[28] Abdel-Rahman, L.H., Al-Farhan, B.S., Abou El-ezz, D., Abd–El Sayed, M.A., Zikry, M.M., and Abu-Dief, A.M., (2022). Green biogenic synthesis of silver nanoparticles using aqueous extract of moringa oleifera: access to a powerful antimicrobial, anticancer, pesticidal and catalytic agents. Journal of Inorganic and Organometallic Polymers and Materials, 32, 1422–1435.

[29] Rozhin, A., Batasheva, S., Kruychkova, M., Cherednichenko, Y., Rozhina, E., and Fakhrullin, R., (2021). Biogenic silver nanoparticles: synthesis and application as antibacterial and antifungal agents. Micromachines, 12.

[30] Meydan, I., Seckin, H., Burhan, H., Gür, T., Tanhaei, B., and Sen, F. (2022). Arum italicum mediated silver nanoparticles: Synthesis and investigation of some biochemical parameters. Environmental Research, 204, 112347.

[31] Karimi, F., Rezaei-savadkouhi, N., Uçar, M., Aygun, A., Elhouda Tiri, R.N., Meydan, I.,Aghapour, E., Seckin, H., Berikten, D., Gur, T., and Sen, F., (2022). Efficient green photocatalyst of silver-based palladium nanoparticles for methyle orange photodegradation, investigation of lipid peroxidation inhibition, antimicrobial, and antioxidant activity. Food and Chemical Toxicology, 169, 113406.

[32] Kirby-Bauer disk diffusion susceptibility test protocol. (2009).

[33] Mosmann, T., (1983). Rapid colorimetric assay for cellular growth and survival: application to proliferation and cytotoxicity assays. Journal of Immunological Methods, 65, 55–63.

[34] Alley, M.C., Scudiero, D.A., Monks, A., Hursey, M.L., Czerwinski, M.J., Fine, D.L., Abbott, B.J., Mayo, J.G., Sjoemaker, R.H., and Boyd, M.R., (1988). Feasibility of drug screening with panels of human tumor cell lines using a microculture tetrazolium assay. Cancer Research, 48, 589–601.

[35] Razavi, M., (2017). Biomaterials for tissue engineering. bentham science publishers.

[36] Singhal, G., Bhavesh, R., Kasariya, K., Sharma, A.R., and Singh, R.P., (2011). Biosynthesis of silver nanoparticles using ocimum sanctum (tulsi) leaf extract and screening its antimicrobial activity. Journal of Nanoparticle Research, 13, 2981–2988.

[37] Saxena, A., Tripathi, R.M., Zafar, F., and Singh, P., (2012). Green synthesis of silver nanoparticles using aqueous solution of Ficus benghalensis leaf extract and characterization of their antibacterial activity. Materials Letters, 67, 91–94.

[38] Karakaya, F., (2021). Yeşil sentez yöntemiyle ruscus aculeatus l. bitkisi kullanılarak gümüş nanopartiküllerin sentezi ve antibiyofilm, antimikrobiyal, antikanser aktivitelerinin incelenmesi. Bartın Üniversitesi.
[39] Lu, X., Wang, J., Al-Qadiri, H.M., Ross, C.F., Powers, J.R., Tang, J., and A.Rasco, B., (2011). Determination of total phenolic content and antioxidant capacity of onion (Allium cepa) and shallot (Allium oschaninii) using infrared spectroscopy. Food Chemistry, 129, 637–644.
[40] Dıblan, S., Kadiroğlu, P., and Yurdaer Aydemir, L., (2018). FT-IR Spectroscopy Characterization and Chemometric Evaluatıon Of Legumes Extracted with Different Solvents. Food and Health, 4, 80–88.
[41] Del Bonis-O'Donnel, J.T., Beyene, A., Chio, L., Demirer, G., Yang, D., and Landry, M.P., (2017). Engineering molecular recognition with bio-mimetic polymers on single walled carbon nanotubes. Journal of Visualized Experiments, 119, 2017, 55030.
[42] Mellado-Mojica, E., Seeram, N.P., and López, M.G., (2016). Comparative analysis of maple syrups and natural sweeteners: Carbohydrates composition and classification (differentiation) by HPAEC-PAD and FTIR spectroscopy-chemometrics. Journal of Food Composition and Analysis, 52, 1–8.
[43] Se, K.W., Ghoshal, S.K., Wahab, R.A., Ibrahim, R.K.R., and Lani, M.N., (2018). A simple approach for rapid detection and quantification of adulterants in stingless bees (Heterotrigona itama) honey. Food Research International, 105, 453–460.
[44] Heydari, R. and Rashidipour, M., (2015). Green synthesis of silver nanoparticles using extract of oak fruit hull (jaft): Synthesis and in vitro cytotoxic effect on MCF-7 cells. International Journal of Breast Cancer, 2015.
[45] Suman, T.Y., Radhika Rajasree, S.R., Kanchana, A., and Elizabeth, S.B., (2013). Biosynthesis, characterization and cytotoxic effect of plant mediated silver nanoparticles using Morinda citrifolia root extract. Colloids and Surfaces B: Biointerfaces, 106, 74–78.

Contents lists available at *Dergipark*

Journal of Scientific Reports-A

journal homepage: *https://dergipark.org.tr/tr/pub/jsr-a*

E-ISSN: 2687-6167 ***Number 55, December 2023***

RESEARCH ARTICLE

Receive Date: 28.07.2023 *Accepted Date: 03.10.2023*

Deep learning-based distributed denial of service detection system in the cloud network

Emine Deniz[1], Soydan Serttaş[2,*]

[1]*Kütahya Dumlupınar University, Department of Computer Engineering, Kütahya, Türkiye, ORCID:0000-0003-0670-3578*
[2]*Kütahya Dumlupınar University, Department of Computer Engineering, Kütahya, Türkiye, ORCID:0000-00001-8887-8675*

Abstract

Cloud computing offers an efficient solution that enables businesses and users to deliver flexible and scalable services by sharing resources. However, this shared resource pool also exposes vulnerabilities to various cyber threats, such as Distributed Denial of Service (DDoS) attacks. These DDoS attacks, due to their potential impact, can be highly destructive and disruptive. They render servers unable to serve users, leading to system crashes. Moreover, they can severely tarnish the reputation of organizations and result in significant financial losses. Consequently, DDoS attacks are among the most critical threats faced by institutions and organizations.

The primary objective of this study is to identify and detect DDoS attacks within cloud computing environments. Given the challenges associated with acquiring a cloud-based dataset, the main motivation behind this research was to construct a dataset within a cloud-based system and subsequently evaluate the intrusion detection capabilities of deep learning (DL) algorithms using this dataset. Initially, an HTTP flood attack was executed after creating a network topology within the OpenStack framework. The study employed Convolutional Neural Network (CNN), Artificial Neural Network (ANN), and Long Short-Term Memory (LSTM) models for attack detection. The performance of these models was assessed using various measurement metrics, and it was found that the LSTM model delivered the most impressive results, achieving an accuracy rate of 98%.

Keywords: Distributed denial of service; Deep learning; Anomaly detection; Cybersecurity; Cloud computing; OpenStack; Convolutional neural network; Long short-term memory; Artificial neural networks.

Corresponding author.
e-mail: soydan.serttas@dpu.edu.tr

1. Introduction

In addition to the many benefits that the internet has brought to our daily lives, there is also the downside of increased vulnerability to cyber threats. Various attacks, each with its own level of intensity and risk, can inflict critical damage on users and organizations. Denial of Service (DoS) and Distributed Denial of Service (DDoS) attacks are among the most prevalent attacks in network communication. These attacks generate abnormal communication traffic on the network, causing the system to slow down compared to normal operations or rendering it unusable for regular users. DoS attacks disrupt a target system's ability to provide services, while DDoS attacks serve the same purpose but originate from multiple sources.

In 2017, the National Institute of Standards and Technology (NIST) detected DDoS attacks and unauthorized intrusions that resulted in losses of up to $65.5 billion [1]. According to research by Kaspersky, the average damage caused by a DDoS attack is $120,000 for small businesses and $2,000,000 for large enterprises [2]. Due to their high capacities and prolonged impact durations, DDoS attacks pose a significant threat to institutions and organizations [3]. In 2007, Estonia experienced a DDoS attack that affected numerous public institutions and individuals [4]. In October 2016, a DDoS attack on one of America's Domain Name System (DNS) service providers made headlines worldwide. Subsequently, in 2018, a massive DDoS attack targeted GitHub servers [5]. These incidents aren't limited to Europe and America; even a private Turkish bank server fell victim to a DDoS attack [6].

The integration of cloud computing with the internet and computer networks has exposed cloud services to cyber threats and attacks [7]. Cloud computing faces various security threats, with a significant concern being the threat to the availability of cloud services. Among these threats, the DDoS attack stands out, directly impacting the accessibility of cloud services. During a DDoS attack, malicious actors intentionally exhaust cloud resources, preventing legitimate users from accessing the cloud's services and resources.

These incidents underscore the need for a reliable method to detect DDoS attacks. Therefore, the development of an effective DDoS detection system plays a crucial role in monitoring suspicious activities in the cloud [8]. In recent years, researchers have turned to Machine Learning (ML) methods for DDoS attack detection. ML algorithms, primarily relying on datasets, can identify abnormal behaviors in the network [9]. However, ML algorithms based on datasets may be slow to detect new attacks. Consequently, DL has gained popularity [10].

The main contributions of this research are as follows:

- The study introduces a novel DDoS attack scenario designed within a general cloud environment.
- A new network topology was created using the OpenStack [11] software, a public cloud testing environment. Training and test datasets containing DDoS attacks were generated with the open-source OpenStack software, which facilitates the creation and management of virtual servers.
- Attack and normal data logs were recorded by executing unique DDoS attack scenarios on the created network.
- Feature extraction was conducted on the collected data
- TensorFlow [12] was integrated into the OpenStack software framework, enabling the development of ANN, CNN, and LSTM models within the cloud network environment.

The novelty of this DDoS detection system lies in its approach of simulating DDoS attacks on a cloud platform and utilizing deep learning algorithms for their detection.

2. Literature review

The University of Minnesota experienced a significant DDoS attack for the first time in 1999. The university's network was unavailable for two days [13]. Since that date, DDoS attacks have increasingly become the most prevalent type of attack on network communications. Fig. 1 illustrates that the number of DDoS attacks has been rising each year.

Over the past few years, numerous detection and prevention techniques have been reported to mitigate DDoS attacks [15-18]. Many studies utilize ML approaches, such as classification, clustering, and prediction methods [19].

Igbe proposed a Dendritic Cell Algorithm (DCA) that utilizes the concept of Artificial Immune System (AIS) for DDoS attack detection. The proposed algorithm achieved an accuracy of 96% in detecting attacks [20].

Elsayed et al. suggested a model that combines One-Class Support Vector Machine (OC-SVM) and LSTM models using an AutoEncoder (AE) to improve performance. However, the proposed model achieved 74% accuracy [21].

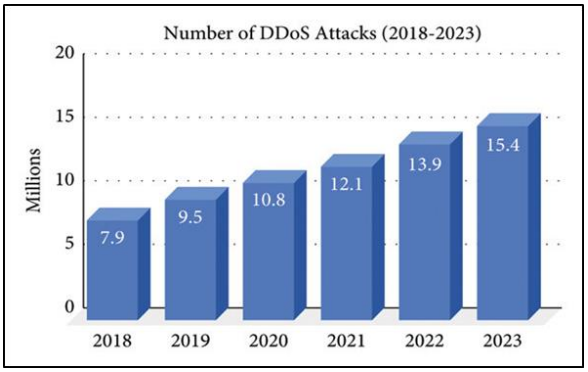

Fig. 1. Cisco's DDoS total attack volume history and forecast (2018-2023) [14].

Another study introduced a DL framework for network attack detection using LSTM and AE. The researchers conducted a comparison between the DL model and traditional ML algorithms using the NSL-KDD dataset. They showed that DL models outperformed ML models [22].

Wang et al. presented a novel model that combines AE with the SVM algorithm. After training, the SVM was utilized to detect anomalies within the extracted features. The model obtained an accuracy value of 88.73% in binary classification tasks using the NSL-KDD dataset [23].

Yavuz and Aygun proposed AE and Denoising AutoEncoder (DAE) techniques for attack detection. The DAE model provided with an accuracy of 88.65% [24].

Heikkonen and Farahnakian suggested an attack detection model that includes four AEs, where each AE output feeds into the next one in the current layer. The performance of the model was evaluated using the well-known KDD-CUP-99 dataset, achieving good performance with a detection rate of 94.53% [25].

Min et al. proposed a model using Memory-Augmented AutoEncoder (MemAE). The model achieved an F1-Score of 95% on the NSL-KDD dataset [26].

Anjum and Shreedhara introduced an ML method that relies on Semi-Supervised Learning for DDoS attack detection. According to their study, the proposed approach achieved an accuracy of 93% [27].

In the existing literature, there are also articles that analyze the utilization of ML in cloud computing [28]. Kushwah and Ali suggested an approach for detecting DDoS attacks in cloud environments consisting of Black Hole Optimization and ANN algorithms. The study used a dataset containing 12,500 training examples and 2,597 test examples. The highest accuracy achieved with the proposed method was reported to be 96% [29]. In another study, SVM and MLP classifiers were compared to detect DDoS TCP flood attacks in general clouds. The MLP model outperformed SVM with an accuracy of 94% compared to SVM's 92% [30]. Doshi et al. tested four different ML algorithms, SVM, DT, K-nearest neighbors (KNN), and Random Forest (RF), on normal and attack data collected from Internet of Things (IoT) based networks. The accuracy values of the four classifiers were 91%, 93%, 94%, and 99%, respectively [31].

Ma et al. proposed a multi-layered CNN model, showing that the CNN model outperformed SVM, DT, and Recurrent Neural Networks (RNN) in their study [32]. Potluri et al. also proposed a CNN-based detection approach, using a 3-layer and 2-dimensional (2D) CNN structure by converting data into images. The proposed CNN model achieved an accuracy of 91.14% in their study [33].

Ding and Zhai also proposed a CNN-based attack detection system. Their model consisted of a convolutional layer followed by three stacked stages with maximum pooling for feature extraction, forming a deep input features layer. The authors compared the outcomes of their model with traditional ML and DL methods using the NSL-KDD dataset. According to their findings, their proposed model demonstrated superior performance over the other approaches [34].

3. Materials and methodology

3.1. Cloud system

Cloud systems, commonly referred to as cloud computing, encompass the utilization of various services including servers, databases, data storage, networks, and software. These services are hosted within remote data centers and accessed via the Internet. Storing files in the cloud allows users to access their data from anywhere with an internet connection. Cloud computing is typically classified into two distinct approaches based on distribution models and service models, as illustrated in Fig. 2.

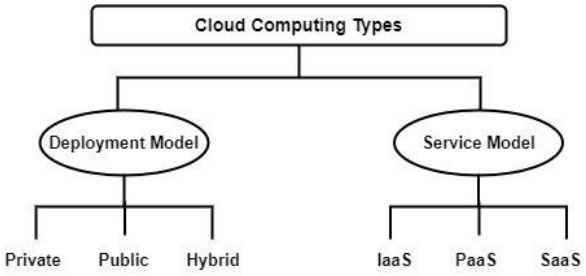

Fig. 2. Cloud computing types.

When considering the Distribution Model, it encompasses Public, Private, and Hybrid clouds. As for the Service Model, it includes IaaS (Infrastructure as a Service), PaaS (Platform as a Service), and SaaS (Software as a Service). Among these models, IaaS (Infrastructure as a Service) holds particular significance as it serves as the bedrock for flexible infrastructure resources, making it a fundamental component of cloud computing.

3.2. OpenStack

OpenStack is an open-source Infrastructure as a Service (IaaS) platform designed for hybrid and public cloud environments [11]. Its networking service ensures adaptable network connectivity in OpenStack cloud setups, maintaining a modular architecture to optimize resource utilization. Key components of OpenStack include:

- Nova: Manages virtual machines through APIs.
- Glance: Handles cloud image management and backups.
- Neutron: Manages virtual network structures.
- Cinder: Provides virtual block storage.

- Keystone: Ensures identity authentication and authorization.
- Swift: Offers additional storage services via HTTP API.

OpenStack is a modular, open-source cloud computing platform renowned for its scalability, support for hybrid clouds, and independence. Consequently, the network topology depicted in Fig. 3 was created to simulate a DDoS attack scenario within the OpenStack software environment.

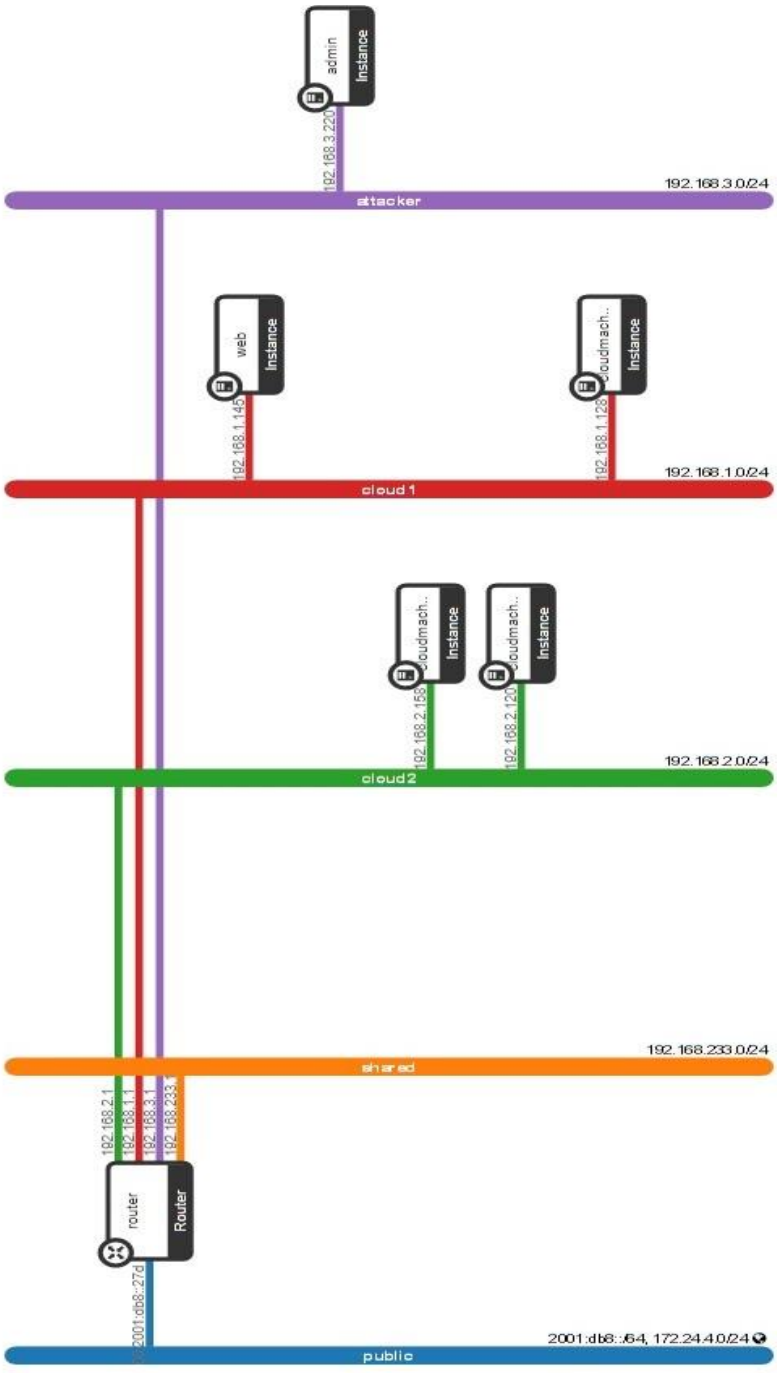

Fig. 3. Depicted network topology.

Each virtual instance is assigned an internal Internet Protocol (IP) address, used for communication among virtual instances belonging to the same tenants. In the context of the OpenStack cloud computing platform, a "tenant" is a structure used to isolate and manage resources like virtual machines, storage, and networks. For instance, various departments within an organization in the cloud communicate using these IP addresses. IP addresses starting with 192.x.x.x are considered internal. Tenants are separated from each other through distinct internal networks, as depicted in the OpenStack network topology shown in Figure 3. Tenant-1 is allocated to the orange network, tenant-2 operates within the green network, tenant-3 operates on the red network, and tenant-4 resides in the purple network. The virtual instance named 'web,' belonging to tenant-3, hosts a web server. All of these tenants establish external connectivity via a router connected to the public network. The web server on the red network, owned by tenant-3, was targeted in an HTTP flooding attack. Tenant-3 also has a virtual instance called 'cloudmachine-3,' which serves as a compute node. Virtual instances 'cloudmachine-1' and 'cloudmachine-2,' belonging to tenant-2, generated the HTTP flooding against the web server in the red network of tenant-3. Similarly, the administrator of tenant-4 initiated a flooding attack against the web server.

3.3. Dataset

A total of one hundred thousand rows of data were collected from the established network topology, comprising fifty thousand rows of normal data and fifty thousand rows of HTTP Flood attack data. Prior to utilizing the acquired data in standard ML and DL applications, preprocessing is necessary. The process of transforming raw data (in this study, pcap files) into structured formats to meet specific criteria is known as feature extraction. Each feature represents a dimension, variable, or quantity associated with a network traffic sample, which can be a packet, flow, or network during a defined time frame. Network traffic encompasses attributes such as source/destination IP addresses, protocol, transport ports, flags, and timestamps. Given that much of the information in pcap files might be unnecessary or not directly usable in DL applications, feature extraction was employed to prepare the data for further analysis.

3.4. Method

The flowchart depicting the process of this study is presented in Fig. 4. Initially, the network scenario described in section 3.2 of the OpenStack software was implemented to collect data related to both DDoS attacks and normal activity, employing the 'tcpdump' tool. Before this acquired data could be used in standard ML and DL applications, it had to undergo processing. The transformation of raw data into structured formats to meet specific criteria is known as feature extraction. The collected data was stored as a Pcap file, and using the Scapy library in Python, essential parameters were extracted from the raw data. These extracted features were then saved in a CSV file. Subsequently, these features were leveraged for attack detection through the use of DL models, such as ANN, CNN, and LSTM models.

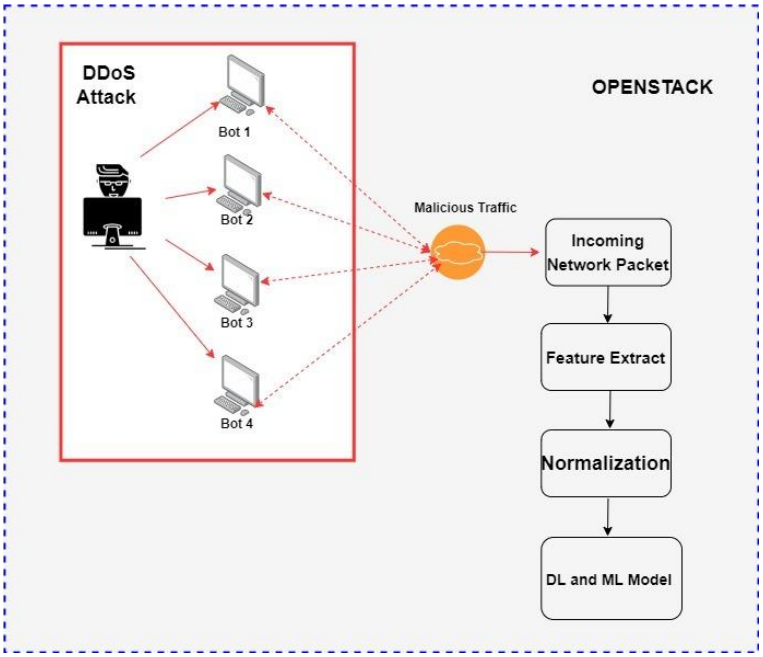

Fig. 4. The proposed system.

3.5. Evaluation

Performance metrics for evaluating deep learning methods are crucial. The typical performance evaluation criteria include accuracy, precision, F1-score, and recall. The ROC (Receiver Operating Characteristic) value is a metric employed to evaluate the performance of a classification model, especially in classification problems such as deep learning models. A higher ROC curve indicates better model performance.

The confusion matrix plays a vital role in providing a comprehensive assessment of the performance of a deep learning model and in understanding the nature of errors it makes. It aids in visualizing and quantifying the correlation between the actual values and the predictions generated by the model. The confusion matrix is constructed by comparing the actual outcomes with the model's predictions, allowing for the calculation of True Positives (TP), True Negatives (TN), False Positives (FP), and False Negatives (FN) values.

Accuracy measures how well a prediction matches the actual outcome and is calculated using the formula shown in Equation 1.

$$Accuracy = \frac{TN+TP}{TN+TP+FP+FN} \tag{1}$$

Precision is a metric obtained by dividing the number of correctly detected DDoS attacks by the total number of detections labeled as true. It measures the system's accuracy in correctly identifying DDoS attacks, differentiating them from other attacks or normal flows. The formula for precision is defined in Equation 2.

$$Precision = \frac{TP}{FP+TP} \tag{2}$$

The recall is calculated by dividing the number of predicted attacks by the total number of actual attacks. As a result, it shows how many DDoS attacks were correctly identified and is also known as the "true positive rate." The formula for recall is provided in Equation 3.

$$Recall = \frac{TP}{FN+TP} \tag{3}$$

The F1 score is a metric that strikes a balance between precision and recall, producing a value between 0 and 1. The formula for F1-Score is defined in Equation 4.

$$F1\ Score = \frac{2*Precision*Recall}{Precision+Recall} \tag{4}$$

4. Results and discussion

4.1. DDoS attack detection using ANN model

An artificial neural network is a computational model inspired by the structure and functioning of the human brain, used for tasks such as pattern recognition and deep learning. Fig. 5 provides a detailed overview of the ANN model's architecture in this study. The initial dense layer employs the ReLU activation function, while the second layer uses the Sigmoid function. The model is compiled with the "CrossEntropy" loss function and employs the "Adam" optimizer.

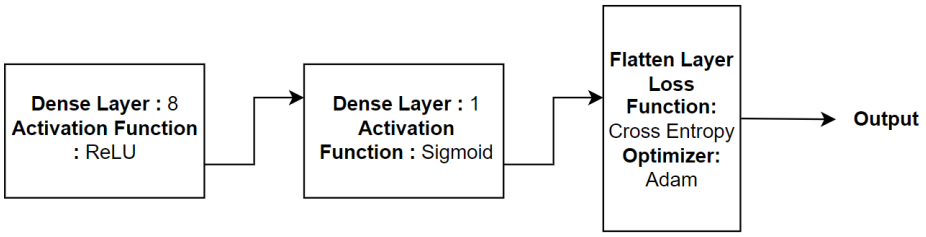

Fig. 5. ANN model architecture.

The ANN model described here follows a two-layer architecture. Generally, the number of parameters within a specific layer of a model corresponds to the count of trainable elements within that layer. As shown in Table 1, the first layer comprises 208 trainable parameters, while the second layer consists of 9 trainable parameters. Consequently, the total count of trainable parameters in the ANN model amounts to 217.

Table 1. ANN model summary.

Layer	Output shape	#Parameters
Dense layer	(,8)	208
Dense layer	(,1)	9

After training the created ANN model with data obtained from the OpenStack platform, the accuracy value was obtained as 85%, the precision value was 98%, the recall value was 77%, and the F1 score was 86%. These evaluation metrics suggest the need for more advanced models in attack detection. In classification problems like this, metrics such as recall, precision, ROC value, and confusion matrix are examined, similar to deep learning models. Fig. 6 presents the ROC curve for the ANN model. When analyzing the ROC curve, it ideally should be

close to 1. However, due to the limited sophistication of the ANN model, the desired ROC curve could not be achieved.

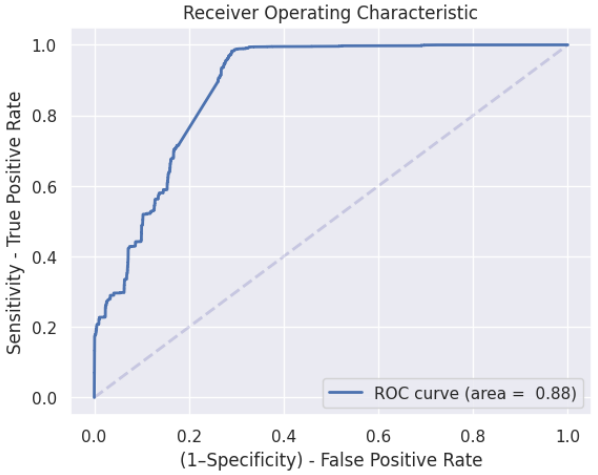

Fig. 6. ROC graph of ANN model.

The confusion matrix for the ANN model is also presented in Fig. 7. The ANN model successfully identified 12,752 instances of attack data but misclassified 489 attack instances as normal data. It correctly identified 16,945 out of 21,759 normal data instances as normal, but it erroneously labeled 4,814 normal data instances as attacks. The ANN model's classification of 4,814 normal data instances as attacks signifies a significant discrepancy. To address this issue and reduce this number, the development of more advanced models is warranted.

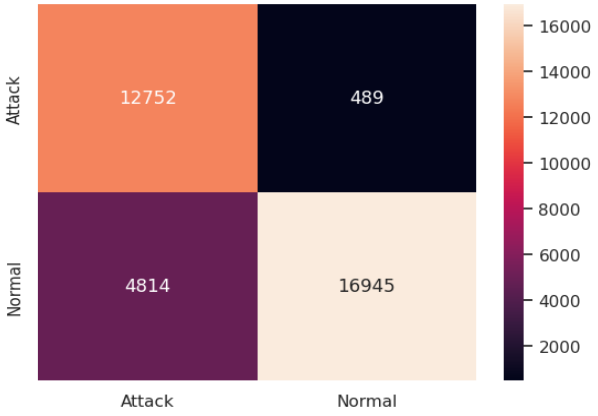

Fig. 7. Confusion Matrix of ANN model.

4.2. DDoS attack detection using CNN model

CNN, is a type of artificial neural network commonly applied in deep learning, particularly for tasks such as image processing and recognition. Fig. 8 shows a detailed overview of the CNN model architecture proposed by the

authors of this study. The CNN model adopts a 10-layer architecture. A dropout layer is employed to mitigate overfitting in the CNN model, while a pooling layer is used to reduce data dimensions and optimize computations. The integration of dropout and pooling layers has been leveraged to enhance the performance and generalization capability of the CNN model utilized in this study. The "ReLU" activation function has applied across all layers. The stride value in CNN determines the steps at which data is shifted and influences the size of the feature map; a larger stride reduces both size and computation cost. Meanwhile, the padding value is utilized to either maintain or decrease the size of the feature map after convolution; 'same' padding retains the size, while 'valid' padding reduces it. In our study, 'same' padding has been employed to maintain the size of the feature map. To reduce the number of parameters and computation cost, a stride size of 2 has been selected. The model has compiled with the "CrossEntropy" loss function and the "Adam" optimizer.

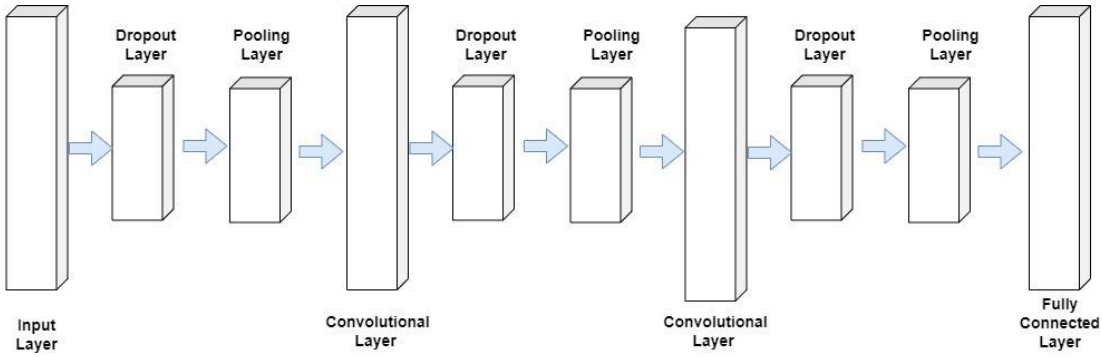

Fig. 8. Proposed CNN model architecture.

Convolutional layers are the layers trained in the CNN model while pooling layers have no trainable parameters. Table 2 displays the layers of the CNN model and the number of trainable parameters in each layer. The total number of trainable parameters in the CNN model is 22,561. The presence of a higher number of trainable parameters in the CNN model, as compared to the ANN model, has resulted in improved outcomes.

Table 2. CNN model summary.

Layer	Output shape	#Parameters
Input layer	(22,32)	1632
Dropout layer	(22,32)	0
Pooling layer	(11,32)	0
Convolutional layer	(11,64)	4160
Dropout layer	(11,64)	0
Pooling layer	(5,64)	0
Convolutional layer	(5,128)	16512
Dropout layer	(5,128)	0
Pooling layer	(2,128)	0
Fully connected layer	(,1)	257

After training the created CNN model with data obtained from the OpenStack platform, the accuracy value was obtained as 97%, the precision value was 98%, the recall value was 92%, and the F1-score was 95%. Figure 9

provides the ROC curve for the CNN model. The ROC curve of the CNN model is close to 1 indicating that the CNN model is more successful than the ANN model in the dataset obtained in this study.

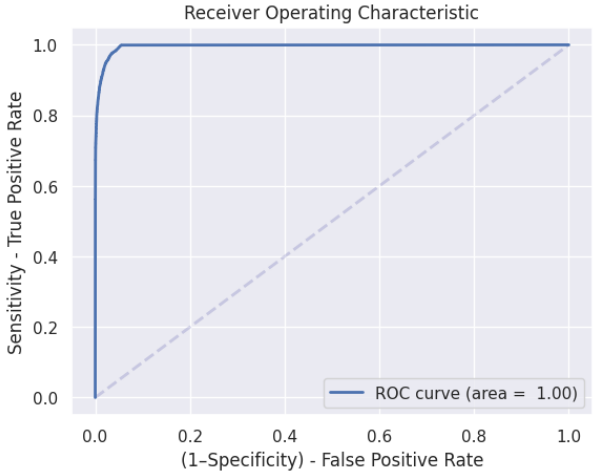

Fig. 9. ROC graph of CNN model.

The confusion matrix for the CNN model is shown in Figure 10. Due to their ability to automatically extract pertinent features, CNN models exhibit better performance compared to the ANN model. The CNN model correctly classified 32,365 instances of attack data as attacks but erroneously labeled 365 attack instances as normal data. It accurately identified 26,418 out of 29,053 normal data instances but misclassified 2,635 normal data instances as attacks. When analyzing the confusion matrix, it becomes apparent that the CNN model has higher accuracy in correctly identifying attack data as attacks and normal data as normal when compared to the ANN model.

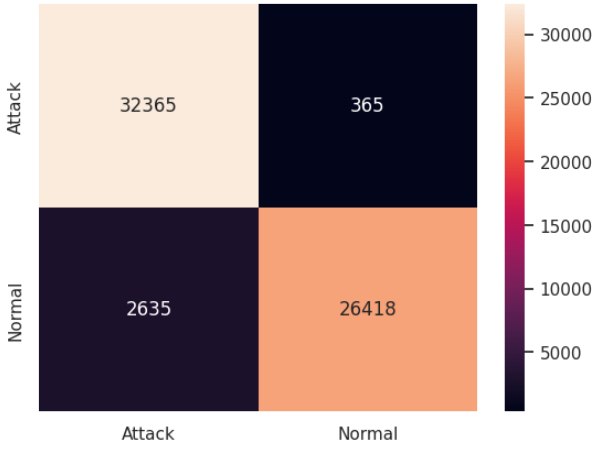

Fig. 10. Confusion Matrix of CNN model.

4.3. DDoS attack detection using LSTM model

LSTM is a specialized deep-learning architecture designed to capture and model long-term dependencies and sequential patterns in data. Figure 11 provides a detailed overview of the LSTM model architecture proposed by the authors of this study. The "ReLU" activation function is used in all layers. The model is compiled with the "CrossEntropy" loss function and the "Adam" optimizer.

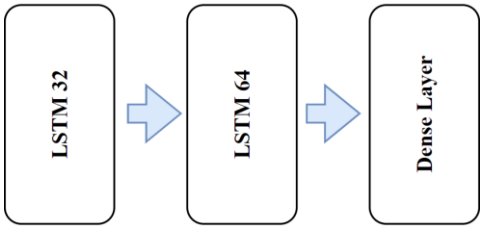

Fig. 11. LSTM model architecture.

The LSTM model has a 3-layer architecture. Table 3 shows that the first layer has 14,848 trainable parameters, the second layer has 4,160, and the last layer has 965. The total number of trainable parameters in the LSTM model is 19,073.

Table 3. LSTM model summary.

Layer	Output shape	#Parameters
LSTM32 layer	(,32)	14848
LSTM64 layer	(,64)	4160
Dense layer	(,1)	965

After training the created LSTM model with data obtained from the OpenStack platform, the accuracy value was obtained as 98%, the precision value was 99%, the recall value was 94%, and the F1-score was 97%. Figure 12 provides the ROC curve for the LSTM model. The ROC curve of the LSTM model being close to 1 indicates that the LSTM model is more successful than the ANN and the CNN models in the dataset obtained in this study.

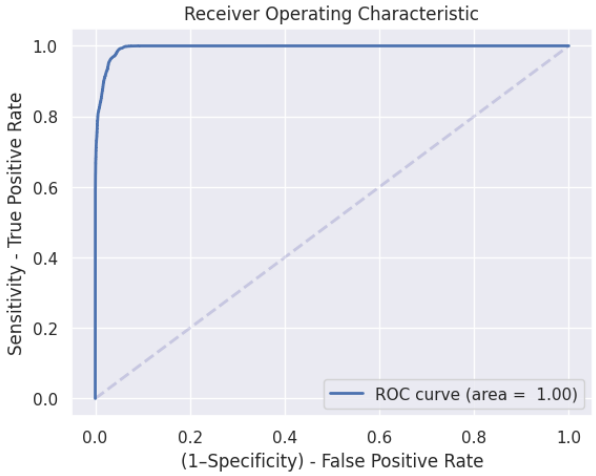

Fig. 12. ROC graph of LSTM model.

The confusion matrix of the LSTM model is presented in Figure 13. The LSTM model has correctly identified 33,234 attack instances as attacks, but misclassified 169 attack instances as normal data. It also correctly classified 34,727 normal instances as normal, but misclassified 1,854 normal instances as attacks. When examining the complexity matrix of the three models, it is evident that the LSTM model performed the best in correctly predicting attack instances as attacks and normal instances as normal.

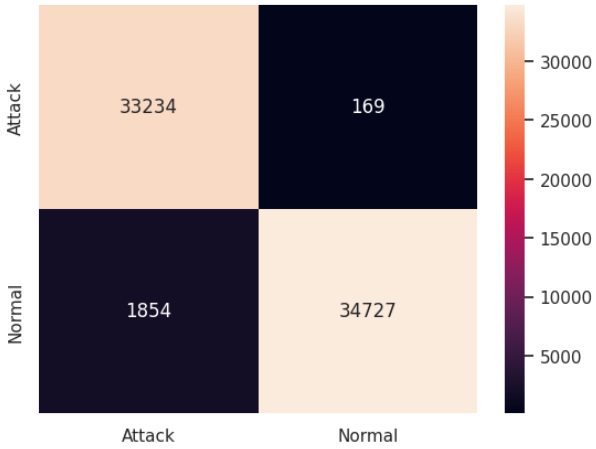

Fig. 13. Confusion Matrix of LSTM model.

4.4. Comparison of deep learning models

To determine which model excels in detecting DDoS attacks, we calculated accuracy, precision, recall, and F1-score values for the DL models. Table 4 presents the assessment metrics for these DL models. All DL models underwent training, validation, and testing using a 70:15:15 dataset split. The "Batch" size signifies the number of samples employed in each iteration during model training, typically ranging from 16 to 512. In this study, we set the

"Batch" sizes to 8, 16, 32, and 64, discovering that a "Batch" size of 32 yielded the most favorable results after DL model training. The "Epoch" number indicates how many times the entire training dataset is presented to the model during training. Each epoch encompasses a full iteration through the dataset, and conducting multiple epochs allows the model to learn from the data repeatedly, potentially enhancing its performance. In this study, we utilized 30 epochs. Furthermore, we implemented early stopping, a technique that interrupts the model training process when the validation loss starts to rise on the validation set. This approach aids in preventing overfitting and ensures that the model halts at an optimal point during training.

Table 4. Evaluation metrics and results of deep learning models (ANN, CNN, LSTM).

Model	Accuracy			Precision	Recall	F1 Score
	Train	Test	Validation			
ANN	0.85	0.85	0.84	0.98	0.77	0.86
CNN	0.97	0.97	0.97	0.98	0.92	0.95
LSTM	**0.98**	**0.98**	**0.98**	**0.99**	**0.94**	**0.97**

When analyzing Table 4, it becomes evident that the LSTM model boasts the highest accuracy at 98% on the acquired dataset. While accuracy is a valuable metric for assessing a model's performance, it should not stand alone. Precision values reveal that the LSTM model achieved 99%, while CNN and ANN both attained 98%. A closer examination of Recall and F1-Score metrics highlights that the LSTM model has significantly outperformed the ANN. The ROC AUC scores for these models were as follows: ANN achieved an AUC of 0.88, while CNN and LSTM both achieved perfect AUC scores of 1. The ROC AUC scores provide valuable insights into the discriminative power of these models. A perfect AUC score of 1 indicates that both CNN and LSTM achieved flawless discrimination between positive and negative classes. On the other hand, while ANN performed well with an AUC of 0.88, it exhibits slightly lower discriminative ability compared to CNN and LSTM.

4.5. Positioning the study in the literature

Cloud systems have increasingly become a crucial technology for data storage, processing, and analysis in today's world. However, as shown in Table 5, research in this field remains limited, highlighting the importance of this study in addressing the gaps in the limited literature related to cloud systems. One significant aspect of this research is the dataset obtained through the utilization of cloud systems. This innovative approach in data collection and processing has enabled more effective handling and analysis of large datasets, emphasizing the contributions and uniqueness of this study.

In contrast, while most of the studies listed in Table 5 rely on traditional machine learning methods such as decision trees, KNN, and SVM, this study adopts deep learning techniques, including LSTM and CNN. This study stands out by achieving exceptionally high accuracy rates compared to other similar research. Specifically, the model's extraordinary effectiveness is evident, with an exceptional 98% accuracy rate achieved through the use of LSTM. These results highlight the successful application of deep learning methods in this study and demonstrate important contributions to the field of data analysis.

Table 5. Linking study results to the literature.

References	Dataset	Methods	Accuracy	Area detection
Sofi, Mahajan, & Mansotra, 2017	public	DT, SVM, MLP	91%, 92%, 96%	-
Sharma, Mahajan, & Mansotra, 2016	public	DT, SVM, ANN	90%, 91%, 94%	-
Igbe, Ajayi, & Saadawi, 2017	public	DCA	96%	-

Elsayed M. S., Le-Khac, Dev, & Jurcut, 2020	public	AE with OC-SVM, LSTM	74%	-
Su, Sun, Zhu, Wang, & Li, 2020	public	AE ile SVM	88%	-
Aygun & Yavuz, 2017	public	AE, DAE	88%	-
Farahnakian & Heikkonen, 2018	public	AE	94%	-
Min, Yoo, Kim, Shin, & Shin, 2021	public	MemAE	95%	-
Derakhsh, Daneshjoo, & Delara, 2018	public	GA	64%	-
Anjum & S, 2019	public	Semi-Supervised Learning	93%	-
Kushwah & Ali, 2017	private	ANN	96%	yes
Sahi, Lai, Li, & Diykh, 2017	private	SVM, MLP	92%, 94%	yes
Doshi, Apthorpe, & Feamster, 2018	private	KNN, SVM, DT	91%, 93%, 94%	yes
Potluri, Ahmed, & Diedrich, 2018	public	CNN	91%	-
Zhang, Yu, & Li, 2018	public	XGBoost	89%	-
This study	**private**	**ANN, CNN, LSTM**	**85%, 97%, 98%**	**yes**

5. Conclusion

DDoS attacks, recognized as a major threat to networks and cloud systems, present substantial risks to computer system security due to their potential impact. ML and DL are two of the most widely explored technologies for intrusion detection systems. Nevertheless, the challenge of acquiring a cloud-based dataset for assessing ML and DL algorithms poses a significant hurdle. The absence of such a dataset served as the primary motivation for this research.

This study introduces the design of a cloud-based DDoS attack detection system and compares the performance of DL algorithms. We established a network topology using the OpenStack framework and gathered DDoS attack data through the simulation of HTTP flood attacks. Subsequently, we employed three distinct DL models - ANN, CNN, and LSTM algorithms - to detect attacks using the collected data. Our analysis encompassed multiple performance metrics, including accuracy, precision, recall, F1-score, and ROC curve assessments.

Among the DL models employed in this study, the LSTM model exhibited notably higher precision, recall, and F1-score values—99%, 94%, and 97%, respectively—compared to the ANN and CNN models, demonstrating its superior performance. The ROC curve analysis effectively illustrated how adeptly the models classified the labels. Based on their ROC curves, the CNN and LSTM models delivered the most promising results in this study.

For future research, we suggest diversifying the cloud network topology by creating various types of attack scenarios and expanding the dataset classes. Additionally, the concurrent execution of DL models and the incorporation of an ensemble voting technique could enhance attack detection capabilities.

Acknowledgements

There is no conflict of interest with any person/institution in the prepared article.

References

[1] M. Mittal, K. Kumar and S. Behal, "Deep learning approaches for detecting DDoS attacks: a systematic review", Soft Computing, 1-37, 2022.

[2] D. Berard, "A single DDoS attack can cost a company more than $400,000", https://www.kaspersky.com/about/press-releases/2015_a-single-ddos-attack-can-cost-a-company-more-than--400000, (accessed Jul. 27, 2023).

[3] C. Canongia, and R. A. Mandarino, "Cybersecurity: The new challenge of the information society", In Handbook of Research on Business Social Networking: Organizational, Managerial, and Technological Dimensions, 165-184, 2012, doi:10.4018/978-1-4666-4707-7.ch003.

[4] A. D. Samsoerizal, E. R. Hidayat, and A. Sukendro, "Analytical study of indonesian cybersecurity: lesson learned from estonian cyberattacks in 2007", International Journal of Arts and Social Science, 32-33, 2022.

[5] Balaban, "Denial-of-service attack", Intel J. Info. Sec. and Cybercrime, 10-59, 2021.

[6] Rawashdeh, M. Alkasassbeh, & M. Al-Hawawreh, "An anomaly-based approach for DDoS attack detection in cloud environment", International Journal of Computer Applications in Technology, 312-324, 2018.

[7] E. T. Ayan, M. S. Zengin, G. Deniz, H. A. Duru and B. Bardak, "Interpretable cybersecurity event detection in turkish: a novel dataset", In 2022 Innovations in Intelligent Systems and Applications Conference, Antalya, Turkey, 2022, pp. 1-6, doi: 10.1109/ASYU56188.2022.9925501.

[8] R. V. Deshmukh, and K. K. Devadkar, "Understanding DDoS attack & its effect in cloud environment", Procedia Computer Science, 202-210, 2015.

[9] N. Bindra, and M. Sood, "Detecting DDoS attacks using machine learning techniques and contemporary intrusion detection dataset", Automatic Control and Computer Sciences, 419-428, 2019.

[10] X. Yuan, P. He, Q. Zhu, and X. Li, "Adversarial examples: attacks and defenses for deep learning", IEEE transactions on neural networks and learning systems, 2805-2824, 2019.

[11] "The Most Widely Deployed Open Source Cloud Software in the World", https://www.openstack.org/ (accessed Feb. 1, 2023).

[12] M. Abadi, A. Agarwal, P. Barham, E. Brevdo, Z. Chen, C. Citro, *et al.* "TensorFlow: large-scale machine learning on heterogeneous distributed systems", http://download.tensorflow.org/paper/whitepaper2015.pdf, (accessed Jul. 20, 2023).

[13] G. C. Kessler, and D. E. Levin, "Denial-of-service attacks", John Wiley and Sons, 12 September 2015, doi.org/10.1002/9781118851678.ch18.

[14] Cisco Annual Internet Report (2018–2023) White Paper, Available: https: //www.cisco.com/c/en/us/solutions/collateral/executive-perspectives/annual-internet-report/white-paper-c11-741490.html, (accessed Jun. 6, 2020).

[15] Mirkovic, and P. Reiher, "A taxonomy of DDoS attack and DDoS defense mechanisms", ACM SIGCOMM Comput. Commun. Rev., 34(2), 39-53, 2004.

[16] G. Carl, G. Kesidis, R. R. Brooks, and S. Rai, "Denial-of-service attack-detection techniques", IEEE Internet computing, 10(1), 82-89, 2006.

[17] A. Y. Nur, and M. E. Tozal, "Record route IP traceback: combating DoS attacks and the variants", Computers & Security, 72, 13-25, 2018.

[18] S. T. Zargar, J. Joshi, and D. Tipper, "A survey of defense mechanisms against distributed denial of service (DDoS) flooding attacks", IEEE communications surveys & tutorials, 15(4), 2046-2069, 2013.

[19] R. Das, & T. H. Morris, "Machine learning and cyber security", International Conference on Computer, Electrical and Communication Engineering - ICCECE, 2017, pp. 1-7.

[20] O. Igbe, O. Ajayi, and T. Saadawi, "Denial of service attack detection using dendritic cell algorithm", 2017 IEEE 8th Annual Ubiquitous Computing, Electronics And Mobile Communication Conference, 2017, pp. 294-299.

[21] S. Elsayed, M. LE-Khac, N. A. Dev, and A. D. Jurcut, "Network anomaly detection using LSTM based

autoencoder", In Proceedings of the 16th ACM Symposium on QoS and Security for Wireless and Mobile Networks, 2020, pp. 37-45.

[22] M. S. Elsayed, N. A. Le-Khac, S. Dev, and A. D. Jurcut, "Ddosnet: A deep-learning model for detecting network attacks", A World of Wireless, Mobile and Multimedia Networks"(WoWMoM), 391-396, 2020.

[23] T. Su, H. Sun, J. Zhu, S. Wang, and Y. Li, "BAT: Deep learning methods on network intrusion detection using NSL-KDD dataset", IEEE Access, 8, 29575-29585, 2020.

[24] R. C. Aygun, and A. G. Yavuz, "Network anomaly detection with stochastically improved autoencoder-based models", In 2017 IEEE 4th International conference on cyber security and cloud computing (CSCloud), 2017, pp. 193-198.

[25] F. Farahnakian, and J. Heikkonen, "A deep auto-encoder based approach for intrusion detection system", In 2018 20th International Conference on Advanced Communication Technology (ICACT), 2018, pp. 178-183.

[26] Min, J. Yoo, S. Kim, and D. Shin, "Network anomaly detection using memory-augmented deep autoencoder", IEEE Access, 9, 104695-104706, 2021.

[27] M. Anjum, and K. S. Shreedhara, "Performance analysis of semi-supervised machine learning approach for DDoS detection", International Journal Of Innovative Research In Technology, 6(2), 144-147, 2019.

[28] Z. Zhong, M. Xu, M. A. Rodriguez, C. Xu, and R. Buyya, "Machine Learning-based Orchestration of Containers: A Taxonomy and Future Directions", ACM Comput. Surv. (CSUR), 2021.

[29] G. S. Kushwah, and S. T. Ali, "Detecting DDoS attacks in cloud computing using ANN and black hole optimization", 2nd International Conference on Telecommunication and Networks, pp. 1-5, 2017.

[30] A. Sahi, D. Lai, Y. Li, and M. Diykh, "An efficient DDoS TCP flood attack detection and prevention system in a cloud environment", IEEE Access, 5, 6036-6048, 2017, doi: 10.1109/ACCESS.2017.2688460.

[31] R. Doshi, N. Apthorpe, and N. Feamster, "Machine learning ddos detection for consumer internet of things devices" IEEE Security and Privacy Workshops (SPW), 2018, pp. 29-35.

[32] Ma, Y. Chai, L. Cui, D. Ma, Y. Fu, and A. Xiao, "A deep learning based DDoS detection framework for internet of things", IEEE International Conference On Communications, 2020.

[33] S. Potluri, S. Ahmed, and C. Diedrich, "Convolutional neural networks for multi-class intrusion detection system", 6th International Conference, MIKE 2018, Cluj-Napoca, Romania, December 20-22, 2018.

[34] Y. Ding, and Y. Zhai, "Intrusion detection system for NSL-KDD dataset using convolutional neural networks", In Proceedings of the 2018 2nd International conference on computer science and artificial intelligence, 2018, pp. 81-85.

Contents lists available at *Dergipark*

Journal of Scientific Reports-A

journal homepage: *https://dergipark.org.tr/tr/pub/jsr-a*

E-ISSN: 2687-6167 ***Number 55, December 2023***

RESEARCH ARTICLE

Receive Date: 11.08.2023 *Accepted Date: 06.10.2023*

Early-stage heart failure disease prediction with deep learning approach

Emin Demir[1*], Ferhat Bozkurt[2], Yusuf Ziya Ayık[3]

[1] *Atatürk University, Institute of Social Sciences, Management Information Systems PhD Program, Erzurum, ORCID:0009-0007-9657-2079*
[2] *Atatürk University, Faculty of Engineering, Department of Computer Engineering, Erzurum, ORCID:0000-0003-0088-5825*
[3] *Atatürk University, Vocational School of Technical Sciences, Computer Technologies Program, Erzurum, ORCID:0000-0002-7857-9417*

Abstract

Cardiovascular diseases rank the highest among diseases in terms of mortality rate and cause millions of deaths every year. Heart failure is a type of cardiovascular disease and its early diagnosis is extremely important for its prevention. It may be vitally important to understand to what extent which body values, characteristics and factors (age, gender, blood pressure, sugar, etc.) affect this disease and to predict whether the individual will have a possible heart attack in the future. In this study, firstly, the correlation level of the relevant body values with the disease is extracted and in the second stage, a method that predicts heart attack with DNN (Deep Neural Network) and CNN (Convolutional Neural Network) deep learning models is proposed. In the study, 918 observations obtained from the kaggle site were used. Firstly, missing data, categorical data, non-numerical features were checked. Then, outliers were cleaned and the relationship of the features in the dataset with the disease state was revealed by feature engineering operations on the data. Finally, deep neural network models were built and the model was trained and hyperparameter adjustment was performed with GridSearhCV to achieve the highest success rate. As a result of the study, Accuracy, Precision, Recall and F1-Score values were found as 0.9375, 0.9629, 0.9176, 0.9397 for DNN and 0.9312, 0.9512, 0.9176, 0.9340 for CNN respectively. The AUC value calculated from the ROC curve was found to be equal to 0.96 in both deep learning models.

Keywords: Deep learning, DNN, CNN, Heart attack prediction

1. Introduction

* Corresponding author. Tel.: +90-533-564-4954.

E-mail address: e_demir@odu.edu.tr

Cardiovascular diseases take nearly 18 million lives each year and are shown as the highest cause of death worldwide. The WHO (World Health Organization) states that the number of deaths due to heart disease will increase even more over the next 10 years. Early diagnosis of such a risky disease is vital to prevent the number of deaths due to the disease [1], [2]. The fact that there are many features to be checked in the diagnosis of heart failure (age, gender, type of chest pain, blood pressure, fasting blood sugar, ECG, etc.) makes the work of physicians seriously difficult [3].

For this reason, decision support systems that shorten the test time of this disease with artificial intelligence methods such as fuzzy logic, machine learning and deep learning and that can help physicians in the diagnosis of the disease have become one of the extremely valuable topics that have been intensively studied in recent years. When the studies carried out in the literature for heart failure prediction are analysed, it is seen that different artificial intelligence approaches and different techniques (pre-processing, extraction, clustering and hyperparameter etc.) have achieved success between 63.33 and 93.44. On the other hand, it is understood from the literature review that the majority of the studies for heart failure prediction are performed with machine learning methods, while the number of similar studies with deep learning is quite low.

In this study, in order to fill this gap in the literature and to help doctors in predicting heart failure, two different models were created with DNN and CNN deep learning methods and the performance of the models was compared with metrics accepted in the literature.

The important contributions of this article are:

- In the study, the kaggle heart failure prediction dataset, which is a combination of 11 common features of the universally accepted Cleveland (n=303), Hungarian (n=294), Swiss (n=123), Long Beach VA (n=200) and Stalog-Kalp (n=270) datasets, was used.
- Two different models were created with DNN and CNN deep learning methods and the performance of the models were compared with metrics accepted in the literature.
- In order to obtain the best result with the created deep learning models, hyperparameter adjustment was performed using GridSearhCV.
- At the end of the study, a model that can achieve Accuracy, Precision, Recall and F1-Score values in all of them in the range of 91% to 96% was proposed.

In the following sections of the study;

Part 2 – Related studies in the literature,
Part 3 – Materials and methods,
Part 4 - Research findings,
Part 5 - Discussion and conclusion

parts are included.

2. Related studies in the literature

At the end of the study, a model that can achieve Accuracy, Precision, Recall and F1-Score values in all of them in the range of 91% to 96% was proposed.

Yan et al. developed a Multi-Layer Perceptron (MLP) based decision support system to support the diagnosis of heart diseases. Using a total of 352 medical records collected from 5 heart patients, over 90% success was achieved. [4]. Das et al. obtained 89.01% accuracy using Statistical Analysis System (SAS) 9.1.3 core software, a neural network ensemble at its core, in the study for the diagnosis of heart disease [5]. In another study conducted by Abdullah and Rajalaxmi for heart disease diagnosis, Random Forest and Decision Tree models were used and 63.33% and 50.67% success was achieved respectively [6]. Shao et al. proposed a hybrid model approach using Logistic Regression, Multivariable Adaptive Regression Splines (MARS), Rough Clustering (RS) and Artificial Neural

Network and were achieved 83.93% success with both MARS-LR and RS-LR [7]. Cihan et al. In their study for the detection of Coronary Artery Disease, Naive Bayes, J48 Decision Tree, Multilayer artificial neural network (ANN) and 1R classification methods were compared with 303 case studies and they were obtained the best result with Multilayer ANN with a rate of 83.498% [8]. In their study, Özmen et al. compared the performance of J48, Logistic Regression, Support Vector Machine (SVM), Naive Bayes, Multilayer Perceptron, Random Forest, Adaboost, Bagging decision Trees and Single Layer Perceptron models considering their advantages and disadvantages. As a result of the comparison, SVM achieved the highest success rate with 89.47% [9]. Ozcan et al. aimed at early detection of heart disease with Support Vector Machine and Forward Propagation ANN using 170 case data and achieved 83.33% success with Forward Propagation ANN and 91.67% success with Support Vector Machine algorithm [10]. Göktaş and Yağanoğlu used Random Forest, K-Nearest Neighbor, SVM and C4.5 decision tree algorithms for heart attack prediction and compared their results. As a result of the study, the highest success rate was obtained in the C4.5 Decision Tree algorithm with an accuracy rate of 83.09%. [11]. In their study for the diagnosis of heart disease, Ekrem et al. achieved 86.88% success with Random Forest classification method by selecting features with particle swarm optimization on 303 cases [12]. In this study by Coşar and Deniz, heart disease early detection algorithm was developed with Random Forest, Logistic Regression and k-NN algorithm. The highest success rate of 88% was achieved with Random Forest [13]. Potur and Erginel applied different feature selection methods on 299 case data and compared Support Vector Machines, Logistic Regression, Multilayer Perceptron, J48 decision tree and Naive Bayes algorithms. The highest success rate of 90% was achieved with Multilayer Perceptron (MLP) [14]. In the study conducted by Gündoğdu for early detection of heart disease, 303 cases were examined and 7 different machine learning algorithms including Linear Discriminant Analysis, Decision Trees, K-Nearest Neighbor, Support Vector Machines, Naive Bayes, Random Forest and Gradient Boosting were compared. The best accuracy rate of 90.02% was obtained with the Random Forest machine learning algorithm [15]. Yilmaz and Yağin in 2021, in the study they aimed to compare the prediction results of Radial Basis Neural Network (RBF) and Multilayer Neural Networks (MLP), they reached an accuracy of 91.1% with MLP and 79.7% with RBF [16]. In the study conducted by Vatansever et al., Decision Tree, Logistic Regression, k-NN, Random Forest, Support Vector Machine and Naive Bayes models were used to predict heart disease with various machine learning algorithms by selecting features with Genetic Algorithm approach. As a result of the study, the highest success rate was obtained with 93.44% in the experiments with the genetic algorithm approach [17]. In the study conducted by Salman and Aksoy, hyperparameter selection was performed with the Random Forest algorithm and then feature selection was performed using the binary particle swarm intelligence method. At the end of the study, 79.66% success rate was achieved [18]. In their study, Coşkun and Kuncan examined 918 cases obtained through kaggle and evaluated the performances of Linear Discriminant Analysis, Support Vector Machines, Gaussian Naive Bayes, Random Forest and Decision Tree machine learning algorithms and found that the highest success rate was 90.76% with Random Forest [19]. In their study, Çil & Güneş compared the performance of Support Vector Machines, Artificial Neural Networks, Naive Bayes, Random Forest algorithms and k-NN machine learning algorithms in detecting heart diseases. As a result, the best success rate was obtained with the Logistic Regression machine learning algorithm with 90.77% [20]. Yilmaz ve Yağin in 2022, compared the performance of Logistic Regression, Support Vector Machine machine and Random Forest learning algorithms for the prediction of coronary heart disease, the highest success was obtained in Random Forest algorithm with 92.90% [21]. Keser and Keskin, in their study, Logistic regression, Gradient Boosting and Artificial Neural Network models were used to predict the survival or mortality of patients with 299 cases and the best prediction result was obtained with the Artificial Neural Network model with 86.67% [22].

3. Material and methods

3.1. Data set

In this study, used the *kaggle* heart failure prediction dataset consisting of 918 observations by combining 11

common features of the universally accepted Cleveland (n=303), Hungarian (n=294), Swiss (n=123), Long Beach VA (n=200) and Stalog (Heart) (n=270) datasets. There are 11 independent and one dependent variables in the data set, and the variables and their explanations are presented in Table 1.

Table 1. Variables in the data set and their descriptions.

Feature	Feature Description	Type
Age	Age of the patient (Years)	Independent
Sex	Gender of the patient (Female/Male)	Independent
ChestPainType	Type of chest pain (4 Values)	Independent
RestingBP	Resting state blood pressure (mm Hg)	Independent
Cholesterol	Serum cholesterol (mg/dl)	Independent
FastingBS	Fasting blood glucose (120 mg/dl > 1 if not 0)	Independent
RestingECG	Resting ECG results (0 normal, 1 ST-T abnormality, 2 possible or definite left ventricular hypertrophy according to Estes criteria)	Independent
MaxHR	Maximum heart rate	Independent
ExerciseAngina	Exercise-induced angina (0, 1)	Independent
Oldpeak	Numerical value measured in depression	Independent
ST_Slope	Slope of the Peak Exercise (0 upward, 1 straight, 2 downward)	Independent
HeartDisease	Probability of a heart attack (0 low, 1 high)	Dependent

The basic statistical information of the non-categorical numerical variables in the data is presented in Table 2. According to Table 2, there are 918 data for each variable. The mean of the age variable is 54. The lowest age is 28 and the highest is 77. The Q3 value of the age variable is less than or equal to 60. In other words, 75% of the age variable is less than or equal to 60. The mean of the Cholesterol variable is 198.79 and the lowest Cholesterol is 0 and the highest is 603. The Q3 value of the variable Cholesterol is less than or equal to 267. The mean of the RestingBP variable is 132.39 and the lowest RestingBP is 0 and the highest is 200. The Q3 value of the RestingBP variable is less than or equal to 140.

Table 2. Basic statistical knowledge of numeric columns.

	n	mean	std	min	25%	50%	75%	max
Age	918	53,51089	9,432617	28	47	54	60	77
RestingBP	918	132,3965	18,51415	0	120	130	140	200
Cholesterol	918	198,7996	109,3841	0	173,25	223	267	603
FastingBS	918	0,233115	0,423046	0	0	0	0	1
MaxHR	918	136,8094	25,46033	60	120	138	156	202
Oldpeak	918	0,887364	1,06657	-2,6	0	0,6	1,5	6,2
HeartDisease	918	0,553377	0,497414	0	0	1	1	1

In the data set, 410 patients (44.66%) did not have a heart attack, while 508 patients (55.34%) had a heart attack (Figure 1).

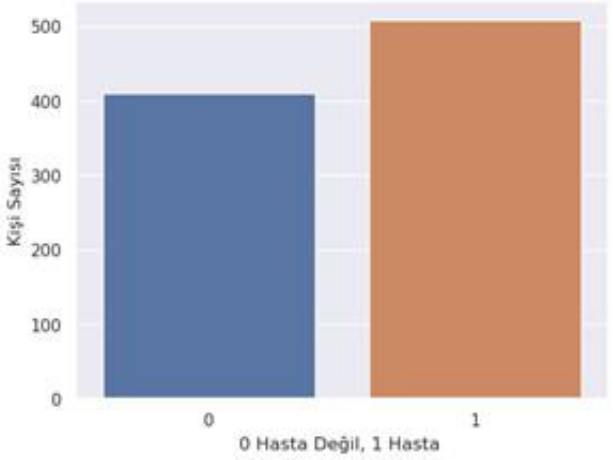

Fig. 1. Distribution of the number of patients in the data set.

3.2. Data preprocessing and feature selection

3.2.1. Data preprocessing and feature selection

In data preprocessing, first, missing data control and categorical and non-numerical features were checked. It was understood that there was no missing data in the data set, but the variables 'Sex', 'RestingECG', 'ExerciseAngina', 'ST_Slope', 'ChestPainType' were understood to be non-numeric categorical data. In order to digitize these variables, the digitization process was carried out using the One-Hot Encoding method since the data set was not very large. As a result of the One-Hot Encoding digitization process, the variables in the dataset are "'Age', 'RestingBP', 'Cholesterol', 'FastingBS', 'MaxHR', 'Oldpeak', 'HeartDisease', 'Sex_F', 'Sex_M', 'RestingECG_LVH', 'RestingECG_Normal', 'RestingECG_ST', 'ExerciseAngina_N', 'ExerciseAngina_Y', 'ST_Slope_Down', 'ST_Slope_Flat', 'ST_Slope_Up', 'ChestPainType_ASY', 'ChestPainType_ATA', 'ChestPainType_NAP', 'ChestPainType_TA'" as increased to 21.

3.2.2. Examination of data distribution and outlier control

In this step, it was examined whether the non-categorical numeric variables ('Age', 'RestingBP', 'Cholesterol', 'FastingBS', 'MaxHR', 'Oldpeak') in the data set were normally distributed. In addition, outlier control was performed for the data.

In this study, Q-Q Plot is used to determine the distribution of the data by visualizing the data. Q-Q Plot performs an assumption check. It is a method based on quantiles to examine whether the data are normally distributed. In the working principle of Q-Q Plot, the data set is sorted and the sorted data and standard normally distributed data are shown on the graph in the coordinate plane. If the two lines overlap linearly at an angle of 45 degrees, it is understood that the data are normally distributed [23], [24].

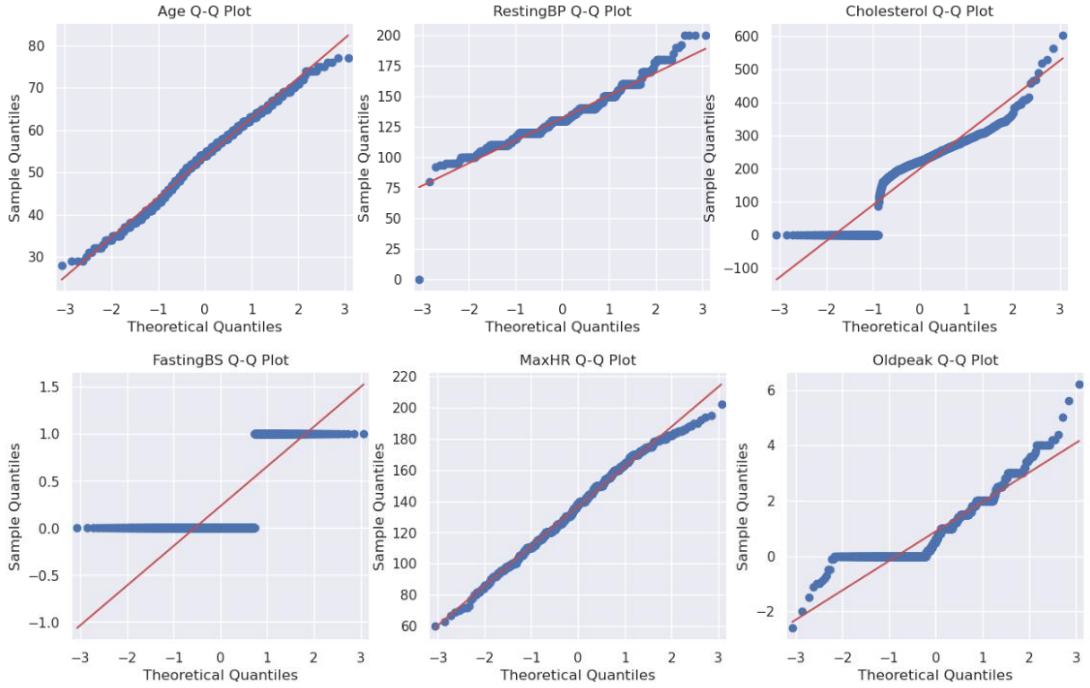

Fig. 2. Q-Q Plot data distribution before excluding outliers for Age, RestingBP, Cholesterol, FastingBS, MaxHR, Oldpeak variables in the dataset.

When the Q-Q Plot presented in Figure 2 is examined, outliers between 0 and 25 are clearly seen in the 'RestingBP' variable. In the variables 'Cholesterol' and 'Oldpeak', the lines parallel to the x-axis mean that the data distribution showed deviations from the normal distribution and this can be interpreted as skewness. As for the 'FastingBS' variable, it is seen that the data are concentrated on two peaks in the graph. However, since the data of the 'FastingBS' variable consists of 1 and 0, there is no skewness in this variable.

There are various methods such as standard deviation, z-score, 1st and 99th percentile to detect outliers. In this study, the standard deviation method was used to detect outliers and exclude them from the data set. In the standard deviation method, the mean of the data set is firstly calculated and then the standard deviation of the data set is found.. A threshold value for outliers is set. When the studies in the literature are examined, it is seen that in the calculation of the threshold value, researchers generally use a multiple of the standard deviation, such as 2 or 3 standard deviations from the mean [25]. In this study, values greater than the final threshold distance were identified as outliers and excluded from the dataset. The Q-Q Plot generated after this process is presented in Figure 3.

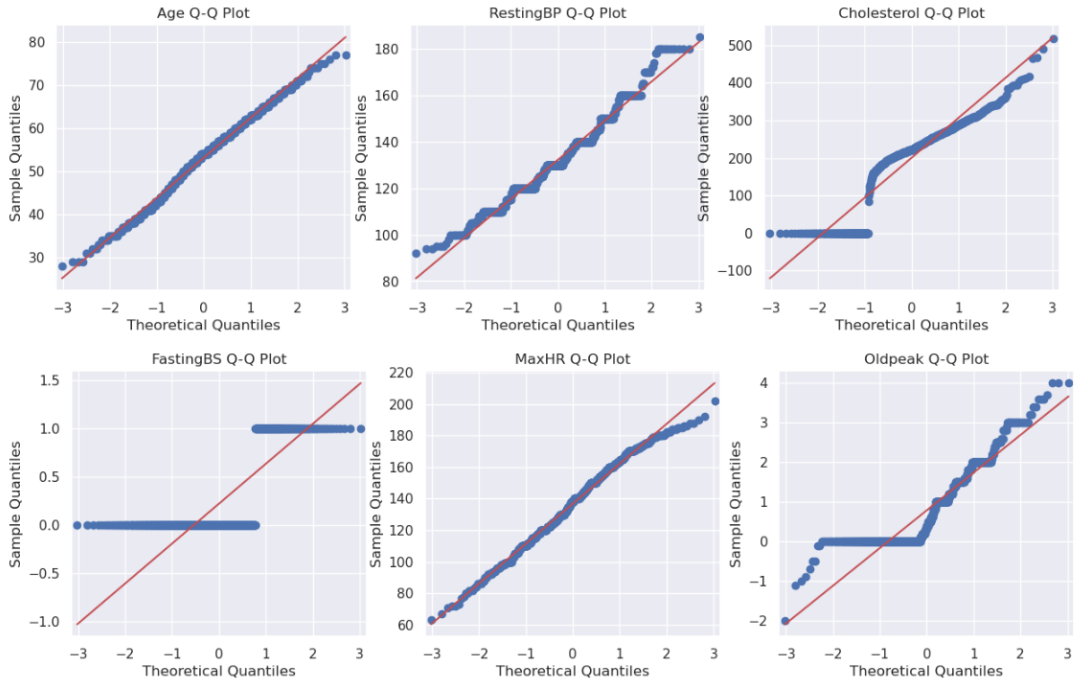

Fig. 3. Q-Q Plot data distribution after excluding outliers in Age, RestingBP, Cholesterol, FastingBS, MaxHR, Oldpeak variables in the dataset.

When the Q-Q graphs presented in Figure 2 and Figure 3 are analyzed comparatively, it is understood that the numerical data are distributed more regularly after the outliers are removed, especially in the 'RestingBP' variable. However, in both figures, 'Cholesterol' and 'Oldpeak' variables still show lines parallel to the x-axis. In order to be understand better whether there is skewness in these variables, the histogram graphs of 'Cholesterol' and 'Oldpeak' variables are given in Figure 4.

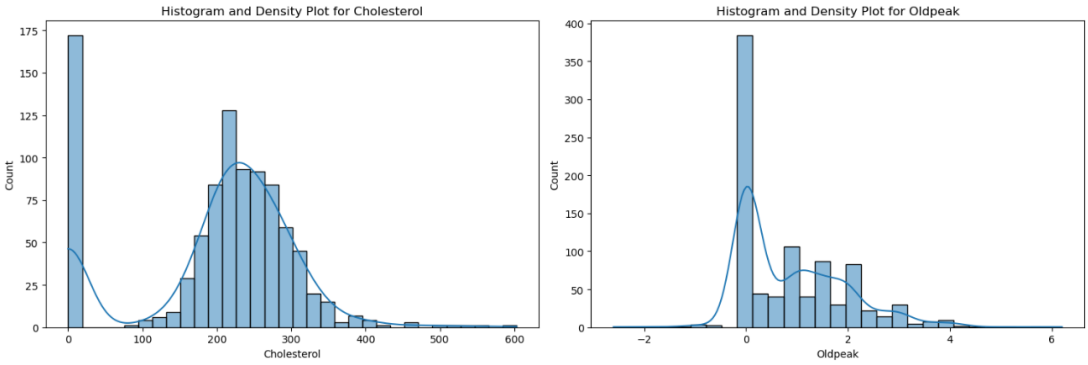

Figure 4. Histogram plot for Cholesterol and Oldpeak variables in the dataset.

Data may be skewed if the data distribution is not symmetrical, if there is skewness on the right side or on the left side, and if the peak value is far from the centre [23]. In line with this explanation, when the histogram graphs

presented in Figure 4 are analysed, the peak value increase in the 'Oldpeak' variable can be interpreted as skewness. Similarly, presence of two different peaks in the data set, if the data are concentrated at two points, this means that the data are bimodally distributed. In a bimodal distribution, the data are not concentrated around one value, but around two different values, and this is evaluated as skewness. This is also observed in the variable 'Cholesterol'.

3.2.3. Normalisation and standardisation processes

When the histogram graphs presented in Figure 4 are analysed, it is understood that there is skewness in the data distribution of 'Cholesterol' and 'Oldpeak' variables. After analysing the distribution of the data, the normalisation step was started. Since 'Oldpeak' and 'Cholesterol' variables were found to be skewed, these variables were scaled with MinMaxScaler (Equation 1). StandardScaler (Equation 2) was used for other numeric variables.

$$X_{scaled} = \frac{X - X_{min}}{X_{max} - X_{min}} \tag{1}$$

$$X_{scaled} = \frac{X - \mu}{\sigma} \tag{2}$$

3.2.4. Correlation analyses

In the correlation analysis step, it was observed that the correlation analysis could not be created for the variables 'ChestPainType_TA' and 'ST_Slope_Down'. This may be due to missing data in the variables or fixed data in the variables in question. Since the entire data set was checked at the beginning of the study and there was no missing data, it was checked whether the variables in question took constant value or not, and it was found that these two variables took constant value. For this reason, these two variables were excluded from the correlation analysis since including or excluding these two variables in the analysis would not change the result. Since the representation of 19 variables in the matrix reduces the legibility of the matrix, only numerical variables are included in the matrix representation (Figure 5).

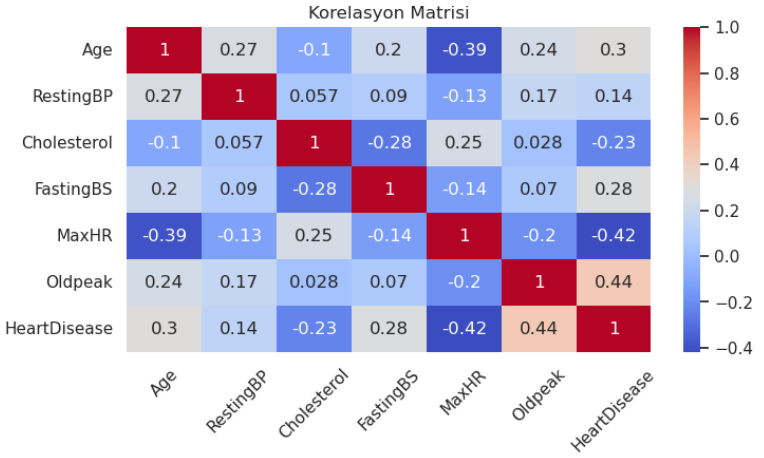

Fig. 5. Correlation matrix of numeric variables in the dataset.

When the correlation matrix of numerical values was analysed, with the variable HeartDisease;

- Oldpeak, RestingBP, FastingBS and Age variables have a positive relationship,
- MaxHR and Cholesterol have a negative relationship,
- The highest relationship level is in Oldpeak and MaxHR variables with 0.44 and -0.42, respectively,
- The lowest relationship level was found in the RestingBP variable with 0.14.

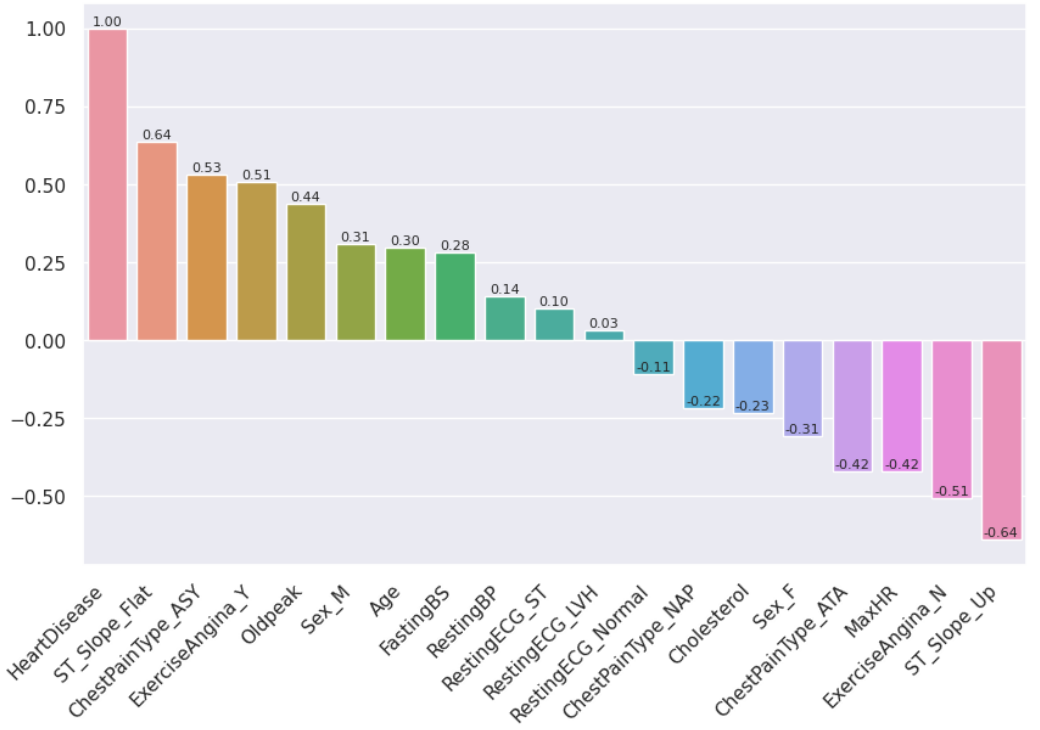

Fig. 6. Column chart with heat map of the correlation analysis of the variables in the dataset.

When the correlation values given in Figure 5 and Figure 6 are analysed, the first information that catches the eye is that gender makes a significant difference in developing the disease. With a correlation value of -0.31 for females and 0.31 for males, there is a negative relationship with the disease in females and a positive relationship in males. 'RestingBP', 'RestingECG_LVH', 'RestingECG_Normal', 'RestingECG_ST' variables have the lowest impact value.

The variables 'ChestPainType_TA', 'ST_Slope_Down', which were found to consist of fixed (same) data, were excluded from the data since they would not change the result in model training.

3.3. Classification

3.3.1. Deep neural network (DNN)

Deep learning is a sub-branch of machine learning. The main difference of deep learning methods from classical artificial neural networks is their multilayer (deep) structure. These layers consisting of interconnected neurons are

divided into 3 parts. These are the input layer consisting of data features, the hidden layer consisting of more than 1 hidden unit (neuron) and finally the output layer (Figure 7). Each layer uses the output of the previous layer as input data. In this way, a hierarchical structure is created by deriving higher level features from lower level features. Deep learning has efficient algorithms for hierarchical feature extraction that represent the data and thus enables learning from the representation of the data [26].

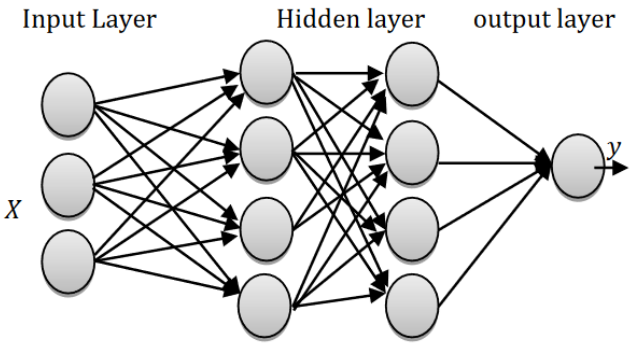

Fig. 7. Example deep neural network image.

DNN aims to minimise the error between calculated predictions and desired values by using the weights w_i of all neurons in the network. Initially randomly assigned weights are updated using the stepwise descent algorithm (Equation 3). At each iteration, a loss/error value is obtained by comparing the difference between the loss function predictions and the actual values. This loss/error is used in the gradient calculation and the weights are updated [26], [27].

$$\Delta w = -\eta \left(\frac{dE}{dw}\right) \tag{3}$$

3.3.2. Convolutional neural networks (CNN)

CNN is an artificial neural network widely used in the field of deep learning, especially in visual data processing such as image classification, object detection, handwriting recognition. There is a convolution layer for filtering and feature map extraction, a pooling layer for dimension reduction, and a fully connected layer that produces output using features obtained from previous layers. CNN is a feed-forward artificial neural network model that optimises the weights and biases of the network using the backpropagation algorithm.

CNN does not use predefined features to locally detect and learn features in the image, but instead learns locally connected neurons (filters). In other words, CNN has the ability to automatically learn features from the image [28]–[30].

3.4. Method

In this research, Deep Neural Network (DNN) and Convolutional Neural Networks (CNN) neural networks were used for early diagnosis of heart attack. For this purpose, a Deep Neural Network with 3 layers and a total of 881 parameters and a Convolutional Neural Networks network with 4257 parameters consisting of 5 layers including convolution, pooling, flatten and two fully connected layers were created. Summary information of these networks is presented in Table 3 and Table 4.

Table 3. DDN model summary.

Layer (type)	Output Shape	Param #
Dense	(None, 32)	608
Dense	(None, 8)	264
Dense	(None, 1)	9

Table 4. CNN model summary.

Layer (type)	Output Shape	Param #
Conv1D	(None, 16, 32)	128
MaxPooling1D	(None, 8, 32)	0
Flatten	(None, 16)	0
Dense	(None, 1)	4112
Dense		17

In order to find the best hyperparameters while training the models, Model Tuning (Model Validation) was performed with GridSearhCV. GridSearhCV returns a parameter array by finding the parameters with the highest success among the variables given as parameters. The parameters specific to each model were tried with experimental methods and the parameters with the highest success rate are presented in Table 5.

Table 5. Parameter space by models and best selected parameters.

Model Name	Parameter Space	Selected with GridSearhCV Best Parameters
DNN	'batch_size': [16, 32], 'epochs': [10,20,100,200], 'hidden_units': [8, 16, 32]	'batch_size': 32, 'epochs': 100, 'hidden_units': 32
CNN	'filters': [16,32, 64], 'kernel_size': [3, 5], 'epochs': [25,100,200], 'batch_size': [16,32]	'filters': 32, 'kernel_size': 3 'epochs': 100, 'batch_size': 16

In both deep learning models, 'binary_crossentropy' was chosen as the loss function, gradient-based 'adam' as the optimizer and 'accuracy' as the metrics. The loss function 'binary_crossentropy' was chosen because the loss function 'binary_crossentropy' is a successful loss function that is widely used in the literature for classification between two classes (true, false).

In addition, KFold and StratifiedKFold methods were used with CV (CrossValidation) values of 2, 3 and 5 for each model. Experimental results were obtained by dividing the data in different ratios such as 80-20, 70-30, 75-25 as training and test data. Random_state was set to a constant value for consistency (so that the data is always split at the same point for training and testing).

4. Research findings

In this study, classification models were developed with Deep Neural Network (DNN) and Convolutional Neural Network (CNN). In order to evaluate the performance of the classification models, the information obtained from Classification Report, Confusion Matrix and ROC Curve are combined and presented in Table 6. In addition, Confusion Matrix (Figure 8), LOS Curve (Figure 9) and combined ROC Curve (Figure 10) are presented in order to visually evaluate the model performance.

Table 6. Information obtained from Classification Report, Confusion Matrix, and ROC curve.

Model	Acc	AUC	Precision	Recall	F1-Score	Support	True Classification		False Classification	
							TP	TN	FP	FN
DNN	0.9375	0.96	0.9629	0.9176	0.9397	160	78	72	3	7
CNN	0.9312	0.96	0.9512	0.9176	0.9340	160	78	71	4	7

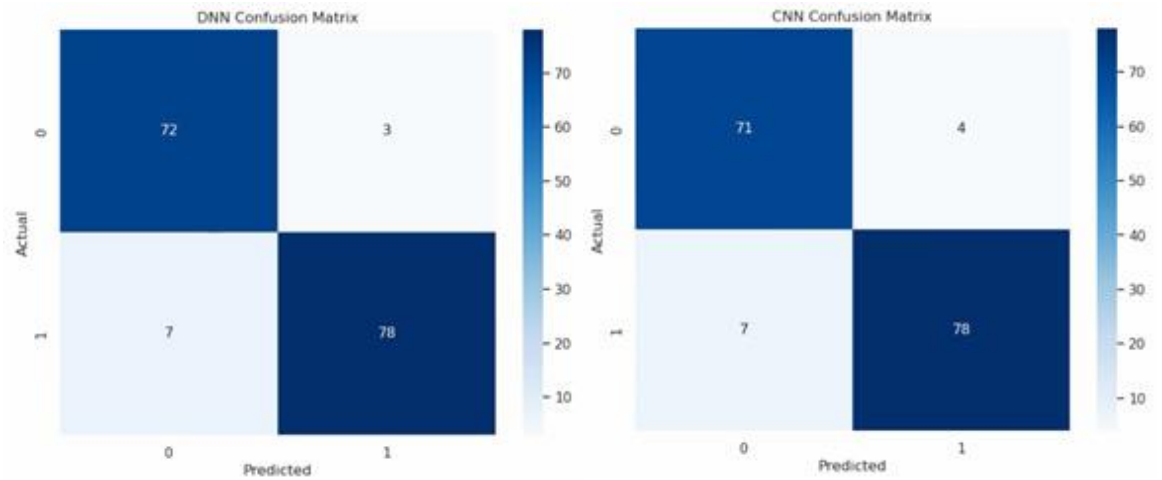

Fig. 8. DNN and CNN confusion matrix.

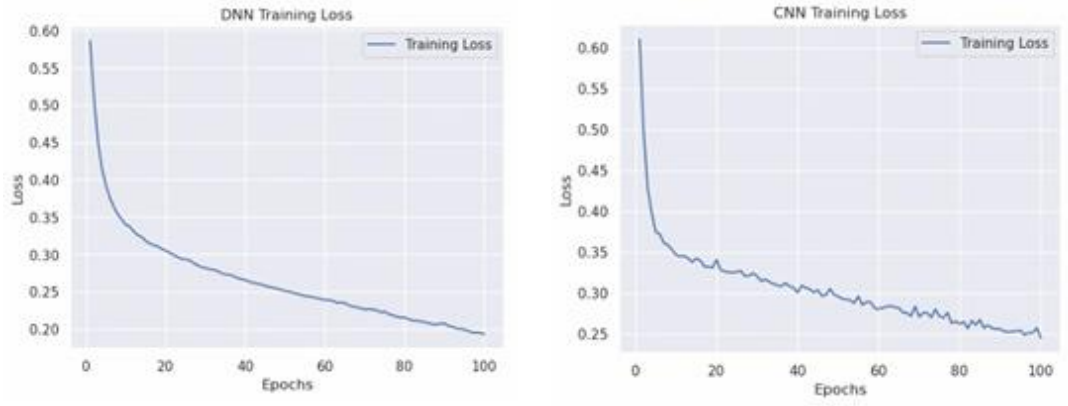

Fig. 9. DNN and CNN Loss curve.

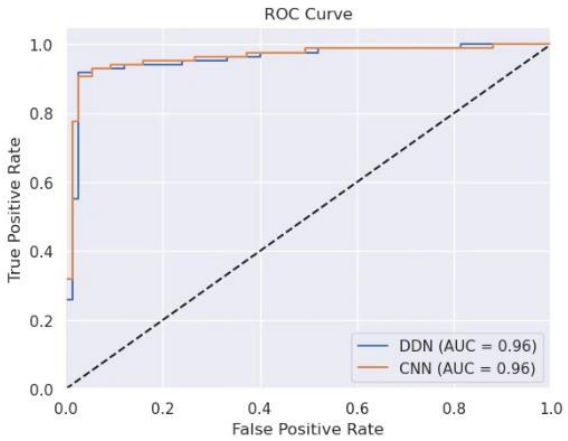

Fig. 10. DNN and CNN combined ROC curve.

5. Discussion and conclusions

In this study, a prediction model was developed with Deep Neural Network (DNN) and Convolutional Neural Network (CNN) using a heart failure prediction dataset consisting of 918 observations with the combination of 11 common features of universally accepted Cleveland (n=303), Hungarian (n=294), Swiss (n=123), Long Beach VA (n=200) and Stalog (Heart) (n=270) datasets obtained through *kaggle*. Classification Report, Confusion Matrix (Figure 8), LOS Curve (Figure 9) and ROC Curve (Figure 10), which are frequently used in the literature, were used to evaluate the performance of the classification models.

In this study, two different deep learning models were created to assist physicians in predicting heart failure and the performance of the models was compared with metrics accepted in the literature. Accuracy, Precision, Recall and F1-Score values obtained with Classification Report for the compared models were 0.9375, 0.9629, 0.9176, 0.9397 for DNN and 0.9312, 0.9512, 0.9176, 0.9340 for CNN respectively. The AUC value calculated on the ROC curve for the compared models was found to be 0.96 for both models equally. Accuracy refers to the correct

classification rate of the generated model. Precision indicates how many of the instances where the generated model predicts positive are actually positive. Recall represents how many true positive samples are correctly predicted and F1-Score represents a balance of precision and sensitivity. The fact that the Accuracy, Precision, Recall and F1-Score values obtained for DNN and CNN are all between 91% and 96% shows that the model classifies the data accurately and balancedly, making very few errors and that the model works quite successfully.

The accuracy percentages of similar studies in the literature are presented in Table 7.

Table 7. Accuracy percentages of similar studies in the literatüre.

Study	Method	Sample	Accuracy (%)
(Abdullah & Rajalaxmi, 2012)	Random Forest	369	63,33
(Salman & Aksoy, 2022)	Random Forest	299	79,66
(Göktaş & Yağanoğlu, 2020)	C4.5 Decision Tree	303	83,09
(Cihan vd., 2018)	Multilayer Artificial Neural Network	303	83,49
(Shao vd., 2014)	Hibrid Model	280	83,93
(Keser & Keskin, 2023)	Artificial Neural Network	299	86,67
(Ekrem vd., 2020)	Random Forest	303	86,88
(Coşar & Deniz, 2021)	Random Forest	918	88,00
(Das vd., 2009)	Statistical Analysis System	303	89,01
(Özmen vd., 2018)	Support Vector Machine	303	89,47
(Potur & Erginel, 2021)	Multilayer Perseptron	299	90,00
(Gündoğdu, 2021)	Random Forest	303	90,20
(Çil & Güneş, 2022)	Artificial Neural Networks	303	90,54
(Coşkun & Kuncan, 2022)	Random Forest	918	90,76
(Yilmaz & Yağin, 2021)	Multilayer Neural Networks	303	91,10
(Ozcan vd., 2019)	Support Vector Machine	170	91,67
Yilmaz & Yağin, 2022)	Random Forest	909	92,90
(Vatansever vd., 2021)	Genetic Algorithm	303	93,44
This Study	**Deep Neural Network**	**918**	**93,75**

When the studies in the literature listed in Table 7 are analysed, it is understood that the success obtained in this study is higher than the previous studies.

Another important contribution of the study to the literature is that it proved that an artificial neural network such as CNN, which is widely used in visual data processing such as image classification, object detection, face recognition, etc., can also give successful results on digital data when used in 1D (dimensional).

On the other hand, in the study describes each stage from data pre-processing to model predict and evaluation in a systematic and detailed manner. It is thought that this study may contribute to researchers in similar deep learning studies that can be carried out in the future.

Acknowledgements

The authors declare that they have no conflict of interest.

References

[1] J. H. Brice, J. K. Griswell, T. R. Delbridge, and C. B. Key, "Stroke: from recognition by the public to management by emergency medical services," *Prehosp Emerg Care*, vol. 6, no. 1, pp. 99–106, 2002, doi: 10.1080/10903120290938904.

[2] M. H. Park *et al.*, "No difference in stroke knowledge between Korean adherents to traditional and western medicine – the AGE study: an epidemiological study," *BMC Public Health*, vol. 6, no. 1, p. 153, Jun. 2006, doi: 10.1186/1471-2458-6-153.

[3] M. H. Fazel Zarandi, A. Seifi, M. M. Ershadi, and H. Esmaeeli, "An expert system based on fuzzy bayesian network for heart disease diagnosis," in *Fuzzy Logic in Intelligent System Design*, P. Melin, O. Castillo, J. Kacprzyk, M. Reformat, and W. Melek, Eds., in Advances in Intelligent Systems and Computing. Cham: Springer International Publishing, 2018, pp. 191–201. doi: 10.1007/978-3-319-67137-6_21.

[4] H. Yan, Y. Jiang, J. Zheng, C. Peng, and Q. Li, "A multilayer perceptron-based medical decision support system for heart disease diagnosis," *Expert Systems with Applications*, vol. 30, no. 2, pp. 272–281, Feb. 2006, doi: 10.1016/j.eswa.2005.07.022.

[5] R. Das, I. Turkoglu, and A. Sengur, "Effective diagnosis of heart disease through neural networks ensembles," *Expert Systems with Applications*, vol. 36, no. 4, pp. 7675–7680, May 2009, doi: 10.1016/j.eswa.2008.09.013.

[6] A. S. Abdullah and R. R. Rajalaxmi, "A data mining model for predicting the coronary heart disease using random forest classifier," *IJCA Proceedings on International Conference in Recent trends in Computational Methods, Communication and Controls (ICON3C 2012)*, vol. ICON3C, no. 3, Apr. 2012, Accessed: Jun. 12, 2023. [Online]. Available: https://www.ijcaonline.org/proceedings/icon3c/number3/6020-1021

[7] Y. E. Shao, C.-D. Hou, and C.-C. Chiu, "Hybrid intelligent modeling schemes for heart disease classification," *Applied Soft Computing*, vol. 14, pp. 47–52, Jan. 2014, doi: 10.1016/j.asoc.2013.09.020.

[8] Ş. Cihan, B. Karabulut, G. Arslan, and G. Cihan, "Koroner arter hastalığı riskinin veri madenciliği yöntemleri ile incelenmesi," *UMAG*, vol. 10, no. 1, Art. no. 1, 2018, doi: 10.29137/umagd.419663.

[9] Ö. Özmen, A. Khdr, and E. Avci, "Sınıflandırıcıların kalp hastalığı verileri üzerine performans karşılaştırması," *Fırat Üniversitesi Mühendislik Bilimleri Dergisi*, vol. 30, no. 3, Art. no. 3, Sep. 2018.

[10] İ. Ozcan, B. Tasar, A. B. Tatar, and O. Yakut, "Destek vektör makinasi algoritması ile kalp hastalıklarının tahmini," *JCS*, vol. 4, no. 2, Art. no. 2, Dec. 2019.

[11] M. E. Göktaş and M. Yağanoğlu, "Veri bilimi uygulamalarının hastalık teşhisinde kullanılması: Kalp krizi örneği," *JISMAR*, vol. 2, no. 2, Art. no. 2, Dec. 2020.

[12] Ö. Ekrem, O. K. M. Salman, B. Aksoy, and S. A. İnan, "Yapay zekâ yöntemleri kullanılarak kalp hastalığının tespiti," *MBTD*, vol. 8, no. 5, Art. no. 5, Dec. 2020, doi: 10.21923/jesd.824703.

[13] M. Coşar and E. Deniz, "Makine öğrenimi algoritmaları kullanarak kalp hastalıklarının tespit edilmesi," *EJOSAT*, no. 28, Art. no. 28, Nov. 2021, doi: 10.31590/ejosat.1012986.

[14] E. A. Potur and N. Erginel, "Kalp yetmezliği hastalarının sağ kalımlarının sınıflandırma algoritmaları ile tahmin edilmesi," *EJOSAT*, no. 24, Art. no. 24, Apr. 2021, doi: 10.31590/ejosat.902357.

[15] S. Gündoğdu, "Kalp hastalık risk tahmini için Python aracılığıyla sınıflandırıcı algoritmalarının performans değerlendirmesi," *DEUFMD*, vol. 23, no. 69, Art. no. 69, Sep. 2021, doi: 10.21205/deufmd.2021236926.

[16] R. Yilmaz and F. H. Yağin, "A comparatıve study for the predıctıon of heart attack rısk and assocıated factors usıng mlp and rbf neural networks," *JCS*, vol. 6, no. 2, Art. no. 2, Dec. 2021, doi: 10.52876/jcs.1001680.

[17] B. Vatansever, H. Aydin, and A. Çetinkaya, "Genetik algoritma yaklaşımıyla öznitelik seçimi kullanılarak makine öğrenmesi algoritmaları ile kalp hastalığı tahmini," *JSTER*, vol. 2, no. 2, Art. no. 2, Dec. 2021, doi: 10.53525/jster.1005934.

[18] O. K. M. Salman and B. Aksoy, "Rasgele orman ve ikili parçacik sürü zekâsi yöntemiyle kalp yetmezliği hastaliğindaki ölüm riskinin tahminlenmesi," *IJ3DPTDI*, vol. 6, no. 3, Art. no. 3, Dec. 2022, doi: 10.46519/ij3dptdi.982670.

[19] C. Coşkun and F. Kuncan, "Evaluation of performance of classification algorithms in prediction of heart

failure disease," *KSU J. Eng. Sci.*, vol. 25, no. 4, Art. no. 4, Dec. 2022, doi: 10.17780/ksujes.1144570.
[20] E. Çil and A. Güneş, "Makine öğrenmesi algoritmalarıyla kalp hastalıklarının tespit edilmesine yönelik performans analizi," *ABMYO Dergisi*, vol. 17, no. 65, Art. no. 65, Nov. 2022.
[21] R. Yilmaz and F. H. Yağin, "Early detection of coronary heart disease based on machine learning methods," *Med Records*, vol. 4, no. 1, Art. no. 1, Jan. 2022, doi: 10.37990/medr.1011924.
[22] S. B. Keser and K. Keskin, "Kalp yetmezliği hastalarının sağ kalım tahmini: Sınıflandırmaya dayalı makine öğrenmesi algoritmalarının bir uygulaması," *Afyon Kocatepe Üniversitesi Fen Ve Mühendislik Bilimleri Dergisi*, vol. 23, no. 2, Art. no. 2, May 2023, doi: 10.35414/akufemubid.1033377.
[23] E. Cevahir, *SPSS ile Nicel Veri Analizi Rehberi Egemen Cevahir*. İstanbul: Kibele Yayınları, 2020.
[24] M. B. Wilk and R. Gnanadesikan, "Probability plotting methods for the analysis of data," *Biometrika*, vol. 55, no. 1, p. 1, Mar. 1968, doi: 10.2307/2334448.
[25] U. Çolak, "Makine Öğrenmesi - Veri Ön İşleme," Medium. Accessed: Sep. 19, 2023. [Online]. Available: https://ufukcolak.medium.com/makine-ogrenmesi-veri-on-isleme-5-58e1ce73c1fb
[26] U. A. Kimanuka and O. Buyuk, "Turkish speech recognition based on deep neural networks," *SDÜ Fen Bil Enst Der*, vol. 22, pp. 319–329, Oct. 2018.
[27] D. P. Kingma and J. Ba, "Adam: A method for stochastic optimization," *International Conference for Learning Representations*, 2015, doi: 10.48550/arXiv.1412.6980.
[28] F. Bozkurt, "A study on CNN based transfer learning for recognition of flower species," *EJOSAT*, no. 32, Art. no. 32, Dec. 2021, doi: 10.31590/ejosat.1039632.
[29] Y. Li, Z. Hao, and H. Lei, "Survey of convolutional neural network," *Journal of Computer Applications*, vol. 36, no. 9, pp. 2508–2515, 2016.
[30] Z. Li, W. Yang, S. Peng, and F. Liu, "A survey of convolutional neural networks: Analysis, applications, and prospects," 2020, doi: 10.48550/ARXIV.2004.02806.

Contents lists available at *Dergipark*

Journal of Scientific Reports-A

journal homepage: *https://dergipark.org.tr/tr/pub/jsr-a*

E-ISSN: 2687-6167 ***Number 55, December 2023***

RESEARCH ARTICLE

Receive Date: 27.09.2023 *Accepted Date: 17.10.2023*

Deep learning-based isolated sign language recognition: a novel approach to tackling communication barriers for individuals with hearing impairments

Naciye Nur Arslan[1*], Emrullah Şahin[2], Muammer Akçay[3]

[1]*Kütahya Dumlupınar University Faculty of Engineering, Departement of Software Engineering, 43000 Kütahya,,*
ORCID: 0000-0002-3208-7986
[2] *Kütahya Dumlupınar University Faculty of Engineering, Departement of Software Engineering, 43000 Kütahya,,*
ORCID: 0000-0002-3390-6285
[3] *Kütahya Dumlupınar University Faculty of Engineering, Departement of Software Engineering, 43000 Kütahya,,*
ORCID: 0000-0003-0244-1275

Abstract

Sign language is a primary and widely used means of communication for individuals with hearing impairments. Current sign language recognition techniques need to be improved and need further development. In this research, we present a novel deep learning architecture for achieving significant advancements in sign language recognition by recognizing isolated signs. The study utilizes the Isolated Sign Language Recognition (ISLR) dataset from 21 hard-of-hearing participants. This dataset comprises 250 isolated signs and the x, y, and z coordinates of 543 hand gestures obtained using MediaPipe Holistic Solution. With approximately 100,000 videos, this dataset presents an essential opportunity for applying deep learning methods in sign language recognition. We present the comparative results of our experiments, where we explored different batch sizes, kernel sizes, frame sizes, and different convolutional layers. We achieve an accuracy rate of 83.32% on the test set.

Keywords: Sign language recognition; deep learning; landmarks; ISLR

1. Introduction

Sign Language Recognition (SLR) is an essential field of research that aims to develop technology to recognize sign language and translate it into written or spoken language [1]. Sign language (SL) is an essential tool for

* Corresponding author.
E-mail address: naciye.arslan@dpu.edu.tr.

communicating with individuals in the deaf community. In sign language, communication is achieved using visual language such as hand gestures, facial expressions, and body language. Sign language varies in structure and syntax between different countries and regions. SLR is necessary to increase communication between deaf individuals and the hearing world and to facilitate the inclusion of deaf individuals into society [2].

Recognizing sign language has various difficulties. In order to distinguish meanings in sign language, it is necessary to make a detailed analysis of body parts, especially hands, arms, and facial movements [3]. Sign language meanings may vary due to signs made by different people when creating a data set. The same sign may appear differently due to position, speed, and acceleration variability during sign movements. Environmental factors such as lighting and background can also make it difficult to recognize signs.

SLR research is divided into two main branches: isolated and continuous [4]. The system, known as isolated SLR, is designed to recognize a single sign performed without any other signs or movements. Isolated SLR is used in applications where single signs need to be recognized, for example, in sign language dictionaries or educational environments. On the other hand, continuous SLR means that the system recognizes sign language sentences or multiple signs performed sequentially. Continuous SLR is often used in applications such as sign language translation systems or real-time communications [5].

In recent years, deep learning has emerged as a powerful tool to overcome the challenges of sign language recognition. Deep learning models, particularly Convolutional Neural Networks (CNNs) and Recurrent Neural Networks (RNNs) and their variations, have demonstrated the state-of-the-art in isolated and continuous sign language recognition tasks [6].

Sign language recognition can be made using landmarks, defined as points corresponding to important joint points on the human body. Landmarks are extracted from video data using computer vision techniques and used to train machine learning models for sign language classification. Landmark-based SLR has gained popularity recently due to its simplicity and effectiveness. Using landmarks to represent sign language movements makes it possible to capture significant spatiotemporal information without requiring large amounts of training data or complex deep learning models.

This work presents a new CNN-based high-performance deep learning architecture for isolated sign language recognition. Our unique architecture, focused on American Sign Language, uses Convolutional Neural Network (CNN) to identify input signals from video-derived point data, achieving the best performance in the current benchmark dataset for ISLR. This work demonstrates the effectiveness of our new CNN-based deep learning architecture combined with landmark-based features for isolated sign language recognition. It provides a basis for further research in this exciting and rapidly evolving field.

2. Related Works

Sign language recognition has become a popular research topic in recent years. Sign language recognition studies for various regions have been carried out in the literature using CNN, LSTM models, and transformer structures.

Aly and colleagues [2] introduced a framework employing DeepLabv3+ and BiLSTM for recognizing Arabic sign language, yielding promising outcomes. Sincan et al. [3] established a foundation for assessing the performance of CNNs and LSTM models in Turkish Sign Language by comparing various architectural approaches. De Coster et al. devised a system that combines OpenPose, a real-time pose estimation framework with transformers, and multi-headed attention to recognize sign language in a Flemish Sign Language dataset, achieving state-of-the-art results [7]. Rastgoo et al. proposed a cascading model for recognizing Persian sign language, focusing on static and dynamic movements. They employed the Single Shot Multi-Box Detector (SSD) and LSTM [8]. Rastgoo et al. introduced a multimodal deep learning model utilizing RGB and depth videos for sign language recognition across three publicly available datasets, demonstrating improved accuracy [9]. Sharma et al. suggested a deep transfer learning approach for continuous sign language sentence recognition. They leveraged pre-trained models to enhance performance [8]. Aloysius et al. conducted a comprehensive review of the literature on vision-based continuous sign

language recognition, emphasizing recent advancements in deep learning techniques and evaluating their effectiveness [5].

Hu et al. introduced a hand model recognition framework that considers the distinctive characteristics of hand joints for recognizing isolated sign language gestures [11]. Zhou et al. proposed an innovative method to address motion blur issues in video sequences using (2+1) D and 3D ResNet, incorporating blur detection to improve sign language recognition [9]. Yang et al. introduced the KSL dataset, a valuable resource for researchers interested in Korean sign language recognition, thereby contributing to the field with a large-scale dataset [13].

In wearable-based systems, Zhang et al. harnessed a multimodal CNN and bidirectional LSTM to achieve end-to-end continuous American Sign Language (ASL) recognition. Their MyoSign system demonstrated high accuracy at both word and sentence levels, leveraging data from Myo armband sensors [14]. Saunders et al. introduced an innovative approach for sign language generation (SLP) using the Progressive Transducer architecture. They converted spoken language sentences into continuous 3D multi-channel sign pose sequences, setting new benchmarks in this area [15]. Several recent studies have also proposed new datasets for sign language recognition. Fink et al. presented two new sign language datasets, LSFB-CONT and LSFB-ISOL, for continuous and isolated sign language recognition in French Belgian Sign Language [16]. Das et al. proposed a hybrid model for Bangla Sign Language recognition and evaluated it on two new datasets, Ishara-Bochon and Ishara-Lipi, providing a valuable resource for the Bengali sign language research community [17]. Rajalakshmi et al. proposed a hybrid neural network architecture for recognizing Indian and Russian sign language and created a new multi-signer dataset for evaluation, promoting research in these underrepresented sign languages [18].

Finally, some recent studies have proposed novel techniques for sign language recognition based on shape trajectories analysis, attention mechanisms, and batch normalization. Fakhfakh et al. developed a shape trajectories analysis approach based on deep learning for recognizing isolated word sign language, demonstrating the effectiveness of shape trajectory analysis in recognizing dynamic gestures [19]. Fang et al. proposed an adversarial multi-task deep learning framework that incorporated multiple modalities and solved the problem of signer independent SLR, improving the generalizability of the recognition system [20]. Luqman et al. proposed an efficient two-stream network for isolated sign language recognition using accumulative video motion, capturing both static and dynamic gesture features for improved recognition [21]. Sarhan and Frintrop proposed a novel method using spatial attention for isolated SLR, enabling the model to focus on relevant regions of the input images for better recognition performance [22]. Takayama et al. proposed a masked batch normalization technique to improve tracking-based sign language recognition using graph convolutional networks, addressing the issue of variable-length sequences in sign language recognition [23]. Wang et al. proposed a framework for multimodal sign language recognition under small sample conditions based on key-frame sampling. This approach combined spatial and temporal features for effective recognition in scenarios with limited training data, providing a viable solution for under-resourced sign languages [24]. Boukdir et al. proposed a deep learning approach for isolated video-based recognition of Arabic sign language, specifically Moroccan sign language, using 2D convolutional recurring neural networks (2DCRNN) and 3D convolutional neural networks (3DCNN) to classify video sequences with high accuracy [25]. Pariwat et al. developed a multi-stroke Thai finger-spelling sign language recognition system using deep learning with vision-based techniques, achieving impressive average accuracies for one, two, and three-stroke alphabets [26]. Furthermore, Rajalakshmi and colleagues proposed a hybrid deep neural network for recognizing Indian and Russian sign gestures, utilizing a combination of spatial feature extraction, attention-based Bi-LSTM, and a modified autoencoder for feature extraction, demonstrating better performance than existing frameworks [27]. These advancements in sign language recognition methods showcase the continuous improvement and innovation in the field, with various techniques and approaches being explored for effective and accurate sign language recognition systems.

In summary, recent research in sign language recognition has covered a wide range of techniques and approaches, including deep learning models, novel architectures, attention mechanisms, and the development of new datasets. These studies demonstrate the ongoing progress in the field and the potential for further advancements in

sign language recognition technology. In our study, we performed sign language recognition on a large newly published landmark-based data set. We conducted a study that will contribute to the literature with our CNN model and our accuracy rate on the new data set.

3. Material and Methods

3.1. Dataset

This study used Isolated Sign Language Recognition (ISLR) Corpus (version 1.0) dataset. The ISLR dataset is published by the Georgia Institute of Technology, the dataset consists of approximately 100,000 isolated signs performed by 21 deaf users using American Sign Language (ASL). Users performed cues from a 250-word vocabulary with hand, face, and pose landmarks obtained via MediaPipe (version 0.9.0.1). The ISLR dataset was primarily designed to be used in educational games aimed at helping deaf children, and their families learn ASL [28].

Videos represent the beacons in the dataset, each taken from a different user and shot in various environments. These videos were collected via smartphone apps without any review for accuracy or quality. Each video contains the coordinates of key points identified in the hands, faces, and poses of the users during the execution of the signs. This landmark data is input into machine-learning models to analyze and recognize signs. Landmark data is represented as x, y, and z coordinates.

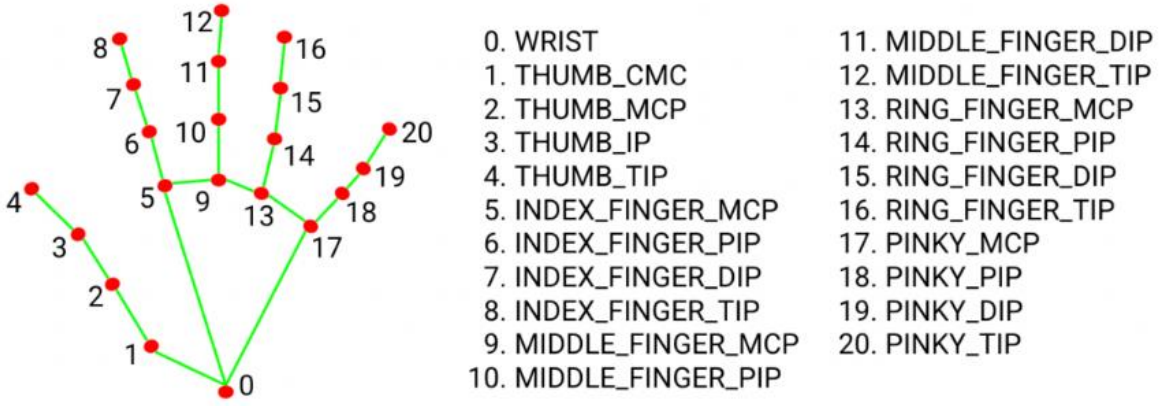

Fig. 1. MediaPipe landmarks for hand [29].

Each frame in the videos contains a total of 543 landmarks. These landmarks are distributed as follows: face (468), left hand (21), pose (33), and right hand (21). Example landmarks of the hand are presented in Fig. 1. Videos in the ISLR dataset vary in the number of frames that describe each sign. The maximum number of frames is about 330, the minimum is 4, and the average is 38. This study aims to contribute to the development of more effective and user-friendly educational tools for deaf individuals by taking advantage of the ISLR dataset.

3.2. Preprocessing of the ISLR Dataset

In the ISLR dataset, the number of frames per video varies, necessitating a preprocessing step to ensure compatibility with the deep learning network used in this study. To facilitate training, a reference frame count of 6 was selected. In this preprocessing stage, videos with more than 6 frames were down sampled by averaging

consecutive frames to reduce the total number of frames to the reference value. Conversely, for videos with fewer than 6 frames, zero-padding was employed by adding frames consisting of zeros until the target frame count was reached. This approach standardized all videos to have 6 frames, thereby enabling efficient training of the deep learning network on the ISLR dataset.

Additionally, from the original 543 landmark points in each frame, 118 dominant landmarks were identified based on their importance in sign language communication. These dominant landmarks predominantly include key points from hands, lips, and pose, which are known to carry significant information in sign language. By focusing on these 118 landmarks, the computational complexity of the deep learning model is reduced while maintaining the essential features required for accurate sign recognition. This refined set of landmarks further enhances the efficiency and effectiveness of the deep learning network's training on the ISLR dataset.

In the final stage, the processed data for each sign consists of 6 frames, each containing 118 landmarks and their corresponding 3-dimensional (x, y, z) coordinates. This standardized data representation ensures consistent input for the deep learning model, enabling accurate and efficient sign recognition in the ISLR dataset.

3.3. Proposed Method

In this study, a novel architecture based on CNN is proposed for recognizing isolated sign language (see Fig. 2). The architecture consists of four total blocks, each containing a Conv1D layer, a Batch Normalization layer, and a ReLU activation function.

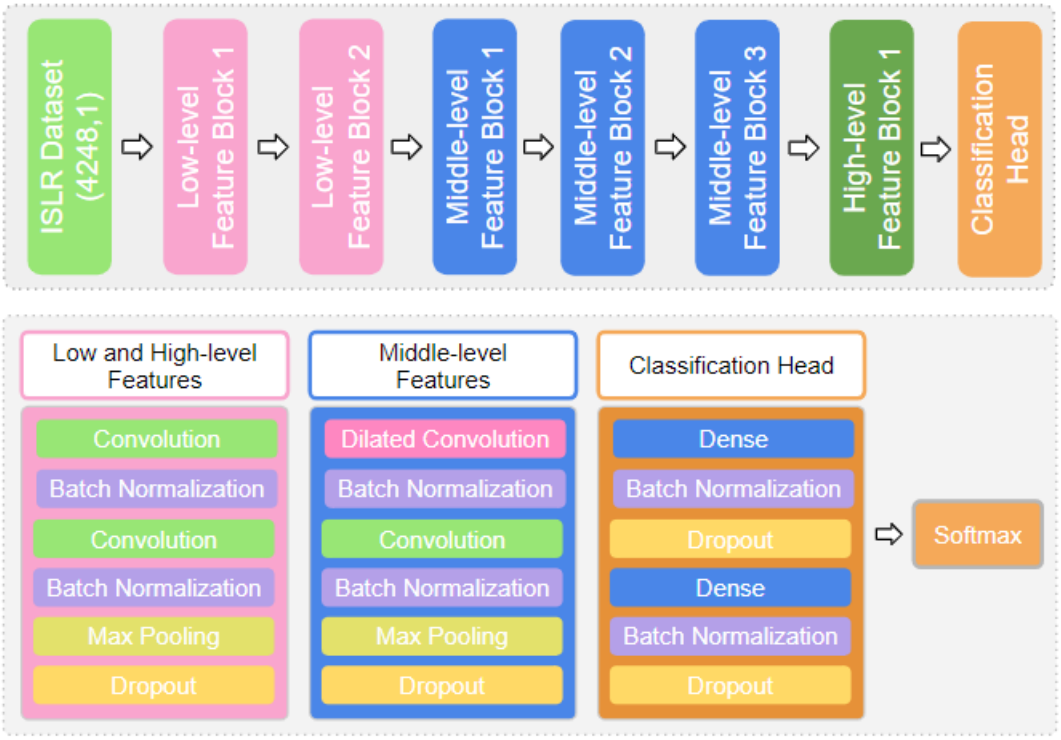

Fig. 2. Proposed model.

In our proposed model, dilation convolution is used in certain blocks. Dilation convolution is a technique that modifies traditional convolutional operations. In regular convolution, the kernel computes with a fixed stride size over the data. In this case, the kernel size is the same as the stride size. However, gaps are inserted between steps on the kernel in dilation convolution. This gap allows the convolution operation to have a wider receptive field. The dilation factor determines the size of this gap. Specifically, dilated convolutions are used in the third and fourth blocks to create an expanded receptive field. This allows the model to capture longer-range dependencies and larger-scale features [30]. Our input data consists of 94477 samples, each comprising 6-frames. Each frame contains 3-dimensional location data (x, y, z) for 118 individual landmarks and their derivative information. Therefore, the input data size is 6 x 118 x 6 = 4248. The total number of parameters in our deep learning model is 10,806,746.

The model blocks are described below:

Low-Level Feature Block 1: At this level, two Conv1D layers with 32 filter sizes and the following batch normalization layers were used. Batch Normalization stabilizes the training process by normalizing the data. Then, the MaxPooling layer with 3 filter sizes and the dropout layer, which deactivates neurons by 30%, were applied. Dropout helps reduce overfitting and helps the model learn more generalized features.

Low-Level Feature Block 2: Similarly, two Conv1D layer with 64 filter size is added, followed by the Batch Normalization layer. The MaxPooling layer with size 3 is applied. The Dropout layer deactivates 40% of the neurons randomly.

Middle-Level Feature Block 1,2, and 3: These blocks use dilated convolutions to expand the receptive field. The dilation convolution is performed by leaving gaps between steps on the kernel, with a dilation_rate=2. Each block includes two Conv1D and two Batch Normalization layers. The filters applied to the conv1d layers are 128,256 and 384, respectively. The MaxPooling1D layer implements a pooling operation of size. The Dropout layer deactivates 50% of the neurons randomly.

High-Level Feature Block 1: The layers in this section consist of two Conv1D layers with 512 filters, two Batch Normalization layers, a MaxPooling1D layer, and a Dropout layer. The MaxPooling1D layer implements a pooling operation of size 3. The Dropout layer deactivates 50% of the neurons randomly.

Classification Head: The Flatten layer flattens the 1D outputs. Then, a two-layer, fully connected structure is added. Each layer consists of 1024 and 512 neurons, respectively. Batch Normalization and Dropout layers are added after each fully connected layer. Finally, a Dense layer with the number of output classes (250) is added. The SoftMax activation function is used in this layer. The model performs convolution and pooling operations with consecutive blocks and then performs classification with fully connected layers.

The ReLU (Rectified Linear Unit) activation function was used in all model layers except the last layer. ReLU is a simple activation function where negative values equal zero and positive values remain unchanged. This function helps the network learn nonlinear features. The SoftMax activation function was used in the last layer, Dense (250). SoftMax is an activation function used in multiclass classification problems. It obtains a probability distribution representing the class probabilities at the output. This allows the model to make the most probable prediction across multiple classes.

3.4. Hyper-parameter Settings

AdamW optimizer, a derivative of the Adam optimizer with weight decay support, was applied. Weight decay controls the magnitude of weight parameters while updating the network's loss to optimize. This can encourage weight parameters for generalization and prevent overfitting. Essentially, it incorporates weight decay into the update steps of the Adam algorithm by adding a term. The term for weight decay is typically multiplied by a factor of the sum of squares of weight parameters and added to the total loss function [31].

Below is the description of the parameters used in the optimizer initialization:

- learning rate: This parameter determines the step size used in each optimization step. It controls how quickly the optimizer adjusts the model weights based on the computed gradients. A learning rate of 1e-3 (0.001) is used in this case.
- weight decay: This parameter determines the strength of weight decay regularization. It is a multiplying coefficient for the weight decay term added to the loss function. A weight decay of 1e-5 (0.00001) is used in this case.
- clip norm: This parameter is used to limit the gradients during optimization. It prevents them from growing too large by capping the norm (magnitude) of the gradients. In this case, a clip-norm value of 1.0 is used.

The Sparse Categorical Cross Entropy Loss function was combined with label smoothing to address the problem [32]. Label smoothing aims to correct harsh label classification errors, allowing the model to generalize better and reduce the risk of overfitting. Sparse Categorical Cross Entropy Loss is a commonly used loss function in multi-class classification problems. However, it can encounter issues when working with complex labels. For example, in some cases, the model may make harsh classification errors in overly confident classes, which can negatively impact the training process. Label smoothing is a technique used to reduce such harsh classification errors by smoothing the labels. Instead of using a label value for each class, this technique represents the actual labels using one-hot encoding, and low but unequal probabilities are assigned to all classes. This allows the model to learn a more balanced class distribution and make more generalized classifications. This loss function calculates the cross-entropy between the predicted probabilities and the true labels, measuring how well the predicted classes match the true labels. The cross-entropy is then averaged across all the samples to give the total loss. The goal during model training is to minimize the loss value. The equation for sparse categorical cross entropy loss is:

$$Loss = \frac{-1}{N} \sum_{i}^{N} \sum_{j}^{M} y_{ij} \log y'_{ij} \quad (1)$$

Here, N represents the total number of samples, M represents the number of classes, y_{ij} represents the jth class of the ith sample's true label, and y'_{ij} represents the predicted probability of the jth class for the ith sample. The negative sign indicates that the goal is to minimize the loss. During the optimization process, the model's parameters are updated iteratively to minimize the loss function.

A learning rate scheduling strategy called Linear Warmup and Cosine Decay was applied. This strategy gradually increases the learning rate at the beginning of model training and slowly decreases it from a specific turning point. This practice helped the model achieve a better balance and achieve better results. The model was trained for 300 epochs.

4. Experimental Results

The proposed CNN architecture was evaluated for recognizing isolated sign language using landmark data. Table 1 presents the evaluation metrics for the proposed model, including Sparse Categorical Accuracy, Sparse Top-5 Accuracy, and Sparse Top-10 Accuracy. Sparse Categorical Accuracy measures the percentage of correct predictions for a given sample set. It is called "sparse" because the predicted classes and actual tags are encoded as integers. To calculate Sparse Categorical Accuracy, the number of correct predictions is divided by the total number of samples.

Table 1. Proposed models benchmark results.

Model Properties	Model Type	Loss	Sparse Accuracy	Top 5	Top 10
	Batch Size 64	2.4967	0.8290	0.9350	0.9516
	Batch Size 96	2.4942	0.8310	0.9325	0.9516

Half Dilated Conv Frame Size 6 Kernel Size 7	Batch Size 128	2.5132	0.8220	0.9312	0.9485
	Batch Size 196	2.5368	0.8118	0.9272	0.9462
	Batch Size 256	2.5427	0.8098	0.9263	0.9453
	Batch Size 384	2.5699	0.8022	0.9218	0.9427
	Batch Size 512	2.5762	0.7986	0.9231	0.9440
Half Dilated Conv Frame Size 6 Batch Size 96	Kernel Size 5	2.5109	0.8249	0.9332	0.9508
	Kernel Size 7	2.4942	0.8310	0.9325	0.9516
	Kernel Size 9	2.5085	**0.8332**	0.9320	0.9476
	Kernel Size 11	2.5156	0.8262	0.9295	0.9454
Kernel Size 9 Frame Size 6 Batch Size 96	Normal Conv	2.4963	0.8289	0.9317	0.9472
	Half Dilated Conv	2.5085	**0.8332**	0.9320	0.9476
	Full Dilated Conv	2.5249	0.8229	0.9292	0.9449
Half Dilated Conv Kernel Size 9 Batch Size 96	Frame Size 4	2.6125	0.8021	0.9185	0.9389
	Frame Size 6	2.5085	**0.8332**	0.9320	0.9476
	Frame Size 8	2.532	0.8198	0.9245	0.9428

Sparse Top-5 Accuracy represents a versatile evaluation metric compared to Sparse Categorical Accuracy. It offers the flexibility to deem a prediction correct if the true label falls within the top five predicted classes. This metric accommodates scenarios where the actual label might not be the most apparent or direct choice. To compute Sparse Top-5 Accuracy, we tally the count of correct predictions (where the accurately guessed class resides among the top five) and divide it by the total number of samples. Similarly, Sparse Top-10 Accuracy gauges the percentage of instances where the accurately guessed class ranks within the top ten predicted classes. This metric enhances the model's predictive adaptability further. To calculate Sparse Top-10 Accuracy, we assess the number of correct predictions (where the accurately guessed class is among the top ten) and divide it by the overall sample count.

The model was trained using different batch sizes, kernel sizes, and convolutions, as shown in the table. Based on the test results, the highest accuracy was achieved using a batch size of 96, a kernel size of nine, and dilated convolutions in the middle layers.

In the first stage, we carried out training in different batch sizes (64,96,128,196,256,384,512) with the addition of semi-dilated conv, that is, dilatation factor, to the intermediate layers, with Kernel size seven and frame size six determined. As a result of this training, we found the highest sparse accuracy rate in test data at 83.10% in 96 batch sizes. While the batch size was 96, we also tried different kernel sizes (7,9,11), and we reached 83.32% accuracy with nine kernel sizes. We observed that the accuracy rate did not increase when tested by applying normal conv to the layers. We applied and tested dilated conv (full dilated conv) on all layers, and as a result, we found that the

accuracy rate was lower than half dilated conv. We trained by changing the number of frames in the dataset to four and eight and achieved maximum accuracy when the frame size was six.

As a result of these comparisons, our model with the best sparse categorical accuracy rate (83.32%) was obtained by applying kernel size 9, batch size 96, frame size six, and half dilation convolution. Additionally, we found the top 5 accuracies at 93.20% and the top 10 accuracies at 94.76%.

5. Conclusions

In conclusion, this study introduced a CNN architecture for recognizing isolated sign language using landmark data. The model was evaluated on a dataset consisting of 94,477 video clips, each containing 118 landmarks with x, y, and z coordinate information. The results demonstrated good accuracy on the validation set, with a sparse categorical accuracy of 83.32%. The top-5 accuracy achieved 93.20% on the validation set, while the top-10 accuracy reached 94.76%.

As the dataset used in this study is newly shared, no existing studies are found in the literature that specifically applied this dataset. Therefore, there is a potential to enhance the model's performance by exploring different preprocessing techniques tailored to this dataset. Additionally, future work could consider selecting different hand, face, and pose landmarks and experimenting with varying the number of frames in the video clips to improve accuracy rates. It could be tested on different sign language datasets to evaluate the proposed model further. Since the dataset used in this study involves many classes, the observed increase in accuracy rate needed to be more substantial. This may be attributed to the need for a well-established standard due to the novelty of the dataset.

This study provides valuable insights into the challenges and potential solutions for recognizing sign language using landmark data. The proposed model and findings can serve as a reference for future research in this field, contributing to the advancement of sign language recognition techniques.

Acknowledgements

This study did not receive any specific funding or financial assistance from governmental, commercial, or non-profit organizations.

References

[1] A. Mittal, P. Kumar, P. P. Roy, R. Balasubramanian and B. B. Chaudhuri, "A modified LSTM model for continuous sign language recognition using leap motion" *IEEE Sensors Journal*, vol. 19, no. 16, pp. 7056-7063, Apr. 2019.

[2] S. Aly and W. Aly, "DeepArSLR: A novel signer-independent deep learning framework for isolated arabic sign language gestures recognition", *IEEE Access*, vol. 8, pp. 83199-83212, Apr. 2020.

[3] O. M. Sincan and H. Y. Keles, "Autsl: A large scale multi-modal Turkish sign language dataset and baseline methods", *IEEE Access*, vol. 8, pp. 181340-181355, Aug. 2020.

[4] R. Rastgoo, K. Kiani and S. Escalera, "Sign language recognition: A deep survey" *Expert Systems with Applications*, vol. 164, pp. 113794, Feb. 2021.

[5] N. Aloysius, & M. Geetha, "Understanding vision-based continuous sign language recognition" *Multimedia Tools and Applications*, vol. 79, no. (31-32), pp. 22177-22209, May 2020.

[6] A. Wadhawan and P. Kumar, "Sign language recognition systems: A decade systematic literature review" *Archives of Computational Methods in Engineering*, vol. 28, pp. 785-813, Dec. 2021.

[7] M. De Coster, M. Van Herreweghe and J. Dambre, "Sign language recognition with transformer networks" in *12th international conference on language resources and evaluation*, May 2020, pp. 6018-6024.

[8] R. Rastgoo, K. Kiani and S. Escalera, "Video-based isolated hand sign language recognition using a deep cascaded model" *Multimedia Tools and Applications*, vol. 79, pp. 22965-22987, Jun. 2020.

[9] R. Rastgoo, K. Kiani and S. Escalera, "Hand pose aware multimodal isolated sign language recognition" *Multimedia Tools and Applications*, vol. 80, pp. 127-163, Sep. 2021.

[10] S. Sharma, R. Gupta and A. Kumar "Continuous sign language recognition using isolated signs data and deep transfer learning" *Journal of Ambient Intelligence and Humanized Computing*, vol. 14, pp. 1-12, Aug. 2021.

[11] H. Hu, W. Zhou and H. Li, "Hand-model-aware sign language recognition" in *Proc. AAAI conference on artificial intelligence*, May 2021, vol. 35, no. 2, pp. 1558-1566.

[12] Z. Zhou, K. S. Kui, V. W. Tam and E. Y. Lam, "Applying (3+ 2+ 1) D residual neural network with frame selection for Hong Kong sign language recognition*"* in *2020 25th International Conference on Pattern Recognition (ICPR)*, Jan. 2021, pp. 4296-4302.
[13] S. Yang, S. Jung, H. Kang and C. Kim, "The Korean sign language dataset for action recognition" in *International conference on multimedia modelling*, Dec. 2019, pp. 532-542.
[14] Q. Zhang, D. Wang, R. Zhao, & Y. Yu, "MyoSign: enabling end-to-end sign language recognition with wearables" in *Proc. of the 24th international conference on intelligent user interfaces*, Mar. 2019, pp. 650-660.
[15] B. Saunders, N. C. Camgoz and R. Bowden, "Continuous 3d multi-channel sign language production via progressive transformers and mixture density networks" *International journal of computer vision*, vol. 129, no. 7, pp. 2113-2135, Mar. 2021.
[16] J. Fink, B. Frénay, L. Meurant and A. Cleve, "LSFB-CONT and LSFB-ISOL: Two new datasets for vision-based sign language recognition" in *2021 International Joint Conference on Neural Networks (IJCNN)*, Jul. 2021, pp. 1-8.
[17] S. Das, M. S. Imtiaz, N. H. Neom, N. Siddique, and H. Wang, "A hybrid approach for Bangla sign language recognition using deep transfer learning model with random forest classifier*" Expert Systems with Applications*, vol. 213, pp. 118914, Mar. 2023.
[18] E. Rajalakshmi, R. Elakkiya, A. L. Prikhodko, M. G. Grif, M. A. Bakaev, J. R. Saini, ... and V. Subramaniyaswamy, "Static and dynamic isolated Indian and Russian sign language recognition with spatial and temporal feature detection using hybrid neural network" *ACM Transactions on Asian and Low-Resource Language Information Processing*, vol. 22, no.1, pp. 1-23, Nov. 2022.
[19] S. Fakhfakh and Y. B. Jemaa, "Deep Learning Shape Trajectories for Isolated Word Sign Language Recognition" *Int. Arab J. Inf. Technol*., vol. 19, no. 4, pp. 660-666, Jul. 2022.
[20] Y. Fang, Z. Xiao, S. Cai and Ni L., "Adversarial multi-task deep learning for signer-independent feature representation" *Applied Intelligence*, vol. 53, no. 4, pp. 4380-4392, Jun. 2023.
[21] H. Luqman, "An Efficient Two-Stream Network for Isolated Sign Language Recognition Using Accumulative Video Motion" *IEEE Access*, vol. 10, pp. 93785-93798, Sep. 2022.
[22] N. Sarhan and S. Frintrop, "Sign, Attend and Tell: Spatial Attention for Sign Language Recognition" in *2021 16th IEEE International Conference on Automatic Face and Gesture Recognition (FG 2021)*, Dec. 2021, pp. 1-8.
[23] N. Takayama, G. Benitez-Garcia and H. Takahashi "Masked batch normalization to improve tracking-based sign language recognition using graph convolutional networks" in *2021 16th IEEE International Conference on Automatic Face and Gesture Recognition (FG 2021)*, Dec. 2021, pp. 1-5.
[24] J. Wang, J. Chen and Y. Cai, "A framework for multimodal sign language recognition under small sample based on key-frame sampling" *In Fifth International Workshop on Pattern Recognition*, vol. 11526, pp. 46-52, Jun. 2020.
[25] A. Boukdir, M. Benaddy, A. Ellahyani, O. E. Meslouhi and M. Kardouchi, "Isolated video-based Arabic sign language recognition using convolutional and recursive neural networks*" Arabian Journal for Science and Engineering*, pp. 1-13, Sep. 2021.
[26] T. Pariwat and P. Seresangtakul , "Multi-stroke thai finger-spelling sign language recognition system with deep learning" *Symmetry*, vol. 13, no.2, pp. 262, Feb. 2021.
[27] E. Rajalakshmi, R. Elakkiya, V. Subramaniyaswamy, L. P. Alexey, G. Mikhail, M. Bakaev, ... and A. Abraham, "Multi-Semantic Discriminative Feature Learning for Sign Gesture Recognition Using Hybrid Deep Neural Architecture*" IEEE Access*, vol. 11, pp. 2226-2238, Jan. 2023.
[28] Deaf Professional Arts Network and the Georgia Institute of Technology, Kaggle ASL dataset, https://www.kaggle.com/competitions/asl-signs/overview (accessed June 12, 2023).
[29] MediaPipe Solutions, Mediapipe hand landmarks, (n.d.). https://developers.google.com/mediapipe/solutions/vision/hand_landmarker (accessed June 12, 2023).
[30] N. N. Arslan, D. Ozdemir and H. Temurtas, "ECG heartbeats classification with dilated convolutional autoencoder" *Signal, Image and Video Processing*, pp. 1-10, Sep. 2023.
[31] R. Llugsi, S. El Yacoubi, A. Fontaine and P. Lupera, "Comparison between Adam, AdaMax and Adam W optimizers to implement a Weather Forecast based on Neural Networks for the Andean city of Quito*"* in *2021 IEEE Fifth Ecuador Technical Chapters Meeting (ETCM)*, Oct. 2021, pp. 1-6.
[32] T. Andrei-Alexandru and D. E. Henrietta, "Low-cost defect detection using a deep convolutional neural network" in *2020 IEEE International conference on automation, quality and testing, robotics (AQTR)*, May 2020, pp. 1-5.

Contents lists available at *Dergipark*

Journal of Scientific Reports-A

journal homepage: *https://dergipark.org.tr/tr/pub/jsr-a*

E-ISSN: 2687-6167 ***Number 55, December 2023***

RESEARCH ARTICLE

Receive Date: 22.08.2023 *Accepted Date: 10.11.2023*

Evaluation of combined use of hsp90 inhibitor mpc-3100 and traditional cancer drug 5-fu on liver cancer cell lines

Özlem Kaplan[1]*

[1]*Alanya Alaaddin Keykubat University, Rafet Kayış Faculty of Engineering, Department of Genetics and Bioengineering, 07425, Antalya, Turkey*

Abstract

Hepatocellular carcinoma (HCC), which constitutes an important part of the global cancer burden, poses an important problem in the field of medicine. Combination therapy targets multiple mechanisms simultaneously using different therapeutic agents together. Heat shock protein 90 (HSP90) inhibitors are emerging as interesting targets in this area, since they play a vital role in the control of cellular processes and impact malignant cell survival and resistance mechanisms. This study evaluated the combined effect of the HSP90 inhibitor MPC-3100 and the traditional chemotherapy drug 5-fluorouracil (5-FU) on HCC. MTT assay was performed to evaluate the individual and combined cytotoxic effects of 5-FU and MPC-3100 on HUH-7 and HepG2 liver cancer cell lines. To assess the effectiveness of combination therapy, the Chou and Talalay method was applied. Both 5-FU and MPC-3100 and 5-FU+ MPC-3100 exhibited dose- and time-dependent cytotoxic effects. Combined administration of the two drugs showed an antagonistic impact on the cell lines. The findings demonstrated that combining 5-FU with MPC-3100 was less effective in inducing cytotoxicity in liver cancer cell lines compared to the use of each drug separately. In this context, the combination of these two drugs in liver cancer is not an appropriate strategy for effective treatment. Current research findings will help design more effective and targeted therapies for HCC and other cancers.

Keywords: MPC-3100, 5-fluorouracil, Combination therapy, Antagonistic effect

1. Introduction

Hepatocellular carcinoma (HCC) is a significant cause of cancer mortality globally [1]. Drug resistance and adverse effects interfere with HCC therapy. Current treatment approaches have a low chance of survival and a high rate of cancer recurrence [2]. The complex molecular and cellular mechanisms in the development of HCC reveal

* Corresponding author. Tel.: +90 242 510 61 20; fax: +90 242 510 61 24
E-mail address: ozlem.kaplan@alanya.edu.tr
http://dx.doi.org/10.1016/j.cviu.2017.00.000

the need for new therapeutic strategies to replace traditional approaches [3]. In this context, the concept of combination therapy has emerged as an effective way to achieve enhanced therapeutic efficacy in HCC. This strategic approach simultaneously targets multiple pathways and aspects of cancer formation by exploiting the potential synergy between different agents. Thus, the combined therapy approach increases the likelihood of better treatment outcomes [4]. The role of HSP90 inhibitors in such synergistic approaches is of great interest. HSP90, the master regulator of protein folding, stabilization and conformational maturation, has emerged as a very important protein in cancer biology [5]. The multifaceted role of HSP90 in governing the fate of various client proteins is crucial in cancer, with implications for growth, survival, and the development of drug resistance. Because of many aberrantly regulated proteins frequently in HCC, HSP90 stands out as a viable therapeutic target [6]. Recently, HSP90 was found as a potential biomarker of HCC, and its expression has proven to have a major diagnostic value for HCC diagnosis [7]. Inhibition of HSP90 becomes an attractive therapeutic target in the context of HCC because it offers the opportunity to affect multiple oncogenic signaling pathways simultaneously. In this study, MPC-3100 was chosen as a promising candidate due to its excellent pharmacological properties [8]. MPC-3100 inhibits ATPase function by targeting Hsp90 N-terminal ATP binding domain. MPC-3100 was shown to inhibit HSP90 activity in luciferase degradation studies with an IC_{50} value of 60nM. MPC-3100 inhibited cell growth in the HCT-116 colon cancer cell line with an IC_{50} value of 540nM. These findings highlighted ability of MPC-3100 to disrupt essential cancer development pathways. MPC-3100 was also found to have broad-spectrum anti-proliferative effect against the NCI-N87 gastric cancer and DU-145 prostate cancer cell lines [8]. MPC-3100 has been demonstrated to decrease tumor development in the NCI-N87 gastric cancer xenograft model. MPC-3100 has a high oral pharmacokinetic profile, excellent overall exposure, and an acceptable hepatic clearance rate, according to pharmacokinetic studies [9]. MPC-3100 was well tolerated in the Phase I human clinical study and displayed pharmacokinetic and pharmacodynamic characteristics comparable to those shown in preclinical research [10]. These pharmacological properties make MPC-3100 stand out as an ideal possibility for further research, especially in the context of combination therapy with conventional chemotherapeutic drugs.

5-fluorouracil (5-FU) is an essential antimetabolite and cell cycle inhibitor. This drug has been frequently used to treat stomach, colorectal, and breast malignancies [11]. 5-FU works against tumors by inhibiting thymidylate synthase and RNA/DNA processing. 5-FU has been studied alone and in combination in many cancer cell lines. In these studies, the IC_{50} values of 5-FU ranged between 2.3-13.0 μM in breast cancer cells [12] and 21.9-43.2 μmol/L in hepatocellular carcinoma cell lines [13]. The FOLFOX4 regimen using 5-FU has shown to be advantageous in the treatment of advanced HCC [14]. The FOLFOX4 regimen encompasses a combination of oxaliplatin, 5-FU and leucovorin, constituting a conventional chemotherapeutic regimen in the treatment of some advanced cancer [15, 16]. This therapy method has improved the overall survival of HCC patients. However, due to the drug's limited efficacy, it may be necessary to use higher doses of 5-FU, which can cause leukopenia, nausea, vomiting and skin rashes [17]. Consequently, It is necessary to find more effective strategies to increase the sensitivity of HCC to chemotherapy and reduce side effects [18].

The objective of this research was to examine at the possible effects of combining the standard chemotherapeutic drug 5-FU with the HSP90 inhibitor MPC-3100. The cytotoxic effect of agents alone and in combination on two liver cancer cell lines were evaluated at 24h and 48h. To assess drugs interactions, the Chou and Talalay method was employed.

2. Materials and Methods

2.1. Chemicals and Reagents

3-(4,5dimethylthiazol-2-yl)-2,5-diphenyltetrazolium bromide (MTT) were purchased from Serva. American Type Culture Collection provided the HUH-7 and HepG2 cell lines. Trypsin-EDTA, penicillin-streptomycin solution, Dulbecco's Modified Eagle's medium (DMEM) High Glucose, L-glutamine, fetal bovine serum (FBS) and

phosphate buffer saline (PBS) were supplied from Biological Industries. MPC-3100 was obtained by AdooQ® Bioscience. 5-FU was purchased from Gold Biotechnology.

2.2. Cell Culture

The cell lines HUH-7 and HepG2 were cultivated in DMEM High Glucose medium containing 10% FBS, 0.1% penicillin-streptomycin and 1% L-glutamine. The cell lines were meticulously maintained under controlled conditions in a humidified environment at 37 °C with 5% CO_2.

2.3. Cell Viability Assay

The cytotoxic effects of MPC-3100 and 5-FU were assessed using the 3-(4,5-dimethylthiazol-2-yl)-2,5-diphenyltetrazolium bromide (MTT) cell proliferation assay. This method relies on the principle of MTT conversion, wherein viable cells transform MTT into insoluble formazan crystals through mitochondrial dehydrogenase activity. These crystals are subsequently dissolved in dimethyl sulfoxide (DMSO) and their absorbance at 570 nm wavelength is measured using a spectrophotometer [19]. The cancer cells were meticulously seeded in 96-well culture plates at a density of $5x10^4$ cells per well and incubated at 37°C with 5% CO_2 for 24 h. After this period, the culture medium was removed from the cells. MPC-3100 and 5-FU were individually dissolved in DMSO. The stock solutions for both drugs were at a concentration of 100 mM. The treatment of the cancer cell lines with the drugs was performed by diluting them from the DMSO stock solution into DMEM High Glucose medium. DMSO is non-toxic to HUH-7 and HepG2 cell lines when the final concentration is 0.1% [20]. In this study, DMSO solvent was used at a final concentration below 0.1%. The cells were treated with MPC-3100 and 5-FU at concentrations ranging from 5 µM to 0.078 µM and 10 µM to 0.156 µM for 24h and 48h, respectively. Individual drug cytotoxicity experiments were performed in serial dilutions, with maximal initial concentrations of 5 µM for MPC-3100 and 10 µM for 5-FU. Taking into account cytotoxicity values of the drugs, the ratio of 5 µM: 5 µM, i.e. 1:1, was investigated in combination tests and this ratio was kept constant. As a control group, cells were not treated with drugs and only DMEM high glucose medium was added. Following incubation, the medium was removed, and 100 µL of MTT solution (prepared fresh by adding 1 mL of 5 mg/mL MTT solution in PBS to 9 mL of medium) was added to each well. The cells were incubated at 37°C for 3 h. Following this, the MTT solution on the cells was aspirated and the resulting formazan crystals were dissolved by adding 100 µL of DMSO. Subsequently, the absorbance was then measured at wavelength of 570 nm using a spectrophotometer [21]. The following formula was used to determine cell viability as a percentage relative to the control group:

% Cell viability = (Absorbance of experimental group/Absorbance of control) x 100.

Nonlinear regression analysis was performed to determine the half-maximal inhibitory concentration (IC_{50}) of each drug, and the IC50 value was determined with a sigmoidal dose-response curve using GraphPad Prism 8.0.2 software.

2.4. Statistical Analysis

Data analysis and comparison were conducted using GraphPad Prism 8.0 software, with significance set at $p < 0.05$. The potential synergistic effect of the drug combination was assessed using the Chou and Talalay method, and the combination index (CI) was calculated utilizing CompuSyn software.

3. Results and Discussion

HUH-7 and HepG2 cells were used to investigate the combined effect of 5-FU and MPC-3100 on liver cancer. HUH-7 and HepG2 cell lines are widely acknowledged as the gold standard and are renowned for faithfully representing the characteristics observed in liver cancer [22]. These cell lines were selected for our investigation because they have a well-established reputation for correctly reflecting the characteristics of liver cancer. HUH-7 and HepG2 cells are epithelial in origin. Gene expression differs between the two cell lines [23]. A known difference between different HepG2 and HUH-7 cells is the different p53 status. HepG2 cells have wild-type p53 expression, whereas HUH-7 cells have mutant-type p53 expression [24]. HSP90's main client protein is p53, which is mutated in more than half of all human malignancies. Previous research has demonstrated that inhibiting HSP90 can cause mutant p53 to be ubiquitylated and degraded via the proteasome way. Because functioning p53 is present, inhibiting HSP90 activity in this manner might cause apoptosis [25]. In conclusion, we found that combining MPC-3100 with 5-FU might activate various pathways in HepG2 and HUH-7 cells. The MTT experiment was used to investigate the effect of 5-FU and MPC-3100 on cell viability after 24 and 48 hours as a single agent and in combination. As shown in Fig. 1, 5-FU and MPC-3100 inhibited cell viability in HepG2 and HUH-7 cells in a time- and dose-dependent manner.

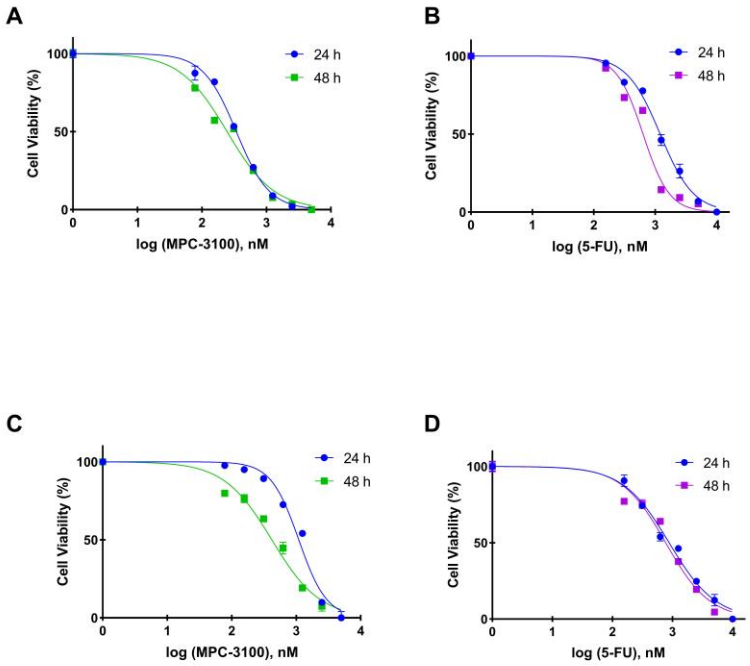

Fig 1. Antiproliferative effect of MPC-3100 (A), 5-FU (B) in HepG2 cell line and MPC-3100 (C), 5-FU(D) in HUH-7 at 24 h and 48 h.

Considering the IC_{50} values given in Table 1, HSP90 inhibitor MPC-3100 inhibited cell growth at low concentrations in both HepG2 and HUH-7 cell lines. Previous research has found that inhibiting HSP90 causes cell death in liver cancer cells. Watanabe et al. showed that treatment of HCC cells with the HSP90 inhibitor 17-AAG resulted in decreased viability of HCC cells and apoptosis of the cells. In addition, 17-AAG treatment caused an increase in the ratio of cells in the G2/M phase and decreased cdc2 protein degradation [26]. Compared to SNX-2112 17-AAG, an HSP90 inhibitor, showed a high inhibition effect on cell growth and triggered caspase-related apoptosis in these cells [27]. Administration of 17-DMAG HCC cells showed a cytotoxic effect on cells by decreasing NF-κB, cyclin D1 and survivin protein levels and increasing p53 protein levels [28]. When cells were treated with DMAG-N-oxide, the mean number of migrating cells was dramatically reduced [29].

Dose-dependent cell death occurred in both HepG2 and HUH-7 cells treated with 5-FU at 24h and 48h, and 5-FU showed a lower concentration of cytotoxic effect on HepG2 cells at 48h compared to HUH-7 cells. 5-FU is a cancer treatment drug that is frequently utilized. It produces cytotoxicity either by inhibiting the activity of the thymidylate synthase (TS) enzyme, preventing basic biosynthetic activity, or by inadvertently incorporating its metabolites into RNA and DNA [30]. However, chemotherapy resistance to 5-FU is a problem for many types of cancer, including liver cancers. When used in combination with other chemotherapies, effectiveness of 5-FU can be increased. Cisplatin combined with hepatic arterial infusion and 5-FU enhanced HCC patient survival compared to patients who did not receive the combination of treatments [31]. Clinical trials involving the combined use of cisplatin and 5-FU are being conducted in HCC patients who develop sorafenib resistance (NTC02967887) [17].

Table 1. IC_{50} values of MPC-3100 and 5-FU in HepG2 and HUH-7 cell lines at 24 h and 48 h.

	IC_{50} (nM)			
	MPC-3100		**5-FU**	
Cell Lines	**24 h**	**48 h**	**24 h**	**48 h**
HepG2	341.5 ± 0.002	245.4 ± 0.004	1203 ± 0.004	633.3 ± 0.005
HUH-7	1097 ± 0.005	419.4 ± 0.005	879.0 ± 0.004	770.6 ± 0.005

Because of multidrug resistance and dose-dependent cytotoxicity, 5-FU-based chemotherapy has poor clinical anti-cancer effectiveness. To address these issues, a new combination of 5-FU and additional anticancer drugs with different mechanisms of action is required. In this research, we investigated if the HSP90 inhibitor MPC-3100 and 5-FU could increase the anti-tumor effect on liver cancer cells. When we tested the effect of both drugs in combination on liver cancer cells, we discovered that co-administration of MPC-3100 and 5-FU had an antagonistic effect on both HepG2 and HUH-7 cell lines, which contradicted the predicted synergy commonly sought in combination (Fig. 2A and 2B). These findings indicate that the combination of the two drugs is less effective at inhibiting cell viability in liver cancer cells than alone. To confirm this antagonism, we administered the cells at a constant rate with a mixture of two drugs. The combination index (CI) was determined using the CompuSyn tool, as described in Chou and Talalay technique [32]. The Chou and Talalay method stand out as a basic approach in drug combination studies. Its foundations are based on the median effect equation. This equation is derived from the basic principle of the law of mass action, which combines single and multi-entity scenarios. The integration of the median-effect equation grounded in the mass action law has accelerated its practical applications [33, 34]. The use of the Chou and Talalay method became widespread after introduced an updated program called CompuSyn in 2005 [35]. This advanced program further streamlines the analysis process by allowing comprehensive evaluations such as dose ranges, combination ratios, design layouts, and even computerized simulations of drug interactions. The synergistic integration of CompuSyn and the Chou and Talalay method has become a powerful tool to unravel the complexity of drug combinations [36]. The study suggests that the synergistic, additional, and antagonistic effects of two agents may be characterized as follows: when CI is less than one, it represents synergistic effects; when CI equals one, it indicates additional effects; and when CI is greater than one, it indicates antagonistic effects [37]. HepG2 (Fig. 2C) and HUH-7 (Fig. 2D) liver cancer cells demonstrated antagonistic activity when MPC-3100 and 5-FU were combined.

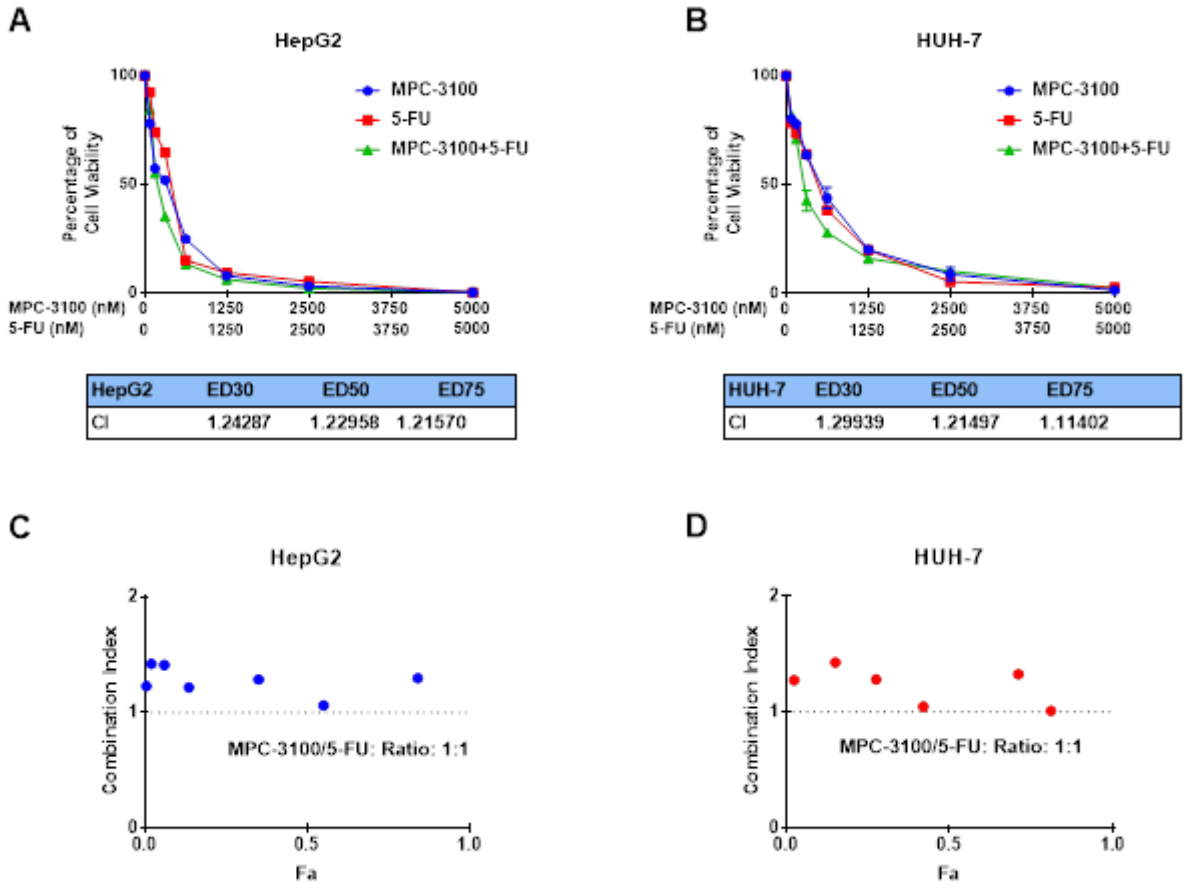

HepG2	ED30	ED50	ED75
CI	1.24287	1.22958	1.21570

HUH-7	ED30	ED50	ED75
CI	1.29939	1.21497	1.11402

Fig. 2. Survival graphs of HepG2 (A) and HUH-7 (B) cancer cell lines treated with the combination of MPC-3100 and 5-FU; graphs were drawn from combination index data versus fraction data (Fa) from the Chou and Talalay median effects analysis for HepG2 (C) and HUH-7 (D).*ED30, ED50, and ED75 are dosages that effectively block 30%, 50%, and 75% of cells or organisms, respectively (These data were calculated using CompuSyn software.). CI, combination index Fa, fraction affected. The values give information on a drug's or treatment's potency, indicating its potential to deliver desired results at specified dose levels.

In the literature, combinations of Hsp90 inhibitors with chemotherapy drugs (eg, cisplatin in glioma, docetaxel and paclitaxel in non-small cell lung cancer, and paclitaxel and cisplatin in head and neck squamous cell carcinoma) have been shown to be synergistic in most cases [38-40]. Liu et al. investigated the effect of SNX-2112, an HSP90 inhibitor, in combination with 5-FU in esophageal cancer and revealed that the combined use of the two drugs showed antagonistic effects in cells. When the molecular mechanism of this unexpected effect was investigated in detail, several possible causes were revealed [41]. Combining SNX-2112 and 5-FU may have opposing effects by reversing G2/M arrest, preventing initial mitochondrial membrane potential reduction, reducing Hsp90 client proteins and suppressing caspase-dependent apoptosis. In our study, the reason for the antagonistic effect of the combination of HSP90 inhibitor and 5-FU in liver cells may include the suggested reasons. In conclusion, while a more precise mechanism of the antagonistic action of HSP90 inhibitor with 5-FU needs to be further demonstrated

in other types of cancer. In clinical practice, the combination of HSP90 inhibitor and 5-FU should be used with caution.

4. Conclusion

This study demonstrates the potential of combining traditional chemotherapy drug 5-FU and next-generation HSP90 inhibitor MPC-3100 as a synergistic approach to treat HCC. The experiment demonstrated the dose- and time-dependent cytotoxic effects of both drugs on the liver cancer cell lines HepG2 and HUH-7, separately. The data from the combined usage of the two drugs revealed unexpected effects. MPC-3100 and 5-FU co-administration had an antagonistic impact on both HepG2 and HUH-7, rather than the predicted additive or synergistic effects. This surprising result highlights the intricate interplay between various drugs, stressing the need of considering all factors when developing combination therapy. It is obvious that combining MPC-3100 with 5-FU may not be an effective technique for increasing cytotoxicity in liver cancer cells. However, this finding serves as a springboard for future study, stimulating searching for novel drugs combinations and techniques to addressing the complicated nature of HCC. Experiences gained from research like ours will help to design more effective and focused treatments to combat HCC and other cancers as the field advances.

Acknowledgements

The author would like to acknowledge Prof Dr. İsa GÖKÇE and Dr. Nazan GÖKŞEN TOSUN for all support to this study.

References

[1] J. M. Llovet *et al.*, "Hepatocellular carcinoma," *Nature Reviews Disease Primers*, vol. 7, no. 1, p. 6, 2021/01/21 2021, doi: 10.1038/s41572-020-00240-3.

[2] Z. Chen *et al.*, "Recent progress in treatment of hepatocellular carcinoma," (in eng), *Am J Cancer Res*, vol. 10, no. 9, pp. 2993-3036, 2020.

[3] A. Alqahtani, Z. Khan, A. Alloghbi, T. S. Said Ahmed, M. Ashraf, and D. M. Hammouda, "Hepatocellular Carcinoma: Molecular Mechanisms and Targeted Therapies," (in eng), *Medicina (Kaunas)*, vol. 55, no. 9, Aug 23 2019, doi: 10.3390/medicina55090526.

[4] R. Bayat Mokhtari *et al.*, "Combination therapy in combating cancer," (in eng), *Oncotarget*, vol. 8, no. 23, pp. 38022-38043, Jun 6 2017, doi: 10.18632/oncotarget.16723.

[5] C. Hu *et al.*, "Heat shock proteins: Biological functions, pathological roles, and therapeutic opportunities," *MedComm*, vol. 3, no. 3, p. e161, 2022, doi: 10.1002/mco2.161.

[6] L. Qin *et al.*, "Biological characteristics of heat shock protein 90 in human liver cancer cells," (in eng), *Am J Transl Res*, vol. 11, no. 4, pp. 2477-2483, 2019.

[7] W. Wei *et al.*, "Diagnostic value of plasma HSP90α levels for detection of hepatocellular carcinoma," *BMC Cancer*, vol. 20, no. 1, p. 6, 2020/01/02 2020, doi: 10.1186/s12885-019-6489-0.

[8] S.-H. Kim *et al.*, "Discovery of (2S)-1-[4-(2-{6-Amino-8-[(6-bromo-1,3-benzodioxol-5-yl)sulfanyl]-9H-purin-9-yl}ethyl)piperidin-1-yl]-2-hydroxypropan-1-one (MPC-3100), a Purine-Based Hsp90 Inhibitor," *Journal of Medicinal Chemistry*, vol. 55, no. 17, pp. 7480-7501, 2012/09/13 2012, doi: 10.1021/jm3004619.

[9] S.-H. Kim *et al.*, "Discovery of an l-alanine ester prodrug of the Hsp90 inhibitor, MPC-3100," *Bioorganic & Medicinal Chemistry Letters*, vol. 25, no. 22, pp. 5254-5257, 2015/11/15/ 2015, doi: 10.1016/j.bmcl.2015.09.053.

[10] W. E. Samlowski *et al.*, "Abstract A96: Phase 1 study of HSP90 inhibitor MPC-3100 in subjects with refractory or recurrent cancer," *Molecular Cancer Therapeutics*, vol. 10, no. 11_Supplement, pp. A96-A96, 2011, doi: 10.1158/1535-7163.Targ-11-a96.

[11] K. Miura *et al.*, "5-fu metabolism in cancer and orally-administrable 5-fu drugs," (in eng), *Cancers (Basel)*, vol. 2, no. 3, pp. 1717-30, Sep 17 2010, doi: 10.3390/cancers2031717.

[12] M. Terashima *et al.*, "Synergistic antitumor effects of S-1 with eribulin in vitro and in vivo for triple-negative breast cancer cell lines," *SpringerPlus*, vol. 3, no. 1, p. 417, 2014/08/08 2014, doi: 10.1186/2193-1801-3-417.

[13] T. Xu *et al.*, "Synergistic Effects of Curcumin and 5-Fluorouracil on the Hepatocellular Carcinoma In vivo and vitro through regulating the expression of COX-2 and NF-κB," (in eng), *J Cancer*, vol. 11, no. 13, pp. 3955-3964, 2020, doi: 10.7150/jca.41783.

[14] S. Qin *et al.*, "Efficacy and safety of the FOLFOX4 regimen versus doxorubicin in Chinese patients with advanced hepatocellular carcinoma: a subgroup analysis of the EACH study," (in eng), *Oncologist*, vol. 19, no. 11, pp. 1169-78, Nov 2014, doi: 10.1634/theoncologist.2014-0190.

[15] Y. Zhang, L. Jiang, J. Ouyang, X. Du, and L. Jiang, "Efficacy and safety of traditional Chinese medicine injections combined with FOLFOX4 regimen for gastric cancer: A protocol for systematic review and network meta-analysis," (in eng), *Medicine (Baltimore)*, vol. 100, no. 41, p. e27525, Oct 15 2021, doi: 10.1097/md.0000000000027525.

[16] V. Conteduca *et al.*, "Oxaliplatin plus leucovorin and 5-fluorouracil (FOLFOX-4) as a salvage chemotherapy in heavily-pretreated platinum-resistant ovarian cancer," *BMC Cancer*, vol. 18, no. 1, p. 1267, 2018/12/19 2018, doi: 10.1186/s12885-018-5180-1.

[17] D. Anwanwan, S. K. Singh, S. Singh, V. Saikam, and R. Singh, "Challenges in liver cancer and possible treatment approaches," (in eng), *Biochim Biophys Acta Rev Cancer*, vol. 1873, no. 1, p. 188314, Jan 2020, doi: 10.1016/j.bbcan.2019.188314.

[18] L. Rinaldi *et al.*, "HCC and Molecular Targeting Therapies: Back to the Future," (in eng), *Biomedicines*, vol. 9, no. 10, Sep 28 2021, doi: 10.3390/biomedicines9101345.

[19] J. van Meerloo, G. J. Kaspers, and J. Cloos, "Cell sensitivity assays: the MTT assay," (in eng), *Methods Mol Biol*, vol. 731, pp. 237-45, 2011, doi: 10.1007/978-1-61779-080-5_20.

[20] Y. J. Chen, C.-W. Chi, W.-C. Su, and H.-L. Huang, "Lapatinib induces autophagic cell death and inhibits growth of human hepatocellular carcinoma," *Oncotarget*, vol. 5, no. 13, p. 4845, 2014.

[21] Ö. Kaplan *et al.*, "Microwave-assisted green synthesis of silver nanoparticles using crude extracts of Boletus edulis and Coriolus versicolor: Characterization, anticancer, antimicrobial and wound healing activities," *Journal of Drug Delivery Science and Technology*, vol. 64, p. 102641, 2021/08/01/ 2021, doi: 10.1016/j.jddst.2021.102641.

[22] G. Schicht, L. Seidemann, R. Haensel, D. Seehofer, and G. Damm, "Critical Investigation of the Usability of Hepatoma Cell Lines HepG2 and Huh7 as Models for the Metabolic Representation of Resectable Hepatocellular Carcinoma," (in eng), *Cancers (Basel)*, vol. 14, no. 17, Aug 30 2022, doi: 10.3390/cancers14174227.

[23] S. Guariniello, G. Di Bernardo, G. Colonna, M. Cammarota, G. Castello, and S. Costantini, "Evaluation of the Selenotranscriptome Expression in Two Hepatocellular Carcinoma Cell Lines," *Analytical Cellular Pathology*, vol. 2015, p. 419561, 2015/06/23 2015, doi: 10.1155/2015/419561.

[24] S. Hussain, J. Schwank, F. Staib, X. Wang, and C. Harris, "TP53 mutations and hepatocellular carcinoma: insights into the etiology and pathogenesis of liver cancer," *Oncogene*, vol. 26, no. 15, pp. 2166-2176, 2007.

[25] P. Muller, R. Hrstka, D. Coomber, D. P. Lane, and B. Vojtesek, "Chaperone-dependent stabilization and degradation of p53 mutants," *Oncogene*, vol. 27, no. 24, pp. 3371-3383, 2008/05/01 2008, doi: 10.1038/sj.onc.1211010.

[26] G. Watanabe, K. E. Behrns, J.-S. Kim, and R. D. Kim, "Heat shock protein 90 inhibition abrogates hepatocellular cancer growth through cdc2-mediated G2/M cell cycle arrest and apoptosis," *Cancer Chemotherapy and Pharmacology*, vol. 64, no. 3, pp. 433-443, 2009/07/01 2009, doi: 10.1007/s00280-008-0888-2.

[27] X. Wang *et al.*, "The Hsp90 inhibitor SNX-2112 induces apoptosis of human hepatocellular carcinoma cells: The role of ER stress," *Biochemical and Biophysical Research Communications*, vol. 446, no. 1, pp. 160-

166, 2014/03/28/ 2014, doi: 10.1016/j.bbrc.2014.02.081.

[28] A. M. Leng *et al.*, "The apoptotic effect and associated signalling of HSP90 inhibitor 17-DMAG in hepatocellular carcinoma cells," *Cell Biology International*, vol. 36, no. 10, pp. 893-899, 2012, doi: 10.1042/CBI20110473.

[29] W. Liu *et al.*, "A novel pan-cancer biomarker plasma heat shock protein 90alpha and its diagnosis determinants in clinic," *Cancer Science*, vol. 110, no. 9, pp. 2941-2959, 2019, doi: 10.1111/cas.14143.

[30] D. B. Longley, D. P. Harkin, and P. G. Johnston, "5-fluorouracil: mechanisms of action and clinical strategies," *Nature reviews cancer*, vol. 3, no. 5, pp. 330-338, 2003.

[31] C. Sethy and C. N. Kundu, "5-Fluorouracil (5-FU) resistance and the new strategy to enhance the sensitivity against cancer: Implication of DNA repair inhibition," *Biomedicine & Pharmacotherapy*, vol. 137, p. 111285, 2021/05/01/ 2021, doi: 10.1016/j.biopha.2021.111285.

[32] T. C. Chou, "Frequently asked questions in drug combinations and the mass-action law-based answers," *Synergy*, vol. 1, no. 1, pp. 3-21, 2014/09/01/ 2014, doi: 10.1016/j.synres.2014.07.003.

[33] C. T. Keith, A. A. Borisy, and B. R. Stockwell, "Multicomponent therapeutics for networked systems," *Nature Reviews Drug Discovery*, vol. 4, no. 1, pp. 71-78, 2005/01/01 2005, doi: 10.1038/nrd1609.

[34] T. C. Chou, "The mass-action law based algorithms for quantitative econo-green bio-research," (in eng), *Integr Biol (Camb)*, vol. 3, no. 5, pp. 548-59, May 2011, doi: 10.1039/c0ib00130a.

[35] N. Zhang, J. N. Fu, and T. C. Chou, "Synergistic combination of microtubule targeting anticancer fludelone with cytoprotective panaxytriol derived from panax ginseng against MX-1 cells in vitro: experimental design and data analysis using the combination index method," (in eng), *Am J Cancer Res*, vol. 6, no. 1, pp. 97-104, 2016.

[36] V. Banerjee *et al.*, "Synergistic potential of dual andrographolide and melatonin targeting of metastatic colon cancer cells: Using the Chou-Talalay combination index method," (in eng), *Eur J Pharmacol*, vol. 897, p. 173919, Apr 15 2021, doi: 10.1016/j.ejphar.2021.173919.

[37] T. C. Chou, "The combination index ($CI < 1$) as the definition of synergism and of synergy claims," *Synergy*, vol. 7, pp. 49-50, 2018/12/01/ 2018, doi: 10.1016/j.synres.2018.04.001.

[38] D. A. Proia *et al.*, "Synergistic activity of the Hsp90 inhibitor ganetespib with taxanes in non-small cell lung cancer models," (in eng), *Invest New Drugs*, vol. 30, no. 6, pp. 2201-9, Dec 2012, doi: 10.1007/s10637-011-9790-6.

[39] S. Ohba, Y. Hirose, K. Yoshida, T. Yazaki, and T. Kawase, "Inhibition of 90-kD heat shock protein potentiates the cytotoxicity of chemotherapeutic agents in human glioma cells," (in eng), *J Neurosurg*, vol. 112, no. 1, pp. 33-42, Jan 2010, doi: 10.3171/2009.3.Jns081146.

[40] J. A. Friedman *et al.*, "HSP90 Inhibitor SNX5422/2112 Targets the Dysregulated Signal and Transcription Factor Network and Malignant Phenotype of Head and Neck Squamous Cell Carcinoma," (in eng), *Transl Oncol*, vol. 6, no. 4, pp. 429-41, Aug 2013, doi: 10.1593/tlo.13292.

[41] Y. Liu *et al.*, "Combination of SNX-2112 with 5-FU exhibits antagonistic effect in esophageal cancer cells," (in eng), *Int J Oncol*, vol. 46, no. 1, pp. 299-307, Jan 2015, doi: 10.3892/ijo.2014.2714.

Contents lists available at Dergipark

Journal of Scientific Reports-A

journal homepage: https://dergipark.org.tr/tr/pub/jsr-a

E-ISSN: 2687-6167 **Number 55, December 2023**

RESEARCH ARTICLE

Receive Date: 31.07.2023 *Accepted Date: 20.11.2023*

Comparative analysis of the classification of recyclable wastes

Serkan Keskin[1,*], Onur Sevli[2], Ersan Okatan[3]

[1] *Burdur Mehmet Akif Ersoy University, Institute of Science and Technology, Department of Computer Engineering, Burdur, 15030, Türkiye, ORCID: 0000-0001-9404-5039*

[2] *Burdur Mehmet Akif Ersoy University, Faculty of Engineering and Architecture, Department of Computer Engineering Burdur, 15030, Türkiye, ORCID: 0000-0002-8933-8395*

[3] *Burdur Mehmet Akif Ersoy University, Gölhisar School of Applied Sciences, Department of Computer Technologies and Information Systems, Burdur,15400, Türkiye, ORCID: 0000-0001-6511-3450*

Abstract

The classification of recycling wastes is of great importance both environmentally and economically. Correct classification of recyclable wastes such as packaging wastes increases the efficiency of the recycling process. This classification process can be done according to the raw material type, colour, shape, size and source of the waste. Correct classification of recycling wastes also provides economic benefits by ensuring more efficient use of resources. The traditional waste classification method involves manually sorting waste into different categories. This method requires a lot of labour and is time consuming. The traditional waste classification method is also prone to human error, which can lead to contamination of recyclable materials. Deep neural networks can quickly identify different types of recyclable materials by analysing images of waste materials. Thus, it can increase efficiency and reduce pollution by sorting them appropriately. In this study, an experimental study was carried out on a data set consisting of 6 classes and 2527 images under the name of "Garbage classification". In this study, a comparative analysis was carried out using the Convolutional Neural Network architectures Resnet101, Convnext and Densenet121. As a result of this study, Resnet101 architecture was more successful than other architectures with an accuracy rate of 97.72%.

Keywords: Classification of Waste; Resnet101; Densenet121; CNN; Deep Learning; Artificial Intelligence

1. Introduction

As a result of population growth, urbanisation and industrialisation, which have been going on for many years throughout the world, a significant amount of resources are used. As a result, large amounts of waste are generated. Increasing waste accumulation has a very harmful effect on both people and the environment. The fact that all of these wastes remain in landfills and cannot be reused, combined with the presence of materials such as plastics that remain in nature forever, creates an extremely dangerous situation for all living things [1]. The construction of high-rise buildings after the forests are cleared, the increase in industrial wastes with the rapid growth of factories and the habit of indiscriminate disposal of wastes into the environment contribute to serious environmental problems that will affect us both today and in the future [2].

Recycled materials have become increasingly popular in recent years as they offer a more environmentally friendly alternative to conventional materials [3]. By using recycled materials, we can reduce the amount of waste going to landfills and conserve natural resources. The search for an automated method for recycling, in a society that values industry and knowledge, the aforementioned is of considerable value [4]. The effects of the situation are not limited to the environmental field, but also extend to social aspects. The economic impact also proves to be favourable.

There is a significant demand for a method that can help to categorise waste that is suitable for recycling in some way. Recent developments in deep learning have contributed to meeting this demand. As a result of these developments there have been several practical applications in augmented computer vision. Driven by extensive data analysis, particularly in relation to object recognition and detection [5], this field is focused on identifying and categorising objects within a given system. Litter can be effectively identified and classified using advanced computer deep learning algorithms in combination with labelled data [6]. Classification of recyclable objects can be done accurately with visual tools.

Instead of relying on traditional visual learning and feature extraction methods, deep learning has more advantages. Deep learning uses large amounts of data to predetermine which features and design elements to extract. This approach gives deep learning a greater potential for learning and adaptation compared to its traditional counterparts [7].

In this study, a dataset containing six waste classes was used. This dataset consists of images showing the appropriate classification of cardboard, paper, glass, plastic, metal and rubbish waste.

The problem of waste management is becoming more and more serious as time passes. In order to address this issue, studies on waste categorisation in the literature have been reviewed.

Yıldız et al. used deep learning and machine learning techniques on a dataset consisting of 6 classes and 2527 images. In the hybrid model they proposed, DenseNet20+DVM model was the prominent model with an accuracy of 89.70% [2]. Sürücü and Ecemiş, working with the same dataset, aim to automatically classify garbage in their study using transfer learning model. Using different transfer learning methods, the Resnet50-V2 model outperformed the other models with an accuracy of 97.07% [8]. In the study conducted by Meng et al. on the same dataset, a convolutional neural network was used to classify garbage. XDenseNet was created to classify visually obtained images. The accuracy rate of the model in the test data set is up to 94.1% [7]. In the study by Rismiyati et al. VGG16, ResNet-50 and Xception models were used. In the study where transfer learning method was also used, it is seen that the Xception model achieved the highest accuracy with 88% [9]. In the study by Meng and Chu, the data set consisting of 2527 images in the convolutional neural network was increased to 10108 images with the flip and rotation method. As a result of the classification, the ResNet50 model was 95.35% successful [4].

In this study, Fu et al. designed a new garbage sorting system based on deep learning. This system has Raspberry Pi 4B hardware and a camera. Transfer learning based classification and an improved MobileNetV3 model were proposed. The proposed system had a success rate of 92.62% [10].

Yang et al. used different methods to improve the robustness of the model and to obtain fast and accurate results using algorithm and data enhancement based on YOLO-V5. Images were created and classified with a camera placed on a garbage container. A 94.5% success rate was achieved with YOLO-V5 [11].

In this study, Yang et al. designed a new incremental learning framework GarbageNet. In addition, a memory pool and a metric-based classifier were developed. To improve the capacity of the model without retraining, 43 classes were evaluated using a dataset of 19459 images. It achieved a best performance of 96.96% with an acceptable extraction rate, outperforming all other valid methods [6].

In the study by Yang and Li, an application was developed for users to easily recognise garbage. They aimed to classify garbage through neural network. The success rate of the system named WaNet was 96.10% [3].

In their study, Cao and Xiang performed a classification study based on transfer learning using a convolutional neural network on imagenet dataset. As a result, an accuracy of 93.2% was achieved [12].

2. Materials and methods

2.1. Data Set

The dataset used to classify the waste in this study was obtained from the Kaggle website, which is open to all users [13]. This dataset is called "Garbage Classification". It contains a total of 6 classes. There are 2527 different images in the dataset, 403 in cardboard class, 410 in metal class, 482 in plastic class, 594 in paper class, 501 in glass class and 137 in rubbish class. The class distribution is given graphically in Figure 1.

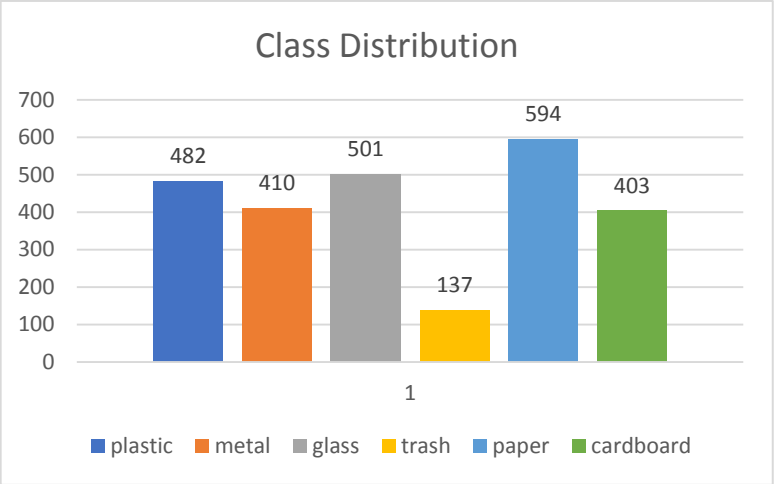

Fig. 1. Class distribution.

2.2. Convolutional neural network (CNN)

CNN consists of various parameters and layers that can be trained. Thanks to its layered structure, the determination of features is more successful and gives more effective results [14]. CNN architecture consists of three main components. These components are convolution, pooling and fully connected layer [5]. During the convolution layer, input data are filtered and features are obtained. Thus, feature maps are created that enable the learning of regional models. Figure 2 illustrates how the architecture can learn more complex objects, such as cats [15] [16], using hierarchically learnt local features. The pooling layer is used to materialise the attributes. The size is reduced through sampling, which also reduces the number of parameters. This leads to a faster learning process. By using a pre-trained model, the model can build on the knowledge already acquired through previous training [16]. In the fully connected layer, the output value is determined according to the neuron inputs of the previous layers [17]. The fully connected layer can also be used to target optimisation. Although CNN architecture is effective for visuals, it is not always sufficient for text-based analyses.

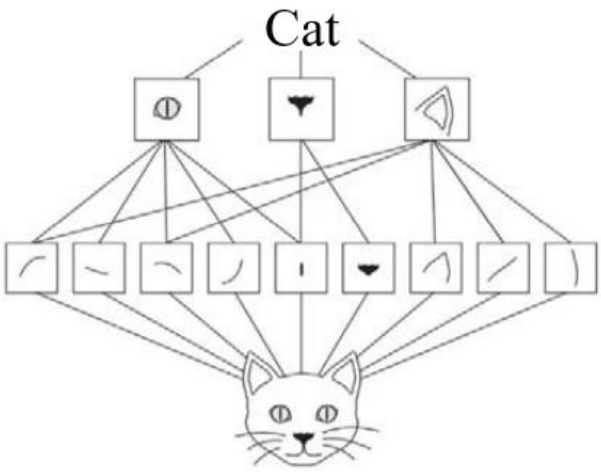

Fig. 2. High level object detection from learned local patterns [16].

2.3. Resnet101 architecture

ResNet is a class of neural networks designed to enhance traditional CNNs. One of the main features that distinguishes ResNets from others is the use of jump connections. This allows for a smaller network size compared to traditional CNNs while maintaining similar performance levels. Although jump connections can be used in any neural network architecture, they are

particularly useful in CNNs as they allow feature maps to be reused between layers at different locations [18]. Another important difference between ResNet and previous models is the increased depth of the network. ResNet is one of the pioneering algorithms in incorporating batch normalisation. The network requires input images of size 224×224×3 [2].

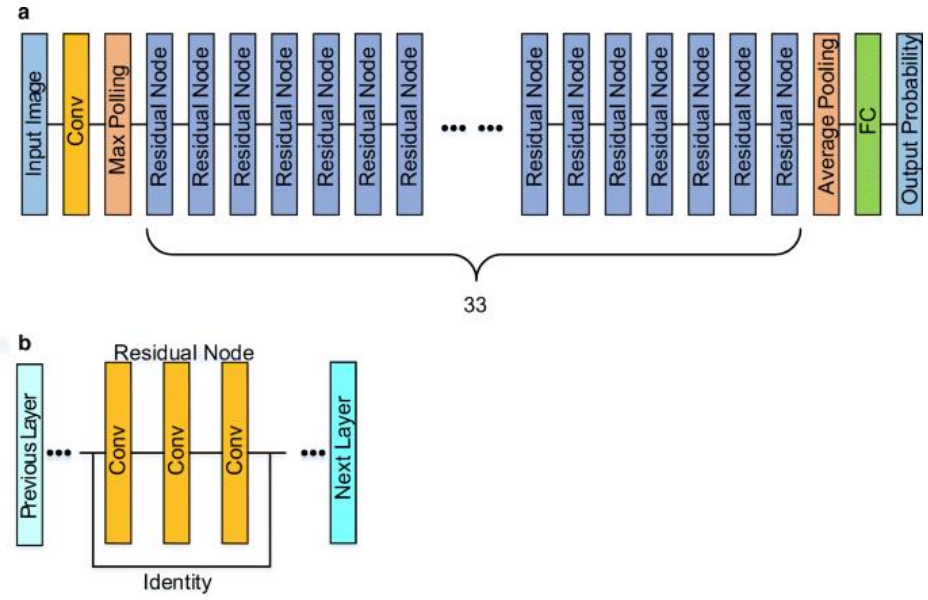

Fig. 3. Resnet101 architecture [19].

Figure 3 shows the Resnet101 architecture. A: Schematics of the ResNet101 architecture, which included 33 residual nodes in total. B: The residual node served as building block for the ResNet101 architecture [19].

In its entirety, ResNet-101 comprises 104 convolutional layers. Within this architecture there are a total of 33 blocks consisting of layers. Of these 33 blocks, 29 of them directly use the output of the previous block. These connections, called residual connections, contain residuals that are used as the primary operand in the resulting aggregation. The output of each block is combined to obtain the input to the next block. The remaining four blocks use the output of the previous block to generate their own outputs. After the convolution layer, there is a next step known as the chunk normalisation layer. This layer performs a convolution operation using a 1x1 filter size and a certain number of steps [20]. The output of this normalisation process is then added to the output of the previous block using the sum operator.

2.4. Convnext architecture

The study titled "ConvNext for the 2020s" published by Liu et al. in 2022 proposes a model inspired by the architectural structure known as Vision Transformers (VIT) [21] [22]. The model, called ConvNext, was classified as a pure CNN model in the study and showed more successful results than VIT architectures. The ConvNext model is characterised by blending the ResNet model with the design and techniques of the VIT architecture family. It results in a modernised and improved form. To address the linearity issue, the developed CNN model incorporates activation functions [23]. Specifically, an architectural update has been made by replacing the traditional choice of ReLU activation function with GeLU (Gaussian Error Linear Unit) in this model. Figure 4 shows an illustration of the Convnext architecture.

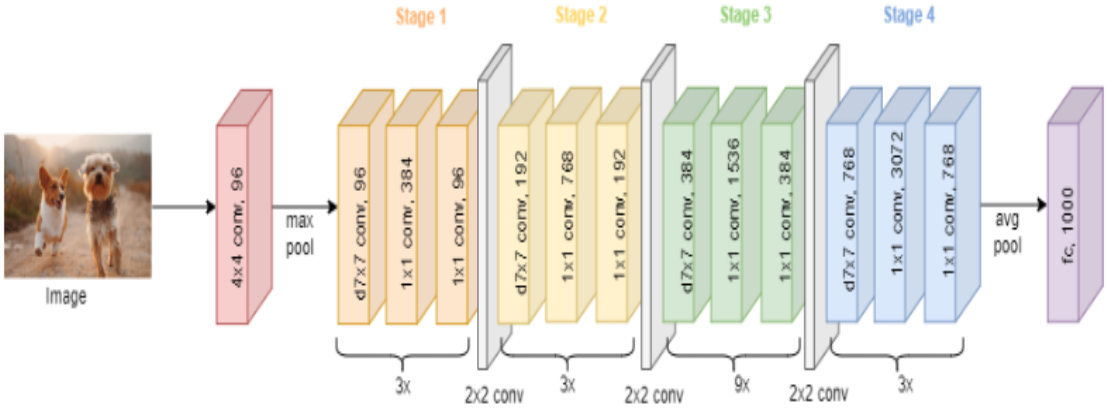

Fig. 4. Convnext architecture [24].

In terms of classification, Convnext exhibits superior performance compared to YOLO's Darknet53. ConvNeXt incorporates the Large Core Sizes optimisation method inspired by the design strategy used by Liu et al [21]. In Swin Transformer, this optimisation method has developed the concepts of Inverse Bottleneck, Deep Convolution and resnet50. As a result, ConvNeXt outperforms Swin Transformer and is able to achieve more successful results in object classification tasks. In object detection, YOLO is hampered by its single-stage detector, making it less effective in processing small objects. To address this limitation, we need higher attribute resolution and a larger detection area to improve its multi-scale target detection capability. Based on ConvNeXt, we increase the feature resolution by modifying the first subsampling layer. In addition, the ConvNeXt Block incorporates coordination attention to improve the network's ability to detect fine features.

2.5. Densenet121 architecture

In the field of deep learning, DenseNet121 is a CNN model that has attracted much attention. This model was introduced in 2016 by Gao Huang, Zhuang Liu, Laurens van der Maaten and Kilian Q. Weinberger in their paper "Densely Connected Convolutional Networks" [25]. The main goal of DenseNet is to streamline the training process of deep networks while at the same time improving their performance. It achieves this by utilising a unique connection structure. A notable feature of DenseNet is that the combined outputs from previous layers are incorporated into the inputs of subsequent layers. Unlike traditional CNN models, which typically combine layers sequentially, DenseNet establishes connections between each layer, the outputs of all previous layers and its own input. This integration, called "heavy coupling", facilitates a more comprehensive flow of information throughout the network. The Densenet121 architecture is shown in figure 5.

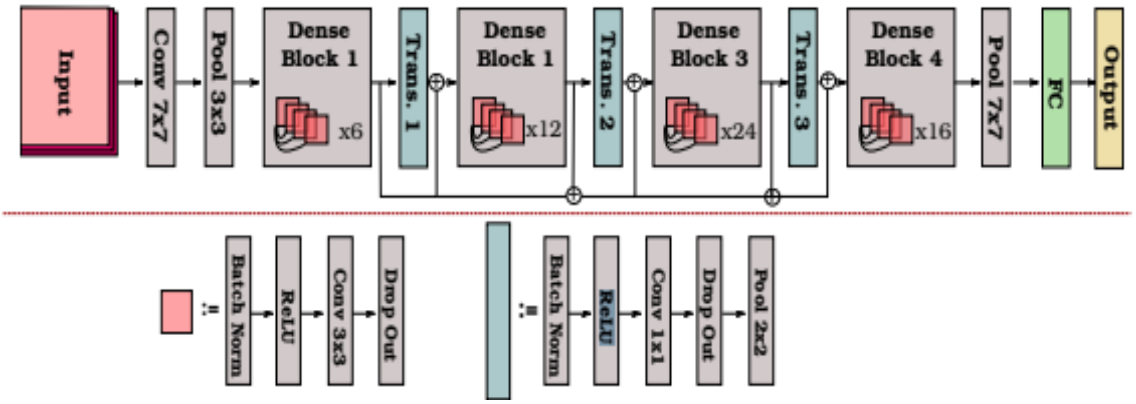

Fig. 5. Densenet121 architecture [26].

DenseNet121 is a complex model consisting of a total of 121 layers. These layers consist of a large number of interconnected smaller layers connected by dense links. This unique structure has the dual effect of reducing the total number of parameters in the network and increasing the efficiency of the training process. It strengthens the model against overlearning [27]. The architecture of DenseNet121 is characterised by its impressive achievements, especially in areas such as object detection, object classification, face recognition and various image processing. Some notable advantages of using DenseNet121 can be listed as follows. The training process is accelerated due to the ease of back propagation with gradients. As the network becomes more complex and interconnected, it becomes increasingly robust to overlearning [28]. The network can improve its performance while minimising the number of parameters required by making complex connections.

3. Experimental methods

In the experimental study, studies were carried out on the data set with Resnet101, Convnext and Densenet121 CNN architectures. These architectures were tested on the cloud servers of the google colab platform with RAM and GPU weight. In Python environment, numpy, pandas, pytorch and albumentations libraries were used. 20% of the images were allocated as test and 80% as training. As training data, there are 385 images from plastic class, 328 images from metal class, 400 images from glass class, 110 images from garbage class, 475 images from paper class and 322 images from cardboard class. The aim is to draw more accurate conclusions on data that the model has never seen. With 10 epochs and 16 batchsize, the training process was completed in 26 minutes 10 seconds for Resnet101, 29 minutes 32 seconds for Convnext and 35 minutes 11 seconds for Densenet121. Thanks to the jumping connections of Resnet101, incoming data is transferred faster from the lower layer to the higher layer. Thus, the process is faster than other architectures. Since the number of connections is denser in Densenet121, the calculation and result are later. Table 1 shows the accuracy rates of the results obtained from CNN architectures.

Table 1. Accuracy rates from CNN architectures (%).

Resnet101	Convnext	Densenet121
97.72	95.54	96.08

After the CNN architectures were trained, Resnet101 was the most accurate with 97.72% accuracy. Resnet101 was followed by Densenet121 with 96.08% and Convnext with 95.54%. The complexity matrices of CNN architectures are given in Table 2, Table 3 and Table 4.

Table 2. Resnet101 confusion matrix.

	plastic	metal	glass	trash	paper	cardboard
plastic	**378**		9	2		
metal		**328**		2		
glass	4		**389**	2		
trash	3		2	**104**		
paper					**462**	9
cardboard					13	**313**

Table 2 shows that Resnet101 CNN architecture has an accuracy rate of 98.41%. Resnet101 model predicted 1974 images correctly and 46 images incorrectly from 2020 images. Resnet101 model correctly predicted 378 images from 385 images for plastic class, 4 images as glass and 3 images as trash class. Resnet101 model predicted all 328 images correctly for the metal class. Resnet101 model correctly predicted 389 images out of 400 images for glass class, 9 images as plastic and 2 images as trash class.

Table 3. Convnext confusion matrix.

	plastic	metal	glass	trash	paper	cardboard
plastic	**363**	1	10	3	1	
metal	3	**326**	2	1		
glass	13		**386**	2		

trash	6	1	2	**101**	2	6
paper				2	**455**	17
cardboard				1	17	**299**

When Table 3 is analysed, it is seen that the accuracy rate of Convnext CNN architecture is 96.63%. Convnext model predicted 1930 images correctly and 90 images incorrectly from 2020 images. Convnext model correctly predicted 363 images from 385 images for plastic class, 13 images as glass, 3 images as metal and 6 images as trash class. For the metal class, Convnext model correctly predicted 326 images from 328 images, incorrectly predicted 1 image as plastic and 1 image as trash class. For the glass class, Convnext model correctly predicted 386 images out of 400 images, incorrectly predicted 10 images as plastic, 2 images as trash and 2 images as metal class.

Table 4. Densenet121 confusion matrix.

	plastic	metal	glass	trash	paper	cardboard
plastic	**371**	2	17	1		3
metal	2	**324**	2	3	1	
glass	10	1	**380**	1		1
trash	2	1	1	**104**	1	1
paper				1	**457**	12
cardboard					16	**305**

Table 4 shows that the accuracy rate of the Densenet121 CNN architecture is 97.11%. Densenet121 model predicted 1941 images correctly and 79 images incorrectly from 2020 images. Densenet121 model correctly predicted 371 images from 385 images for plastic class, 10 images as glass, 2 images as metal and 2 images as trash class. Densenet121 model correctly predicted 324 images from 328 images for metal class, incorrectly predicted 2 images as plastic, 1 image as glass and 1 image as trash class. Densenet121 model correctly predicted 380 images out of 400 images for glass class, incorrectly predicted 17 images as plastic, 1 image as trash and 1 image as metal class.

As an example, Figure 6 shows the classification image for control purposes after the process with Resnet101 architecture.

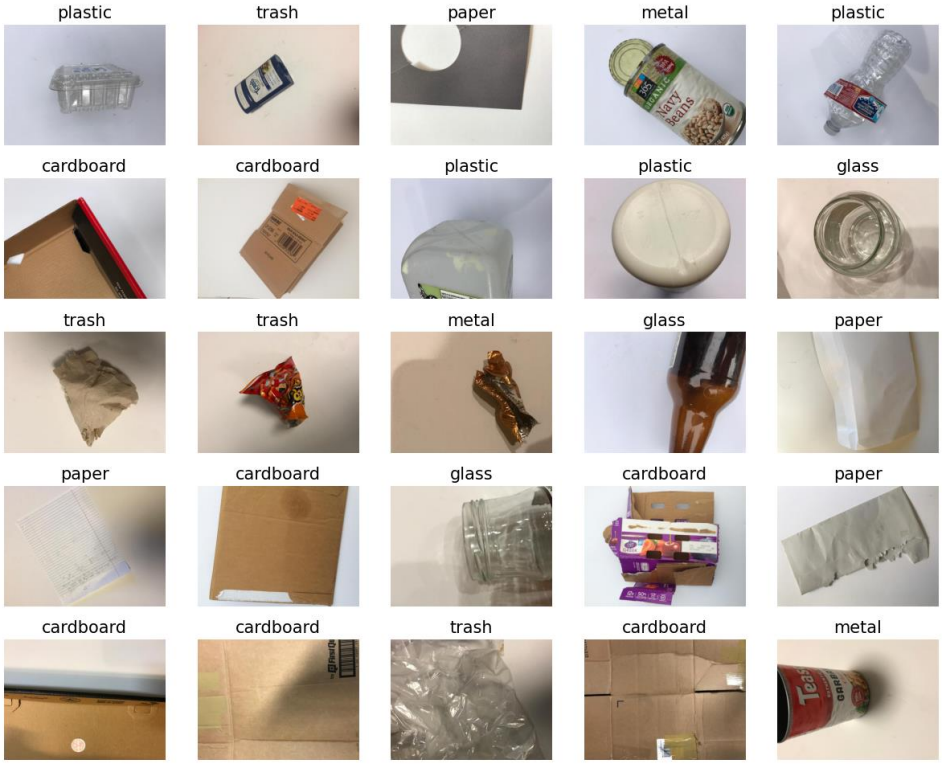

Fig. 6. Resnet101 classification image.

Table 5 shows a comparative table of the study and other studies.

Table 5. Comparison table of the same and similar studies.

Study Name	Method	Accuracy Ratio (%)
Yıldız et al., 2023 [2]	DenseNet20+DVM	89.70
Sürücü and Ecemiş, 2022 [8]	Resnet50-V2	97.07
Meng et al., 2020 [7]	XDenseNet	94.10
Rismiyati et al., 2020 [9]	Xception	88.00
Meng and Chu 2020 [4]	ResNet50	95.35
Fu et al., 2021 [10]	MobileNetV3	92.62
Yang et al., 2021 [11]	Yolo-V5	94.50
Yang et al., 2021 [6]	GarbageNet	96.96
Yang and Li, 2020 [3]	WaNet	96.10
Cao ve Xiang, 2020 [12]	Inception V3	93.20
This study	**Resnet101**	**97.72**
This study	**Convnext**	**95.53**
This study	**Densenet121**	**96.08**

The data set used in the studies of Yıldız et al, Sürücü and Ecemiş, Meng et al, Rismiyati et al, Meng and Chu in Table 5 is the same as the data set of our study. Other studies were conducted with different data sets. As can be seen from Table 5, the Resnet101 architecture used in our study was more successful than both the studies on the same data set and the other studies. The fact that the Resnet101 architecture is more successful than the others can be explained by the fact that the network goes deeper and adds the output of the previous layers directly to its history. Thanks to the 101 layer of Resnet, more accuracy gains have been obtained from the significantly increased depth by preventing data corruption problems during image processing.

4. Conclusion

In today's world, deep learning has proven to be highly effective in image processing and classification. Deep learning techniques have been applied with great success in various sectors such as health, agriculture, energy and industry. Training deep learning techniques on a variety of datasets, including images or other types of data, allows them to effectively learn complex patterns and features that cannot be recognised by conventional methods. Detection of such discriminations can be difficult using traditional techniques. Integrating deep learning approaches into waste classification systems improves their efficiency and accuracy. Ultimately, it encourages the proper management and recycling of various waste materials. The act of classifying landfill waste involves sorting it into different waste types and then incorporating it into the recycling system. This process is critical to minimise environmental impact, conserve natural resources and enable longer life and economic utilisation of waste. By recycling waste, the depletion of essential natural resources required for the production of new products is prevented. In addition, the recycling process enables the use of recycled materials instead of raw materials, resulting in significant energy savings and no reduction in greenhouse gas emissions during production. It helps the global effort to combat climate change. In the study, results from 3 different CNN architectures were obtained. The results obtained were compared and Resnet101 architecture stood out as more successful than other architectures with an accuracy rate of 97.72%. In addition, we get faster results with Resnet101 compared to other architectures. The classification and recycling of garbage waste is a vital issue not only today but also tomorrow. In future studies, we think that big data analytics can be used to better understand waste streams and consumer habits. In this way, we aim to develop more strategic approaches to reduce waste generation and improve sorting processes.

Acknowledgement

This research received no specific grants from any funding agency in public, commercial or non-profit sectors.

References

[1] C. Hark and S. Kiziloluk, ‘Geri Dönüştürülebilir Atiklarin Siniflandirilmasi’, Accessed: May 11, 2023. [Online]. Available: https://www.researchgate.net/publication/366153733

[2] E. N. Yildiz *et al.*, ‘Önerilen Derin Öğrenme ve Makine Öğrenmesi Tabanlı Hibrit Model ile Çevresel Atıkların Sınıflandırılması’, *Fırat Univ. J. Eng. Sci.*, vol. 35, no. 1, pp. 353–361, Mar. 2023, doi: 10.35234/FUMBD.1230982.

[3] Z. Yang and D. Li, ‘WasNet: A Neural Network-Based Garbage Collection Management System’, *IEEE Access*, vol. 8, pp. 103984–103993, 2020, doi: 10.1109/ACCESS.2020.2999678.

[4] S. Meng and W. T. Chu, ‘A Study of Garbage Classification with Convolutional Neural Networks’, *Indo - Taiwan 2nd Int. Conf. Comput. Anal. Networks, Indo-Taiwan ICAN 2020 - Proc.*, pp. 152–157, Feb. 2020, doi: 10.1109/Indo-TaiwanICAN48429.2020.9181311.

[5] Y. Lecun, Y. Bengio, and G. Hinton, ‘Deep learning’, *Nat. 2015 5217553*, vol. 521, no. 7553, pp. 436–444, May 2015, doi: 10.1038/nature14539.

[6] J. Yang, Z. Zeng, K. Wang, H. Zou, and L. Xie, ‘GarbageNet: A Unified Learning Framework for Robust Garbage Classification’, *IEEE Trans. Artif. Intell.*, vol. 2, no. 4, pp. 372–380, Aug. 2021, doi: 10.1109/TAI.2021.3081055.

[7] S. Meng, N. Zhang, and Y. Ren, ‘X-DenseNet: Deep Learning for Garbage Classification Based on Visual Images’, *J. Phys. Conf. Ser.*, vol. 1575, no. 1, p. 012139, Jun. 2020, doi: 10.1088/1742-6596/1575/1/012139.

[8] A. Makalesi, S. Sürücü, and İ. N. Ecemiş, ‘Garbage Classification Using Pre-Trained Models’, *Mayıs 2022 Eur. J. Sci. Technol. Spec. Issue*, vol. 36, no. 36, pp. 73–77, 2022, doi: 10.31590/ejosat.1103628.

[9] Rismiyati, S. N. Endah, Khadijah, and I. N. Shiddiq, ‘Xception Architecture Transfer Learning for Garbage Classification’, *ICICoS 2020 - Proceeding 4th Int. Conf. Informatics Comput. Sci.*, Nov. 2020, doi: 10.1109/ICICoS51170.2020.9299017.

[10] B. Fu, S. Li, J. Wei, Q. Li, Q. Wang, and J. Tu, ‘A Novel Intelligent Garbage Classification System Based on Deep Learning and an Embedded Linux System’, *IEEE Access*, vol. 9, pp. 131134–131146, 2021, doi: 10.1109/ACCESS.2021.3114496.

[11] G. Yang *et al.*, ‘Garbage Classification System with YOLOV5 Based on Image Recognition’, *2021 6th Int. Conf. Signal Image Process. ICSIP 2021*, pp. 11–18, 2021, doi: 10.1109/ICSIP52628.2021.9688725.

[12] L. Cao and W. Xiang, ‘Application of Convolutional Neural Network Based on Transfer Learning for Garbage Classification’, *Proc. 2020 IEEE 5th Inf. Technol. Mechatronics Eng. Conf. ITOEC 2020*, pp. 1032–1036, Jun. 2020, doi: 10.1109/ITOEC49072.2020.9141699.

[13] ‘Garbage Classification | Kaggle’. https://www.kaggle.com/datasets/asdasdasasdas/garbage-classification (accessed May 21, 2023).

[14] G. Çınarer , K. Kılıç and T. Parlar , "A Deep Transfer Learnıng Framework For The Stagıng Of Dıabetıc Retınopathy", Journal of Scientific Reports-A, no. 051, pp. 106-119, Dec. 2022

[15] F. Chollet, 'Deep Learning with Python, Second Edition', *Deep Learning with Python*, 2021. https://www.manning.com/books/deep-learning-with-python-second-edition (accessed May 21, 2023).

[16] E. Somuncu and N. A. Atasoy, 'Realization of character recognition application on text images by convolutional neural network', *J. Fac. Eng. Archit. Gazi Univ.*, vol. 37, pp. 17–27, 2022, doi: 10.17341/gazimmfd.866552.

[17] Z. Li, F. Liu, W. Yang, S. Peng, and J. Zhou, 'A Survey of Convolutional Neural Networks: Analysis, Applications, and Prospects', *IEEE Trans. Neural Networks Learn. Syst.*, vol. 33, no. 12, pp. 6999–7019, Dec. 2022, doi: 10.1109/TNNLS.2021.3084827.

[18] M. Shafiq and Z. Gu, 'Deep Residual Learning for Image Recognition: A Survey', *Appl. Sci. 2022, Vol. 12, Page 8972*, vol. 12, no. 18, p. 8972, Sep. 2022, doi: 10.3390/APP12188972.

[19] F. Li *et al.*, 'Deep learning-based automated detection of glaucomatous optic neuropathy on color fundus photographs', *Graefe's Arch. Clin. Exp. Ophthalmol.*, vol. 258, no. 4, pp. 851–867, Apr. 2020, doi: 10.1007/S00417-020-04609-8/FIGURES/4.

[20] A. Demir, F. Yilmaz, and O. Kose, 'Early detection of skin cancer using deep learning architectures: Resnet-101 and inception-v3', *TIPTEKNO 2019 - Tip Teknol. Kongresi*, vol. 2019-January, Oct. 2019, doi: 10.1109/TIPTEKNO47231.2019.8972045.

[21] Z. Liu, H. Mao, C.-Y. Wu, C. Feichtenhofer, T. Darrell, and S. Xie, 'A ConvNet for the 2020s'. pp. 11976–11986, 2022. Accessed: Jul. 20, 2023. [Online]. Available: https://github.com/facebookresearch/ConvNeXt

[22] X. Zhai, A. Kolesnikov, N. Houlsby, and L. Beyer, 'Scaling Vision Transformers'. pp. 12104–12113, 2022.

[23] E. Yüzgeç *et al.*, 'Alzheimer ve Parkinson Hastalıklarının Derin Öğrenme Teknikleri Kullanılarak Sınıflandırılması Classification of Alzheimer's and Parkinson's Diseases Using Deep Learning Techniques', *Fırat Üniversitesi Müh. Bil. Derg. Araştırma Makal.*, vol. 35, no. 2, pp. 473–482, 2023, doi: 10.35234/fumbd.1234638.

[24] 'ConvNeXt'. https://tech.bertelsmann.com/en/blog/articles/convnext (accessed Jul. 26, 2023).

[25] G. Huang, Z. Liu, L. van der Maaten, and K. Q. Weinberger, 'Densely Connected Convolutional Networks'. pp. 4700–4708, 2017. Accessed: Jul. 25, 2023. [Online]. Available: https://github.com/liuzhuang13/DenseNet.

[26] N. Radwan, 'Leveraging Sparse and Dense Features for Reliable State Estimation in Urban Environments', 2019, doi: 10.6094/UNIFR/149856.

[27] M. Chhabra and R. Kumar, 'A Smart Healthcare System Based on Classifier DenseNet 121 Model to Detect Multiple Diseases', *Lect. Notes Networks Syst.*, vol. 339, pp. 297–312, 2022, doi: 10.1007/978-981-16-7018-3_23/FIGURES/6.

[28] X. Zhang, X. Chen, W. Sun, and X. He, 'Vehicle Re-Identiication Model Based on Optimized DenseNet121 with Joint Loss', doi: 10.32604/cmc.2021.016560.

Contents lists available at *Dergipark*

Journal of Scientific Reports-A

journal homepage: *https://dergipark.org.tr/tr/pub/jsr-a*

E-ISSN: 2687-6167 ***Number 55, December 2023***

RESEARCH ARTICLE

Receive Date: 18.09.2023 *Accepted Date: 31.10.2023*

Investigation of bending behavior of foam core sandwich plates with different face and core materials at different layer thicknesses

Derya Çıraklı[1] , Uğur Albayrak[2*] , Mustafa Halûk Saraçoğlu[3]

[1]*Kütahya Dumlupınar University, Institute of Graduate Studies, Department of Civil Engineering, 43100, Kütahya, TÜRKİYE.*
ORCID: 0000-0001-8364-3420
[2]*Eskişehir Osmangazi University, Faculty of Engineering and Architecture, Department of Civil Engineering, 26480, Eskişehir, TÜRKİYE.*
ORCID: 0000-0001-7326-3213
[3]*Kütahya Dumlupınar University, Faculty of Engineering, Department of Civil Engineering, 43100, Kütahya, TÜRKİYE.*
ORCID: 0000-0003-3842-5699

Abstract

Sandwich plates consist of a total of three layers with a thick core layer between two thin face layers. While the face layers provide resistance against bending, the core layer provides resistance against shear. General purpose finite element software programs are one of the most convenient and widely used analysis procedures for investigating the behavior of structures. Many design parameters can be easily examined by these analysis programs. In this study, the bending of simply supported sandwich square plates on four sides with a ratio of core layer thickness to face layer thickness between 7 and 9 was investigated by using the general purpose finite element software program. The effect of the thickness change was investigated by changing the face and core layer thicknesses of the sandwich plates with a fixed total thickness. At the same time, the face and core materials were changed and the most suitable design in bending behavior was revealed. For this purpose, 110 analyzes were performed with 2 different face materials, 5 different core materials, 11 different thickness ratios, and the results were presented with graphics. It was concluded that the elasticity modulus of the material used in the face layer is a parameter that directly affects the midpoint deflection value. In sandwich plates, when the elasticity modulus of the face layer increases the resistance to bending also will increase.

Keywords**:** *Finite element method, Foam-core sandwich plate, Mid-point deflection, Thin plate, Static analysis.*

1. Introduction

Sandwich plates are widely used in civil engineering, offshore, marine and military fields, construction, aviation, automobile, aerospace, marine, etc. It is used in the construction of various structures in these areas. Also, they are also preferred for construction of filters, sports cars, wind turbine blades, aircrafts, boats, defense vehicles, etc.

The sandwich plates consist of two face sheets at the bottom and top and a core layer. As shown in Figure 1, an adhesive layer is used to bond the thin and rigid face sheets to the thick and light core layer. [1]. While the core layer of the structure increases the rigidity of the structure by carrying shear loads, the face sheets carry the bending stresses [2].

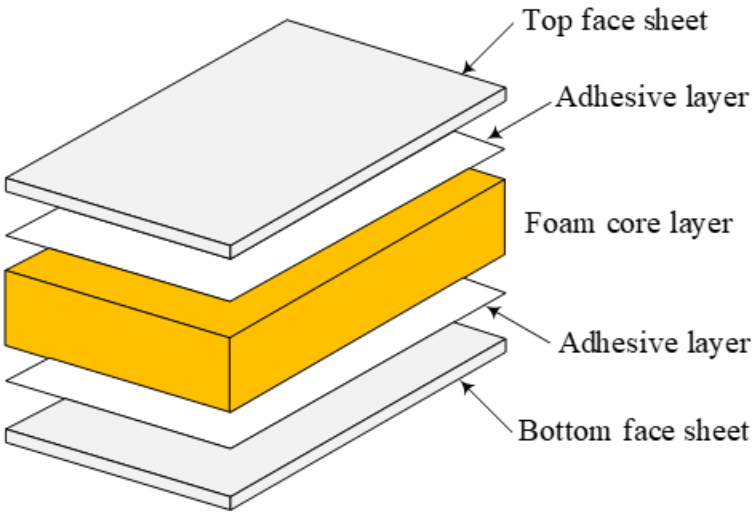

Fig. 1. Sandwich plate.

Insulating qualities, light weight, durability, impact resistance, damage and fatigue resistance are the advantages of sandwich plates.

Joints of the sandwich plates usually decrease the efficiency, and this is one of the disadvantages of sandwich plates. When cutting the sandwich plates, they can be easily damaged. They also require additional surface treatment.

Light materials such as honeycomb, balsa wood, EPS (expanded polystyrene), and foam are used as core materials. Carbon fabrics, glass fiber, GRP (glass reinforced polyester), FRP (fiber reinforced polymer), FRC (fiber reinforced composite) or isotropic materials such as steel and, aluminum are used as face sheet materials.

Many researchers have conducted studies on sandwich structures, which are special types of composite materials and economical, durable, very light materials. Garg et al. published a detailed study about sandwich structures made with functionally graded materials. In their study, a literature survey has been carried out for different theories and methods for static, vibration, and buckling analysis [3]. Xiong et al. investigate the developments and characterizations of sandwich structures with different core types in their review study [4]. Altunsaray, investigated the static deflections of sandwich plates. In the study, carbon/epoxy material used for the face sheets and balsa wood material used for the core. The obtained results were compare with the finite element method solutions [2]. Demirhan and Taşkın, presented static analysis of sandwich plates with foam cores. They derived the governing

equations and found the numerical results from the Navier's method [5]. Taşkın and Demirhan analyze the bending of simply supported porous sandwich plates by using the four-variable shear deformation theory. In their study, equilibrium equations are derived from the virtual displacement principle [6]. Some researchers have experimentally studied the bending behavior of sandwich plates. Moreira and Rodrigues investigate the static and dynamic analysis of soft core sandwich panels numerically and experimentally. For this purpose they formulate a new finite element by applying spring concept. They validate the numerical solutions with experiment results. Heywood et al. studied about the profiled sandwich panels with deep foam cores in flexure experimentally. And also they were developed numerical model and compare the results [7-8]. Li et al. developed a new model for functionally graded material sandwich plate in their study. They deduce the governing equations by using the static equilibrium method and verify the results with solutions solved with Navier approach [9]. Liaw and Little developed the governing equations for bending of multilayer sandwich plates in their study by variational methods [10]. Carbas investigated the static behavior of sandwich plates with different boundary conditions numerically and experimentally in thesis study [12].Mota et al. investigate the mechanical behavior of a sandwich plate with aluminum foam core in their study [15]. Yazdani et al. investigate the bending of composite sandwich plates using generalized differential quadrature method based on first order shear deformation theory [16]. Fan et al. investigate the nonlinear bending of sandwich plates with graphene nanoplatelets under various loads and boundary conditions [17].

In this study, static analyzes of uniformly distributed loaded foam core sandwich plates with different core materials and different layer thicknesses were investigated by using the general purpose finite element software program. The plates are simply supported on all four sides. The effect of materials and layer thickness in bending of sandwich plates are investigated. For this purpose, a simply supported square sandwich plate was considered, and uniformly distributed loads were applied to the plate. The sandwich plates with 11 different face and core layer thicknesses are modeled to investigate the effect of layer thickness. As a result of these analyzes, the effect of foam core material on foam core sandwich plates with the same conditions was investigated. The effect of the layer thickness for the design of the sandwich plates under bending has been determined.

2. Materials and methods

The classical laminated plate theory which is a pure plane stress model is used for the sandwich plates. The transverse rigidity of the material in the core layer of sandwich plates is lower than the transverse rigidity of the material in the face layers.

For sandwich plates, the mid plane deflection is considered to be small, and the following assumptions are made based on plate theory [11].

- The thicknesses of the face layers are thin compared to the core layer thickness.
- The face bending stiffness was ignored.
- The torsional and bending moments are carried by the top and bottom face layers.
- The shear stresses are carried by the core layer
- The shear stresses do not change throughout the thickness.

An example sandwich plate section is shown in Figure 2.

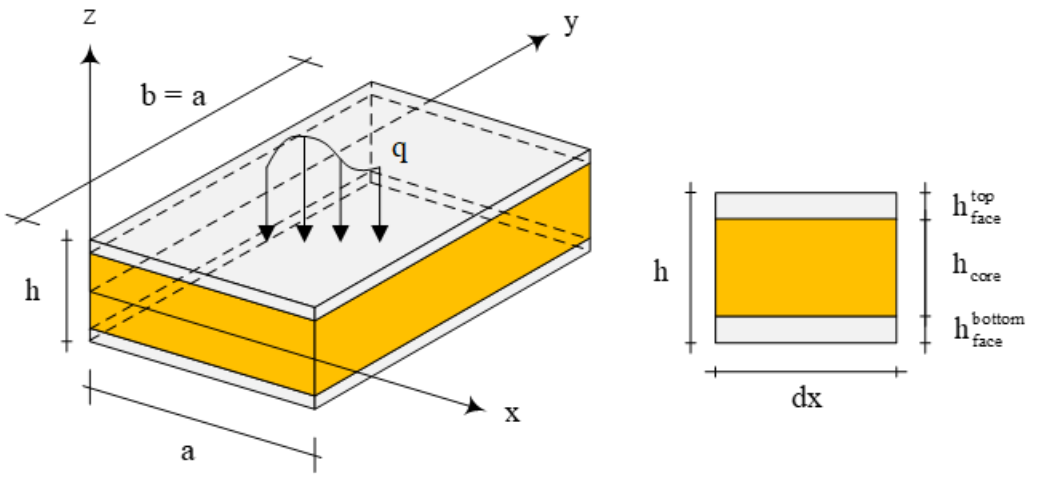

Fig. 2. Geometry and cross section of a rectangular sandwich plate.

In Figure 2, the thickness of the core part of the sandwich plate is shown as h_{core}, the upper layer thickness is shown as $h_{topface}$, and the bottom layer thickness is shown as $h_{bottomface}$.

Bending and torsional stiffnesses of sandwich plates are expressed by moments and derivatives of deflection [12]. These rigidities can be described as follows:

$$D_x = -\frac{M_x}{\partial^2 w/\partial x^2} \quad D_y = -\frac{M_y}{\partial^2 w/\partial y^2} \quad D_{xy} = -\frac{M_{xy}}{\partial^2 w/\partial x \partial y} \tag{1}$$

The transverse stiffnesses D_{Qx} and D_{Qy} are expressed by shear forces and shear strains [13]:

$$D_{Qx} = \frac{Q_x}{\gamma_{xz}} \quad D_{Qy} = \frac{Q_y}{\gamma_{yz}} \tag{2}$$

Poisson's ratios are described as[13]:

$$\nu_x = \frac{\partial^2 w/\partial y^2}{\partial^2 w/\partial x^2} \quad \nu_y = -\frac{\partial^2 w/\partial x^2}{\partial^2 w/\partial y^2} \tag{3}$$

There is a relationship between bending rigidities and Poisson ratios as $\nu_x D_y = \nu_y D_x$.

Bending curvatures and torsional curvatures are expressed as follows [13]:

$$\frac{\partial^2 w}{\partial x^2} = -\frac{M_x}{D_x} + \nu_y \frac{M_y}{D_y} + \frac{1}{D_{Qx}} \frac{\partial Q_x}{\partial x}$$
$$\frac{\partial^2 w}{\partial y^2} = -\frac{M_y}{D_y} + \nu_x \frac{M_x}{D_x} + \frac{1}{D_{Qy}} \frac{\partial Q_y}{\partial y} \quad (4)$$
$$\frac{\partial^2 w}{\partial x \partial y} = -\frac{M_{xy}}{D_{xy}} + \frac{1}{2D_{Qx}} \frac{\partial Q_x}{\partial y} + \frac{1}{2D_{Qy}} \frac{\partial Q_y}{\partial x}$$

The moment expressions used in the equilibrium equations for sandwich plates are as in Equation 5 [13]:

$$M_x = -\frac{D_x}{1-\nu_x \nu_y}\left[\frac{\partial}{\partial x}\left(\frac{\partial w}{\partial x} - \frac{Q_x}{D_{Qx}}\right) + \nu_y \frac{\partial}{\partial y}\left(\frac{\partial w}{\partial y} - \frac{Q_y}{D_{Qy}}\right)\right]$$
$$M_y = -\frac{D_y}{1-\nu_x \nu_y}\left[\frac{\partial}{\partial y}\left(\frac{\partial w}{\partial y} - \frac{Q_y}{D_{Qy}}\right) + \nu_x \frac{\partial}{\partial x}\left(\frac{\partial w}{\partial x} - \frac{Q_x}{D_{Qx}}\right)\right] \quad (5)$$
$$M_{xy} = -\frac{D_{xy}}{2}\left[\frac{\partial}{\partial x}\left(\frac{\partial w}{\partial y} - \frac{Q_y}{D_{Qy}}\right) + \frac{\partial}{\partial y}\left(\frac{\partial w}{\partial x} - \frac{Q_x}{D_{Qx}}\right)\right]$$

By substituting these expressions in the equilibrium equations, differential equilibrium equations are obtained for sandwich plates. The equilibrium equations are as follows [13]:

$$\frac{\partial M_{xy}}{\partial y} + \frac{\partial M_x}{\partial x} - Q_x = 0$$
$$\frac{\partial M_{xy}}{\partial x} + \frac{\partial M_y}{\partial y} - Q_y = 0 \quad (6)$$
$$\frac{\partial Q_x}{\partial x} + \frac{\partial Q_y}{\partial y} + q = 0$$

For an isotropic simply supported uniformly distributed loaded square plate mid point deflection value can be calculated as follows [13]:

$$w_{\max} = \frac{4qa^4}{\pi^6 D} \quad (7)$$

In this equation D is the flexural rigidity of the plate and can be calculated with the mechanical properties of isotropic material (Poisson's ratio and modulus of elasticity) and thickness of the plate h as below:

$$D = \left(Eh^3\right) \Big/ \left(12\left(1-\upsilon^2\right)\right) \tag{8}$$

Table 1 shows the mechanical properties of the materials used in this study.

Table 1. Mechanical properties of sandwich plate materials.

Type	**Material**	**E (MPa)**	**G (MPa)**	**K (MPa)**	**ν**
Face Sheet 1	Steel	206000.000	79300.000	171666.667	0.300
Face Sheet 2	Aluminum	69000.000	25940.000	68986.203	0.333
Foam Core 1	PVC H200	230.000	86.466	225.494	0.330
Foam Core 2	PVC H60	45.000	20.737	18.072	0.085
Foam Core 3	linear PVC foam (Airex R63.80)	56.000	21.000	56.000	0.333
Foam Core 4	AIREX® R82.110 High Performance Structural Foam	83.000	30.000	118.571	0.383
Foam Core 5	CoreLite PVC 100 Closed-Cell PVC Foam Sheet	89.980	37.000	52.795	0.216

In Table 1, ν is the Poisson's ratio, K is the bulk modulus, G is the shear modulus, and E is the elasticity modulus.

The calculation results of the examples discussed in this study were obtained using the ANSYS finite element package program. The three-dimensional Figure 3 shows the solid finite element, SOLID186 from the ANSYS element library, used in the study.

The SOLID186 element is a high-order three-dimensional 20-node solid element with second-order displacement behavior. Each of the 20 nodes of this element has three degrees of freedom. It supports properties such as plasticity, hyperelasticity, stress hardening, large displacement and large strain.

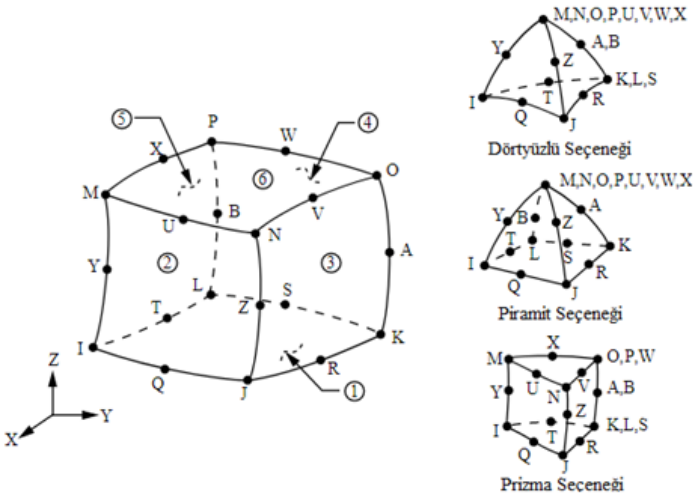

Fig. 3. SOLID 186 element [14].

3. Example problems

In this study, static analyzes of square sandwich plate models with 1000 x 1000 mm plane width with different layer thicknesses with same total thickness, which are formed by using two different rigid materials in the face layer and five different foam materials in the core layer performed. The sandwich plates were subjected to uniformly distributed load of q = 100 kN/m^2. The materials used in the sandwich plate examples were shown in Table 1.

Boundary conditions of the plates are simply supported on all four sides. In the analysis, combinations of three different parameters, namely Layer Thickness Effect (k), Face Material Effect (F), and Core Material Effect (C), will be discussed

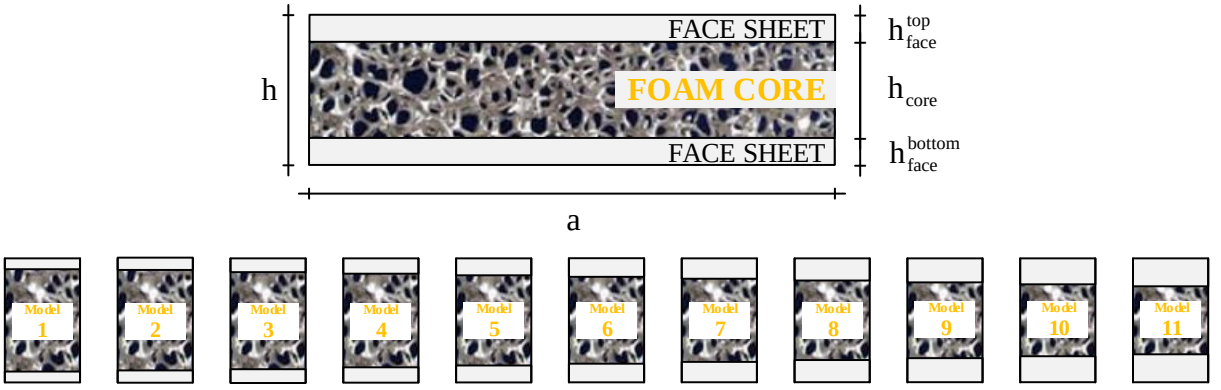

Fig. 4. Cross-sectional scheme of the 11 sandwich plate models.

In order to ensure the thin plate assumptions, the slenderness ratio of the plate was taken constant as a/h = 100. Accordingly, the total thickness of the square plate was taken as 10 mm in the 1000 mm x1000 mm samples. In the

samples, the face thicknesses were taken as equal. Plates of the same total thicknesses were obtained by increasing the core thicknesses and decreasing the face thicknesses with the $k = h_{core} / h_{face}$ equation. Different 11 sandwich plate models with k constants between 7 and 9 are considered as illustrated in Figure 4. The geometric properties of the examined plates are shown in the Table 2 below.

Table 2. Geometric properties of sandwich plates (mm).

model no	k	a	h	h_{face}	h_{core}
1	9.0	1000	10	0.91	8.18
2	8.8	1000	10	0.93	8.14
3	8.6	1000	10	0.94	8.12
4	8.4	1000	10	0.96	8.08
5	8.2	1000	10	0.98	8.04
6	8.0	1000	10	1.00	8.00
7	7.8	1000	10	1.02	7.96
8	7.6	1000	10	1.04	7.92
9	7.4	1000	10	1.06	7.88
10	7.2	1000	10	1.08	7.84
11	7.0	1000	10	1.11	7.78

4. Results and discussion

In the uniformly loaded simply supported square sandwich plates, the critical deflections occur at the mid point of the plate. Different models were analyzed to demonstrate the effect of the thickness and material changes of the layers on the critical deflection value for the sandwich plate.

A total of 55 problems (11 models for each 5 core materials) have been considered to investigate the Layer Thickness Effect (k) and Core Material Effect (C) by selecting the face material as steel. Mid point deflections vs layer thickness effect (k) for uniformly loaded square sandwich plates with the steel face are plotted in Figure 5 with different 5 core materials.

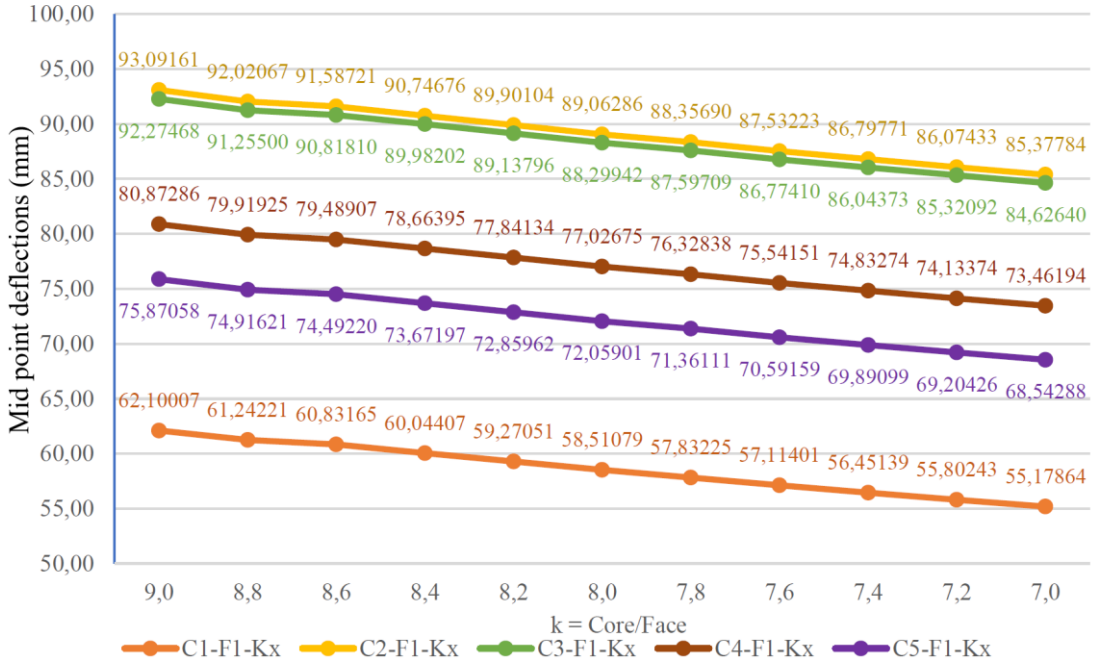

Fig. 5. Mid point deflections vs layer thickness effect k for steel face sandwich plates.

As can be seen from the Figure 5, the maximum deflection value of the sandwich plate decreases as the face layer thickness increases.

The elasticity modulus of the face layer is much higher than that of the core layers. So the strength of the core layer to the distributed load is very low compared to the face layer. For this reason, as the face layer's thickness increases and the core layer's thickness decreases, the sandwich plate's mid point deflection will decrease.

A total of 55 problems (11 models for each 5 core materials) have been considered to investigate the Layer Thickness Effect (k) and Core Material Effect (C) by selecting the face material as aluminum. Mid point deflections vs layer thickness effect (k) for uniformly loaded square sandwich plates with the aluminum face are plotted in Figure 6 with different 5 core materials.

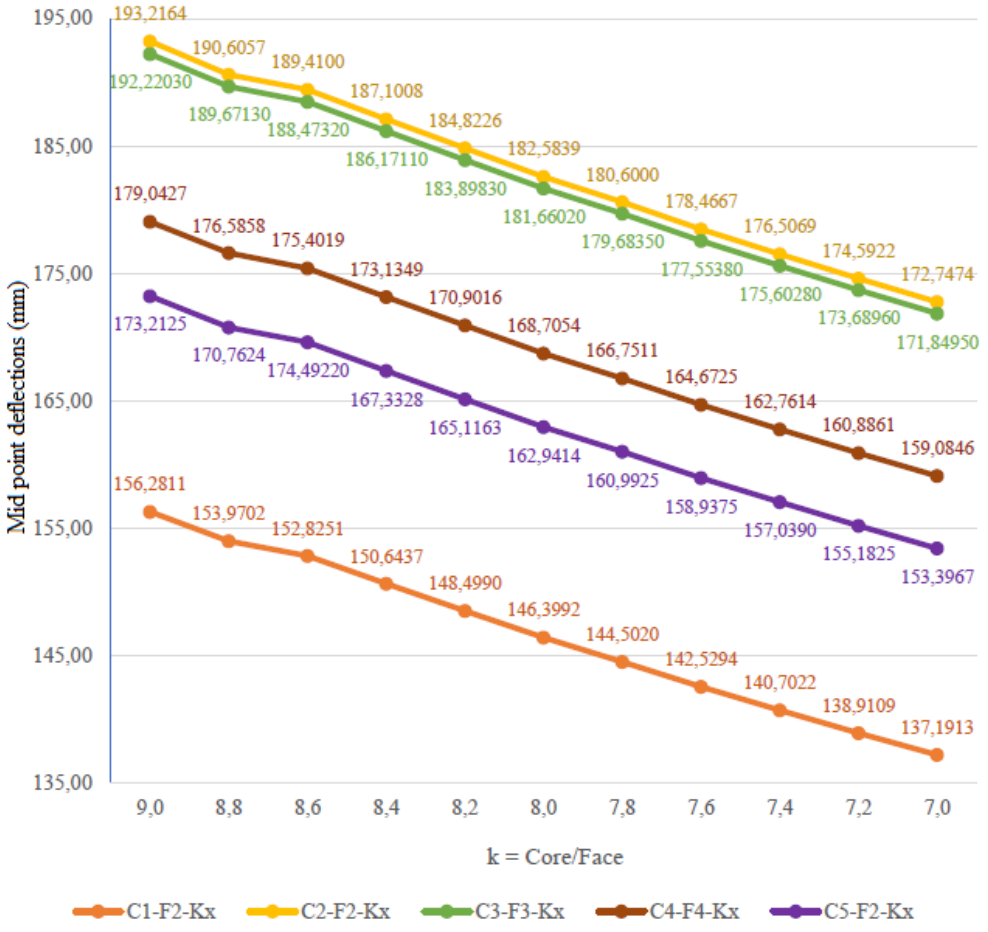

Fig. 6. Mid point deflections vs layer thickness effect k for aluminum face sandwich plates.

As can be seen from the Figure 6, the maximum deflection value of the sandwich plate decreases as the face layer thickness increases.

The elasticity modulus of the aluminum face layer is much higher than that of the core layers. So the strength of the core layer to the distributed load is very low compared to the face layer. For this reason, as the face layer's thickness increases and the core layer's thickness decreases, the sandwich plate's mid point deflection will decrease.

In Figure 7 mid point deflection according to the layer thickness effect k variation of sandwich square plates with both steel and aluminum faces is shown.

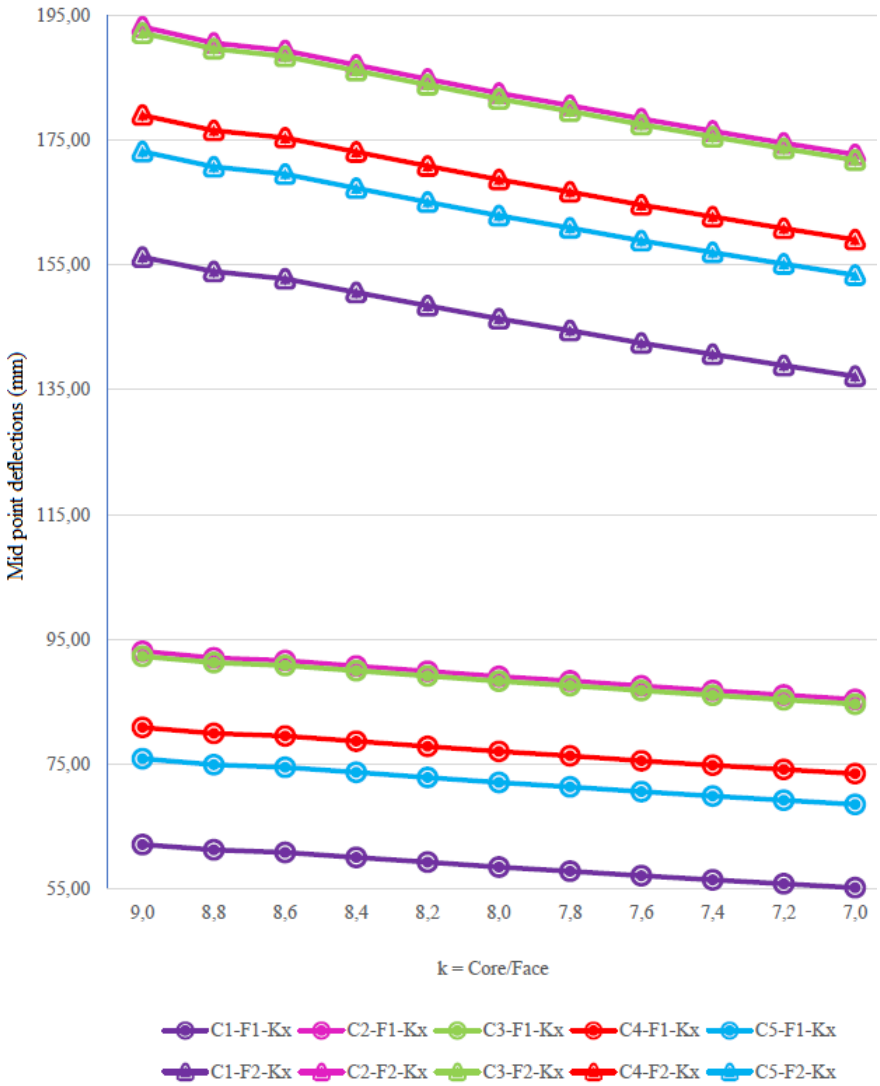

Fig. 7. Mid point deflections vs layer thickness effect k for steel and aluminum face sandwich plates.

As can be seen from the Figure 7, when the k value decreases mid point deflection also decreases. Also, as the elasticity modulus of the core layer material used in sandwich plates increases, the critical deflection that occurs at the midpoint of the sandwich plate decreases accordingly. As the elasticity modulus decreases, the critical deflection value occurring at the midpoint of the sandwich plate increases.

In the models that has steel face layer, mid point deflection varies between 55 and 93 mm dependent to core material. But these values are changes between 137 and 193 mm for aluminum face layered sandwich plates. The midpoint deflection value order according to the core material is similar in both face layer materials.

5. Conclusions

In this study, uniformly distributed loaded, 110 sandwich square plates simply supported on all four sides, consisting of different face and core thicknesses with different materials were investigated by using a finite element package program.

As the face layer thickness is increased and the core layer thickness is decreased, the maximum deflections that occurred at the midpoint of the plate were decreased (Figure 5-7).

When different materials are used, minimum midpoint deflection occurs in the model with the highest material modulus and a more rigid structure is obtained.

As the thickness of the face layer increases and the thickness of the core layer decreases, the bending resistance of the sandwich plate increases further. When the face layer is steel, the maximum mid-point deflection of the square sandwich plate changes between 93 mm and 55 mm approximately, but 193mm and 137 mm for the aluminum face layers. The mid point deflection is a parameter that depends on the material quality as well as the layer thickness.

As a result of the analysis, it was concluded that the face material is more dominant than the core material in the design of the uniformly distributed loaded simply supported sandwich square plates with constant thickness, and the sandwich plates with higher face layer thickness are more rigid.

Acknowledgments

This study was derived from the master's thesis.

References

[1] D. Çıraklı., (2023). Investigation of bending and buckling behaviors of foam core sandwich plates [Master Thesis]. Kütahya Dumlupınar University.

[2] Altunsaray, E. (2018). Static deflections analysis of long rectangular sandwich plates. Gazi Journal of Engineering Sciences, 4(1), 57–66. https://doi.org/10.30855/gmbd.2018.04.01.008

[3] Garg, A., Belarbi, M. O., Chalak, H. D. and Chakrabarti, A. (2021). A review of the analysis of sandwich FGM structures. In Composite Structures, 258, Elsevier Ltd., https://doi.org/10.1016/j.compstruct.2020.113427

[4] Xiong, J., Du, Y., Mousanezhad, D., Eydani Asl, M., Norato, J. and Vaziri, A. (2019). Sandwich structures with prismatic and foam cores: A Review. In Advanced Engineering Materials, 21(1). Wiley-VCH Verlag. https://doi.org/10.1002/adem.201800036

[5] Demirhan, P.A., Taşkın, V. (2016). Static analysis of simply supported foam core sandwich plate. Journal of International Scientific Publications: Materials, Methods and Technologies, 10, 325–336. www.scientific-publications.net

[6] Taskin, V., Demirhan, P. A. (2021). Static analysis of simply supported porous sandwich plates. Structural Engineering and Mechanics, 77(4), 549. https://doi.org/10.12989/SEM.2021.77.4.549

[7] Moreira, R. A. S., Rodrigues, J. D. (2010). Static and dynamic analysis of soft core sandwich panels with through-thickness deformation. Composite Structures, 92(2), 201–215. https://doi.org/10.1016/j.compstruct.2009.07.015

[8] Heywood, M. D., Ogden, R. G., Moutaftsis, D. (2014). Profiled sandwich panels with deep foam cores in flexure. In Proceedings of Institution of Civil Engineers: Construction Materials, 167(1), 42–56. https://doi.org/10.1680/coma.12.00016

[9] Li, D., Deng, Z., Xiao, H., Jin, P. (2018). Bending analysis of sandwich plates with different face sheet materials and functionally graded soft core. Thin-Walled Structures, 122, 8–16. https://doi.org/10.1016/j.tws.2017.09.033

[10] Liaw, B. D., Little, R. W. (1967). Theory of bending multi-layer sandwich plates. AIAA Journal, 5(2), 301–304. https://doi.org/10.2514/3.3956

[11] Libove, C., Batdorf S.B. (1948). A General Small-Deflection Theory for Flat Sandwich Plates, NTRS-NASA Technical Reports Server, Document ID:19930091966.
[12] Carbaş, M. (2007). Experimental and numerical analysis of static behaviour of sandwich plates with different boundary conditions [Master Thesis]. İstanbul Technical University.
[13] Timoshenko, S. , Woinowsky-Krieger, S. (1959). Theory of Plates and Shells. In McGraw-Hill, Inc.
[14] Swanson Analysis System Inc., A. (2005). ANSYS User's manual.
[15] Mota, A. F., Loja, M. A. R., Infante Barbosa, J. and Vinyas, M. (2021). Mechanical behavior of a sandwich plate with aluminum foam core, using an image-based layerwise model. Mechanics of Advanced Materials and Structures, 29(25), 4074–4095. https://doi.org/10.1080/15376494.2021.1919801
[16] Yazdani, M., Ghassemi, A. and Hedatati, M. (2013). Bending analysis of composite sandwich plates using generalized differential quadrature method based on FSDT. The Journal of Simulation and Analysis of Novel Technologies in Mechanical Engineering (JSME), 6(1), 47–62. www.jsme.ir
[17] Fan, X., Wang, A., Jiang, P., Wu, S. and Sun, Y. (2022). Nonlinear bending of sandwich plates with graphene nanoplatelets reinforced porous composite core under various loads and boundary conditions. Mathematics, 10(18). https://doi.org/10.3390/math10183396

Contents lists available at *Dergipark*

Journal of Scientific Reports-A

journal homepage: *https://dergipark.org.tr/tr/pub/jsr-a*

E-ISSN: 2687-6167 ***Number 55, December 2023***

RESEARCH ARTICLE

Receive Date: 17.04.2023 *Accepted Date: 30.10.2023*

Rapid processes for the production of nanocrystal yttria-stabilized tetragonal zirconia polycrystalline ceramics: ultrasonic spray pyrolysis synthesis and high-frequency induction sintering

Muhterem Koç[1*], Osman Şan[2]

[1*]*Kütahya Dumlupınar University, Department of Industrial Design, Kütahya, 43100, Turkey. ORCID: 0000-0003-3661-4410*
[2]*Kütahya Dumlupınar University, Department of Materials Science and Engineering, Kütahya, 43100, Turkey, ORCID: 0000-0001-6033-5804*

Abstract

In this study, nanocrystalline 3 mol % yttria-stabilized tetragonal zirconia polycrystalline (Y-TZP) ceramic was produced by sintering with a high-frequency induction heating (HFIH) system of granular powders obtained by ultrasonic spray pyrolysis (USP) at 600 °C. The granular nano-sized powders (10-30 nm) were micron in size (average size: 700 nm), spherical in shape and amorphous. The influences of the HFIH sintering temperature (1400-1600 °C), applied current time (60-300 sec.) and the mechanical pressure (10 MPa and 20 MPa) on the final density and grain size of the products were investigated. The amorphous granular Y-TZP powders compressed with the HFIH system allow very rapid condensation in the tetragonal phase at high density and avoid grain growth. High density (relative density over 95) nanocrystalline Y-TZP ceramic with ~70 nm size could be obtained from the simultaneous application of 20 MPa pressure and an induced current within 300 sec. of sintering time at 1500 °C. In this condition, the sample's maximum hardness and fracture toughness values were reached at 14.9 GPa and 3.8 MPa·$m^{1/2}$, respectively. Y-TZP powders produced in nano-micro structure with the USP system were sintered with the HFIH system and rapid production was achieved by preventing grain growth.

Keywords: Granular powder, Y-TZP, rapid processes, microstructure.

[*] Corresponding author. Tel.: +90 (274) 443 44 61
E-mail address: muhterem.koc@dpu.edu.tr
https://orcid.org/0000-0003-3661-4410

1. Introduction

The zirconia based ceramic materials has been widely used in modern technologies because of the unique combination of physicochemical properties such as mechanical strength, hardness, toughness, refractory properties as well as the high resistance to aggressive media. The performance of zirconia material increased by the stabilization as tetragonal phase using some additives such as Y_2O_3, CaO, CeO_2, MgO, etc. [1–4]. The use of 3 mol% yttria was main additive and it was proved that the zirconia ceramic has excellent strength and toughness [5]. Moreover, the study of Wakai et al. [6] revealed that when yttria- stabilized zirconia ceramics have been produced, they have exhibited superplastic properties.

The superplastic deformation behavior of the yttria-stabilized tetragonal zirconia is primarily dependent on small grain sizes [7–9]. However, it is difficult to obtain the grains which are smaller than 100 nm in size. The conventional pressureless sintering required a high temperature and long-time sintering for sufficient densification and thus this condition leads to grain growth phenomenon by diffusion. Therefore, it is necessary to analyze the fabrication of zirconia ceramics such as hot pressing [10,11], spark plasma sintering [12], hot isostatic press [13,14], high frequency induction sintering [15–18]. In these processes, the applied pressure has great importance on the rearrangement of the particles during the compaction as well as the densification. The powder compaction not only depends on the applied pressure, but also the nature of thermal environment, the size, the size distribution, and the shape of the particles greatly determine the densities [19,20]. However, the research was focused on the effect of applied pressure on the densification which were correlated by the grain growth to find optimum conditions [21,22].

It is known that the densification of ceramics is achieved by two mechanisms: (i) the shrinkage of the open pores and (ii) the grain boundary diffusion. In the conventional pressureless sintering, the transition from the open pore structure to the closed pore takes over a long period of time. In this process, the grain growth is low, in which the pores repress the grain growth. The main grain growth is seen during the process where the open porous structure disappears. At this stage, high mass transport occurs with diffusion by increasing intergranular contact. In sintering under pressure, the two processes are quick and the period in which the high packing process is penetrated is of even greater importance. In this way, the mass transport takes place at high level and the grain growth increases rapidly. Therefore, in the sintering processes under pressure, the relationship between the duration of sintering and the grain growth must be carefully determined. This process can lead to high grain growth in a much shorter period of time depending largely on the applied pressure [21]. Recently, forming of a second phase at the grain boundary or grain boundary precipitation to control of grain growth in sintering process has been studied. [23,24]. However, the thing that shouldn't be forgotten here is that the primary properties of the starting powder are much more effective. The subject matter which is more important than producing second phase is morphology of the powders, deformation ability, porosity and porosity distribution and homogeneous phase structure control.

In order to obtain yttria stabilized zirconia nanocrystalline ceramic, some methods such as co-precipitation [25], sol–gel technique [26] and USP system [27] have been employed to prepare the starting nano powders. There are two basic process difficulties in material production from nano-sized powders. First, the fine powders show rapid aggregation in the production process which makes high density packing impossible. Secondly, the nano-powders rapidly form grain growth at high temperatures, therefore, the preparation of the nano-sized starting powders cannot contribute positively to the physical properties of the produced material. Recently, intense efforts have been made to process nano-sized powders. The most remarkable method in this area is the production of nano-powders as agglomerate granules. The USP system seems to be quite successful in establishing these controlled agglomeration conditions. Particularly, easy controllable parameters such as the composition of the solution to be fed into the system, surface energy and reactor temperature allow agglomerated powder production with different properties. In this system, the initial stoichiometry in the produced powders is preserved on grain basis, and agglomerations of primary crystals and the micro-spherical particles composed of nano-sized particles can be produced as porous or dense structure depending on the reactor temperature [19]. Kang et al. [25] synthesized hollow Y-TZP powders (600 and 900 °C) and transformed them into nano-scale particles by planetary milling. As a result of the conventional sintering process (1300-1500 °C), these powders were found to be below 1 μm at 1300 and 1400 °C and 2.3 μm due

to the grain growth at 1500 °C. The sintering of these powders under pressure with fast sintering is expected to provide higher performance. On the other hand, no literature has been found on the sintering of Y-TZP powders produced by the USP system directly (without the milling process) under pressure with HFIH method.

In our present work, the Y-TZP nanocrystalline ceramics were fabricated by the rapid processes such as HFIH of the granule powder obtained by USP system. The granule powder was obtained from yttrium and zirconium hydroxide colloidal solution at the reactor temperature of 600 °C. The effects of the sintering temperature (1400-1600 °C) for different holding times (60-300 sec.) on the relative density, average grain size, phase microstructure, and vickers micro hardness of the Y-TZP nanocrystalline ceramics were investigated.

2. Materials and Methods

The Y-TZP granular particles were prepared by the USP technique using an ultrasonic nebulizer. Zirconium (IV) nitrate hydrate ($ZrO(NO_3)_2 \cdot 6H_2O$) (99 %,Sigma), yttrium (III) nitrate hydrate ($Y(NO_3)_3 \cdot 6H_2O$) (%99.8,Sigma), ammonium hydroxide solution (NH_4OH) (30-32%, Sigma) and nitric acid HNO_3 (70%, Sigma) were selected as starting materials. The synthesis of ZrO_2-Y_2O_3 solution was carried out by co-precipitation method. Precursor solution of 0.97 mol ZrO_2 and 0.03 mol Y_2O_3 were prepared by dissolving in deionized water and mixed using magnetic stirrer at 500 rpm until obtaining a clear solution. Then, the NH_4OH solution was added dropwise into a continuously stirred precursor solution (pH∼9) and subsequently the mixture was filtered for the removal of precipitate. The precipitate was washed three times with deionized water in order to ensure that the NO_3 and NH_4OH was completely removed from the precipitate. Yttrium and zirconium hydroxide colloidal sol solution was adjusted to pH 3 using nitric acid. Then the Y-TZP particles were produced with the ultrasonic spray pyrolysis (USP) system at 600 °C reactor temperature. The overall concentration of zirconium and yttrium sources was fixed at 0.1 M in deionized water and ethanol (water/ethanol ∼3). The frequency of the ultrasonic nebulizer and the feed rate of the carrier gas were 1.63 MHz and 2 Lt/min, respectively. Quartz tube with a length of 120 cm and a width of 5 cm was used for powder production. The powders produced from the USP system were collected in three gas washing bottles connected in series at the outlet. The details of the ultrasonic spray pyrolysis system were given elsewhere [28].

In the sintering process of powders, a HFIH system with a frequency of 900 kHz and a power of 2.5 kW was used. The sintering process was carried out at different dwelling times (60-300 sec.) between 1400 and 1600 °C. Powder sintering was performed in a vacuum tank, under pressure and with the help of graphite mould. The powders were placed in the system by being filled in a graphite mould (outer diameter: 20 mm, inner diameter: 10 mm and height: 20 mm) and were pressed under pressure of 10 and 20 MPa during the sintering process with the help of a uniaxial pressing. The heating rate was over 1000 °C/min and the temperature was measured on graphite mould by optical pyrometer (600-2200 °C). Sintering process consisted of the following steps: (i) firstly a vacuum of 30 mTorr was applied to the system, (ii) the powder in the graphite mould was compressed with uniaxial pressing (iii) the sintering process started by activating the induction system, (iv) when the sintering process finished, it was allowed to cool down to the room temperature, the vacuum was closed, the pressure was removed, and the sample was taken out of the mould.

Thermal decomposition behavior of USP powder was determined by TG-TGA analysis (Perkin Elmer–Diamond) up to 1500 °C at heating rate of 10 °/min. The phases of the prepared powder and samples were determined by XRD (Rigaku-MiniFlex) analysis. XRD analyses were performed at a speed of 2°/min with 0.01° steps using CuKα radiation between 20° and 80°. The crystal size of Y-TZP bulk materials was calculated by Scherrer formulation applied to XRD analysis. The density of the samples was determined by the method of Archimedes. The morphology of the powders and the samples were determined by the scanning electron micrographs (SEM) (Zeiss Supra 50 VP) (Bulk samples were polished and investigated by performing platinum plating on surfaces that were thermally etched at 1250 °C). Particle size distribution was determined by SEM image (using Image J software) and Malvern/Mastersizer 3000. The structure of the particles was characterized by TEM (JEOL JEM 2100F HRTEM). The Vickers microhardness and fracture toughness values of the materials were measured by the notch marks made under 1 kg of force applied for 15 seconds (Duraline M Mikro-Vickers). At least five measurements were taken for

each sample. The fracture toughness was calculated from the crack length under load.

3. Results and Discussion

3.1. Properties of USP granule particles

Fig. 1a-d shows the physical characteristics of the Y-TZP granule powders through the analysis of XRD phase (a), particle size distribution (b), SEM microstructure (c), TEM (d). The obtained results are as follows: (i) it was found that that the granule powder in amorphous structure could be obtained with the low reactor temperature (600 °C) (Fig. 1-a), (ii) the size distribution of the granules was suitable for high density packaging; the average size of the powders was 700 nm and showed a monomodal distribution between 118 nm and 2099 nm (Fig. 1-b), (iii) the granules preserved sufficient spherical structure, there was no primary particles (Fig. 1-c), (iv) micro-sized granules were composed of the primary particles where the grains were in nano-sizes (10-30 nm) (Fig. 1-d).

In the present study, the appropriate reactor temperature was firstly determined. As known, the amorphous powders show high sintering properties and thus the reactor temperature was adjusted to obtain the granule powder in amorphous phase; the applied reactor temperature of 600 °C did not lead to crystallization. On the other hand, the powders must be granule grains, so the temperature should be sufficient to improve the agglomeration. Perez–Page et al. investigated yttria stabilized zirconia powders with the USP system for temperatures between 700 °C and 1200 °C and revealed that these powders were crystallized at 700 °C temperature and the crystallization increased depending on the increase in reactor temperature [29]. In our present study, the selected reactor temperature was relatively low. Powder produced at 600 °C was amorphous with the spherical granules in micron size. The powder was expected to be densify by the induction sintering process under the target pressure, which will provide high density packing with low grain growth.

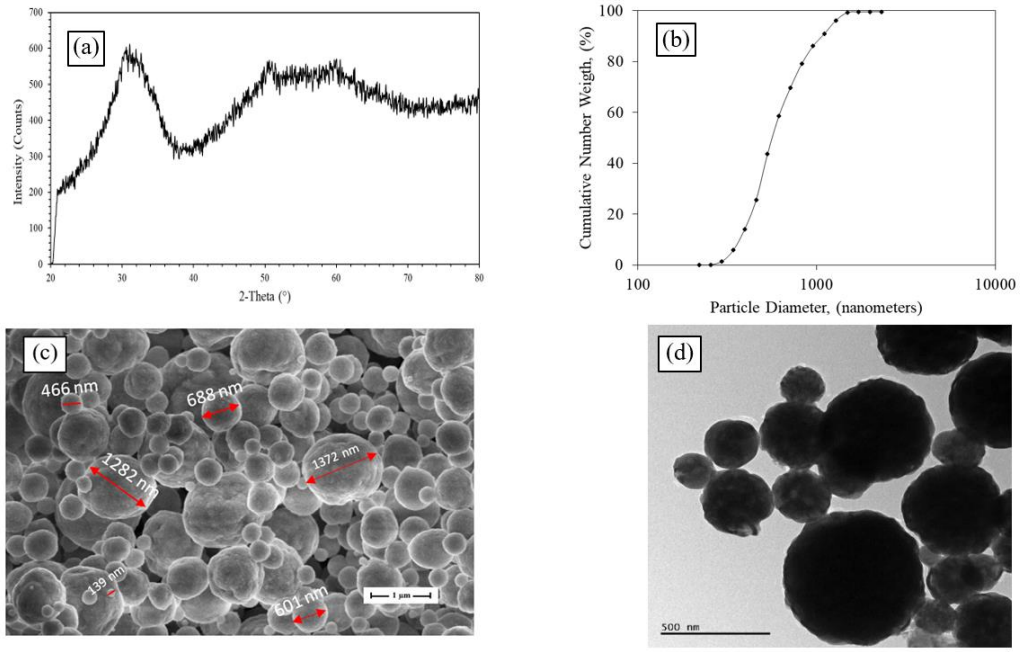

Fig. 1. The characterization of Y-TZP granule powder obtained by USP system: (a) XRD analysis, (b) particle size distribution, (c) SEM image, (d) TEM analysis.

3.2. High frequency induction heating sintering

Sinterability of the amorphous spherical Y-TZP granule powders by HFIH method was investigated for two different pressure values. When the pressure value was at 10 MPa and the sintering temperature was in between 1400 and 1500 °C and the sintering time was 300 s, the grain size of the material obtained was in between 200 and 250 nm. In this process, there were voids within the microstructures (Fig. 2) and the grain growth was low. When the sintering temperature was 1600 °C, it was observed that the relative density was reached to a great extent (> 96%) but the uncontrolled growth of the grains occurred, and these grains had average size of 2-5 μm. Here, the increase in grain growth may not be the only reason for the high sintering temperature. It is known that the soaking time during the sintering process has a great effect on the characteristics of the grain. Therefore, during the sintering process at 1600°C where grain growth occurred, the dwelling time was reduced to 60 sec. In this short sintering process, the density of 98% was provided, but the grain growth was still high and extremely irregular; there were grains with 200 nm size as well as up to 2 μm (Fig. 3). Grain growth could not be prevented by the sintering process performed under these conditions. Therefore, pressing pressure was increased in order to be able to achieve packing at lower temperatures to prevent the grain growth.

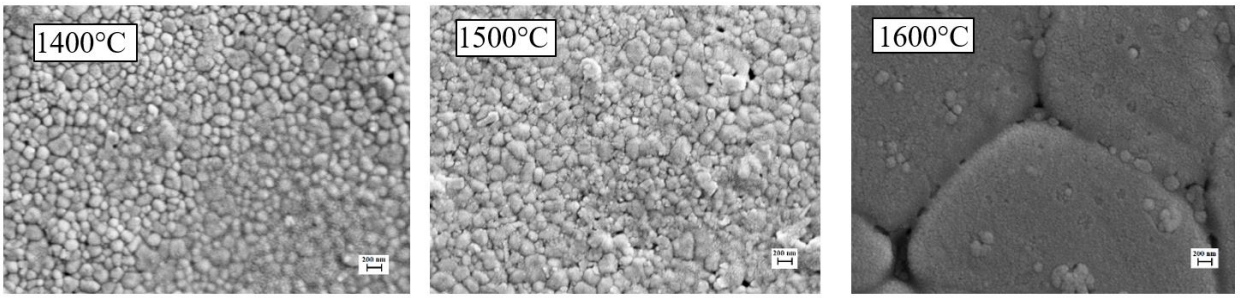

Fig. 2. Microstructures of samples sintered at different temperatures for 300 sec. at a pressure of 10 MPa.

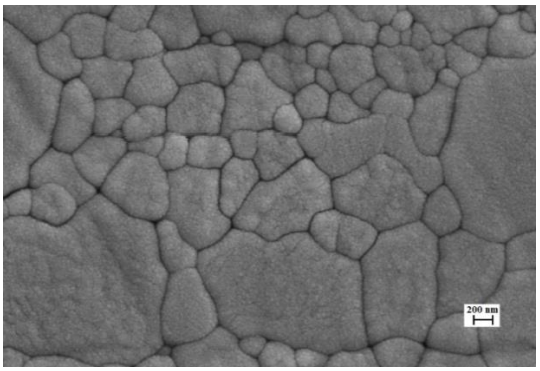

Fig. 3. Microstructure of samples sintered at 1600 °C for 60 sec. under pressure of 10 MPa.

When the pressure was 20 MPa, grain growth in the samples obtained as a result of sintering for 300 seconds at 1400-1500 °C was within the acceptable limits (<500 nm). While the material density of the sample with a sintering

temperature of 1400 °C was 92%, this value was 95% at 1500 °C. When the sintering temperature was 1600 °C (Fig. 4), it was seen that the grain growth increased, and the average grain size was found to be 5 µm. Therefore, when density and grain growth results were evaluated, the product with 95% density with a dwelling time of 300 seconds at 1500°C gave the best results. In this case, the grain size was below approximately 500 nm and there was a uniform grain size distribution (Fig. 4). Fig. 5 shows the XRD analysis of the samples sintered at 1400-1600 °C. The materials successfully crystallized into the tetragonal zirconia phase during the short-term sintering process (Fig. 5). The crystal size of the sample produced at 1500 °C with high density and low grain growth is approximately 73 nm. This value was also similar to the low temperature sintered (1400 °C) powders (about 71 nm). However, this value increased with sintering at high temperature (1600 °C) and reached up to 88 nm. An increase in crystal size increased the grain growth at high level. Therefore, in this study, the sintering temperature was determined as 1500 °C for low-grain growth and high-density material production.

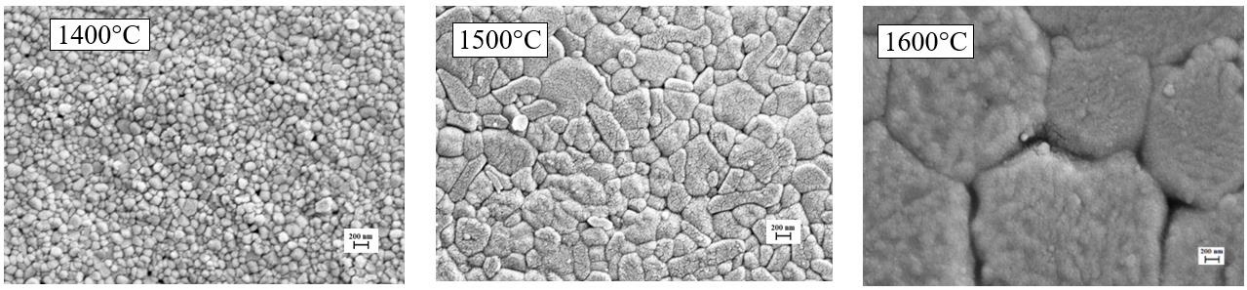

Fig. 4. Microstructures of samples sintered at different temperatures for 300 sec. at a pressure of 20 MPa.

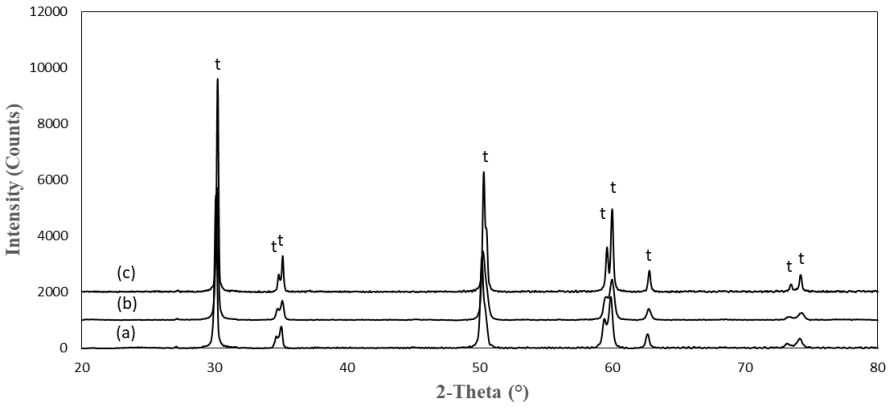

Fig. 5. XRD patterns of samples sintered at 1400-1600°C for 300 sec. under 20 MPa pressure; (a) 1400 °C, (b) 1500 °C, (c) 1600 °C (t: tetragonal phase).

3.3. Mechanical performance

The mechanical performances of Y-TZP ceramics obtained in this study were examined with the hardness and toughness measurements carried out for 15 seconds under a load of 1 kgf in polished surfaces. The hardness

performance of the samples with low pressure processing was also low (Fig. 6). The hardness values of the samples prepared at high pressure (20 MPa) increased, with increasing density values (Fig. 7). The highest hardness value was determined to be 14.9 GPa for the sample sintered at 1500 °C under pressure of 20 MPa for 300 sec. At 1600 °C, the hardness value of the samples decreased, and the density was still high (see Fig. 7). This decrease in hardness was associated with grain growth. Fig. 8 indicates the cracks under load. Toughness values were calculated by using crack size according to the equation of Anstis [30] and the toughness values were found to be 3.2-3.8 MPa. $M^{1/2}$. In the HFIH system, this value for the sample which was sintered at 1500 °C under 20 MPa pressure for 300 sec. was calculated to be 3.8 MPa $M^{1/2}$. The fracture toughness result of the sintered 3-5 mol% Y_2O_3 stabilized zirconia specimen is quite compatible with the literature [31].

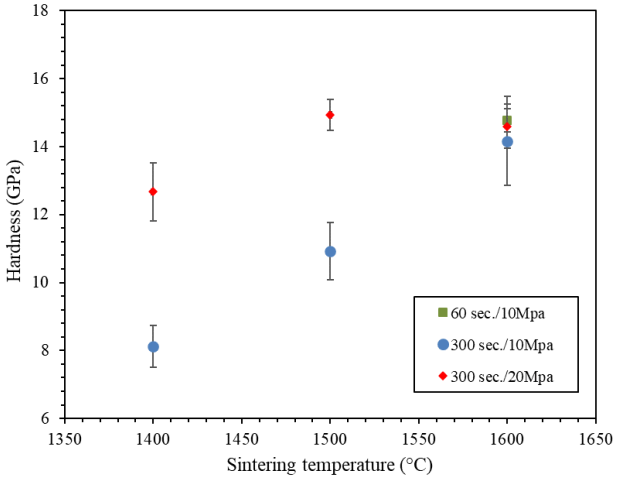

Fig. 6. Hardness of samples sintered at different temperatures.

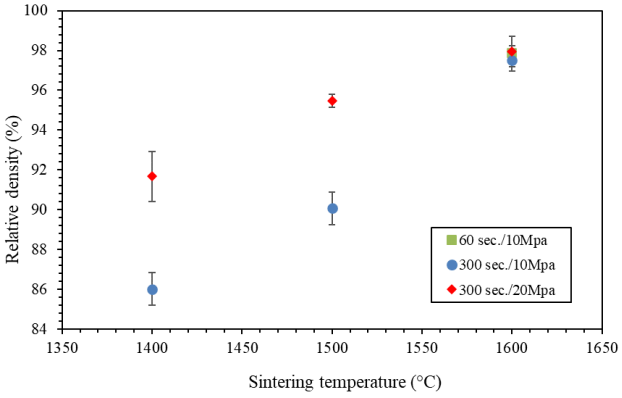

Fig. 7. Relative density of samples sintered at different temperatures.

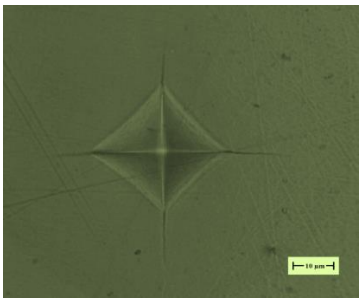

Fig. 8. Optic photographs of the Vickers indentation in the sample sintered at 1500°C for 300 sec under pressure of 20 MPa for fracture toughness evaluation.

The sinterability of amorphous granules obtained through USP system under pressure with HFIH was schematically illustrated in Fig. 9a-c. The phases of this process were as follows: (i) the cold packaging of the powders under pressure indicated loose compaction (Fig. 9-a) (ii) the pressure with applied temperature led to shrinkage and disintegration of the agglomerates as well as the transformation of amorphous powders into oxide form (Fig. 9-b) (iii) the densification and crystallization stage (Fig. 9-c). It is useful to draw attention to the following; initially the granules had high compaction and later in the second stage they were collapsed in the mould and dispersed without any change in their initial positions; the positions of the spherical granules can be distinguished from Fig 9-b.

Fig. 10 shows the TG analysis of Y-TZP powders with a total weight loss of 16.24%. This weight loss was due the -OH groups driven away because of the conversion of zirconium hydroxide into oxide form. Under the influence of pressure and temperature, the granules became extremely smaller due to the conversion mentioned above. Thus, the granules became loose and were compacted in nano size. This process played an important role in packing of the granules. At the end of this process, a structure of high density and homogeneous distribution was obtained.

As the sintering process continued, condensation increased and grain growth in the samples remained limited. It is thought that the powders produced by the USP system were initially amorphous. Crystallizations coexisted with the deformation process suppressing the grain growth. Thus, products of low-grain growth and high-density with a homogeneous microstructure were obtained. In sintering with the HFIH heating system, the amorphous powders obtained by USP system were found to be of great importance in terms of preventing the grain growth.

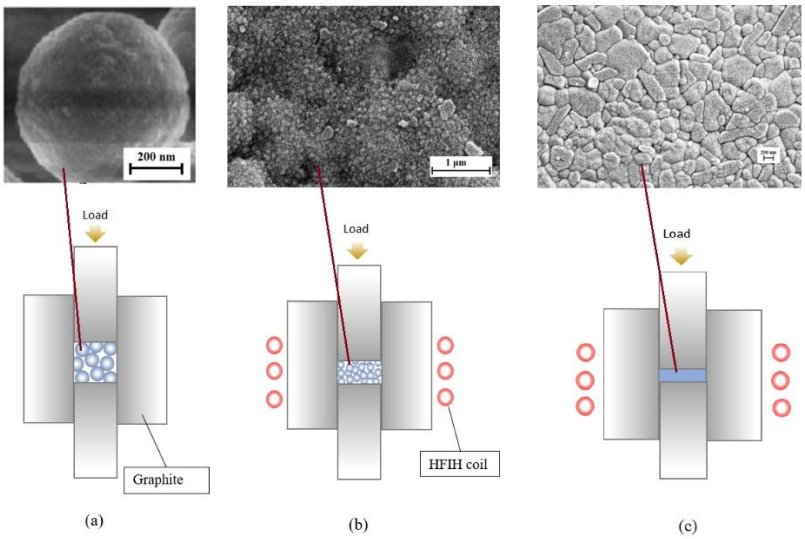

Fig. 9. The mechanism of sintering of the powders produced by the USP system with the HFIH system, a) before sintering, b) sintering at 1400 °C under 20 MPa pressure for 60 sec. c) sintering at 1500 °C under 20 MPa pressure for 300 sec.

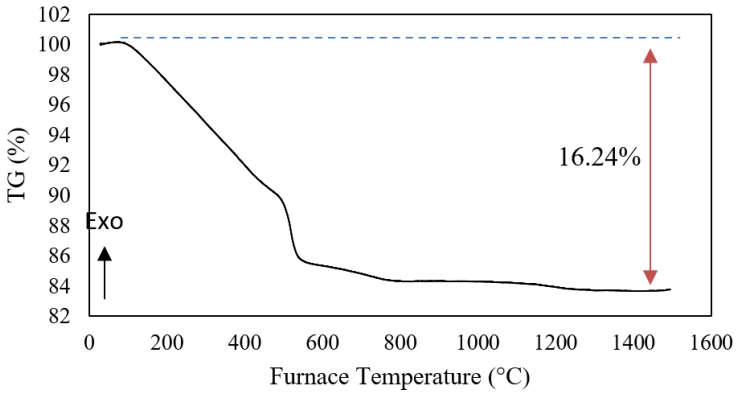

Fig. 10. TG analysis of Y-TZP powders produced by USP system.

4. Conclusions

In this study, amorphous Y-TZP powders were obtained by USP system, which is a rapid powder production process, at 600 °C in a nano-structured spherical shape. These powders were successfully sintered (fast sintering) with HFIH system. The granule particles having average size of 700 nm were obtained from the primary particles of 10-30 nm in size. It was determined that these powders crystallized in the tetragonal zirconia phase as a result of sintering at high temperatures (1400-1600 °C) and the crystal size increased from 71 nm to 88 nm depending on the sintering temperature. Grain growth occurred in powders exposed to high temperatures for high density at low

pressure. Y-TZP powders were sintered at 1500 °C under 20 MPa pressure for 300 seconds, preventing grain growth, and material with an average particle size of 200 nm was obtained. It was determined that this material had a hardness value of 14.9 GPa and a toughness value of 3.8 $MPa \cdot m^{1/2}$. These results showed that the granular Y-TZP powders with amorphous structure obtained with the USP system provided an advantage in grain growth prevention in the sintering process through the HFIH system According to the results of this study, grain growth, which is an important problem in the production of Y-TZP ceramics, was successfully prevented by rapid sintering processes.

Acknowledgement

The authors would like to thank Kütahya Dumlupınar University and Advanced Technologies Center (İLTEM) for their support in the analysis.

References

[1] J. Li, J. Peng, S. Guo, L. Zhang, Application of response surface methodology (RSM) for optimization of the sintering process of preparation calcia partially stabilized zirconia (CaO-PSZ) using natural baddeleyite, J. Alloys Compd. 574 (2013) 504–511.
[2] G. Rauchs, T. Fett, D. Munz, R. Oberacker, Tetragonal-to-monoclinic phase transformation in CeO_2 -stabilized zirconia under multiaxial loading, J. Eur. Ceram. Soc. 22 (2002) 841–849.
[3] Y. Zhao, Y. Gao, Structural evolution of plasma-sprayed nanoscale 3 mol% and 5 mol% yttria-stabilized zirconia coatings during sintering, Appl. Surf. Sci. 425 (2017) 1033–1039.
[4] L. Hao, D.R. Ma, J. Lawrence, X. Zhu, Enhancing osteoblast functions on a magnesia partially stabilised zirconia bioceramic by means of laser irradiation, Mater. Sci. Eng. C. 25 (2005) 496–502.
[5] M. Trunec, Z. Chlup, Higher fracture toughness of tetragonal zirconia ceramics through nanocrystalline structure, Scr. Mater. 61 (2009) 56–59.
[6] F. Wakai, S. Sakaguchi, Y. Matsuno, Superplasticity of Yttria-Stabilized Tetragonal $Zr0_2$ Polycrystals, Advanced Ceramic Materials 1 (1986) 259-263.
[7] A. Bravo-Leon, Y. Morikawa, M. Kawahara, M.J. Mayo, Fracture toughness of nanocrystalline tetragonal zirconia with low yttria content, Acta Mater. 50 (2002) 4555–4562.
[8] T. Okamoto, K. Yasuda, T. Shiota, Grain motion statistics of polycrystalline zirconia during superplastic deformation, Scr. Mater. 64 (2011) 253–255.
[9] Y. Ye, J. Li, H. Zhou, J. Chen, Microstructure and mechanical properties of yttria-stabilized ZrO_2/Al_2O_3 nanocomposite ceramics, Ceram. Int. 34 (2008) 1797–1803.
[10] A.S. Gandhi, V. Jayaram, A.H. Chokshi, Dense Amorphous Zirconia – Alumina by Low-Temperature Consolidation of Spray-Pyrolyzed Powders, J. Am. Ceram. Soc. 82 (1999) 2613–2618.
[11] L. Gan, Y. Park, H. Kim, J. Kim, J. Ko, J. Lee, Journal of the European Ceramic Society Fabrication and microstructure of hot pressed laminated $Y_2O_3/Nd:Y_2O_3/Y_2O_3$ transparent ceramics, Journal of the European Ceramic Society Volume 36, (2016) 911–916.
[12] R. Poyato, J. MacÍas-Delgado, A. García-Valenzuela, R.L. González-Romero, A. Muñoz, A. Domínguez-Rodríguez, Electrical properties of reduced 3YTZP ceramics consolidated by spark plasma sintering, Ceram. Int. 42 (2016) 6713–6719.
[13] C. Ergun, Enhanced phase stability in hydroxylapatite/zirconia composites with hot isostatic pressing, Ceram. Int. 37 (2011) 935–942.
[14] A. Gionea, E. Andronescu, G. Voicu, C. Bleotu, V.A. Surdu, Influence of hot isostatic pressing on ZrO_2–CaO dental ceramics properties, Int. J. Pharm. 510 (2016) 439–448.
[15] K.A. Khalıl, S.W. Kim, Mechanical wet-milling and subsequent consolidation of ultra-fine Al2O3-(ZrO2+3%Y2O3) bioceramics by using high-frequency induction heat sintering, Trans. Nonferrous Met. Soc. China. 17 (2007) 21–26.
[16] S.W. Kim, S.L. Cockcroft, K.A. Khalil, K. Ogi, Sintering behavior of ultra-fine Al_2O_3-(ZrO_2+Xmol% Y_2O_3)

ceramics by high-frequency induction heating, Mater. Sci. Eng. A. 527 (2010) 4926–4931.
[17] S.W. Kim, K.A. Khalil, S.L. Cockcroft, D. Hui, J.H. Lee, Sintering behavior and mechanical properties of HA-X% mol 3YSZ composites sintered by high frequency induction heated sintering, Compos. Part B Eng. 45 (2013) 1689–1693.
[18] I.J. Shon, I.K. Jeong, J.H. Park, B.R. Kim, K.T. Lee, Effect of Fe2O3 addition on consolidation and properties of 8 mol% yttria-stabilized zirconia by high-frequency induction heated sintering (HFIHS), Ceram. Int. 35 (2009) 363–368.
[19] M. Gaudon, E. Djurado, N.H. Menzler, Morphology and sintering behaviour of yttria stabilised zirconia (8-YSZ) powders synthesised by spray pyrolysis, Ceram. Int. 30 (2004) 2295–2303..
[20] M. Chen, J. He, Y. Zhang, Z. Ding, J. Luo, Densification and grain growth behaviour of high-purity MgO ceramics by hot-pressing, Ceram. Int. 43 (2017) 1775–1780.
[21] Z. He, J. Ma, Grain-growth rate constant of hot-pressed alumina ceramics, Mater. Lett. 44 (2000) 14–18.
[22] A.S. Gandhi, V. Jayaram, A.H. Chokshi, Low temperature densification behaviour of metastable phases in ZrO_2–Al_2O_3 powders produced by spray pyrolysis, Mater. Sci. 306 (2001) 785–789.
[23] K. Matsui, H. Yoshida, Y. Ikuhara, Phase-transformation and grain-growth kinetics in yttria-stabilized tetragonal zirconia polycrystal doped with a small amount of alumina, J. Eur. Ceram. Soc. 30 (2010) 1679–1690.
[24] S. Tekeli, Influence of alumina addition on grain growth and room temperature mechanical properties of 8YSCZ/Al2O3 composites, Compos. Sci. Technol. 65 (2005) 967–972.
[25] Y.W. Hsu, K.H. Yang, K.M. Chang, S.W. Yeh, M.C. Wang, Synthesis and crystallization behavior of 3 mol% yttria stabilized tetragonal zirconia polycrystals (3Y-TZP) nanosized powders prepared using a simple co-precipitation process, J. Alloys Compd. 509 (2011) 6864–6870.
[26] R. Dwivedi, A. Maurya, A. Verma, R. Prasad, K.S. Bartwal, Microwave assisted sol-gel synthesis of tetragonal zirconia nanoparticles, J. Alloys Compd. 509 (2011) 6848–6851.
[27] Y.N. Ko, S.M. Lee, J.H. Kim, J. Lee, Y.C. Kang, Processing Research Sintering characteristics of nano-sized yttria-stabilized zirconia powders prepared by spray pyrolysis, J. Ceram. Process. Res. 13 (2012) 405–408.
[28] M. Koç, Synthesis and Characterization of Nanostructured Y-TZP-Al_2O_3 Granule Composite Microspheres, PhD thesis, Kütahya Dumlupınar University Institute of Science, Kütahya, (2018) 152s.
[29] M. Perez-Page, R. Guzalowski, D.N.F. Muche, R.H.R. Castro, P. Stroeve, Synthesis of porous yttria-stabilized zirconia microspheres by ultrasonic spray pyrolysis, Mater. Lett. 188 (2017) 41–44.
[30] A. Nastic, A. Merati, M. Bielawski, M. Bolduc, O. Fakolujo, M. Nganbe, Instrumented and Vickers Indentation for the Characterization of Stiffness, Hardness and Toughness of Zirconia Toughened Al_2O_3 and SiC Armor, J. Mater. Sci. Technol. 31 (2015) 773–783.
[31] J. Lubauer, F. H., Schuenemann, R., Belli, U., Lohbauer, Speed‐ sintering and the mechanical properties of 3–5 mol% Y_2O_3‐ stabilized zirconias, Odontology (2023) 1-8.

Contents lists available at *Dergipark*

Journal of Scientific Reports-A

journal homepage: *https://dergipark.org.tr/tr/pub/jsr-a*

E-ISSN: 2687-6167 ***Number 55, December 2023***

RESEARCH ARTICLE

Receive Date: 21.06.2023 *Accepted Date: 20.11.2023*

Structural and electronic properties of fluorine-doped lithium oxide as a solid electrolyte interphase for lithium air batteries

Nilüfer Ertekin[1]*

[a]*Department of Electrical and Electronics Engineering, Yalova University, Yalova, Turkey, ORCID: 0000-0003-3955-2489*

Abstract

In Lithium-Air Batteries (LABs), the solid electrolyte interphase (SEI) layer plays a crucial role as a protective barrier and regulates the transport of lithium ions, preventing deterioration of the electrode and electrolyte during undesired reactions. The SEI layer acts as a barrier between the lithium anode and electrolyte, enhancing the stability and efficiency of LABs during charge/discharge cycles. In this study, the effectiveness of a composite SEI layer consisting of Li_2O and LiF was investigated. Fluorine-Doped Lithium Oxide was proposed, and the dynamical stability of this configuration was verified using Density Functional Theory and analysis of the phonon spectrum, leveraging its quantum mechanical accuracy for this purpose. The study of the electronic properties of the structure revealed a noteworthy decrease in the band gap. This decrease in the band gap is particularly significant as it contributes to the improved performance of lithium-air batteries. Furthermore, additional investigations were conducted to examine the effects of doping other halogen atoms, including chlorine and bromine, and increasing the concentration of fluorine. In the meticulous process of sublattice doping, careful consideration of electronegativity, ionic radius, and experimental doping probability is crucial. However, improper selection rendered such structures unstable, posing challenges in achieving stable configurations for practical applications. According to the results, doping one fluorine in each unit cell does not lead to instability.

Keywords: Lithium air batteries; Solid electrolyte interphase; Band gap; Phonon spectrum; Fluorine-doped lithium oxide

* *Corresponding author. Tel.: +90(226) 8156373.*

E-mail address: nilufer.ertekin@yalova.edu.tr

.

1. Introduction

Rechargeable lithium-air batteries have the potential to be used in long-distance electric vehicles as well as other energy storage applications due to their high energy density [1]. They fall under the broad classification of next-generation lithium-based batteries [2-3]. The basic principle of a lithium-air battery relies on the reaction of Lithium metal and Oxygen in the ambient air resulting in lithium oxide $\mathbf{Li_2O}$ as the discharge product. $\mathbf{Li_2O}$ gets converted back into lithium metal and oxygen is released through the charging process respectively. The following cycles will continue this process [4]. Since oxygen from the air is used as one of the reactants in lithium-air batteries, which eliminates the need to store one of the reactants inside, these batteries have the potential to have very high energy densities. This characteristic facilitates a significantly higher level of energy storage compared to what is achievable with conventional lithium-ion batteries.

The key components of a lithium-air battery typically include Anode, cathode, and electrolyte. Typically, metallic lithium or lithium compounds are used as the anode in lithium-air batteries. It acts as a lithium-ion source while the battery is being discharged. Despite low electrode potential and high theoretical capacity, lithium metal anodes have several limitations that prevent their use in rechargeable batteries. The formation of lithium dendrites during cycling is one of the most significant challenges with lithium metal anodes [5-7]. Dendrite needle-like structures that grow on the surface of the lithium electrode can pierce the separator and cause short circuits, poor battery performance, and safety risks. Side reactions and electrolyte decomposition, volume changes and mechanical stress, limited coulombic efficiency, and safety concerns are other challenges that associated with lithium metal anodes. To decrease these difficulties, several strategies are being used and reported. In lithium-based battery systems, an essential component called the solid-electrolyte interphase (SEI) develops at the area where the electrolyte and lithium metal anode meet. It is an electrochemically produced layer that performs as a passivation layer, preventing additional interactions of the reactive lithium metal with the electrolyte [8]. In general, the SEI layer is composed of both inorganic and organic materials, such as lithium carbonate ($\mathbf{Li_2CO_3}$), lithium oxide ($\mathbf{Li_2O}$), lithium alkyl carbonates, lithium fluoride ($\mathbf{LiF}$), and other decomposition products [9- 11]. In comparison to $\mathbf{Li_2CO_3}$ and due to acceptable mechanical stability and lithium ionic conductivity of $\mathbf{Li_2O}$ and good electrochemical stability of $\mathbf{LiF}$, a composite of $\mathbf{Li_2O}$ and $\mathbf{LiF}$ is more promising as SEI. Rezaee et al [12] reported that Lithium oxide with fluorine doping is a novel material for solid electrolyte interphase applications and investigated its physical characteristics using Molecular dynamic simulations in detail. However, to best of our knowledge, there is not any study on the validation and stability of the structure and its electronic properties. Therefore, to introduce this structure as the proper material for SEI applications it is important to prove its dynamic stability and investigate the electronic properties in Quantum Mechanics [13]. Quantum Mechanics is a fundamental theory in physics and describes the energies and behaviour of materials in the smallest scales. It offers a framework to understand the behaviour of particles, atoms, molecules, and electrons in atoms.

In the current study, the validity, and electronic properties of $\boldsymbol{Li_{(2-x)}O_{(1-x)}F_x}$ were investigated. Density Functional Theory (DFT) was employed for this purpose, leveraging its quantum mechanical accuracy to offer a more nuanced representation of electronic stability. Furthermore, the study emphasized the observed decrease in the band gap as a clear indication of lower resistance—an essential characteristic for the Solid Electrolyte Interface (SEI) in effectively mitigating undesired side reactions. The dynamic stability of the structure was tested by the Phonon spectrum [14]. The term "phonon spectrum" refers to the energy range of quantized vibrational modes in a material. A phonon's energy is quantized and is frequency dependent. The range of energy values of these vibrational modes have been expressed by the phonon spectrum. For extensive consideration, the acceptable concentration of fluorine and the doping effect of other halogen materials was checked too. Electronic behaviours and properties of SEI as a lithium anode protection layer play an important role in LAB's performance. To this end, the Efficacy of doping Florin in $\boldsymbol{Li_2O}$ structure was investigated and was compared with pure $\boldsymbol{Li_2O}$. All modeling and analysis have been done under Quantum Mechanics Methods that provide a close agreement with the experimental results.

2. Computational details

The geometrical, electronic, and phonon calculations were performed using the Density Functional Theory (DFT) methods [15] implemented in Quantum ESPRESSO Package [16]. The Generalized Gradient Approximation (GGA) with Perdew-Burke-Ernzerhof (PBE) [17] type parameterization has been applied to represent the electrons' interchange and correlation interaction energy. Electronic structure calculations and geometry optimizations including lattice constant and atomic positions are done based on an iterative solution of the Kohn-Sham equation [18] and ultrasoft Pseudopotentials by minimizing the total energy. To attain a balance between computational accuracy and efficiency in energy and force calculations, convergent thresholds of 10^6 Ry and 0.001 Ry/Bohr, respectively, were employed. These specific values have proven effective in ensuring the convergence of energy calculations to a sufficiently accurate result and stabilizing forces to reach equilibrium, thus optimizing the reliability of computational outcomes while preserving computational efficiency. Throughout the investigation, periodic boundary conditions were used. For Band Gap energies, both valence band maximum (VBM) and conduction band minimum (CBM) were extracted.

3. Results and discussion

3.1. Perfect Li_2O

As a foundation, all the structures studied in this study have been developed using antifluorite unit cells of Li_2O [19]. As shown in Figure1-a and under ambient pressure and temperature, Li_2O has 12 basic atoms, a cubic cell, space group of Fm3m. The structure is optimized and gets to its minimized energy with lattice parameters, total energy, force, and stress per atom at 4.6 Å [20], -249.48 Ry, 0.000003 Ry/Bohr, 0.4 kbar respectively.
The phonon spectrum, energy band diagram, and Partial Density of states for Li_2O were displayed in Figure 1-b-c. It is evident that the phonon dispersion does not exhibit any imaginary mode, which indicates the system's inherent dynamical stability. This finding confirms that the Pristine Li_2O represents a local minimum. The band gap of the structure was 5.2ev and the PDOS of the system represented the distribution of available energy states and atomic orbitals. There was good conformity with Previous studies [21-22].

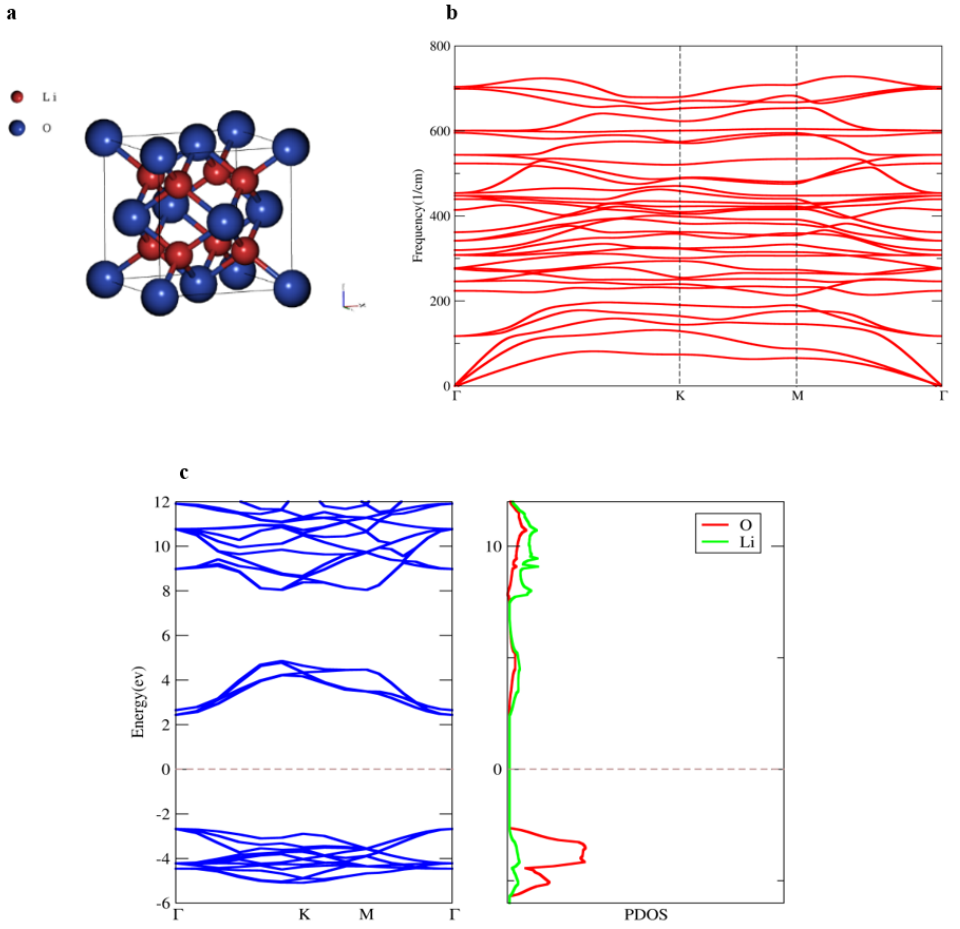

Fig.1 a- Configuration, b- Phonon spectrum, c- Band structure and PDOS, of the antifluorite unit cell of Li_2O

3.2. Fluorine doped Li_2O

3.2.1 A single atom

To modify and improve the structure fluorine was doped in an oxygen site. fluorine has a single negative charge and the destruction of local electrostatic charge conservation leads to the formation of metastable microstates within the system [23]. In the meticulous process of doping within the sublattice, careful consideration of electronegativity, ionic radius, and experimental doping probability is crucial. With an electronegativity of 4.193, fluorine competes with oxygen (3.610) for O-sites, utilizing its heightened electronegativity to attract lithium electrons and form robust ionic bonds, contributing significantly to the stability of the $Li_{(2-x)}O_{(1-x)}F_x$ structure. Additionally, the proximity of the ionic radii of F^{-} (1.285) and $O^{(2-)}$ (1.350 Å) enhances the precision of the doping process, ensuring a seamless integration of fluorine into the sublattice. This nuanced interplay highlights the importance of a comprehensive

approach in doping strategies, where both electronegativity and ionic radius are carefully balanced to maximize the effectiveness of fluorine in modifying the compound's structure [12].

Therefore, a Lithium atom was deleted and the system reached its balance local electrostatic charge. The defective $Li_{(2-x)}O_{(1-x)}F_x$ structure ($x = \frac{\text{number of doped} - F}{\text{number of O in perfect crystal}}$ [24]) was created and optimized to minimize energy. Afterward and due to validity, the configuration phonon calculation was used and vibrational frequencies were calculated and plotted.

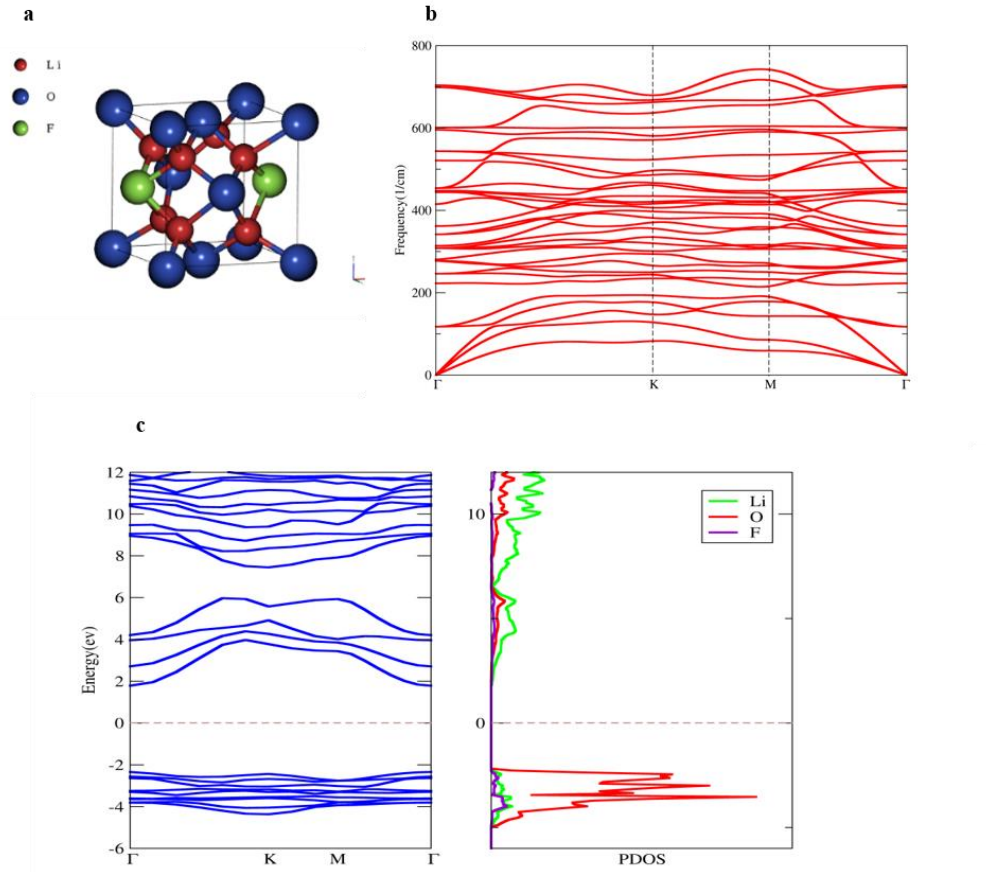

Fig. 2 a- Configuration, b- Phonon spectrum, c- Band structure and PDOS, of Fluorine doped Li_2O

Figure 2a-b displays the doping structure and its phonon spectrum. The phonon spectrum includes both positive and negative frequencies, representing the real and imaginary components of the vibrations, respectively. Negative frequencies indicate unstable or imaginary modes, whereas positive frequencies correlate to observable vibrations of the lattice in a material. Negative frequencies represent energetically unfavourable structures and are derived mathematically so the physically observable positive frequencies are the primary focus of the phonon spectrum analysis. Due to all real modes, the structure as shown in Figure2-b is stable.

From the PDOS, one can observe the contributions of specific atomic orbitals or groups, where a high density of states indicates a greater probability of finding electrons at those energy levels.

3-2-2 Two atoms

In this section, the effect of doping of another fluorine in structure was investigated. The configuration was shown in Figure 3-a. As can be seen from Figure 3-b, the phonon spectrum encompasses both positive (real) and negative (imaginary) frequencies. Because of imaginary frequencies, this formation is dynamically unstable. This is because of the high electronegativity of fluorine [25]. Fluorine is the most electronegative element, meaning it has a strong affinity for electrons. When a single fluorine atom is doped into Li_2O, it can replace an oxygen atom and form a stable $Li_{(2-x)}O_{(1-x)}F_x$compound. The electronegativity of fluorine allows it to effectively attract and bond with the surrounding atoms, maintaining the structural integrity and charge balance of the compound. However, when two fluorine atoms are introduced, the high electronegativity of fluorine can lead to an excessive electron transfer. This disrupts the charge balance within the crystal structure of Li_2O.

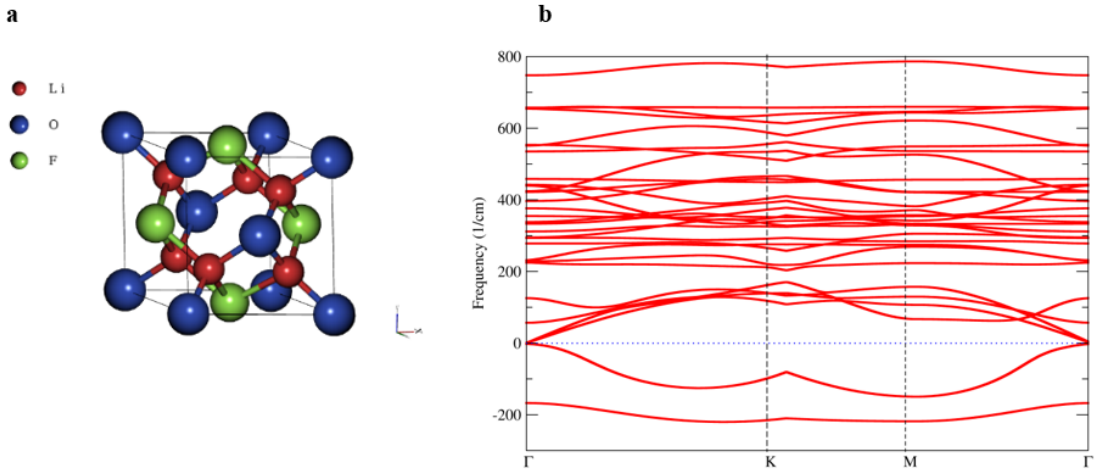

Fig. 3 a- Configuration, b- Phonon spectrum, of 2Fluorine doped Li_2O

The study was continued and the effect of enlarging the system to two single cells where each cell has a single fluorine was tested. Figure 4 shows two cell configurations and related phonon spectrums. Due to the real frequencies of this diagram, this structure is dynamically stable. In summary, just one Fluorine can be doped in each unit cell of Li_2O.

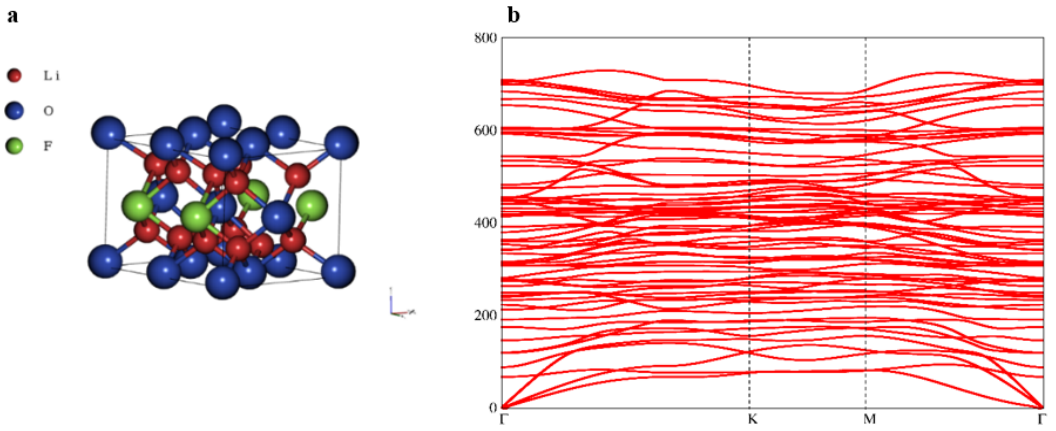

Fig. 4 a- Configuration, b- Phonon spectrum, 1Fluorine dopped in each unit cell of Li2O

3-3 Chlorine/ Bromine doped Li_2O

In this section effect of doping other elements was investigated. To this end, Chlorine and Bromine were introduced into the structure as a dopant. The configuration of doped structures was displayed in Figure 5 and Figure 6 respectively. As shown in the figure and referring to their phonon spectrums these systems were not stable.
Electronegativity quantifies an atom's capability to attract shared electrons within a chemical bond. When incorporating a foreign atom into a crystal lattice through doping, it is crucial to consider the disparity in electronegativity between the dopant atom and the host atoms. A significant electronegativity difference can cause an uneven distribution of electron density, which may result in imbalances in charge and instabilities in the structure. On the Pauling scale, oxygen has a greater electronegativity value than chlorine (around 3.44 vs. 3.16). It means that in a chemical bond, oxygen has a greater inclination to shared electrons and doping halogens except for fluorine which has similar electronegativity with oxygen, can lead to uneven distribution of electron density and disrupt the charge balance within the crystal lattice.

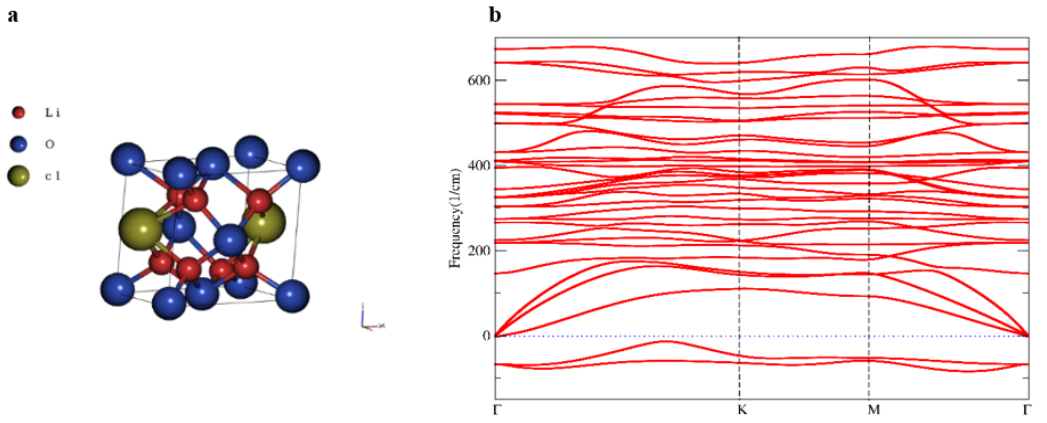

Fig. 5 a- Configuration, b- Phonon spectrum, of Cholerine doped Li_2O

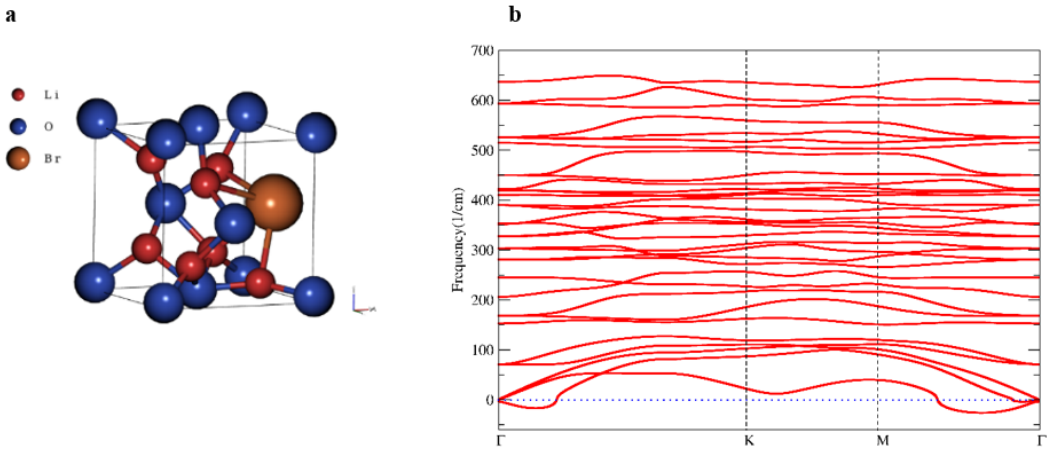

Fig. 6 a- Configuration, b- Phonon spectrum, of Cholerine doped Li_2O

The ramifications of introducing heteroatoms into the pristine structure of Li_2O were compiled in Table 1. Considering the ionic radii and electronegativity associated with heteroatoms, the strategic incorporation of one fluorine in each unit cell is recommended, as it imparts heightened stability. This doping mechanism precipitates a reduction in the band gap of the solid electrolyte interface (SIE), thereby amplifying the performance of Li-air batteries.

Table 1. Stability of configuration based on doped type

Doped type	Stability	Doped type	Stability
No doped	Yes	2 Fluorine doped in 2 unit cell	Yes
1 Fluorine doped in 1 unit cell	Yes	1 Chlorine doped in 1 unit cell	No
2 Fluorine doped in 1 unit cell	No	1 Bromine doped in 1 unit cell	No

3. Conclusion

Utilizing solid-electrolyte interphase (SEI) layers as protective coatings on the lithium anode is an effective strategy to maintain coulombic efficiency and extend the cycle life of Lithium-Air Batteries (LABs). In this study, the effectiveness of $Li_{(2-x)}O_{(1-x)}F_x$ as a novel solid-electrolyte interphase (SEI) was examined. The stability and reliability of this configuration were confirmed through analysis of the phonon spectrum and DFT calculations. The low resistance of SEI plays a critical role in minimizing unwanted side reactions, ensuring the stability of the electrode-electrolyte interface, enhancing the transport of charges, and reducing ohmic polarization. Therefore, analysing and optimizing the electronic properties of the layer is essential for achieving these objectives. To investigate the electronic properties, the band energies of $Li_{(2-x)}O_{(1-x)}F_x$ were calculated. The introduction of fluorine (F) dopants in the oxygen (O) site of the Li_2O structure resulted in a decrease in the band energies, indicating a lower resistance of the SEI layer. This decrease in resistance contributes to improved performance and stability of battery systems. Additionally, the effects of chlorine and bromine halogens as dopants were examined. However, due to their lower electronegativity compared to oxygen, these configurations were found to be dynamically unstable. Based on the findings, it is suggested to consider doping one fluorine atom in each unit cell as a viable approach. This strategy offers potential benefits in terms of enhancing the performance and stability of the battery system.

Acknowledgements

There is no conflict of interest with any person/institution in the prepared article.

References

[1] F. Wu, Y. Yu, "Toward true lithium–air batteries," *Joule*., vol. 2, no. 5, pp. 815–817, May 2018, doi: 10.1016/j.joule.2018.04.019.
[2] K. Virmani, C. Deepak, S. Sharma, U. Chadha, S.K. Selvaraj, "Nanomaterials for automotive outer panel components: a review," *Eur. Phys. J. Plus*., vol. 136, pp. 1–29, Sep. 2021, doi:10.1140/epjp/s13360-021-01931-w.
[3] V. Blay, R.E. Galian, L.M. Muresan, D. Pankratov, P. Pinyou, G. Zampardi, "Research frontiers in energy-related materials and applications for 2020–2030," *Adv. Sustain. Syst.*, vol. 4, no. 2 pp. 1900145, Feb. 2020, doi:10.1002/adsu.201900145.
[4] Tao Liu, at al., "Grey Current Challenges and Routes Forward for Nonaqueous Lithium–Air Batteries," *Chemical Reviews*, vol.120, no.14, pp. 6558-6625, Feb. 2020 doi: 10.1021/acs.chemrev.9b00545.
[5] N. Imanishi, O. Yamamoto, "Perspectives, and challenges of rechargeable lithium–air batteries,", *Materials Today Advances*, vol. 4, pp. 100031, Dec. 2019, doi: 10.1016/j.mtadv.2019.100031.
[6] Ding, Y, Li, Y, Wu, Z-S., "Recent advances and challenges in the design of Li–air batteries oriented solid-state electrolytes," *Battery Energy*, vol. 2, no. 2, pp. 20220014, Mar. 2023, doi :10.1002/bte2.20220014.
[7] Wang, Z, Yu, J, Rao, M, et al., "Challenges, mitigation strategies and perspectives in development of Li metal anode," *Nano Select*., vol. 1, no. 6, pp. 622– 638, Oct. 2020, doi:10.1002/nano.202000123.
[8] Liu, Y., He, P., Zhou, H., "Rechargeable Solid-State Li–Air and Li–S Batteries: Materials, Construction, and Challenges," *Adv. Energy Mater*., vol. 8, no. 4, pp. 1701602, Feb. 2018, https://doi.org/10.1002/aenm.201701602.

[9] L._Suo, et al., "Fluorine-donating electrolytes enable highly reversible 5-V-class Li metal batteries," *Proc Natl Acad Sci U S A*, vol. 115, no. 6, Jan. 2018, doi: 10.1073/pnas.1712895115.
[10] Cao, R., Chen, K., Liu, J. et al., "Li–air batteries: air stability of lithium metal anodes," *Sci. China Chem*., Apr. 2023. doi:10.1007/s11426-023-1581-2.
[11] Zahoor, Awan, et al.,"Lithium air battery: alternate energy resource for the future," *Journal of Electrochemical Science and Technology*, vol. 3.1, pp. 14-23, Mar. 2012, doi: 10.5229/JECST.2012.3.1.14.
[12] Rezaee, S., Araghi, H., Noshad, H. et al., "Physical characteristics of fluorine-doped lithium oxide as advanced material for solid-electrolyte-interphase applications of lithium–air batteries," *Eur. Phys. J. Plus*, vol. 137, pp. 1194 Oct. 2022, doi:10.1140/epjp/s13360-022-03345-8.
[13] Kubo, Ryogo, Arisato Kawabata, and Shun-ichi Kobayashi, "Electronic properties of small particles," *Annual Review of Materials Science*, vol. 14, pp. 49-66, Agu. 1984, doi: 10.1146/annurev.ms.14.080184.000405.
[14] Rani, B. et al.; "Electronic Structure-, Phonon Spectrum-, and Effective Mass- Related Thermoelectric Properties of PdXSn (X = Zr, Hf) Half Heuslers," *Molecules*, vol. 27, no. 19, pp. 6567, Oct. 2022. doi: 10.3390/molecules27196567.
[15] K. Capelle, "A Bird ' s-Eye View of Density-Functional Theory," *Brazilian Journal of Physics*, vol. 36, no. 4A, pp. 1318-1343, Dec. 2006, doi: 10.1590/S0103-97332006000700035.
[16] Giannozzi, P, et al., "QUANTUM ESPRESSO: Modular and Open-Source Software A Project for Quantum Simulations of Materials," J. Phys.: Condens. Matter, vol. 21, no. 39, pp.395502, Sep. 2009, doi: 10.1088/0953-8984/21/39/395502.
[17] J.P. Perdew, K. Burke, M. Ernzerhof, "Generalized Gradient Approximation Made Simple," *Physical review letters*, vol. 77, no. 18 pp. 3865–3868, Oct. 1996, doi: 10.1103/PhysRevLett.77.3865.
[18] Kohn, Walter, and Lu Jeu Sham, "Self-consistent equations including exchange and correlation effects," *Physical review*, vol. 140, no. 4A, Nov. 1965, doi: 10.1103/PhysRev. 140.A1133.
[19] M.M. Islam, T. Bredow, C. Minot, "Theoretical analysis of structural, energetic, electronic, and defect properties of Li_2O," *J. Phys. Chem*., B. vol. 110, no. 19, pp. 9413–9420, Apr. 2006, doi:10.1021/jp0566764.
[20] Kah Chun Lau, Larry A. Curtiss, and Jeffrey Greeley, "Density Functional Investigation of the Thermodynamic Stability of Lithium Oxide Bulk Crystalline Structures as a Function of Oxygen Pressure," *the Journal of Physical Chemistry C*, vol.115, no. 47, pp. 23625-23633, Oct. 2011, doi: 10.1021/jp206796h.
[21] Stefan Albrecht, Giovanni Onida, and Lucia Reining, "Ab initio calculation of the quasiparticle spectrum and excitonic effects in Li_2O," *Physical Review B* vol. 55, pp. 10278, Apr. 1997, doi: 10.1103/PhysRevB.55.10278.
[22] Mazharul M. Islam, homas Bredow, and Christian Minot, "Theoretical Analysis of Structural, Energetic, Electronic, and Defect Properties of Li_2O," *Journal of Physics and Chemistry B* vol.110, no. 19, pp. 9413-9420, Apr. 2006, doi: 10.1021/jp0566764.
[23] Ertekin, Nilüfer, and Sasan Rezaee, "Effect of anion and cation vacancies pairs in conduct of the Ba1− 3xTiO31− x and BaTi $_{(1-\ 3x2)}$ $O_{3(1-\ x)}$ (x= 0.0033) as a memristor," *Materials Today Communications*, vol 31, pp. 103333, Jun. 2022, doi: 10.1016/j.mtcomm.2022.103333.
[24] Ertekin, N., Rezaee, S., "Lithium-Doped Barium Titanate as Advanced Cells of ReRAMs Technology," J. *Electron. Mater.*, vol 52, pp. 1575–1589, Feb. 2023. doi:10.1007/s11664-022-10124-9.
[25] Xiaofang Li, Xiaofeng Wu, Shengwei Liu, Yuhan Li, Jiajie Fan, Kangle Lv, "Effects of fluorine on photocatalysis," *Chinese Journal of Catalysis*, vol 41, no 10, pp. 1451-1467, Oct. 2020, doi:10.1016/S1872-2067(20)63594-X.

Contents lists available at *Dergipark*

Journal of Scientific Reports-A

journal homepage: *https://dergipark.org.tr/tr/pub/jsr-a*

E-ISSN: 2687-6167 ***Number 55, December 2023***

RESEARCH ARTICLE

Receive Date: 02.09.2023 *Accepted Date: 06.12.2023*

Investigation of temperature effects in RC-Steel composite industrial building model with FEM

Furkan Günday*

Department of Civil Engineering, Faculty of Engineering, Giresun University, Giresun, Turkey, ORCID:0000-0003-2979-9373

Abstract

Today, composite structure design has become very popular. The most important goal in composite structure design is to create the most efficient structural system under load by using materials that respond positively to different cross-section effects. Industrial type buildings, on the other hand, consist of very wide openings. In addition, industrial buildings are required to be designed to be constructed quickly and simply. For all these reasons, there has been an increase in the construction of industrial buildings in the form of reinforced concrete-steel composite structures. The effect of temperature in buildings is a parameter that should be considered both in design and use. It is a scientific fact that the expansion and contraction coefficients of reinforced concrete and steel are different. The temperature effect has an even more important place in composite construction systems where both are used together. For all these reasons, in this study, a reinforced concrete-steel composite industrial building model was created and its responses at -50°C and 50°C were examined. As a result of the findings obtained, the effect of temperature in reinforced concrete-steel composite industrial structures should definitely be taken into account both in the design and in the use and maintenance stages.

Keywords: Industrial buildings; temperature effect; composite structures; finite element method

1. Introduction

Industrial buildings; It is the factory where all kinds of products are made and the buildings and structures for processes such as processing, assembly, mixing, cleaning, washing, packaging, storage, distribution and repair. All kinds of factories, sawmills, laundries, textile production facilities, energy production facilities, food processing

* Corresponding author. Tel.: +0-000-000-0000 ; fax: +0-000-000-0000 .
E-mail address: furkan.gunday@giresun.edu.tr
http://dx.doi.org/10.1016/j.cviu.2017.00.000

.

facilities, filling and unloading facilities, dry cleaning facilities, mineral processing facilities, refineries and similar places are included in this class. Simply, industrial buildings are factories or other large facilities used primarily to produce or store raw materials, goods or services for economic purposes. They are specially planned from top to bottom, taking into account the storage processes. They are generally divided into some main classes according to the design, construction process and needs. These classes are generally divided into warehouse and distribution, production, light manufacturing (textile, furniture and home electronics, etc.), refrigeration and cold storage, data hosting centers, biotechnology, some shopping centers. Due to its complex structures, the industrial building construction process should be applied much more meticulously than other building construction processes. The industrial building construction process includes planning, design, pre-construction, security, post-construction processes, respectively. In terms of planning and design, they often have an architecture with large openings. For this reason, it has been seen that composite construction systems have been chosen recently in order to meet these and other special needs. It is ensured that all stages of the production process, from the supply chain to the assembly operation, are optimized in order to achieve the highest quality and efficiency in the industry sector. Every decision is thought through to the smallest detail, every detail is planned, and ultimately the most accurate solutions are produced. The buildings where all these activities are carried out must be designed correctly in terms of architecture and engineering. While designing industrial facilities and structures, it is necessary to plan with an understanding that is suitable for all production processes and business plans that are considered and progressed according to the principle of efficiency. In this way, possible problems that may arise in the future are solved from the very beginning. In addition, in order to keep up with the competitive conditions, the project must be designed correctly at the planning stage. With the design reflecting your brand and corporate identity, analysis of land and climate conditions, correct air conditioning, energy efficient design, efficient and effective use of natural resources, selection of building materials, recyclable and re-functional project design, management of industrial and industrial wastes, sustainability, storage and logistics. All factors, such as relevant planning, should be taken into account. It is known that simple, useful and short construction time is the most basic principle in planning and design purposes. In the post-construction process, maintenance of industrial buildings is very important. The main reason for this necessity is the production disruption and the fact that it includes a large number of people. Otherwise, with the collapse of the building due to neglect, both great loss of life and great financial losses can be experienced [1-11]. Some examples of industrial buildings are given in Fig 1.

Fig. 1. Examples of industrial buildings.

Composite structures have emerged as a result of an approach that highlights the positive aspects of different types of materials against different effects. Composite building systems have become an indispensable carrier system for high-rise building applications in the world, as they effectively reduce the self-weight of the building compared to reinforced concrete buildings and provide good performance in creating the desired structure ductility against seismic loads. These are the buildings that are designed and constructed by using different structural elements such as reinforced concrete structural elements and steel construction elements and concrete-light concrete at the same time in the structural load-bearing system. They can be applied in different types of buildings according to the needs. In recent years, composite structure design has come to the fore in industrial buildings. Especially, reinforced concrete-steel composite structure designs are known to be one of the most common types of composite structures [12-19]. Also, the effects of fire in a concrete-steel composite structure were investigated very closely [20].

Industrial buildings are exposed to the effects of temperature depending on the purpose of use or from the weather conditions of the environment. The temperature effect is of great importance in the design phase or in the use phase. In industrial buildings designed as a composite building system, the temperature effect is much more important. Ultimately it is a scientific fact that the expansion and contraction coefficients of different materials are different. This is true for concrete and steel. For these reasons, in this study, the temperature effect of the industrial building type designed with a reinforced concrete-steel composite structure system was investigated. The deformations of the structural carrier system under the influence of temperature are very important in order to interpret the effect. Researchers [21-32] have investigated the effect of temperature and fire in reinforced concrete, steel, etc. building systems, which also contribute to this study, with various methods.

The aim of this study is to examine the effect of temperature on the carrier systems of composite industrial buildings made of reinforced concrete and steel. It is known that industrial buildings are exposed to temperature effects due to their intended use. This type of buildings are the types of buildings where there are productions as freezers or where high temperatures occur. It is foreseen that this situation is likely to affect the structural carrier system. It is also a proven fact that the effect of temperature has different expansion and contraction properties in different material types. For all these reasons, in this study, a reinforced concrete-steel composite industrial building model was created with a simple architecture for a more realistic representation of the data. The reaction of the system was observed by applying the temperature effect of -50 °C and +50 °C degrees to this model. The selected temperature degrees, on the other hand, have been taken as reference by paying attention to the temperature effects that are likely to be exposed, and the previous studies given as a reference in the introduction.

2. Material and method

The finite element method is the process of transforming functions in an infinite dimensional function space into functions in a finite dimensional function space and then into vectors that can be traced in vector space by numerical methods. Finite element analysis (FEA) allows detailed visualization of where structures are bent or twisted and shows the distribution of stresses and displacements. Finite element method (FEM) software offers a wide variety of simulation options to control the complexity of both modeling and analysis of a system. Similarly, the desired level of accuracy and associated computation time requirements can be managed simultaneously to cater to most engineering applications. FEM ensures that all designs are built, refined, and optimized before the design is produced [33-35]. In this study, the finite element method was used in the modeling and analysis parts. As the software, the internationally valid SAP2000 software, which is the finite element software, was used.

2.1. RC-Steel Composite Industrial Building Model

Column elements were chosen as reinforced concrete. The fact that column rigidity is very important for structures and that reinforced concrete is more resistant to temperature effects than steel was effective in this selection. Industrial buildings are known for using wide openings in their plans. For this reason, steel profiles come

to the forefront with their favorable position in wide openings. In the model design, two openings of 7.5 meters in the X direction and 4 openings of 6 meters in the Y direction were selected. The height of the first floor is 4.5 meters, and a second floor of 3 meters has been designed considering that there will be offices, lounges, etc. on it. The columns are designed as 50x70 reinforced concrete rectangular section. Concrete class is determined as C30 according to Turkish standards (TS 500). The beams were chosen as W18X76 steel I profile (American Society for Testing and Materials - ASTM). The slabs are designed as shell-thin, 0.04 meters of steel. Care was taken to use symmetrical and dimensional elements in the design of the model. The reason for this is that the temperature effect is desired to be seen more clearly without being dependent on any other effect. The YZ and XZ plans of the RC-steel composite industrial building model are given in Fig 2. The 3D finite element model of the RC-steel composite industrial building model is given in Fig 3.

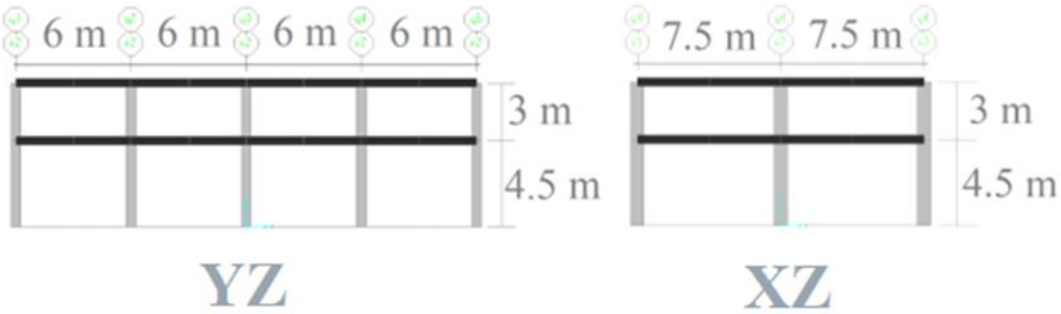

Fig. 2. The YZ, XZ plans and dimensions.

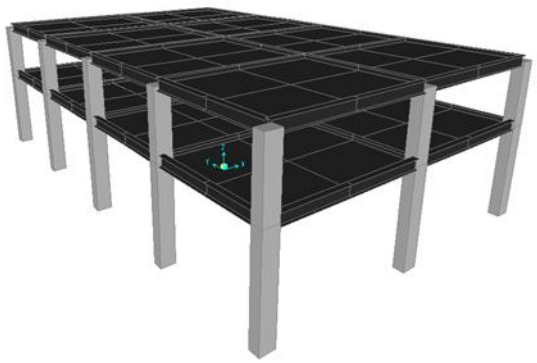

Fig. 3. The 3D finite element model of the RC-steel composite industrial building model.

3. Findings and discussion

The finite element model created should be analyzed for findings. The RC-steel composite industrial building model was first analyzed in the normal condition without the effect of temperature and the findings were obtained.

Afterwards, temperatures of 50°C and -50°C were applied to the whole system, respectively, and separate analyzes were made for each degree. It is aimed to reach a conclusion by comparing the obtained analysis findings (displacements) separately for each load-bearing element type (columns, beams and slabs).

The 3D deformation of the RC-steel composite industrial building model is given in Fig 4. as a result of the analysis performed only under the effect of dead loads without the effect of temperature.

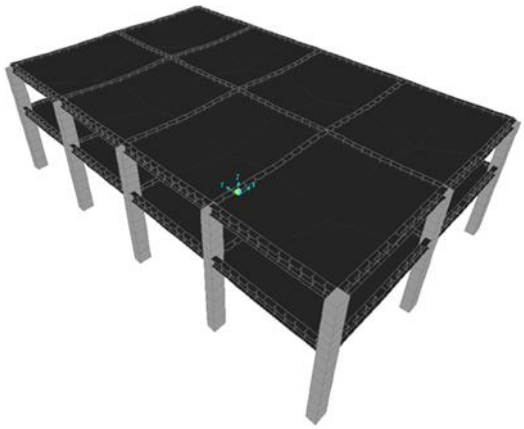

Fig. 4. The 3D deformation of the RC-steel composite industrial building model without the effect of temperature.

The 3D deformation of the RC-steel composite industrial building model is given in Fig 5. as a result of the analysis performed only under the effect of dead loads and with 50°C the effect of temperature.

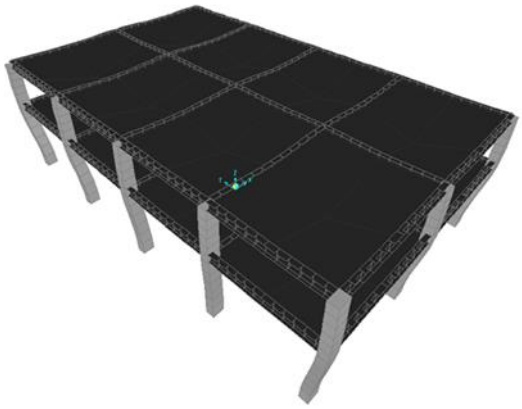

Fig. 5. The 3D deformation of the RC-steel composite industrial building model at 50°C.

The 3D deformation of the RC-steel composite industrial building model is given in Fig 6. as a result of the analysis performed only under the effect of dead loads and with -50°C the effect of temperature.

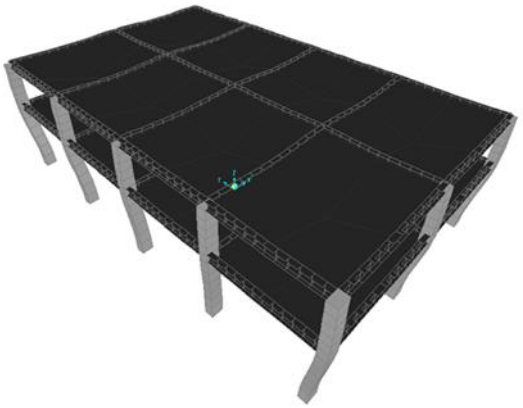

Fig. 6. The 3D deformation of the RC-steel composite industrial building model at -50°C.

When the 3-dimensional deformations are examined, the effects of expansion and contraction at 50°C and -50°C are clearly seen. However, since the building is a composite structure, it is necessary to reach a clearer result by examining the maximum displacements of the structural elements (columns, beams, slabs).

For the columns, displacements at normally, displacements at 50°C, displacements at -50°C and comparison of temperature effect are given in Table 1.

Table 1. Comparison of temperature effect on columns maximum displacement values.

Situation	U_{1max} (m)	U_{2max} (m)	U_{3max} (m)
Normally	0.000006522	0.000002526	-0.000253
At 50°C	-0.004403	-0.007038	0.003626
At -50°C	0.004414	0.007042	-0.003972
Normally and 50°C Absolute Value Difference (m)	0.004396478	0.007035474	0.003373
Normally and 50°C Absolute Value Difference (%)	67409.96627	278522.3278	1333.201581
Normally and -50°C Absolute Value Difference (m)	0.004407478	0.007039474	0.003719
Normally and -50°C Absolute Value Difference (%)	67578.62619	278680.6809	1469.960474
50°C and -50°C Absolute Value Difference (m)	1.1E-05	4E-06	0.000346
50°C and -50°C Absolute Value Difference (%)	0.249829662	0.056834328	9.542195256

The columns from which U_{1max}, U_{2max}, U_{3max} values are obtained at normally, 50°C and -50°C are given in Fig 7. comparatively. It is known that the absolute values of displacements are almost equal in unselected symmetrical columns due to the symmetrical design. These columns have only sign difference (negative or positive). The main reason for this situation is that the displacement directions are on the negative or positive axis.

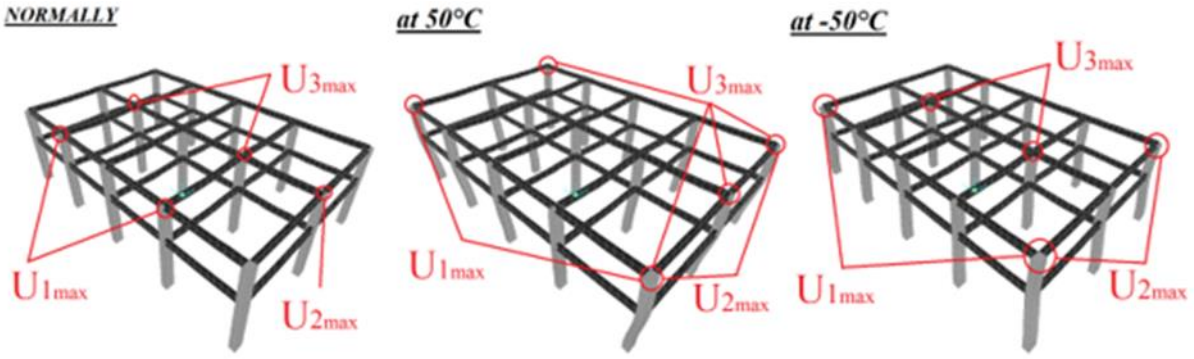

Fig. 7. Columns with maximum displacement (U_1, U_2, U_3).

For the beams, displacements at normally, displacements at 50°C, displacements at -50°C and comparison of temperature effect are given in Table 2.

Table 2. Comparison of temperature effect on beams maximum displacement values.

Situation	U_{1max} (m)	U_{2max} (m)	U_{3max} (m)
Normally	0.000002015	-0.00000105	-0.00189
At 50°C	-0.004391	-0.007029	0.003275
At -50°C	-0.004395	0.00703	-0.005406
Normally and 50°C Absolute Value Difference (m)	0.004388985	0.00702795	0.001385
Normally and 50°C Absolute Value Difference (%)	217815.6328	669328.5714	73.28042328
Normally and -50°C Absolute Value Difference (m)	0.004392985	0.00702895	0.003516
Normally and -50°C Absolute Value Difference (%)	218014.1439	669423.8095	186.031746
50°C and -50°C Absolute Value Difference (m)	4E-06	1E-06	0.002131
50°C and -50°C Absolute Value Difference (%)	0.091095422	0.014226775	65.06870229

The beams from which U_{1max}, U_{2max}, U_{3max} values are obtained at normally, 50°C and -50°C are given in Fig 8. comparatively. It is known that the absolute values of displacements are almost equal in unselected symmetrical beams due to the symmetrical design. These beams have only sign difference (negative or positive). The main reason for this situation is that the displacement directions are on the negative or positive axis.

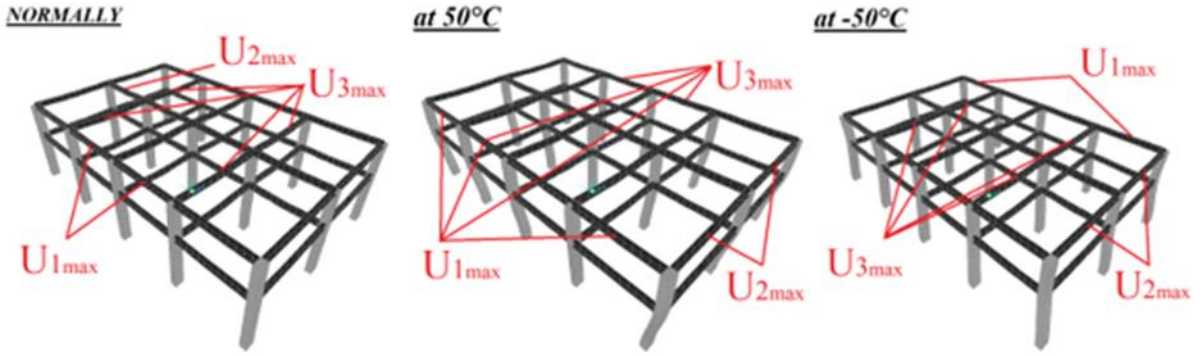

Fig. 8. Beams with maximum displacement (U_1, U_2, U_3).

For the slabs, displacements at normally, displacements at 50°C, displacements at -50°C and comparison of temperature effect are given in Table 3.

Table 3. Comparison of temperature effect on slabs maximum displacement values.

Situation	U_{1max} (m)	U_{2max} (m)	U_{3max} (m)
Normally	-0.000002379	0.000000594	-0.013039
At 50°C	-0.002198	-0.005276	-0.010209
At -50°C	0.002202	-0.005277	-0.016559
Normally and 50°C Absolute Value Difference (m)	0.002195621	0.005275406	-0.00283
Normally and 50°C Absolute Value Difference (%)	92291.76124	888115.4882	-21.70411841
Normally and -50°C Absolute Value Difference (m)	0.002199621	0.005276406	0.00352
Normally and -50°C Absolute Value Difference (%)	92459.89912	888283.8384	26.99593527
50°C and -50°C Absolute Value Difference (m)	4E-06	1E-06	0.00635
50°C and -50°C Absolute Value Difference (%)	-0.181983621	-0.018953753	-62.20001959

The slabs from which U_{1max}, U_{2max}, U_{3max} values are obtained at normally, 50°C and -50°C are given in Fig 9. comparatively. It is known that the absolute values of displacements are almost equal in unselected symmetrical slabs due to the symmetrical design. These slabs have only sign difference (negative or positive). The main reason for this situation is that the displacement directions are on the negative or positive axis.

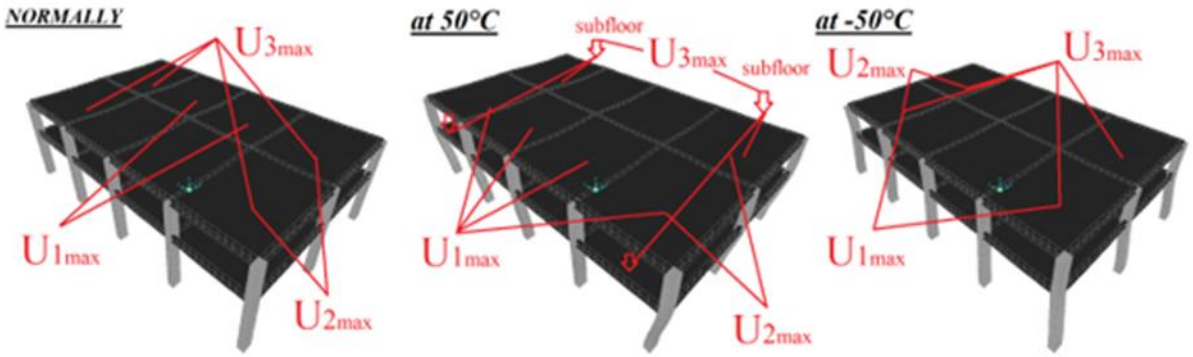

Fig. 9. Slabs with maximum displacement (U_1, U_2, U_3).

The maximum displacement values (U_{1max}, U_{2max}, U_{3max}) obtained were made into comparative graphs for columns, beams and slabs. The graph of maximum displacement for columns is given in figure 10, the graph of maximum displacement for beams in figure 11, and the graph of maximum displacement for slabs is given in figure 12. In the graphs, blue color represents U_{1max}, orange color U_{2max} and gray color U_{3max}.

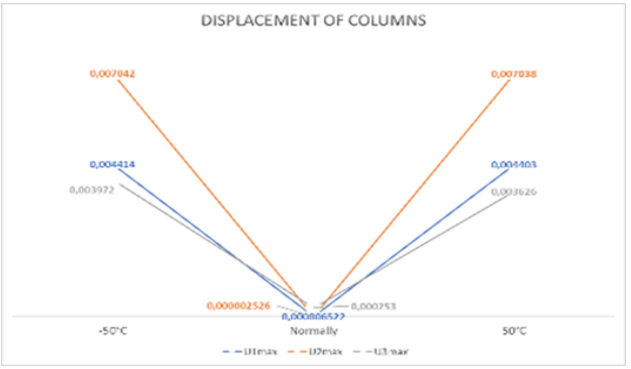

Fig. 10. Displacement of columns graph.

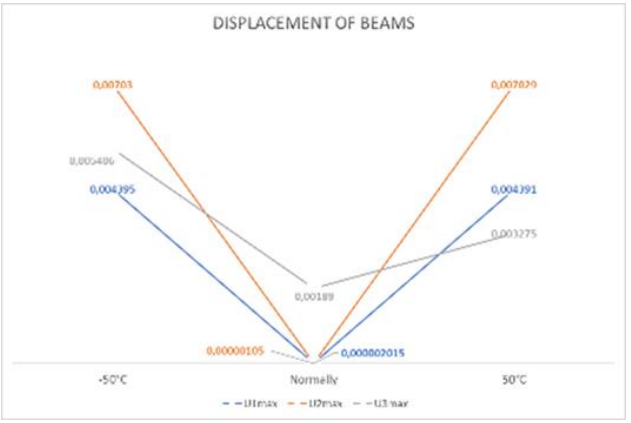

Fig. 11. Displacement of beams graph.

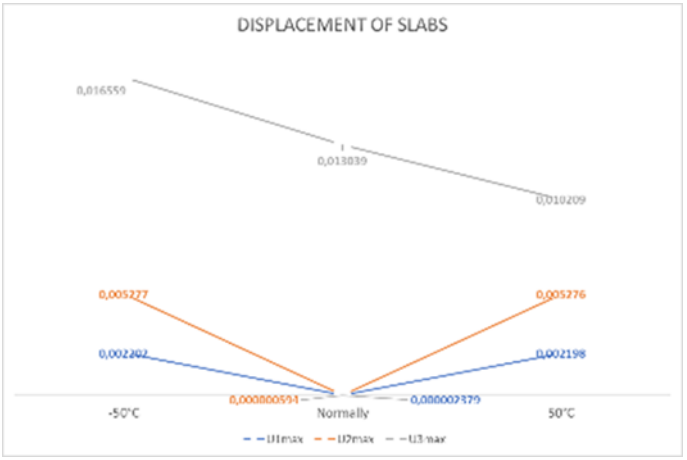

Fig. 12. Displacement of slabs graph.

4. Conclusions

When the 3-dimensional deformations of the reinforced concrete-steel industrial structure model are examined at 50°C and -50°C, the expansion and contraction conditions are clearly seen.

In the reinforced concrete columns of the model, the maximum displacement in the x direction under the effect of 50°C temperature was -0.004403 meters in the y direction -0.007038 meters and 0.003626 meters in the z direction. Under the temperature effect of -50°C, it was seen as 0.004414 meters in the x direction, 0.007042 meters in the y direction, and -0.003972 meters in the z direction. Initially, these displacement values are 0.000006522 meters in the x direction, 0.000002526 meters in the y direction, and -0.000253 meters in the z direction. In this case, reinforced concrete columns made very high horizontal displacements compared to the first case with the effect of temperature. From this, it can be concluded that the temperature effect has a very negative effect on the horizontal stiffness. In the vertical, it was noted that the column moves in the positive direction at 50°C. It is concluded that there are fluctuations in the columns with the expansion of the system. In addition, there is a very large increase of approximately 1333.20% when compared to the initial vertical maximum column displacement. Although it is relatively less than the horizontal increase, this situation draws attention. At -50°C, the vertical displacement is in the negative direction and is the same as the start. This is an indication of the shrinkage effect. Again, considering the initial vertical maximum column displacement, there is a huge increase of about 1470%. In this case, it can be said that the vertical rigidity is negatively affected. It has been observed that the negative temperature effect causes more displacements in the horizontal and vertical columns than the positive temperature effects. From this point of view, negative temperature values for the columns are more dangerous in this model. In addition, it was clearly seen that the columns most affected by the temperature effect were the corner columns. In the initial case, on the contrary, the columns with the maximum displacement are the columns positioned in the middle. In addition, although the columns are reinforced concrete, it has been observed that they are adversely affected by the temperature effects.

The maximum displacement in the x direction of the steel profile beams of the model under the effect of 50°C was -0.004391 meters in the y direction -0.007029 meters and 0.003275 meters in the z direction. Under the temperature effect of -50°C, it was seen as -0.004395 meters in the x direction, 0.00703 meters in the y direction, and -0.005406 meters in the z direction. Initially, these displacement values are 0.000002015 meters in the x direction, -0.00000105 meters in the y direction, -0.00189 meters in the z direction. In this case, the steel profile beams have made very high horizontal displacements compared to the first case with the effect of temperature. From this, it can be concluded that the temperature effect has a very negative effect on the horizontal stiffness. In the vertical, it was noted that there was a positive movement of the beam at 50°C. It was concluded that with the expansion of the system, there are fluctuations in the beams as well as in the columns. In addition, there is a large increase of approximately 73.28% when compared to the initial vertical maximum beam displacement. This increase is quite small compared to the columns. At -50°C, the vertical displacement is in the negative direction and in the same direction as the start. This is an indication of the shrinkage effect. Again, considering the initial vertical maximum beam displacement, there is a large increase of about 186.03%. In this case, it can be said that the vertical rigidity is negatively affected. It has been observed that the negative temperature effect of the beams in the horizontal and vertical directions, as in the columns, causes more displacements than the positive temperature effects. From this point of view, negative temperature values for beams in this model are more dangerous, especially in vertical displacements. In addition, it is clearly seen that the beams most affected by the temperature effect are the horizontal side beams and the vertical beams. This situation is almost similar in the initial state.

The maximum displacement in the x-direction was -0.002198 meters in the y-direction, -0.005276 meters in the y-direction, and -0.010209 meters in the z-direction, in the steel slabs of the model under the effect of 50°C temperature. Under the temperature effect of -50°C, it was seen as 0.002202 meters in the x direction, -0.005277 meters in the y direction, and -0.016559 meters in the z direction. Initially, these displacement values are -0.000002379 meters in the x-direction, 0.000000594 meters in the y-direction, and -0.013039 meters in the z-direction. In this case, the steel slabs have made very high displacements in the horizontal compared to the first

situation, as in the columns and beams, with the effect of temperature. From this, it can be concluded that the temperature effect has a very negative effect on the horizontal stiffness. On the vertical, it was noted that the displacement value of the slab decreased at 50°C. It has been concluded that the horizontal stresses that occur with the expansion of the system affect this situation. In addition, there is a decrease of approximately -21.70% according to the initial vertical maximum slab displacement. This increase is quite small compared to columns and beams. At 50°C and -50°C, the vertical displacement is in the negative direction and in the same direction as the start. Considering the initial vertical maximum beam displacement at -50°C, there is an increase of approximately 27%. In this case, it can be said that the vertical rigidity is negatively affected. However, this effect is very small compared to columns and beams. In this case, it can be said that the section thickness, being a plate element, and the stresses coming from the columns and beams have an effect. It has been observed that the negative temperature effect of the slabs causes more displacements than the positive temperature effects, as in the columns and beams. In the vertical, there is a situation that seems positive even at the beginning at the positive temperature value. From this point of view, negative temperature values for slabs in this model are dangerous, especially in horizontal displacements. In addition, the slabs that are most affected by the effect of temperature are the slabs with low continuity on the side frames, the same as the normal situation in the horizontal and vertical.

It has been understood that the greatest displacement differences are observed in the U_2 direction, due to the fact that the stiffness in the U_2 direction is the lowest in addition to the temperature effect.

In the light of all this information, it has been observed that there are great changes in the horizontal displacements of the 50°C and -50°C RC-Steel composite industrial building model under the influence of temperature and are adversely affected. Significant increases were observed in vertical displacements, although not as much as in horizontal displacements. It is predicted that in this degree of stiffness losses, major damages may occur in the building under combined loads. It was concluded that the temperature effect of 50°C and -50°C adversely affected the rigidity and stability of the system. In addition, it is a fact that the loss of life and property will be high in case of damage to industrial buildings. It is known that there is a possibility of reaching temperatures of 50°C and -50°C for industrial buildings. For this reason, attention should be paid to the effects of temperature in the design, use and maintenance of industrial buildings. Temperature insulation of the industrial buildings' carrier elements must be done.

Acknowledgements

There is no conflict of interest with any person/institution in the prepared article.

References

[1] M. Stratton, "Industrial Buildings," in *Conservation and Regeneration,* 1st ed. London, England: Taylor & Francis, 2000.

[2] J. T. San-José, R. Losada, J. Cuadrado, and I. Garrucho, "Approach to the quantification of the sustainable value in industrial buildings," *Building and Environment*, vol. 42, pp. 3916-3923, 2007, doi: 10.1016/j.proeng.2013.04.118.

[3] M. A. Habib, M. Hasanuzzaman, M. Hasanuzzaman, A. Salman, R. and Mehadi, "Energy consumption, energy saving and emission reduction of a garment industrial building in Bangladesh," *Energy*, vol. 112, pp. 91-100, 2016, doi: 10.1016/j.energy.2016.06.062.

[4] D. Katunsky, A. Korjenic, J. Katunska, M. Lopusniak, S. Korjenic and S. Doroudiani, "Analysis of thermal energy demand and saving in industrial buildings: A case study in Slovakia," *Building and Environment*, vol. 67, pp. 138-146, 2013, doi: 10.1016/j.buildenv.2013.05.014.

[5] X. Dou, D. Xie, Z. Wang, P. Xiao, and H. Wang, "Improved buoyancy-driver hybrid ventilation system for multiple-heat-source industrial buildings," *Case Studies in Thermal Engineering*, vol. 26, no. 101059, 2021, doi: 10.1016/j.csite.2021.101059.

[6] G. Gourlis, and I. Kovacic, "Building Information Modelling for analysis of energy efficient industrial buildings – A case study," *Renewable and Sustainable Energy Reviews*, vol. 68, pp. 953-963, 2017, doi: 10.1016/j.rser.2016.02.009.

[7] J. Reisinger, M. A. Zahlbruckner, I. Kovacic, P. Kán, and X. Wang-Sukalia, "Framework proposal for automated generation of production layout scenarios: A parametric design technique to connect production planning and structural industrial building design," in *Proc. EG-ICE 2021 Workshop on Intelligent Computing in Engineering in Berlin*, *Universitätsverlag der TU Berlin,* 2021, pp. 22-33, doi: 10.14279/depositonce-12021.

[8] J. Reisinger, M. A. Zahlbruckner, I. Kovacic, P. Kán, X. Wang-Sukalia, and H. Kaufmann, "Integrated multi-objective evolutionary optimization of production layout scenarios for parametric structural design of flexible industrial buildings," *Journal of Building Engineering*, vol. 46, pp. no. 103766, 2022, doi: 10.1016/j.jobe.2021.103766.
[9] B. Glumac, and N. Islam, "Housing preferences for adaptive re-use of office and industrial buildings: Demand side," *Sustainable cities and society*, vol. 62 no. 102379, 2020, doi: 10.1016/j.scs.2020.102379.
[10] R. A. Danhaive, and C. T. Mueller, "Combining parametric modeling and interactive optimization for high-performance and creative structural design," in *Proceedings of IASS Annual Symposia, International Association for Shell and Spatial Structures (IASS)*, 2015, pp. 1-11, doi: 10.1016/j.autcon.2015.02.011
[11] D. Chinese, G. Nardin, and O. Saro, "Multi-criteria analysis for the selection of space heating systems in an industrial building," *Energy*, vol. 36, pp. 556-565, 2011, doi: 10.1016/j.energy.2010.10.005.
[12] A. Tedia, and S. Maru, "Cost, Analysis and Design of Steel-Concrete Composite Structure Rcc Structure," *Journal of Mechanical and Civil Engineering*, vol. 11, pp. 54-59, 2014, doi: 10.9790/1684-11125459.
[13] Q. Q. Liang, *Analysis and Design of Steel and Composite Structures*. 1st ed. London, England: CRC Press, 2014.
[14] Y. C. Wang, "Steel and Composite Structures," in *Behaviour and Design for Fire Safety*, 1st ed. London, England: CRC Press, 2002.
[15] J. Nie, J. Wang, S. Gou, Y. Zhu, and J. Fan, "Technological development and engineering applications of novel steel-concrete composite structures," *Frontiers of Structural and Civil Engineering*, vol. 13, pp. 1-4, 2019, doi: 10.1007/s11709-019-0514-x.
[16] A. Kasımzade, and S. Tuhta, "Analytical Numerical and Experimental Examination of Reinforced Composites Beams Covered with Carbon Fiber Reinforced Plastic," *Journal of Theoretical and Applied Mechanics*, vol. 42, pp. 55-70, 2012, doi: 10.2478/v10254-012-0004-1.
[17] S. Tuhta, "GFRP retrofitting effect on the dynamic characteristics of model steel structure," *Steel and Composite Structures*, vol. 28, 223–231, 2018, doi: 10.12989/scs.2018.28.2.223.
[18] S. Tuhta, "Analytical and Operational Modal Analysis Applications in Composite Structures," in *Investigation of Wind Pressure Effect on Modal Parameters of GFRP Water Tank with OMA*, Ankara, Turkey: Nobel Academic Publishing, 2022.
[19] S. Tuhta, "Analytical and Operational Modal Analysis Applications in Composite Structures," in *Determination of Wind Speed Effect on Dynamic Parameters of Full-Scale Lighting Pole by OMA*, Ankara, Turkey: Nobel Academic Publishing, 2022.
[20] Y.C. Wang, "Performance of steel–concrete composite structures in fire," *Prog. Struct. Engng Mater*, vol. 7 pp. 86-102, 2005, doi: 10.1002/pse.197.
[21] Y. Anderberg, "Modeling steel behavior," *Fire Saf. J*, vol. 13 pp. 17–26, 1988, 10.1061/(ASCE)MT.1943-5533.000004.
[22] A. H. Buchanan, *Structural design for fire safety*. NY, USA: Wiley, 2001.
[23] G.-Q. Li, and S. X. Guo, "Experiment on restrained steel beams subjected to heating and cooling," *J. Constr. Steel Res*, vol. 64, pp. 268–274, 2008, doi: 10.1007/s12205-017-0403-6.
[24] V. Kodur, M. Dwaikat, and R. Fike, "High-Temperature Properties of Steel for Fire Resistance Modeling of Structures," *Journal of Materials in Civil Engineering*, vol. 22, pp. 423-434, 2010, doi: 10.1061/(ASCE)MT.1943-5533.0000041.
[25] W.Y. Wang, B. Liu, and V. Kodur, "Effect of Temperature on Strength and Elastic Modulus of High-Strength Steel," *Journal of Materials in Civil Engineering*, vol. 25, 174-182, 2013, doi: 10.1061/(ASCE)MT.1943-5533.0000600.
[26] V. Kovalchuk, Y. Hnativ, J. Luchko, and M. Sysyn, "Study of the temperature field and the thermo-elastic state of the multilayer soil-steel structure," *Roads and Bridges - Drogi I Mosty*, vol. 19, pp. 65-78, 2020, doi: 10.7409/rabdim.020.004.
[27] E. Ünlüoğlu, İ. Topçu, and B. "Yalaman, Yüksek Sıcaklıkta Kalmış Yapılarda Pas Payının Betonarme Çelik Donatı Özeliklerine Etkisi," *Teknik Dergi*, vol. 18, pp. 4145-4155, 2007. [Online]. Available: https://dergipark.org.tr/tr/download/article-file/136674
[28] K. Arslan, D. Çelik, Y. Öztürk, and M. E. Efe, "Betonarme Soğutma Kulesi Tipi Yapıların Rüzgâr ve Sıcaklık Yükleri Etkisi Altındaki Davranışı," *Journal of the Institute of Science and Technology*, vol. 11, pp. 1218-1229, 2020, doi: 10.21597/jist.769510.
[29] İ. Oruç, "Rüzgâr, Sıcaklık ve Deprem Etkisi Altındaki Yüksek Yapılarda Taşıyıcı Sistemlerin Tasarımı ve Analizi," Yüksek Lisans Tezi, Konya Teknik Üniversitesi Lisansüstü Eğitim Enstitüsü, Konya, 2021.
[30] N. Mahsanlar, "Yüksek sıcaklık etkisinde beton davranışı," Yüksek Lisans Tezi, Yıldız Teknik Üniversitesi Fen Bilimleri Enstitüsü, İstanbul, 2007.
[31] Y. Z. Yüksel, "Sıcaklık etkisi altındaki tabakalı kompozit plakların statik ve titreşim davranışlarının incelenmesi," Yüksek Lisans Tezi, Bursa Teknik Üniversitesi Fen Bilimleri Enstitüsü, Bursa, 2018.
[32] S. Elhıdır, S. Tuhta, and F. Günday, "Analysis of Reinforced Concrete Chimneys under the Effect of Temperature Change with Finite Element Method," *JournalNX*, vol. 8, pp. 14–19, 2022, doi: 10.17605/OSF.IO/74G5Z.
[33] A. A. Kasımzade, *Finite Element Method Fundamentals and Applications in Structural Mechanics*. Ankara, Turkey: Nobel Academic Publishing, 2018.
[34] A. A. Kasımzade, *Structural Design and Analysis in The Light of Current Regulations with SAP2000 on The Basis of FEM*. Ankara, Turkey: Nobel Academic Publishing, 2022.
[35] S. Tuhta, "Investigation of Steel Slit Panel Effect on Modal Parameters of Reinforced Concrete Structure by Finite Element Method," *International Journal of Innovations in Engineering Research and Technology*, vol. 8, pp. 104-112, 2021, doi: 10.17605/OSF.IO/E26D8.

Contents lists available at *Dergipark*

Journal of Scientific Reports-A

journal homepage: *https://dergipark.org.tr/tr/pub/jsr-a*

E-ISSN: 2687-6167 ***Number 55, December 2023***

RESEARCH ARTICLE

Receive Date: 23.05.2023 *Accepted Date: 13.12.2023*

Contributions to the Aphodiinae (Coleoptera-Scarabaeidae) fauna of the Eskişehir Bozdağ

Mehmet Gülmez[1,*], Yakup ŞENYÜZ[2]

[1,*]*Sivas Cumhuriyet Üniversitesi, Fen Fakültesi, Moleküler Biyoloji ve Genetik Bölümü, 58100, Sivas, Türkiye, ORCID: 0000-0001-6547-7190*
[2]*Kütahya Dumlupınar Üniversitesi, Fen Edebiyat Fakültesi, Biyoloji Bölümü, Kütahya, 43100, Kütahya, Türkiye, ORCID: 0000-0002-9769-9406*

Abstract

Insects are amazing creatures used to determine the biodiversity of terrestrial ecosystems. It is well known that the order Coleoptera, which includes dung beetles, has a wide variety of species. Thus, depending on the three elevations of the Eskişehir Bozdağ region, the fauna of the subfamily Aphodiinae was studied in this study. As a result, this study included 14 species and 3 subspecies from 12 genera that are members of the Scarabaeidae subfamily Aphodiinae. The first records for the province of Eskişehir are *Volinus sticticus* (Panzer 1798), *Esymus pusillus pusillus* (Herbst, 1789), *Nimbus johnsoni* (Baraud, 1976), and *Euorodalus paracoenosus* (Balthasar & Hrubant 1960). Furthermore, three new species have been recorded for the Central Anatolia Region: *Nimbus johnsoni* (Baraud, 1976), *Esymus pusillus pusillus* (Herbst, 1789), and *Volinus sticticus* (Panzer, 1798).

Keywords: Aphodiinae; Dung beetles; Eskişehir; Fauna; Scarabaeidae; Turkey.

* Corresponding author. Tel.: +90 505 851 5052.
E-mail address: mgulmez26@gmail.com
http://dx.doi.org/10.1016/j.cviu.2017.00.000

1. Introduction

Scarabaeidae has twelve subfamilies, according to Löbl and Löbl, 2016 [1], the Catalogue of Palaearctic Coleoptera. The Scarabaeinae and Aphodiinae subfamilies are the largest. The Aphodiinae subfamily, known as small dung beetles, is represented by 2.204 species and 98 subspecies of about 258 genera worldwide [2]. In addition, this subfamily is distributed in the Palaearctic region, with 1.084 species belonging to 155 genera in 6 tribes [3, 4, 5]. Also, in Turkey, 152 species and four subspecies belong to 45 genera in this subfamily, with the new genus published by Şenyüz (2017) [4]. The Aphodiinae subfamily, spread worldwide, is the dominant species group in scarab communities in the Palearctic region [6, 7]. Most of the species from these subfamilies show special morphological, behavioral, and ecological adaptations to the consumption of mammal (mainly herbivore) feces [8].

Many studies have understood that dung removed and buried by dung beetles has many ecological benefits. The most important of these are soil fertilization and aeration, improvement of the nutritional cycle, intake of nutrients by plants, increased meadow quality, intestinal parasites [12, 13, 14, 15, 16] and biological control of harmful flies [9], increasing plant yield [10], soil bioperturbation, and pollination [11, 22] Due to their mentioned ecological niches, these insects have been proposed as an ideal group for biodiversity inventories and imaging [9, 17, 18].

This study aims to determine the 12-month seasonal activities of species belonging to the Aphodiinae subfamily at different altitudes. As a result of the study, both the seasonal and altitude preferences of these species will be determined.

2. Materials and Methods

This study was done from October 2012 to September 2013 in Bozdağ region at Eskişehir. The specimens were collected at three different localities (Table 1 and Figure 1) at altitudes varying between 207 to 1133 m. from October 2012 to September 2013, dung baited pitfall traps [19] were placed at each locality, and fresh cattle dung ($\approx$ 1000 g) was used as forage for each trap. All the pitfall traps remained in the field for 72 hours. The collected samples were brought to the laboratory with jars with ethyl alcohol. In the laboratory, the dung beetle specimens were identified using Zeiss Stemi 2000 stereomicroscope following the -identification keys of Dellacasa et al., 2001 [20] and Baraud J. (1976) [21]. Turkey distribution data of the species belonging to the studied subfamily were obtained. [23, 24, 25, 26, 27, 28, 29, 30, 31, 32, 33, 34, 35, 36, 37, 38, 39, 40, 41, 42, 43, 44, 45, 46, 47, 48, 49, 50, 51, 52, 53, 54].

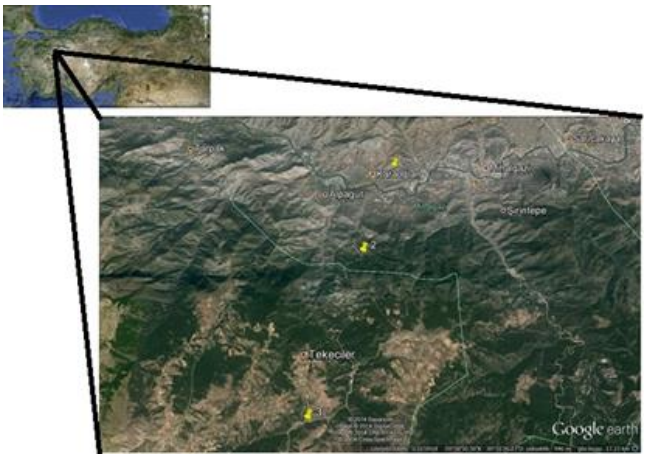

Fig. 1. Map of Locaiton.

Table 1. Data of locations of the study area.

Location	Latitude	Longitude	Elevation (m)
Karaoğlan-Mihalgazi	40˚01'.334"	30˚32'.019"	207 m.
Kalekaya Top- Erenler Site	39˚59'.569"	30˚31'.186"	612 m.
Sulukaraağaç Site	39˚56'.159"	30˚29'.590"	1133 m.

3. Result

Family SCARABAEIDAE Latreille, 1802

Subfamily APHODIINAE Leach, 1815

Tribe APHODIINI Leach, 1815

Genus *Aphodius* Hellwig, 1798: 101

Aphodius fimetarius (Linnaeus, 1758)

Material examined: Karaoğlan-Mihalgazi, 207 m., 22-25.I.2013, Gülmez M. leg. and det., 1 ex.; 16-19.V.2013, Gülmez M. leg. and det., 1 ex.; Kalekaya Top-Erenler Site 612 m., 17-20.XI.2012, Gülmez M. leg. and det., 1 ex.; 16-19.V.2013, Gülmez M. leg. and det., 1 ex.; Sulukaraağaç Site, 1133 m., 18-21.VII.2013, Gülmez M. leg. and det., 1 ex.

Distribution in Turkey: It is widespread in all geographical regions [23, 27, 32, 33, 35, 36, 37, 38, 39, 40, 41, 42, 43, 44, 45, 46, 48, 51, 52, 54].

Genus *Volinus* Mulsant & Rey, 1870c: 537

Volinus sticticus (Panzer 1798)

Material examined: Sulukaraağaç Site, 1133 m., 17-20.XI.2012, Gülmez M. leg. and det., 1 ex., 16-19.V.2013, Gülmez M. leg. and det., 2 exx.

Distribution in Turkey: It is distributed only in the Marmara Region [36, 41].

Genus *Acrossus* Mulsant, 1842: 269

Acrossus luridus (Fabricius, 1775)

Material examined: Sulukaraağaç Site, 1133 m., 16-19.V.2013 Gülmez M. leg. and det., 1 ex.

Distribution in Turkey: It is widespread in all geographical regions [23, 28, 32, 33, 35, 36, 37, 38, 39, 40, 41, 42, 45, 46, 48, 51].

Genus *Bodilus* Mulsant & Rey, 1870c: 518

Bodilus lugens (Creutzer, 1799)

Material examined: Karaoğlan-Mihalgazi, 207 m., 17-20.XI.2012, Gülmez M. leg. and det., 1 ex.; Kalekaya Top-Erenler Site 612 m., 18-21.VII.2013, Gülmez M. leg. and det., 1 ex.

Distribution in Turkey: It is distributed in all geographical regions [23, 28, 32, 35, 36, 38, 45, 48, 52].

Bodilus ictericus (Laicharting 1781)

Bodilus ictericus ictericus (Laicharting 1781)

Material examined: Kalekaya Top-Erenler Site 612 m., 17-20.XI.2012, Gülmez M. leg. and det., 1 ex.; Sulukaraağaç Site, 1133 m., 17-20.VI.2013, Gülmez M. leg. and det., 6 exx.; Sulukaraağaç Site, 1133 m., 18-21.VII.2013, Gülmez M. leg. and det., 1 ex., 17-20.VIII.2013, Gülmez M. leg. and det., 1 ex.

Distribution in Turkey: It is spread in Marmara, Aegean, and Central Anatolia Region [23, 32, 36, 48, 54].

Genus *Colobopterus* Mulsant, 1842: 165

Colobopterus erraticus Linnaeus, 1758

Material examined: Karaoğlan-Mihalgazi, 207 m., 16-19.V.2013, Gülmez M. leg. and det., 2 exx.; Sulukaraağaç Site, 1133 m., 16-19.V.2013, Gülmez M. leg. and det., 1 ex., 17-20.VI.2013, Gülmez M. leg. and det., 1 ex.; 18-21.VII.2013, Gülmez M. leg. and det., 1 ex.

Distribution in Turkey: It is widespread in all geographical regions [17, 23, 25, 28, 29, 32, 33, 35, 36, 37, 38, 39, 40, 41, 42, 45, 48, 53, 54].

Genus *Esymus* Mulsant & Rey, 1870c: 519

Esymus pusillus (Herbst, 1789)

Esymus pusillus pusillus (Herbst, 1789)

Material examined: Sulukaraağaç Site, 1133 m., 17-20.XI.2012, Gülmez M. leg. and det., 1 ex.; 17-20.IV.2013, Gülmez M. leg. and det., 7 exx.; 16-19.V.2013, Gülmez M. leg. and det., 9 exx.; 17-20.VI.2013, Gülmez M. leg. and det., 1 ex.

Distribution in Turkey: It is distributed in Marmara, Aegean, Blac Sea, and Eastern Anatolia Region [32, 36, 44, 45, 51].

Genus *Eudolus* Mulsant & Rey, 1870

Eudolus quadriguttatus (Herbst, 1783)

Material examined: Kalekaya Top-Erenler Site 612 m., 17-20.IV.2013, Gülmez M. leg. and det., 1 ex.; 17-20.IV.2013, Gülmez M. leg. and det. 1 ex.; 17-20.IV.2013, Gülmez M. leg. and det., 1 ex.

Distribution in Turkey: It is distributed in all geographical regions [28, 32, 33, 36, 37, 38, 39, 40, 42, 45, 52, 54].

Genus *Melinopterus* Mulsant, 1842

Melinopterus consputus (Creutzer, 1799)

Material examined: Karaoğlan-Mihalgazi, 207 m., 15-18.II.2013, Gülmez M. leg. and det., 1 ex.; Kalekaya Top-Erenler Site 612 m., 22-25.I.2013, Gülmez M. leg. and det., 13 exx.

Distribution in Turkey: It is spread in all geographical regions, except the Black Sea and Eastern Anatolia Region [23, 32, 33, 38, 48].

Melinopterus prodromus (Brahm, 1790)

Material examined: Karaoğlan-Mihalgazi, 207 m., 22-25.I.2013, Gülmez M. leg. and det., 18 exx.; Kalekaya Top-Erenler Site 612 m., 17-20.XI.2012, Gülmez M. leg. and det., 1 ex.; 22-25.I.2013, Gülmez M. leg. and det., 27 exx.; 15-18.II.2013, Gülmez M. leg. and det., 1 ex.; 17-20.IV.2013, Gülmez M. leg. and det., 1 ex.; Sulukaraağaç Site, 1133 m., 22-25.I.2013, Gülmez M. leg. and det., 2 exx.; 16-19.III.2013, Gülmez M. leg. and det., 6 exx.

Distribution in Turkey: It is distributed in all geographical regions [23, 28, 32, 33, 36, 38, 40, 41, 45, 48, 52].

Melinopterus pubescens (Sturm, 1800)

Material examined: Karaoğlan-Mihalgazi, 207 m., 22-25.I.2013, Gülmez M. leg. and det., 1 ex.

Distribution in Turkey: It is widespread in all geographical regions in our country, except Marmara and Eastern Anatolia Region [17, 23, 28, 33, 36, 38, 48].

Genus *Nimbus* Mulsant & Rey, 1870c: 578

Nimbus johnsoni (Baraud, 1976)

Material examined: Karaoğlan-Mihalgazi, 207 m., 22-25.I.2013, Gülmez M. leg. and det., 1 ex.; Kalekaya Top-Erenler Site 612 m., 17-20.XI.2012, Gülmez M. leg. and det., 3 exx.; 22-25.I.2013, Gülmez M. leg. and det., 78 exx.; 16-19.III.2013, Gülmez M. leg. and det. 1 ex.; Sulukaraağaç Site, 1133 m., 19-22.X.2012, Gülmez M. leg. and det. 1 ex.; 17-20.XI.2012; Gülmez M. leg. and det. 1 ex.; 13-16.XII.2012, Gülmez M. leg. and det. 4 exx.; 22-25.I.2013, Gülmez M. leg. and det. 632 exx.; 15-18.II.2013, Gülmez M. leg. and det. 1 ex.; 16-19.III.2013, Gülmez M. leg. and det. 4 exx.

Distribution in Turkey: It is distributed in the Aegean and Mediterranean Regions [33, 51].

Nimbus obliteratus (Panzer, 1823)

Material examined: Karaoğlan-Mihalgazi, 207 m., 17-20.XI.2012, Gülmez M. leg. and det., 1 ex.; Kalekaya Top-Erenler Site 612 m., 17-20.XI.2012, Gülmez M. leg. and det., 2 exx.; 22-25.I.2013, Gülmez M. leg. and det., 55 exx.; Sulukaraağaç Site, 1133 m., 19-22.X.2012, Gülmez M. leg. and det., 2 exx; 13-16.XII.2012, Gülmez M. leg. and det., 8 exx.; 22-25.I.2013, Gülmez M. leg. and det. 242 exx.; 15-18.II.2013, Gülmez M. leg. and det. 2 exx.; 16-19.III.2013, Gülmez M. leg. and det 1 ex.; 17-20.VI.2013, Gülmez M. leg. and det. 1 ex.

Distribution in Turkey: It is distributed in Aegean and Central Anatolia Region [23, 48, 51].

Nimbus contaminatus (Herbst 1783)

Material examined: Sulukaraağaç Site, 1133 m., 22-25.I.2013, Gülmez M. leg. and det. 1 ex.

Distribution in Turkey: It is distributed in Marmara and Central Anatolia Region [23, 32, 42, 48].

Genus *Otophorus* Mulsant, 1842: 178

Otopherus haemorrhoidalis Linnaeus, 1758

Material examined: Kalekaya Top-Erenler Site 612 m., 17-20.XI.2012, Gülmez M. leg. and det. 2 exx.; 16-19.V.2013, Gülmez M. leg. and det. 6 exx.; Sulukaraağaç Site, 1133 m., 18-21.VII.2013, Gülmez M. leg. and det. 1 ex.

Distribution in Turkey: It is distributed in all geographical regions, except the Eastern and Southeastern Anatolia Region [23, 28, 32, 36, 37, 38, 40, 41, 45, 48, 53].

Genus *Eupleurus* Mulsant, 1842: 170

Eupleurus subterraneus (Linnaeus 1758)

Eupleurus subterraneus subterraneus (Linnaeus 1758)

Material examined: Karaoğlan-Mihalgazi, 207 m., 17-20.VI.2013, Gülmez M. leg. and det. 1 ex.

Distribution in Turkey: It is spread out in all geographical regions [23, 28, 33, 36, 40, 41, 45, 46, 51].

Genus *Euorodalus* G. Dellacasa, 1983a: 260

Euorodalus paracoenosus (Balthasar & Hrubant 1960)

Material examined: Sulukaraağaç Site, 1133 m., 16-19.V.2013, Gülmez M. leg. and det. 9 exx.

Distribution in Turkey: It is distributed in all geographical regions, except the Black Sea and Southeastern Anatolia Region [32, 33, 36].

4. Conclusions

This study found 14 species and three subspecies of 12 genera belonging to the Aphodiinae subfamily of Scarabaeidae. These species have different altitudes and month preferences. *Aphodius fimetarius*, *Melinopterus prodromus*, *Nimbus johnsoni*, and *Nimbus obliteratus* preferred every three altitudes, 207-612-1133m., within different months. *Melinopterus pubescens* and *Eupleurus subterraneus subterraneus* were found at just 207m in just one month, respectively, January, and June. *Eudolus quadriguttatus* was found 612m. in other months. Despite *Volinus sticticus* and *Esymus pusillus pusillus* preferred at 1133m. within different months, *Nimbus contaminatus* (January), *Acrossus luridus* (May), and *Euorodalus paracoenosus* (May) also preferred this altitude in only one month.

Volinus sticticus, *Esymus p. pusillus*, *Nimbus johnsoni*, *Euorodalus paparacoenosus racoenosus* are the first record for Eskişehir province. Moreover, *Volinus sticticus*, *Esymus pusillus pusillus*, *Nimbus johnsoni* species are new records for the Central Anatolia Region. Information on these species is important for different studies (systematic, molecular, population, etc.) that are planned to be planned in the future

Acknowledgments

Thank you very much for field work to Prof. Dr. Ferhat ALTUNSOY and his help in my study of Kemal DİNDAR. This study was a part of the master thesis of Mehmet GÜLMEZ, who first author. Additionally, a part of this study was presented as an oral presentation in the symposium proceedings of SEAB2017 by Yakup ŞENYÜZ.

References

[1] I. Löbl and D. Löbl, "Catalogue of Palaearctic Coleoptera, Volume 3, Scarabaeodiea, Scirtoidea, Dascilloidea, Buprestioidea, Byrrhoidea, Revised and updated edition", Leiden; Boston; Brill, 1-1011, 2016.

[2] O. Bánki et al., "Catalogue of Life Checklist" (Version 2021-10-18) 2021.
[3] G. Dellacasa, M. Dellacasa, D. Král, and A. Bezděk, "Tribe Aphodiini Leach, 1815. In: Löbl I. and Löbl D. (Eds.); Catalogue of Palaearctic Coleoptera, Scarabaeoidea, Scirtoidea, Dascilloidea, Buprestoidea Byrrhoidea. Revised and Updated Edition", *Brill, Leiden/Boston*, vol. 3, no. 98, pp.155, 2016
[4] Y. Şenyüz, "A New Genus and Species of Aphodiini (Coleoptera: Aphodiidae) from Istanbul in Turkey", *Journal of the Entomological Research Society*, vol. 19, no.2, pp. 113-119, 2017.
[5] R. L. Cajaiba E. Périco, W. Barreto, P. Leote and M. Santos, "Are small dung beetles (Aphodiinae) useful for monitoring neotropical forests' ecological status? Lessons from a preliminary case study in the Brazilian Amazon", *Forest Ecology and Management*, vol. 429, pp. 115–123, 2018, doi: https://doi.org/10.1016/j.foreco.2018.07.005.
[6] I. Hanski and Y. Cambefort "Dung Beetle Ecology", *Princeton New Jersey*, 481, 1991.
[7] F. C. Cabrero-Sa~nudo and R. Zardoya, "Phylogenetic Relationships Of Iberian Aphodiini (Coleoptera: Scarabaeidae) Based On Morphological And Molecular Data", *Molecular Phylogenetics And Evolution*, vol. 31, pp. 1084–1100, 2004, doi: https://doi.org/10.1016/j.ympev.2003.10.019.
[8] F. C. Cabrero-Sa~nudo and J. M. Lobo "Biogeography of Aphodiinae dung beetles based on the regional composition and distribution patterns of genera", *Journal of Biogeography*, vol. 36, pp. 1474–1492, 2009, doi: https://doi.org/10.1111/j.1365-2699.2009.02093.x.
[9] C. L. Liberal, A. M. I. Farias, M. V. Meiado, B. K. C. Filgueiras and L. Lannuzzi, "How Habitat Change And Rainfall Affect Dung Beetle Diversity İn Caatinga, A Brazilian Semi-Arid Ecosystem", *Journal of Insect Science*, vol. 11, no. 5, pp. 20-29, 2011, doi: https://doi.org/10.1673/031.011.11401.
[10] H. T. Larsen and A. Forsyth, "Trap Spacing and Transect Design for Dung Beetle Biodiversity Studies", *Biotropica*, vol. 37, no.2, pp. 322–325, 2005, doi: https://doi.org/10.1111/j.1744-7429.2005.00042.x.
[11] H. Küchmeister, A. C. Webber, İ. S. İlberbauer-Gottsberger, G. Gottsberger, "A polinização e sua relação com a termogênese em espécies de Arecaceae e Annonaceae da Amazônia Central", *Acta Amazônica*, vol. 28, pp. 217-245, 1998, doi: https://doi.org/10.1590/1809-43921998283245.
[12] E. Andresen, "Effects of Season and Vegetation Type on Community Organization of Dung Beetles in a Tropical Dry Forest", *Biotropica*, vol. 37, no. 2, pp. 291–300, 2005, doi: https://doi.org/10.1111/j.1744-7429.2005.00039.x.
[13] E. Nichols S. Spector, J. Louzadab, T. Larsen, S. Amezquita and M. E. Favila, "Ecological Functions And Ecosystem Services Provided By Scarabaeinae Dung Beetles", *Biological Conservation*, vol. 141, pp. 1461–1474, 2008, doi: https://doi.org/10.1016/j.biocon.2008.04.011.
[14] H. T. Larsen, A. Lopera and A. Forsyth, "Understanding Trait-Dependent Community Disassembly: Dung Beetles, Density Functions, And Forest Fragmentation", *Conservation Biology*, vol. 22, no. 5, pp. 1288–1298, 2007, doi: https://doi.org/10.1111/j.1523-1739.2008.00969.x.
[15] M. Alaouna, "Expression patterns of immune associated genes in Euoniticellus intermedius and characterization of the embryonic cell line", A dissertation submitted to the Faculty of Science, University of the Witwatersrand, Johannesburg, in fulfillment of the requirements for the degree of MSc. Johannesburg: pp. 124, 2012.
[16] R. F. Braga, V. Korasaki, E. Andresen and J. Louzada, "Dung beetle community and functions along a habitat-disturbance gradient in the Amazon: A Rapid Assessment of Ecological Functions Associated to Biodiversity", *Plos One*, vol. 8, no. 2, pp. 1-12, 2013, doi: https://doi.org/10.1371/journal.pone.0057786.
[17] Y. Şenyüz, K. Dindar and M. Gülmez, "Additions to Scarabaeoidea (Coleoptera) Fauna of Eskişehir", *Anadolu Universty Journal of Science and Technology - C - Life Science and Biotechinical*, vol. 4, no. 1, pp. 13-23, 2015, doi: https://doi.org/10.18036/btdc.42796.
[18] T. Breeschoten, C. Doorenweerd, S. Tarasov and A. P. Vogler, "Phylogenetics and biogeography of the dung beetle genus *Onthophagus* inferred from mitochondrial genomes", *Molecular Phylogenetics and Evolution*, vol. 105, pp. 86–95, 2016, doi: https://doi.org/10.1016/j.ympev.2016.08.016.
[19] C. M. Veiga, J. M. Lobo and F. Martín -Piera, "Las trampas pit- fall con cebo, sus posibilidades en el estudio de las comunidades coprófagas de Scarabaeoidea (Col.). II. Análisis de efectividad", *Review Ecological Biology Sol*, vol. 26, pp. 91–109, 1989.

[20] G. Dellacasa, P. Bordat and M. Dellacasa, "A revisional essay of world Genus -group taxa of Aphodiinae (Coleoptera: Aphodiidae)", *Memorie della Società Entomologica Italiana*, vol. 79, pp. 1-482, 2001.
[21] J. Baraud, "Description de nouveaux Aphodiidae palearctiques (Col. Scarabaeoidea)". *Revue Suisse de Zoologie, Geneve Tome*, vol. 83, no. 2, pp. 401-404, 1976.
[22] S. Sakai and T. Inoue, "A new pollination system: Dung-beetle pollination discovered in *Orchidantha inouei* (Lowiacea,Singiberales) in Sarawak, Malaysia". *American Journal of Botany*, vol. 86, pp. 56-61, 1999.
[23] D. E. Ersoy and A. Hasbenli, "Additional data to the Aphodiinae fauna (Coleoptera: Scarabaeidae) of the Sündiken Mountains Turkey", *Bilge International Journal of Science and Technology Research*, vol. 4, no. 2, pp. 110-124, 2020, doi: https://doi.org/10.30516/bilgesci.762169.
[24] N. Tuatay, A. Kalkandelen and N. Aysev, "Catalogue of insect of Plant Protection museum", T.*C. Tarım Bakanlığı Ziraii Mücadele Genel Müdürlüğü Yayınları*, Ankara, pp. 119, 1972.
[25] G. M. Carpaneto, "Una Nuova Specie Di *Aphodius* (*Colebopterus*) Dell'Armenia Turca. (Col. Aphodiidae)", *Frag. Ent. Roma*, vol. 9, pp. 21-33, 1973.
[26] G. M. Carpaneto, E. Piattella and R. Pittino, "The scarab beetles of Turkey: An updated checklist and chorotype analysis (Coleoptera, Scarabaeoidea)", *Biogeographia*, vol. 21, pp. 217-240, 2000.
[27] N. Lodos, "The study of the harmful insect fauna of Marmara and Aegean regions", *Publications of Food, Agriculture and Animal Husbandary Ministry of Republic of Turkey, Ankara*, pp. 301, 1978.
[28] N. Lodos, F. Önder, E. Pehlivan, R. Atalay, E. Erkin, Y. Karsavuran, S. Tezcan and S. Aksoy, "Faunistic Studies on Scarabaeoidea (Coleoptera) of Western Black Sea, Central Anatolia and Mediterranean Regions of Turkey", *Ege Üniversitesi basım evi*, pp. 64, 1999.
[29] R. Pittino, "Due nuovi *Onthophagus* Latr. anatolici del gruppo *ovatus* (L.) (Coleoptera, Scarabaeidae)". *Frag. Ent*., vol. 16, pp. 189-203, 1982.
[30] R. Pittino, "New or noteworthy taxa of the Genus *Onthophagus* (subg. Palaeonthophagus) from south-estern Europe and the Near East (Coleoptera, Scarabaeidae)", *Frag. Ent*, vol. 36, pp. 145-214, 2004.
[31] S. Tezcan and E. Pehlivan, "Evaluation Of The Lucanoidea And Scarabaeoidea (Coleoptera) Fauna Of Ecological Cherry Orchards İn İzmir And Manisa Provinces Of Turkey", *Ege Üniv. Ziraat Fakültesi Dergisi*, vol. 38, no. 2-3, pp. 31-37, 2001.
[32] M. Dellacasa and T. Kırgız, "Records of Aphodiinae (Coleoptera, Scarabaeoidea, Aphodiidae) from Edirne province and neighbouring areas (European Turkey)", *Italian Journal of Zoology*, vol. 69, pp. 71–82, 2002.
[33] A. Bellmann, "Beitrag zur Kenntnis der Aphodiinae der Türkei (Coleoptera: Scarabaeoidea)", *Ent. Z. Stuttgart*, vol. 117, pp. 132-136, 2007.
[34] S. Anlaş, D. Keith and S. Tezcan, "Notes on the pitfall trap collected Scarabaeoidea (Coleoptera) species in Bozdağlar Mountain of western Turkey", *Anadolu Doğa Bilimleri Dergisi*, vol. 2, pp. 1- 5, 2011a.
[35] S. Anlaş, D. Keith and S. Tezcan, "Notes on the seasonal dynamics of some coprophagous Scarabaeoidea (Coleoptera) species in Manisa province, western Anatolia" *Türk. Entomol. Dergisi*, vol. 35, pp. 447-460, 2011b.
[36] I. Rozner and G. Rozner, "Additional data to the Lamellicornia Fauna of Turkey (Coleoptera: Lamellicornia)", *Natura Somogyiensis, Kaposvár*, vol. 15, pp. 69-100, 2009.
[37] Y. Şenyüz, "Kütahya ili yakın çevresi Scarabaeidae (Coleoptera) faunasının tespiti", Eskişehir Osmangazi Üniversitesi, Fen Bilimleri Enstitüsü, Biyoloji Ana Bilim Dalı, Yüksek Lisans Tezi, Kütahya, s. 104, 2004.
[38] Y. Şenyüz, "Türkmen dağı Aphodiinae (Scarabaeidae, Coleoptera) Altfamilyasının Faunası", Dumlupınar Üniversitesi, Fen Bilimleri Enstitüsü, Biyoloji Ana Bilim Dalı, Zooloji Bilim Dalı, Doktora Tezi, Kütahya, s.90, 2009.
[39] Y. Şenyüz and Y. Şahin, "Faunistic Studies on Aphodiinae Subfamily (Coleoptera, Scarabaeidae) of Kütahya (Turkey)" *Linzer Biologische Beiträge*, vol. 14, no. 2, pp.1757-1766, 2009.
[40] Y. Şenyüz, K. Dindar and F. Altunsoy, "Contributions to the knowledge of Scarabaeidae (Coleoptera) fauna of the Middle and East Black Sea Region of Turkey", *Munis Entomolgy Zoology*, vol. 8, pp. 772-781, 2013a.
[41] Y. Şenyüz, K. Dindar, M. Gülmez and H. İzgördü, "A faunistic study on the species of Aphodiinae and Scarabaeinae (Coleoptera: Scarabaeidae) in Bursa", *Journal of Science of Dumlupinar University*, vol. 32, pp. 1-12, 2013b.

[42] Y. Şenyüz, K. Dindar, H. Çalışkan and D. Ü. Şirin, "Chorological Categories and Faunistic Records of Dung Beetles (Coleoptera: Scarabaeoidea: Scarabaeidae) from the Sündiken Mountains, Turkey", *Pakistan J. Zool*., vol. 48, no.1, pp. 137-150, 2017.
[43] Y. Şenyüz, M. Gülmez, K. Dindar and H. İzgördü, 2017, "A Preliminary Study On The Fauna Of Dung Beetle (Coleoptera, Scarabaeidae) At Horzum Village Of Şanlıurfa", *Journal of Science and Technology of DPU*, vol. 39, pp 21-30, 2017.
[44] Y. Şenyüz, J. M. Lobo and K. Dindar, "Altitudinal gradient in species richness and composition of dung beetles (Coleoptera: Scarabaeidae) in an eastern Euro-Mediterranean locality: Functional, seasonal and habitat influences" *European Journal of Entomology*, vol. 116, pp. 309–319, 2019, doi: 10.14411/eje.2019.034.
[45] A. Polat, E. Yıldırım and S. Ziani, "A contribution to the knowledge of the Aphodiinae and Scarabaeinae fauna of Turkey (Coleoptera: Scarabaeoidea: Scarabaeidae)" *Linzer biol. Beitr*, vol. 49, no. 1, pp. 733-744, 2017.
[46] İ. Özgen, Y. Şenyüz and A. Temizer, "Contributions to the Knowledge of Scarabaeoidea (Coleoptera) Fauna of Southeast and East Anatolia Region of Turkey", *Anadolu Doğa Bilimleri Dergisi*, vol. 5, no. 1, pp. 20-29, 2014.
[47] E. C. Küçükkaykı, Y. Şenyüz, D. Ü. Şirin, H. Çalışkan and C. Destire, "New Contriutions to Scarabaeidae (Insecta:Coleoptera) Fauna of The Eskişehir Province" *Anadolu University Journal Science Technology –C Life Science Biotechnology*, vol. 3, pp 23-30, 2013.
[48] D. E. Ersoy, "Sündiken dağlarının (Eskişehir) Aphodiinae ve Rutelinae Altfamilyalarının Sistematiği ve Faunası (Coleoptera: Scarabaeidae)" Gazi Üniversitesi; Yüksek Lisans Tezi, Biyoloji Fen Bilimleri Enstitüsü; Ankara, s. 164, 2014.
[49] M. Gülmez, "Eskişehir Bozdağ'ında Scarabaeinae ve Aphodiinae Alt Familyalarının Fenolojik ve Vertikal Dağılışları" Dumlupınar Üniversitesi, Fen Bilimleri Enstitüsü, Biyoloji Ana Bilim Dalı, Zooloji Bilim Dalı, Yüksek Lisans Tezi, Kütahya, s. 122, 2014.
[50] H. Sürgüt, A. Tüven, S. V. Varli, A. Polat, and S. Tezcan, "An Evaluation on the pitfall trap collected Scarabaeoidea (Coleoptera) species in Western Turkey", *Munis Entomolgy Zoology*, vol. 9, pp. 812-818, 2014.
[51] K. Dindar, "Kütahya Gümüş Dağı Aphodiinae ve Scarabaeinae'lerinin (Coleoptera: Scarabaeidae) Mevsimsel ve Vertikal Dağılışı", Dumlupınar Üniversitesi, Fen Bilimleri Enstitüsü, Biyoloji Ana Bilim Dalı, Zooloji Bilim Dalı, Yüksek Lisans Tezi:, Kütahya, s. 106, 2013.
[52] G. Coşkun, "Van Gölü Havzası Scarabaeidae (Coleoptera) familyası üzerine faunistik ve sistematik araştırmalar", Doktora Tezi, Çukurova Üniversitesi, Fen Bilimleri Enstitüsü, Adana, s. 348, 2012.
[53] Ö. Şahiner, "Orta ve Doğu Karadeniz Bölgesi Aphodiinae ve Scarabaeinae (Coleoptera: Scarabaeidae) altfamilyaları üzerinde sistematik çalışmalar", Yüksek Lisans Tezi, Hacettepe Üniversitesi, Fen Bilimleri Enstitüsü, Ankara, s. 123, 2013.
[54] D. E. Ersoy and A. Hasbenli, "Kazan Tepeleri (Ankara-Türkiye) Scarabaeidae (Coleoptera) Faunasına Katkılar", *Türkiye Tarımsal Araştırmalar Dergisi*, vol. 9, no. 1, pp 60-71, 2021, doi: https://doi.org/10.19159/tutad.1052881.

Contents lists available at *Dergipark*

Journal of Scientific Reports-A

journal homepage: *https://dergipark.org.tr/tr/pub/jsr-a*

E-ISSN: 2687-6167 ***Number 55, December 2023***

RESEARCH ARTICLE

Receive Date: 03.10.2023 *Accepted Date: 11.12.2023*

Synthesis and characterization of b-site controlled la-based high entropy perovskite oxides

İlker Yıldız

Central Laboratory, Middle East Technical University (METU), Ankara, 06800, Turkey, ORCID: 0000-0001-5761-655X

Abstract

High entropy perovskite oxide materials are a highly promising class of materials with a wide range of potential applications. They offer a unique combination of perovskite oxides and high entropy oxides, making them suitable for various fields, particularly in electrochemical energy storage systems and hydrogen production. Given the growing demand for clean energy and efficient energy storage solutions, the development of high entropy materials holds great significance. In this study, a cost-effective and rapid fabrication method was employed to produce several single-phase high entropy perovskite oxides by altering the B-site cations. The results demonstrated that these high entropy perovskite oxides could be synthesized with the same crystal structure, despite having significantly different elemental compositions. These variations in elemental composition led to differences in lattice parameters, metal-oxygen bond strengths, and oxygen vacancy content within the materials. Understanding and manipulating these factors can have important implications for the design of high entropy materials for energy storage and other applications.

Keywords: XPS; SEM; XRD; entropy oxides; perovskite

1. Main text

High entropy oxides (HEOs) are a significant breakthrough in multicomponent alloy and oxide systems [1], [2], and [3]. High entropy materials consist of five or more elements in one side of the single crystal phase. This feature gives a unique combination of properties that are unattainable in single crystal phase with conventional solid solutions [3], [4]. For example, high entropy perovskite oxides (HEPOs) combine the characteristics of high entropy oxides, such as long-term crystal and electronic structure stability, and the advantages of perovskite oxides, i.e., adjustable physicochemical properties [5], [6], and [7]. HEPOs are an intriguing and rapidly developing category of materials that have attracted considerable interest within the scientific community in recent times. These compounds are notable for their distinct crystal structures and the novel mix of cations they contain within the perovskite

framework, resulting in remarkable properties and a diverse array of potential uses. HEPOs have emerged as a forefront area of research that sits at the intersection of materials science, chemistry, and condensed matter physics.

Perovskite oxides are typically represented by the formula ABO_3, where the A-site consists of rare earth, alkaline, or alkaline-earth cations with a 12-fold coordination to oxygen atoms, while the B-site comprises transition metal cations coordinated by 6 oxygen atoms [8], [9]. Lanthanum-based perovskite oxides have found widespread use in various applications and have demonstrated excellent performance in electrochemical systems [10], [11], [12], and [13]. Furthermore, there have been reports of high entropy oxides and high entropy perovskite oxides synthesized using various methods. For instance, Jiang et al. synthesized 13 high entropy perovskite oxides such as $Sr(Zn_{0.2}Sn_{0.2}Ti_{0.2}Hf_{0.2}Mn_{0.2})O_3$, $Ba(Zr_{0.2}Sn_{0.2}Ti_{0.2}Hf_{0.2}Ce_{0.2})O_3$, and their derivatives using a high-energy ball mill [14]. Bayraktar et al. produced $(FeMnCrCoZn)_3O_4$, a high entropy spinel oxide, through a simple co-precipitation method [15]. Similarly, Nguyen et al. synthesized $La(CrMnFeCoNi)O_3$ using a sol-gel method [6].

Various rapid synthesis techniques have been developed to reduce production time for high entropy perovskite oxides. For example, Wang et al. utilized the flash sintering method to synthesize $Sr(Ti_{0.2}Y_{0.2}Zr_{0.2}Sn_{0.2}Hf_{0.2})O_3$, which is a promising approach for rapid synthesis [16]. Wu et al. synthesized a range of high entropy oxides using rapid joule heating, applying high currents (20-25 A) directly to the powders [17]. Dong et al. also employed rapid joule heating to synthesize high entropy oxide nanoparticles [18]. These methods have the advantage of significantly reducing the time required for high entropy oxide production.

In this study, equimolar $La(FeCoCrMnZn)O_3$ and non-equimolar $La(Fe_xCo_yCrMnZn)O_3$ (where x and y alternate between 0.1 and 0.3) high entropy perovskite oxides (HEPOs) were successfully synthesized using a modified sol-gel pechini method. The results revealed that all of the synthesized HEPOs share the same crystal structure, and their electronic structure is consistent, with the exception of the oxygen content. However, the variation in the mole fractions of elements leads to lattice distortion and an imbalance in the electronic structure, ultimately resulting in the formation of oxygen vacancies.

1.1. Structure and Method

The HEPOs were synthesized via sol-gel pechini method. The stoichiometric amount of metal nitrates was mixed with deionized (DI) water and stirred continuously until obtain a homogenous solution. After obtaining the solution, gelation agents such as citric acid and acrylamide were added to solution with molar ration of 3:1. Then, the solution stirred and heated until formed a gel. Afterwards, the gel is dried overnight to remove the physically bonded NO_2, and H_2O. Then finally these powders calcinated at 900 °C to obtain a single-phase high entropy perovskite oxide with desired chemical formulas.

1.2. Characterization of High Entropy Perovskite Oxides

The crystal structure of the $La(Fe_{0.2}Co_{0.2}Cr_{0.2}Mn_{0.2}Zn_{0.2})O_3$ (HEPO), $La(Fe_{0.1}Co_{0.3}Cr_{0.2}Mn_{0.2}Zn_{0.2})O_3$ (HEPO-Fe1), and $La(Fe_{0.3}Co_{0.1}Cr_{0.2}Mn_{0.2}Zn_{0.2})O_3$ (HEPO-Fe3) were studied by powder X-ray diffraction (XRD, Rigaku) with Cu Ka radiation from 10-90°. The surface morphologies and elemental distribution of the samples were analyzed using Scanning Electron Microscopy (SEM). Additionally, the chemical composition of the HEPOs was determined through X-ray Photoelectron Spectroscopy (XPS), utilizing Al Kα radiation. To ensure accurate measurements, all the XPS peaks were calibrated with the standard C 1s spectrum at 284.6 eV.

2. Results

The XRD patterns of the synthesized HEPOs are depicted in Figure 1. In Figure 1a, one can observe the XRD patterns for all synthesized HEPOs. The diffraction peaks at 23.1°, 32.9°, 40.4°, and 47.1° correspond to the main peaks of the orthorhombic HEPO structure, representing the (110), (020), (022), and (220) planes, respectively. As

demonstrated in the Rietveld refinement results shown in Figure 1b, c, and d, the HEPOs exhibit a pure single orthorhombic crystal structure with very low χ^2 values.

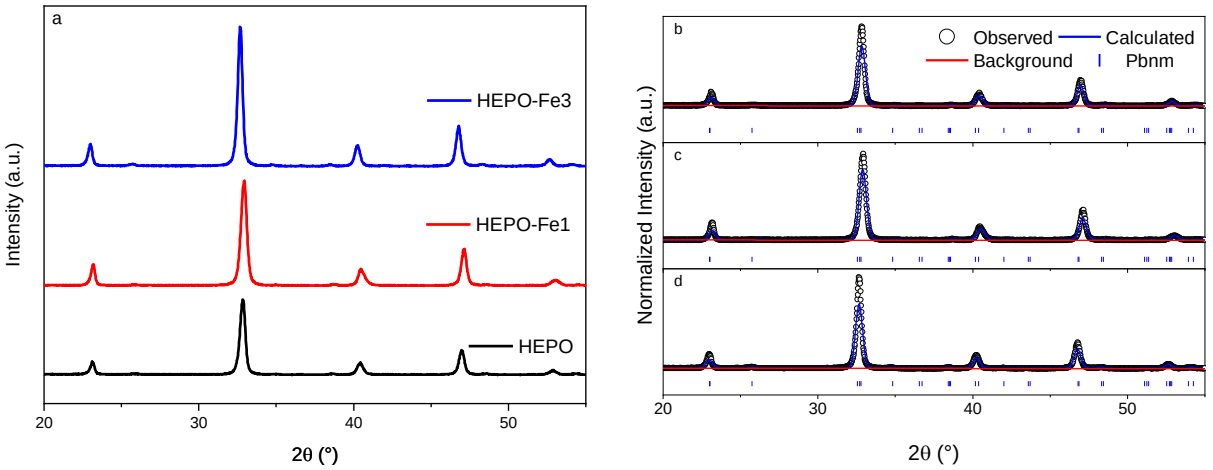

Fig. 1. (a) XRD patterns of the high-entropy perovskite series, (b)HEPO, (c)HEPO-Fe1, (d)HEPO-Fe3.

There are no additional peaks related to oxides or hydroxides of the elements, indicating the high purity of the synthesized HEPOs. Importantly, the type of crystal structure remains constant even when the B-site cation mole fractions vary. The primary effect of changes in the amount of elements is the alteration of the lattice parameters. This difference in lattice parameters is evident from the peak shift in the XRD pattern, as shown in Figure 1. The Rietveld refinement confirms that HEPOs possess an orthorhombic crystal structure with the Pbnm space group. The lattice parameters can be found in Table 1.

Table 1. Rietveld refinement analysis of HEPOs. Lattice Constants (*Å*).

Powder	**a**	**b**	**c**	**Volume (*Å*^{3})**	**Space Group**	**c2**
HEPO	5.53	5.49	7.78	236.248	Pbnm	1.49
HEPO-Fe1	5.51	5.47	7.77	234.400	Pbnm	1.71
HEPO-Fe3	5.53	5.51	7.79	237.093	Pbnm	2.39

The morphology and elemental distribution of the HEPOs were investigated through SEM and energy-dispersive X-ray spectroscopy (EDS) analysis. Figure 2 presents the SEM images of the HEPOs. It is evident that all the samples exhibit a similar shape and size, which underscores the precise control achieved during the synthesis process. The particle sizes fall within the range of 700-800 nm, and the particles display uneven and non-spherical morphologies.

The EDS mapping results, as shown in Figure 2, indicate that the elements are uniformly and homogeneously distributed throughout the particles and lattice. There is no elemental segregation observed for La, Fe, Co, Mn, Cr, Zn, and O. This implies that there are no oxide phases of the transition metals within the samples. Furthermore, this consistent distribution pattern is observed for all HEPOs, reinforcing the reliability and reproducibility of the synthesis method.

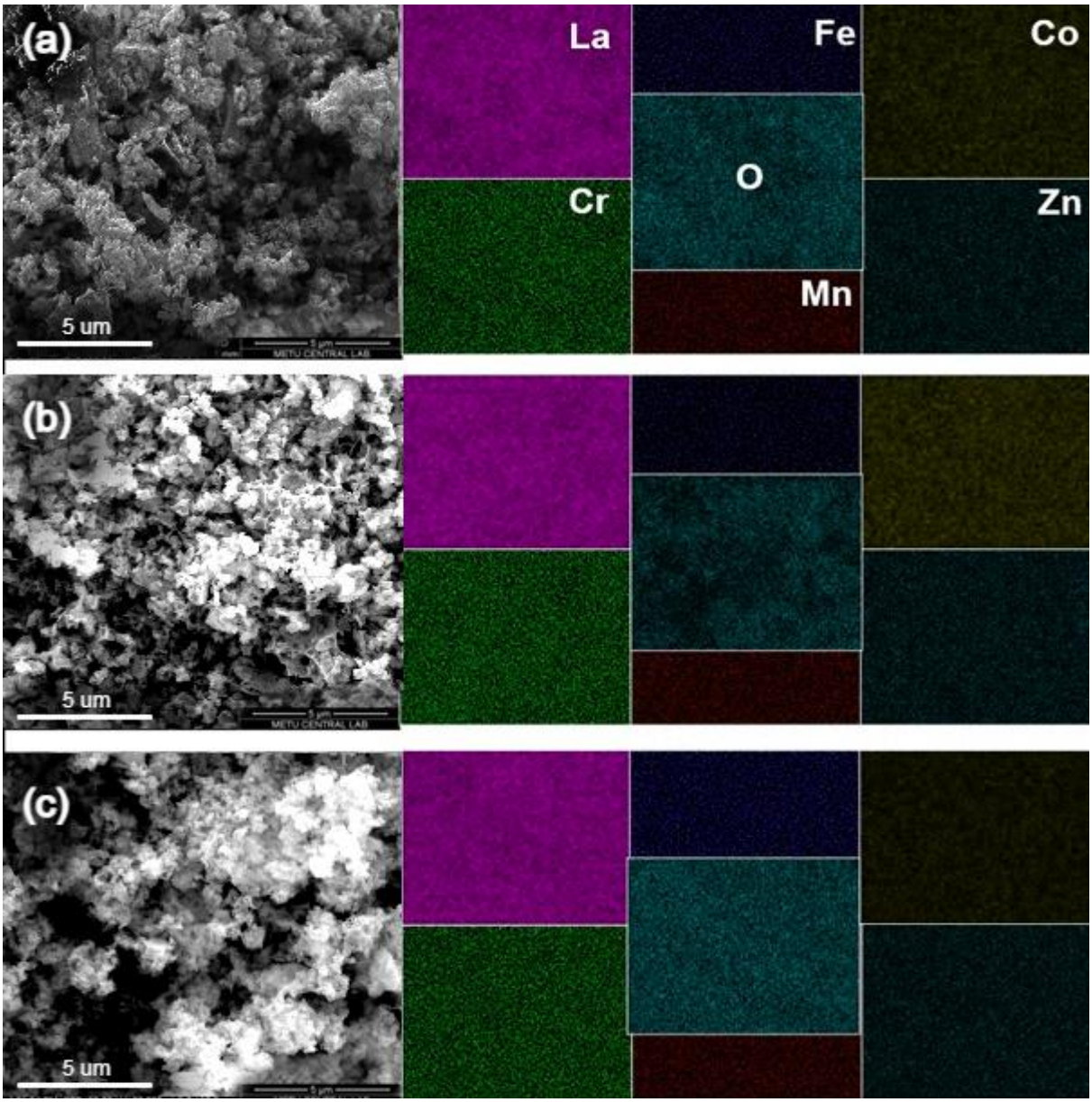

Fig. 2. SEM images and corresponding EDS mappings of (a) HEPO, (b) HEPO-Fe1, (c) HEPO-Fe3.

The XPS core level spectra of each element in the high entropy perovskite oxide structures are depicted in Figure 3. Every element's core level spectra were deconvoluted corresponding peaks. Figure 3 a, b, and c show the core level spectra of La for HEPO, HEPO-Fe1, and HEPO-Fe3, respectively. The La XPS spectra deconvoluted into four peaks corresponding to binding energies of 834.47 eV, 838.79 eV, 850.26 eV, and 855.58 eV. The spin-orbit splitting (SOS) observed in the La 3d5/2 and La 3d3/2 core-level XPS peaks is precisely measured at an energy differential of 16.8 eV. This energy separation, a characteristic feature of La core-level electron binding energies,

reflects the interaction between the spin angular momentum and orbital angular momentum of the electrons in the La atomic species under investigation [19].

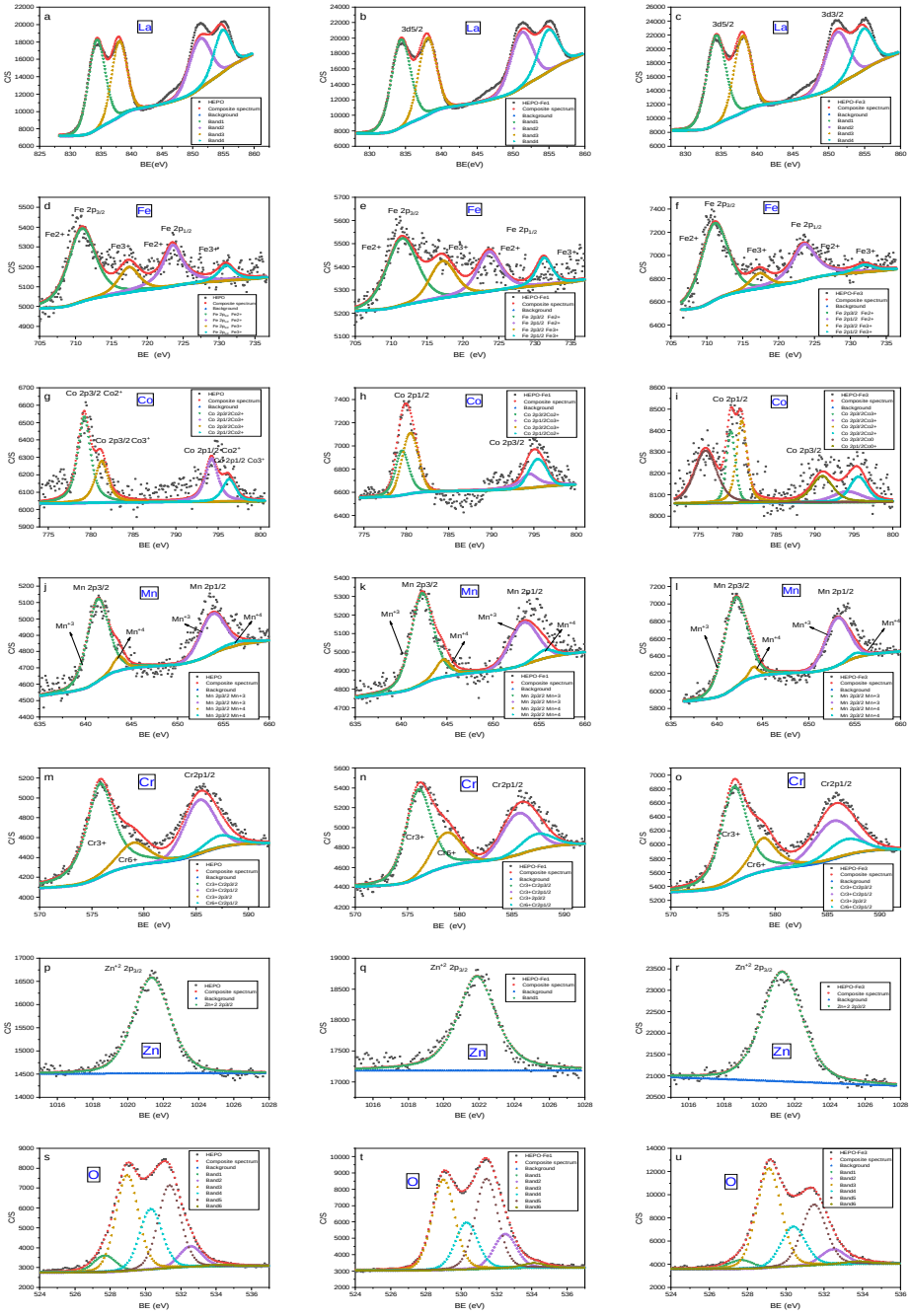

Fig. 3. XPS core level spectra of HEPO, HEPO-Fe1, HEPO-Fe3 for all elements, respectively.

Fe XPS core-level spectra are shown in Figure 3 d, e, and f for synthesized HEPOs. The Fe 2p core-level XPS spectrum exhibits a bifurcation into two spin-orbit doublets: Fe 2p3/2 and Fe 2p1/2, discernible at binding energies of 711.7 eV and 724.4 eV, respectively. Concurrently, the spectrum manifests shake-up satellite peaks at 719.1 and 736.2 eV. This complexity is further elucidated by the presence of two distinguishable peaks within each of the Fe 2p3/2 and Fe 2p1/2 components, indicative of two distinct chemical states of Fe, specifically Fe^{2+} and Fe^{3+} [20].

Consistent with existing literature, we have employed a fitting procedure for the Co 2p3/2 peaks, yielding binding energy values of 780.05 eV and 781.7 eV, which are attributed to Co^{3+} and Co^{2+} states, respectively. Similarly, for the Co 2p1/2 peaks, binding energy values of 795.73 and 797.32 eV correspond to Co^{3+} and Co^{2+} states, respectively. Additionally, weak satellite peaks at 786.9 eV and 805.08 eV are observed for HEPOs, as depicted in Figure 3g, h, and i. Notably, Co^{2+} is associated with the higher binding energy, aligning with prior XPS investigations of cobalt oxides [21], [22].

The Mn 2p spectra for HEPO, HEPO-Fe1, and HEPO-Fe3 are displayed in Figure j, k, l, respectively. The Mn XPS spectra are characterized by two discernible peaks situated at 642.7 and 654 eV, corresponding to the Mn 2p3/2 and Mn 2p1/2 spin orbits, respectively. Notably, additional features are observed within these spectral regions, with peaks at 642.3 and 653.7 eV associated with Mn^{3+} oxidation states, while peaks at 644.1 and 654.4 eV can be attributed to Mn^{4+} oxidation states [20].

The XPS spectra of the Cr2p core level, as illustrated in Figure 3m, n, and o, reveal the presence of two distinct sets of spin–orbit components centered at binding energies (BEs) of approximately 576.0 eV and 578.3 eV for the 2p3/2 state and 585.6 eV and 587.8 eV for the 2p1/2 state in all examined samples. This observation suggests the coexistence of two distinct chromium-based chemical species on the surface of the studied materials. The predominant component, characterized by the lower BE values of its two spin-orbit features, is attributed to Cr(III) species that are integrated within mixed transition metal spinel oxides, aligning with existing literature findings [23].

The XPS analysis of the O 1s spectra for HEPOs, as depicted in Figure 3s, t, u, can be resolved into four distinctive peaks. The initial peak corresponds to lattice oxygen species, typically associated with O^{2-}, situated at a binding energy of 529.6 eV. Following this, there is a peak attributed to highly oxidative oxygen species, typically represented by O_2^{2-} or O^-, positioned at 530.4 eV. Subsequently, there is a peak indicative of hydroxyl groups or surface-adsorbed oxygen, situated at a binding energy of 531.4 eV, typically corresponding to OH^- or O_2. Lastly, there is a peak associated with adsorbed molecular water or carbonates on the surface, appearing at 532.5 eV, which is typically representative of H_2O or CO_3^{2-} [24].

The core-level XPS spectra for Zn^{2+} in the 2p3/2 energy level typically exhibits a distinct peak as shown in Figure 3p, q, r. In XPS, the energy of emitted electrons is measured, and these energy levels correspond to the binding energy of 1022 eV. The XPS spectrum for Zn^{2+} 2p3/2 core-level electrons display a sharp and discernible peak at this binding energy. The precise shape and intensity of this peak can yield valuable information about the chemical state and local environment of the zinc atoms within the sample [25]. Measured binding energies are important in order to decide oxidation state of any characterized material also in the context of energy storage.

3. Conclusion

In conclusion, this study has underscored the immense promise of high entropy perovskite oxide materials as a versatile class of substances poised for extensive applications. With combining the distinctive characteristics of perovskite oxides and high entropy oxides, these materials exhibit remarkable potential in various domains, most notably in the realms of electrochemical energy storage systems and hydrogen production. Given the pressing global demand for environmentally sustainable energy solutions and efficient energy storage technologies, the advancement of high entropy materials assumes paramount importance. Within the scope of this investigation, we have successfully employed a cost-effective and expeditious fabrication method to synthesize a series of single-phase high entropy perovskite oxides by introducing alterations in the B-site cations. Our findings have elucidated that these high entropy perovskite oxides can be synthesized while maintaining consistent crystal structures, despite possessing

notably distinct elemental compositions. These variances in elemental makeup, however, have imparted consequential disparities in lattice parameters, metal-oxygen bond strengths, and oxygen vacancy levels within the materials. This newfound insight into the manipulation and comprehension of these crucial factors opens exciting avenues for the tailored design and optimization of high entropy materials for diverse applications, especially within the realm of energy storage. The potential ramifications of this research extend beyond the confines of our laboratory, offering an encouraging outlook for the development of next-generation materials that can drive sustainable energy technologies and bolster our collective pursuit of a greener future.

Acknowledgements

I would like to express my sincere gratitude to Assist. Prof. Dr. Çiğdem Toparlı for her valuable support throughout the research process. I also want to thank to Tuncay Erdil for his helpful feedback and support.

References

[1] E. P. George, D. Raabe, and R. O. Ritchie, "High-entropy alloys", *Nature Reviews Materials*, *4*(8), 515–534, 2019, https://doi.org/10.1038/s41578-019-0121-4
[2] M. V. Kante *et al.,* "A High-Entropy Oxide as High-Activity Electrocatalyst for Water Oxidation, *ACS", Nano*, *17*(6), 5329–5339, 2023, https://doi.org/10.1021/acsnano.2c08096
[3] C. M. Rost *et al.,* "Entropy-stabilized oxides", *Nature Communications*, *6*(1), 8485, 2015. https://doi.org/10.1038/ncomms9485
[4] F. Okejiri *et al.,* "Room- Temperature Synthesis of High- Entropy Perovskite Oxide Nanoparticle Catalysts through Ultrasonication- Based Method", *ChemSusChem*, *13*(1), 111–115, 2020, https://doi.org/10.1002/cssc.201902705
[5] Z. Liu *et al.,* "High-Entropy Perovskite Oxide: A New Opportunity for Developing Highly Active and Durable Air Electrode for Reversible Protonic Ceramic Electrochemical Cells", *Nano-Micro Letters*, *14*(1), 217, 2022 https://doi.org/10.1007/s40820-022-00967-6
[6] T. X. Nguyen, Y. Liao, C. Lin, Y. Su, & J. Ting, "Advanced High Entropy Perovskite Oxide Electrocatalyst for Oxygen Evolution Reaction", *Advanced Functional Materials*, *31*(27), 2101632, 2021, https://doi.org/10.1002/adfm.202101632
[7] L. Wang, M. D. Hossain, Y. Du, & S. A. Chambers, "Exploring the potential of high entropy perovskite oxides as catalysts for water oxidation", *Nano Today, 47*, 101697, 2022, https://doi.org/10.1016/j.nantod.2022.101697
[8] X. Xu, Y. Zhong, & Z. Shao, "Double Perovskites in Catalysis, Electrocatalysis, and Photo(electro)catalysis", *Trends in Chemistry*, *1*(4), 410–424., 2019, https://doi.org/10.1016/j.trechm.2019.05.006
[9] W. J. Yin *et al.,* "Oxide perovskites, double perovskites and derivatives for electrocatalysis, photocatalysis, and photovoltaics", *Energy & Environmental Science*, *12*(2), 442–462, 2019, https://doi.org/10.1039/C8EE01574K
[10] J. Androulakis *et al.,* "LaSrMnCoO6: a new cubic double perovskite oxide", *Journal of Solid State Chemistry*, *173*(2), 350–354, 2023, https://doi.org/10.1016/S0022-4596(03)00109-9
[11] X. Cheng *et al.,* "Oxygen Evolution Reaction on $La_{1-x}Sr_xCoO_3$ Perovskites: A Combined Experimental and Theoretical Study of Their Structural, Electronic, and Electrochemical Properties", *Chemistry of Materials*, *27*(22), 7662–7672, 2015 https://doi.org/10.1021/acs.chemmater.5b03138
[12] T. Erdil *et al.,* "Facile Synthesis and Origin of Enhanced Electrochemical Oxygen Evolution Reaction Performance of 2H-Hexagonal $Ba_2CoMnO_{6-\delta}$ as a New Member in Double Perovskite Oxides", *ACS Omega*, *7*(48), 44147–44155, 2022, https://doi.org/10.1021/acsomega.2c05627
[13] J. T. Mefford *et al.,* "Water electrolysis on La1−xSrxCoO3−δ perovskite electrocatalysts", *Nature Communications*, *7*(1), 11053, 2016, https://doi.org/10.1038/ncomms11053
[14] S. Jiang *et al.,* "A new class of high-entropy perovskite oxides", *Scripta Materialia*, *142*, 116–120, 2018, https://doi.org/10.1016/j.scriptamat.2017.08.040

[15] D. O. Bayraktar, E. Lökçü, C. Ozgur, T. Erdil, & C. Toparli, "Effect of synthesis environment on the electrochemical properties of (FeMnCrCoZn)(3)O-4 high- entropy oxides for Li- ion batteries", *International Journal of Energy Research*, *46*(15), 22124–22133, 2022, https://doi.org/10.1002/er.8749
[16] K. Wang *et al.*, "Fabrication of high-entropy perovskite oxide by reactive flash sintering", *Ceramics International*, *46*(11), 18358–18361, 2020, https://doi.org/10.1016/j.ceramint.2020.04.060
[17] H. Wu *et al.*, "Rapid Joule-Heating Synthesis for Manufacturing High-Entropy Oxides as Efficient Electrocatalysts", *Nano Letters*, *22*(16), 6492–6500, 2022, https://doi.org/10.1021/acs.nanolett.2c01147
[18] Q. Dong *et al.*, "Rapid Synthesis of High- Entropy Oxide Microparticles", *Small*, 2104761, 2022, https://doi.org/10.1002/smll.202104761
[19] S. Mickevičius *et al.*, "Investigation of epitaxial LaNiO3−x thin films by high-energy XPS", *Journal of Alloys and Compounds*, *423*(1–2), 107–111, 2006, https://doi.org/10.1016/j.jallcom.2005.12.038
[20] X. L. Wang, E. M. Jin, G. Sahoo, & S. M. Jeong, "High-Entropy Metal Oxide (NiMnCrCoFe)3O4 Anode Materials with Controlled Morphology for High-Performance Lithium-Ion Batteries", *Batteries*, *9*(3), 147, 2023, https://doi.org/10.3390/batteries9030147
[21] C. Alex, S. Sarma, S. C. Peter, & N. S. John, "Competing Effect of Co^{3+} Reducibility and Oxygen-Deficient Defects Toward High Oxygen Evolution Activity in Co_3O_4 Systems in Alkaline Medium", *ACS Applied Energy Materials*, *3*(6), 5439–5447, 2020 https://doi.org/10.1021/acsaem.0c00297
[22] E. Lökçü, Ç. Toparli, & M. Anik, "Electrochemical Performance of $(MgCoNiZn)_{1-x}Li_xO$ High-Entropy Oxides in Lithium-Ion Batteries", *ACS Applied Materials & Interfaces*, *12*(21), 23860–23866, 2020, https://doi.org/10.1021/acsami.0c03562
[23] P. Gupta, R. Bhargava, R. Das, & P. Poddar, "Static and dynamic magnetic properties and effect of surface chemistry on the morphology and crystallinity of DyCrO3 nanoplatelets", *RSC Advances*, *3*(48), 26427, 2013, https://doi.org/10.1039/c3ra43088j
[24] M. Suthar, A. K. Srivastava, R. K. Joshi, & P. K. Roy, "Nanocrystalline cerium-doped Y-type barium hexaferrite; a useful catalyst for selective oxidation of styrene", *Journal of Materials Science: Materials in Electronics*, *31*(19), 16793–16805, 2020, https://doi.org/10.1007/s10854-020-04234-5
[25] A. Radoń, Ł. Hawełek, D. Łukowiec, J. Kubacki, & P. Włodarczyk,, "Dielectric and electromagnetic interference shielding properties of high entropy (Zn,Fe,Ni,Mg,Cd)Fe2O4 ferrite", *Scientific Reports*, *9*(1), 20078, 2019, https://doi.org/10.1038/s41598-019-56586-6

Contents lists available at *Dergipark*

Journal of Scientific Reports-A

journal homepage: *https://dergipark.org.tr/tr/pub/jsr-a*

E-ISSN: 2687-6167 ***Number 55, December 2023***

RESEARCH ARTICLE

Receive Date: 02.09.2023 *Accepted Date: 18.12.2023*

Minimization of metabolic energy expenditure in collaborative order picking

Mahmut Tutam[1*]

[a]*Erzurum Technical University, Department of Industrial Engineering, Erzurum, Turkiye, ORCID:0000-0002-2018-5458*

Abstract

Order picking is one of the most repetitive, labor-intensive, and physically demanding operations in warehouses. Picking hundreds of orders daily requires high metabolic energy expenditure and is characterized by poor ergonomics posing high risks for musculoskeletal disorders. In traditional order picking, the order picker walks around racks in a warehouse throughout the day. Alternatively, it is aimed at minimizing inefficient time and musculoskeletal strains with ride-on order picking by allowing the order picker to stand on an operator's platform of an order-picking truck and ride the truck between stop locations. However, the order picker must step down from the platform at each stop location and step up onto the platform before riding the truck to the next stop location. Therefore, riding the truck with frequent stops leads to more metabolic energy expenditure and musculoskeletal disorders than walking, although it is faster. Benefiting advantages of both traditional and ride-on order picking, a relatively new order picking truck (collaborative order picking truck) is deployed in warehouses to reduce inefficient walking time and ergonomic riding disorders. In collaborative order picking, the order picker can walk from a stop location directly to the next pick location while the truck moves to the next stop location autonomously or ride the truck to the next stop location in case of having a large distance between stop locations. This paper develops an optimization model to minimize total metabolic energy expenditure in collaborative order picking by finding the shortest route and the best collaboration decision (walk or ride). Based on the Monte Carlo simulation, the metabolic energy expenditure with collaborative order picking is analyzed. Our results indicate metabolic energy savings with collaborative order picking up to 200% and 83% compared to traditional and ride-on order picking, respectively.

Keywords: Order picking; Collaborative Robot; Optimal Routing; Ergonomics; Metabolic Energy Expenditure;

* Corresponding author. Tel.: +90-444-5388-2604.
E-mail address: mahmut.tutam@erzurum.edu.tr
http://dx.doi.org/10.1016/j.cviu.2017.00.000

.

1. Introduction

Order picking is one of the most critical operations in warehouses to retrieve customers' orders from storage locations in time [1], which is confirmed to be one of the most physically demanding and time-consuming operations in warehouses [2]. In addition to physical and temporal constraints, increasing labor costs compels companies to increase the productivity of order picking operations. Therefore, order pickers are pressured to handle more orders in a shorter time frame [3-4]. Accordingly, order picking operations are intensively studied in the literature by focusing mainly on travel time minimization, hence the maximization of order picking productivity [5-6]. However, ergonomics is relatively less mentioned in academic studies [7] even though order pickers are exposed to high ergonomic disorders due to abnormal postures, excessive force, and task repetition [6-7]. Moreover, operational models did not include human factors sufficiently [10]. Apparently, ignoring ergonomics in order picking operations results in an incomplete representation of real-world practice [1] and leads to the most common occupational disease for order pickers, musculoskeletal disorders [11].

Despite technological advances, traditional order picking (TOP) is still significantly used in small- or middle-sized warehouses [10-12], which is characterized by walking long distances (see Fig. 1.a). Even though walking is one of the best exercises for physical and mental health, prolonged walking is associated with musculoskeletal discomfort and injuries [14]. Moreover, the throughput of the picking operations is constrained by the walking speed of the order picker, resulting in inefficient time.

Responding to physical/temporal constraints and increasing labor costs, companies tend to use ride-on order picking (ROP) by extending the speed limit to riding, which is faster than walking (see Fig. 1.b). Therefore, the order picker can travel faster large distances between stop locations. Note that each pick location has a corresponding stop location for the truck at the center of each picking aisle. However, riding leads to more Metabolic Energy Expenditure (MEE) and musculoskeletal disorders because the order picker must step down/up from/onto the platform at each stop location, which is approximately 1,200 times per shift [15]. Therefore, picking faster with ROP may lead to more ergonomic disorders than walking, especially for tours with frequent stops.

(a) (b)

Fig. 1. (a) Traditional order-picking [16]; (b) ride-on order-picking [17].

Recently, collaborative order picking (COP) has been introduced to simultaneously reduce the inefficient time for walking (see Fig. 2.a) and ergonomic disorders for riding (see Fig. 2.b). The order picker can walk to the next pick location while the collaborative order-picking truck moves autonomously to the next stop location or ride the truck.

Therefore, the order picker can freely switch between walking to minimize ergonomic riding disorders and riding to reduce inefficient walking time. This raises our research question when the order picker walks or rides the collaborative order-picking truck. As walking requires less MEE than riding and riding is faster than walking, the decision can be made based on both ergonomic and temporal perspectives. Unlike early studies, this paper mainly focuses on the ergonomic perspective of the problem. By doing so, the MEE with COP is calculated for an order picker. Starting from an Input/Output (I/O) point, the truck visits all stop locations in a pick list. After picking all items in the pick list, the order picker drops the pallet or roll cage at the I/O point and gets another pallet or roll cage to collect items in another pick list. Note that walking is only allowed in picking aisles, and the order picker is forced to ride the truck in cross aisles for safety reasons. Therefore, a significant penalty is applied for walking between picking aisles.

(a) (b)

Fig. 2. Collaborative order-picking with (a) walking and (b) riding [18].

As shown in Fig. 3, the order picker starts from the I/O point located on the left corner of the warehouse and rides the truck directly to the first stop location (Stop Location 20), where the pallet or roll cage of the truck coincides with Pick Location 20 to minimize the handling time. After stopping the truck at Stop Location 20, the order picker steps down from the operator's platform and walks to the exact pick location (Pick Location 20) by following a Euclidian distance. Before walking back to Stop Location 20, s/he picks the item in the pick list. Afterward, s/he drops the item into the pallet or roll cage.

Depending on the distance between Stop Locations 20 and 9, the order picker may walk to Pick Location 9 or ride the truck to Stop Location 9. With the given parameter values in Fig. 3, the order picker rides the truck to Stop Location 9. Therefore, s/he steps onto the operator's platform of the collaborative order-picking truck at Stop Location 20 and rides the truck to Stop Location 9 while standing on the platform. After completing the order-picking operation, the order-picker decides to walk directly to Pick Location 5 using a Euclidean distance while the truck moves autonomously to Stop Location 5. Repeating this process for each pick location, the tour terminates after collecting all items. Eventually, the order picker drops the pallet or roll cage to the I/O point and takes another empty pallet or roll cage to collect items on the following pick list.

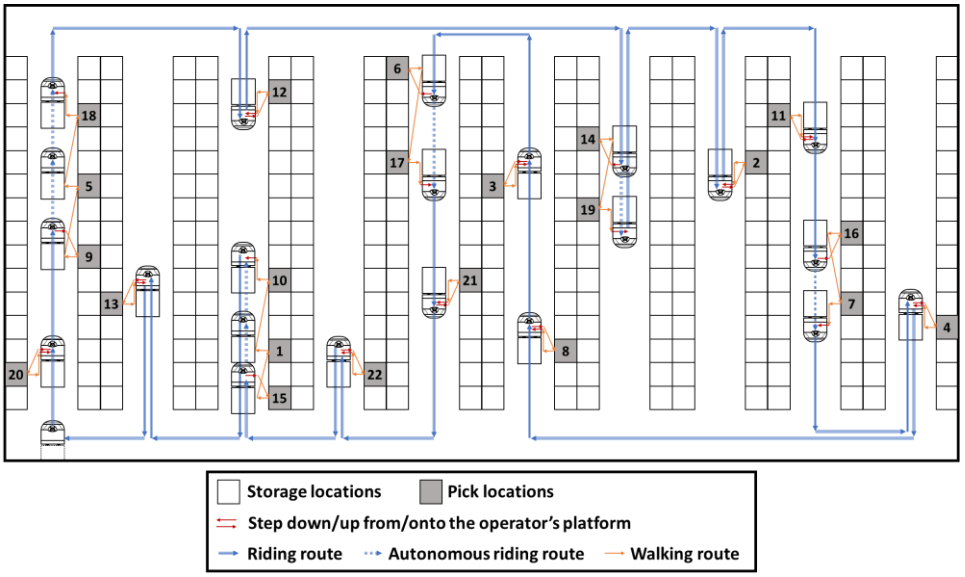

It can be observed in Fig. 3 that the visiting sequence of pick locations does not match with the pick list number; hence, the visiting sequence to collect all items must be determined. Therefore, we develop an optimization model to

Fig. 3. An illustrative example of COP with 22 pick locations in a 10-aisle warehouse.

minimize the total MEE by determining the shortest route and best collaboration decision (walk or ride). Based on the Monte Carlo simulation, we test different pick-list sizes and present the intractability of the optimization model for middle- or large-sized instances. Moreover, we implement the dynamic programming approach proposed by [19] for middle- or large-sized problems. Eventually, we report the improvement in MEE with COP for different pick list sizes compared to TOP and ROP.

We review the order picking problem literature by concentrating specifically on ergonomic problems in Section 2. Section 3 includes optimization model, energy expenditure calculations and solution approach to find the optimal collaboration strategy. Section 4 provides computational results. The last section serves as a summary of the paper and offers recommendations for future research.

2. Literature Review

Order-picking literature mainly focuses on routing, layout design, storage assignment, order batching, and zoning problems by only considering temporal or economic values rather than ergonomic values, which are mentioned very infrequently [13]. Limiting our focus on ergonomic problems in order picking, we address interested readers in order-picking problems to review papers [10, 19, 20].

Biomechanical models are used to analyze the effect of physical activities on the musculoskeletal system [21]. [22] proposed an algorithm to evaluate the biomechanical stresses of manual materials handling jobs. [23] proposed a metabolic rate prediction model to estimate the metabolic rates of manual material handling jobs by considering the characteristic of a worker and the description of the material handling job. [24] studied the cognitive ergonomics of order-picking operations and investigated the effect of color, position, address information, and shelf coding on product recognition and acquisition time.

[25] developed an interactive ergonomic evaluation system based on the order picker`s assessment of video recordings. [26] developed heuristic algorithms to determine the storage locations of products by including strategies

to increase the accuracy of picks and reduce ergonomic problems. [27] evaluated order-picking operations regarding time consumption and ergonomic risks based on video recordings and physiological measurements. [28] conducted a laboratory experiment to compare the effects of ergonomic training with the lifting equation of the National Institute for Occupational Safety and Health (NIOSH). [29] identified ergonomic risks for different grocery warehouses and suggested intervention policies to reduce exposure to ergonomic problems. [30] used the verbal protocol method to investigate the thoughts of order pickers during and after an order picking operation. [31] proposed a scheduling framework for order picking operations, including physical and cognitive order-picker characteristics in a semi-automated order picking warehouse.

[32] compared two handle designs for pallet jacks based on usability, comfort, and biomechanical and physiological factors. [33] investigated alternative learning curves to assess learning effects on order-picking operations. [34] studied the effects of horizontal/vertical bin locations, bin angle, and hand usage on arm movements. [13] proposed a framework to integrate human factors into order-picking planning models. Evaluating human factors in order-picking operations, [35] provided a guideline for the usage of qualitative methods. Considering energy expenditure and operation time, [36] developed a multi-objective method and analyzed an integrated storage assignment approach. [37] proposed a heuristic algorithm to pick safely clustered items at each stop location and used a simulated annealing method to minimize total tour time. [20] reviewed the research literature on order-picking systems and discussed the integration of human factors in designing and managing order-picking systems. Converting ergonomic efforts to cost, [38] proposed a method to evaluate ergonomic factors in order picking operations under consideration of availability and rest allowance of order pickers. [39] developed a mathematical model to analyze different rack layout configurations by considering both economic and ergonomic performance measures. Integrating storage assignment and zoning problems, [8] developed an optimization to minimize the maximum ergonomic burden among order pickers.

[40] compared flat and tilted pallet containers using qualitative observation and Rapid Entire Body Assessment (REBA) methods. [41] described the usage of handheld scanners in order-picking operations to eliminate wrist motions. Considering the rotation of pallets, [42] developed a mathematical model to estimate the ergonomic and cost aspects of order picking operations. [43] explored the impact of head-worn displays and user interface designs in order picking operations. [44] calculated energy expenditure for order picking operations in three different layout configurations in addition to developing cost functions. Determining optimal layout and storage assignments, [45] developed two mixed integer programming models to minimize the total travel distance and total ergonomic strain for order pickers. [45] studied the layout configuration and item allocation problems with the objective of either minimizing total tour distance or total ergonomic strains.

[46] investigated the impact of technological items on order pickers' health. Decomposing the order picking operation into four activity levels, [47] proposed a technical method including activity information to evaluate the ergonomic risk for order pickers. [48] compared two order-picking systems based on average physical activity. [49] evaluated the impact of a smart workwear system on postural exposure.

[50] investigated the relationship between the positive effect of using digital technologies and the intensification of order-picking operations. [51] developed a heuristic approach to solve joint order batching and scheduling problems by considering the fatiguing effect of order-picking operations. [52] reviewed the literature and conducted interviews to identify human factors resulting in quality issues in order picking operations. Considering the time, energy expenditure, and health risks in order picking operations, [53] developed a multi-objective optimization model for the storage assignment problem. [54] proposed a method to use context information in an activity recognition model. [55] presented a safe and flexible mechatronic interface for the integration of generic mobile robots and collaborative robots. [56] explored the kinematics of nine workers' back and shoulder movements by using an optical motion capture system. Proposing a difficulty ranking system, [57] introduced a new aisle layout and a storage assignment strategy concerning ergonomic criteria. [58] assessed ergonomic risks of warehouse workers based on a marker-based motion capture system. [59] proposed a structured ergonomic evaluation methodology to assess the discomfort levels and risk factors at manual material handling tasks. [60] proposed a

method for the biomechanical analysis of manual material handling tasks. [61] conducted a field study to investigate the familiarization period for a passive shoulder exoskeleton and shows its benefit to material handling workers.

The literature review concludes that our study differs from the order-picking problem literature by focusing on ergonomic values in COP rather than economic or temporal values. Unlike earlier studies, we determine the optimal route and best collaboration strategy (walking or riding) to minimize the total MEE.

3. Model Description

To determine the shortest route and best collaboration strategy, a variant of the traveling salesman problem is formulated using MEE formulations given by [23] and [62]. The order picker can travel in both directions and change direction in picking aisles. We do not include MEE to pick items from racks since it does not affect the decision for the optimal route and the best collaboration strategy.

3.1. Notation

The following notation is used to develop the optimization model.

Nomenclature

Set (indices)

P (p, q)	the set for pick locations with indices p and q (0 for the I/O point)

Parameters

M	a relatively large number
L	the length of each aisle (m)
d_a	distance between centres of two adjacent aisles (m)
d_o	distance from the operator's platform to the centre of a pallet or roll cage
v	the width of a picking- or cross-aisle (m)
d_e	Euclidian distance from the operator's platform to a pick location ($d_e = [d_o^2 + (0.5v)^2]^{1/2}$, m)
b_w	body weight (kg)
g	grade of the ground surface (%)
s_W	walking speed (m/s)
s_R	riding speed (m/s)
E_{st}	MEE for standing ($E_{st} = 0.023*b_w$, Kcal/min)
E_w	MEE for walking ($E_w = 0.01*[51+2.54*b_w+s_W^2+0.379*b_w*g*s_W]$, Kcal/min)
E_{sp}	MEE for stepping down/up from/onto the operator`s platform ($E_{sp} = 0.00285*b_w$, Kcal/step)
E_{pq}^W	total MEE for walking between pick locations p and q
E_{pq}^R	total MEE for riding between pick locations p and q

Decision Variables

w_{pq}	1, walking between pick locations p and q; 0, otherwise
r_{pq}	1, riding the truck between pick locations p and q; 0, otherwise
u_p	sequence of pick locations visited

3.2. Optimization Model

The optimization model can be stated as follows:

Minimize

$$\sum_{p\in P\cup\{0\}}\sum_{q\in P\cup\{0\}}\left[E_{pq}{}^{W}w_{pq}+E_{pq}{}^{R}r_{pq}\right] \tag{1}$$

Subject to:

$$\sum_{p\in P\cup\{0\}}\left[w_{pq}+r_{pq}\right]=1 \qquad \forall q\in P\cup\{0\} \tag{2}$$

$$\sum_{q\in P\cup\{0\}}\left[w_{pq}+r_{pq}\right]=1 \qquad \forall p\in P\cup\{0\} \tag{3}$$

$$u_p-u_q+\left(|P|+1\right)\left(w_{pq}+r_{pq}\right)\le|P| \qquad \forall p\in P,\forall q\ne p\in P \tag{4}$$

$$1<u_p<|P| \qquad \forall p\in P \tag{5}$$

$$w_{pq}\in\{0,1\} \qquad \forall p\in P\cup\{0\},\forall q\in P\cup\{0\} \tag{6}$$

$$r_{pq}\in\{0,1\} \qquad \forall p\in P\cup\{0\},\forall q\in P\cup\{0\} \tag{7}$$

$$u_p\in\mathbb{Z}^{+} \qquad \forall p\in P \tag{8}$$

Objective function (1) minimizes the MEE for each order-picking route by determining the best route and collaboration strategy. Constraint (2) enforces that there is exactly one arrival to one pick location from other pick locations. Constraint (3) ensures there is only one departure from a pick location. Constraints (4) and (5) force the optimization model to have a single route covering all pick locations [63]. Finally, binary restrictions on decision variables w_{pq}, r_{pq} are imposed, and the integrality of the decision variable u_p is ensured (Constraints 6-8).

3.3. Metabolic Energy Expenditure Calculations

This section provides an algorithm to calculate the MEE between pick locations p and q. As a result, it establishes an energy expenditure matrix that can be employed in the optimization model. Assuming the leftmost aisle is the first aisle, aisles are numbered sequentially through to the rightmost aisle from the reader's point of view and denoted by a_p or a_q. Similarly, we let l_p or l_q represent the distance of storage location p or q from the bottom of each picking aisle (namely, storage location number). Then, each pick location $p \in P$ or $q \in P$ can be identified by a tuple of $< a_p, l_p > \in \{a_0, a_1, \ldots, a_{|P|}\}$ x $\{l_0, l_1, \ldots, l_{|P|}\}$ or $< a_q, l_q > \in \{a_0, a_1, \ldots, a_{|P|}\}$ x $\{l_0, l_1, \ldots, l_{|P|}\}$. Note that $p = 0$ or $q = 0$ corresponds to the tuple of $< a_0, l_0 >$, representing the I/O point. Algorithm 1 is developed to calculate the MEE for walking or riding. Depending on the TOP, ROP, and COP, $E_{pq}{}^{W}$, $E_{pq}{}^{R}$ or min $[E_{pq}{}^{W}, E_{pq}{}^{R}]$ are used in calculations.

Algorithm 1. MEE Calculations for walking or riding.

for $p = 0{:}|P|$
  for $q = 0{:}|P|$
    if $p = q$ % no travel from pick location p to pick location q when $p = q$
      $E_{pq}{}^{W} = M$ and $E_{pq}{}^{R} = M$
    else if $p = 0$ % MEE from I/O point to any pick location
      $E_{pq}{}^{W} = (E_w + E_{st})\,[d_a\,(a_q - 1) + l_q + v] / (60 s_W)$ (for TOP);
      $E_{pq}{}^{W} = M$ (for COP);
      $E_{pq}{}^{R} = E_{st}\,[d_a\,(a_q - 1) + l_q + 0.5v] / (60 s_R) + E_{sp} / 2 + (E_w + E_{st})\,(d_e) / (60 s_W)$
    else if $q = 0$ % MEE from any pick location to I/O point
      $E_{pq}{}^{W} = (E_w + E_{st})\,[d_a\,(a_p - 1) + l_p + v] / (60 s_W)$

$E_{pq}^{W} = M$ (for COP);

$E_{pq}^{R} = E_{st}\,[d_a\,(a_p - 1) + l_p + 0.5v] / (60s_R) + E_{sp} / 2 + (E_w + E_{st})\,(d_o) / (60s_W)$

else if $a_p = a_q$ % MEE when picks p and q are in the same aisle

if $l_i = l_j$ % no MEE for picking multiple items from the same location

$E_{pq}^{W} = 0$ and $E_{pq}^{R} = 0$

else % MEE when picks p and q are in the same aisle, but in different locations

$E_{pq}^{W} = (E_w + E_{st})\,[|l_p - l_q| + v] / (60s_W)$ (for TOP);

$E_{pq}^{W} = (E_w + E_{st})\,\{[(l_p - l_q)^2 + (0.5v)^2]^{1/2} + 0.5v\} / (60s_W)$ (for COP);

$E_{pq}^{R} = E_{st}\,[|l_p - l_q|] / (60s_R) + E_{sp} + (E_w + E_{st})(0.5v + d_o + d_e) / (60s_W)$;

end

else if $a_p \neq a_q$ % travel distance when picks p and q are not in the same aisle

$E_{pq}^{W} = \min\{(E_w + E_{st})\,[2L - l_p - l_q + d_a\,|a_p - a_q| + 2v] / (60s_W),\ (E_w + E_{st})\,[l_p + l_q + d_a\,|a_p - a_q| + 2v] / (60s_W)\}$

$E_{pq}^{W} = M$ (for COP);

$E_{pq}^{R} = \min\{E_{st}\,[2L - l_p - l_q + d_a\,|a_p - a_q| + v] / (60s_R) + E_{sp} + (E_w + E_{st})\,(0.5v + d_o + d_e) / (60s_W),$

$E_{st}\,[l_p + l_q + d_a\,|a_p - a_q| + v] / (60s_R) + E_{sp} + (E_w + E_{st})\,(0.5v + d_o + d_e) / (60s_W)\}$

else % other cases

$E_{pq}^{W} = M$ and $E_{pq}^{R} = M$

end

end

end

3.4. Solution Approach

The optimization model is coded in MATLAB and solved by using Application Programming Interface (API) with Gurobi Optimizer version 9.5.2 build v9.5.2rc0 (win64). The model is run on 8GB RAM with a 3.60GHz Intel® Core™ i7-4790 processor. The time limit parameter is set to 7200 seconds (2 hours), and the solution performance is summarized in Table 1. As shown, increasing the pick list size increases the solution time. Moreover, the solution is not obtained in the given time frame for middle- and large-sized problems.

Table 1. Solution time (seconds).

	Samples										
List Size	**1**	**2**	**3**	**4**	**5**	**6**	**7**	**8**	**9**	**10**	**Avg (s)**
5	< 1	< 1	< 1	< 1	< 1	< 1	< 1	< 1	< 1	< 1	**< 1**
10	1	1	1	1	1	1	1	1	1	1	**1**
15	4	2	2	2	1	5	2	8	2	1	**3**
20	16	5	8	8	6	11	10	14	18	9	**11**
25	21	22	69	9	41	40	10	77	19	37	**34**
30	146	154	92	22	88	309	15	78	20	94	**102**
35	779	68	145	142	434	2019	755	4222	---	1818	---
40	449	1093	830	2614	1733	2598	820	2277	2635	394	**1544**
45	---	1285	2026	---	---	---	1676	---	1414	826	---
50	---	---	4763	---	---	---	---	1416	---	6639	---
55	---	---	---	---	---	---	---	3152	---	---	---

60-200	---	---	---	---	---	---	---	---	---	---	---

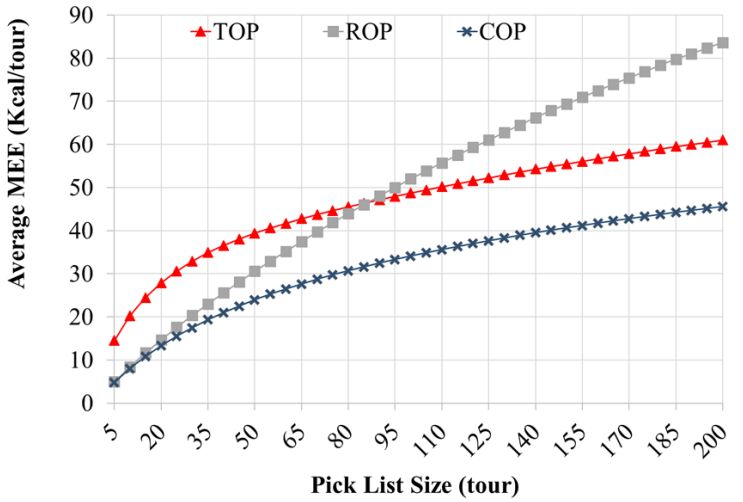

Fig. 4. Improvement in MEE for TOP, ROP, and COP.

Because of solution intractability for middle- and large-sized problems, we implement the dynamic programming approach proposed by Ratliff & Rosenthal [19]. The solution results given in the following section are generated by using the dynamic programming approach. The maximum solution time for any pick list size is less than one minute.

4. Computational Results

In this section, we compare the performances of TOP and ROP with COP for different pick list sizes. Based on actual warehouse dimensions, the following parameter values are used. There are 10 aisles, each with a length of 25 m. The width of a picking- or cross-aisle is 2.7m. Considering a pallet size of 1.2m, the distance between the centerlines of two adjacent picking aisles is 5.3m, including side-to-side clearance between pallets. The number of pick list sizes ranges from 5 picks to 200 picks, with an increase of 5. Therefore, 40 different pick list sizes are tested. The average walking and riding speeds are 0.7m/s and 2.5 m/s, respectively. Considering only one pallet or roll cage is attached to the truck, the distance from the operator's platform to the center of a pallet or roll cage is 1.1m. The body weight of the order-picker is assumed to be 80 kg.

We use Monte Carlo simulation to randomly generate aisle and storage location numbers of pick locations ($< a_p, l_p >$). We replicate the solution 1000 times for each pick list size and take the average to generate Fig. 4. Note that each pick list is used three times to solve problems for TOP, ROP, and COP.

As shown in Fig. 4, COP outperforms TOP and ROP regardless of the pick list size. The relative MEE improvement of COP over TOP ranges between 33.7% and 199.6%, with an average value of 57.1%. Similarly, the relative improvement of COP over ROP varies between 1.9% and 83.2%, with an average value of 49.1%. Depending on the pick list size, ROP and TOP perform better than the other. With the given parameter values, ROP and TOP perform similarly when the pick list size varies between 85 and 90. TOP performs poorly for pick lists with fewer than 85 pick locations, whereas ROP performs well for small pick list sizes. Therefore, walking between rare pick locations or riding the truck with frequent stops leads to more MEE.

5. Conclusion and Recommendations

This paper investigates the metabolic energy expenditure of traditional, ride-on, and collaborative order picking. In traditional order picking, the order picker walks around racks in a warehouse throughout the day. Allowing the order picker to stand on an operator's platform of an order-picking truck, the order picker rides the truck between stop locations in ride-on order picking. However, the order picker must step down from the platform at each stop location and step up onto the platform before riding the truck to the next stop location. Taking advantage of both traditional and ride-on order picking, the order picker can switch between walking along and riding the truck in collaborative order picking. Therefore, further research is required to investigate the trade-off between walking and riding in terms of metabolic energy expenditure, as prolonged walking or frequent stepping down/up from/onto the truck can be associated with high metabolic energy expenditure.

We develop an optimization model to minimize the metabolic energy expenditure in collaborative order picking by finding the shortest route with the best collaboration decision (walk or ride). Moreover, we proposed an algorithm to calculate the metabolic energy expenditure between pick locations. Note that the algorithm is developed for the particular design provided. If different layout configurations are used, it will need to be adjusted accordingly. Comparing collaborative order picking with traditional and ride-on order picking, our results show a significant saving in metabolic energy expenditure. The traditional order picking is useful for large pick list sizes with frequent stops, whereas the ride-on order picking is beneficial for small-sized pick lists.

In this paper, we investigate a traditional warehouse layout. Non-traditional layouts can also be explored. Different routing or storage policies can also be investigated. The suggested algorithm is designed for a single-block layout. An algorithm tailored for two- or multi-block designs can be developed separately. Consideration of various shape factors (width-to-depth ratio) may lead to more metabolic energy savings.

Acknowledgements

This work is supported by The Scientific and Technological Research Council of Türkiye [grant number: 1059B191900637]. Special thanks to Dr. René De Koster for generously sharing valuable information on the Collaborative Order Picking system examined within the scope of this study. I would also like to extend my appreciation to the referees whose valuable suggestions contributed to the improvement of this article.

References

[1] E. H. Grosse, C. H. Glock, M. Y. Jaber, and W. P. Neumann, "Incorporating human factors in order picking planning models: framework and research opportunities," *Int. J. Prod. Res.*, vol. 53, no. 3, pp. 695–717, Feb. 2015, doi: 10.1080/00207543.2014.919424.

[2] J. A. Tompkins, J. A. White, Y. A. Bozer, and J. M. A. Tanchoco, *Facilities planning*, 4th ed. New York, NY: John Wiley & Sons, 2010.

[3] K. Azadeh, R. De Koster, and D. Roy, "Robotized and Automated Warehouse Systems: Review and Recent Developments," *Transp. Sci.*, vol. 53, no. 4, pp. 917–945, Jul. 2019, doi: 10.1287/trsc.2018.0873.

[4] Y. Jaghbeer, R. Hanson, and M. I. Johansson, "Automated order picking systems and the links between design and performance: a systematic literature review," *Int. J. Prod. Res.*, vol. 58, no. 15, pp. 4489–4505, Aug. 2020, doi: 10.1080/00207543.2020.1788734.

[5] R. De Koster, T. Le-Duc, and K. J. Roodbergen, "Design and control of warehouse order picking: A literature review," *Eur. J. Oper. Res.*, vol. 182, no. 2, pp. 481–501, Oct. 2007, doi: 10.1016/j.ejor.2006.07.009.

[6] M. Masae, C. H. Glock, and E. H. Grosse, "Order picker routing in warehouses: A systematic literature review," *Int. J. Prod. Econ.*, vol. 224, p. 107564, 2020, doi: 10.1016/j.ijpe.2019.107564.

[7] B. Gajšek, G. Đukić, T. Opetuk, and H. Cajner, "Human in Manual Order Picking Systems," in *Ćosić P. (ed.)*

Management of Technology – Step to Sustainable Production (MOTSP) conference proceedings, 2017, pp. 5–17.
[8] A. Otto, N. Boysen, A. Scholl, and R. Walter, "Ergonomic workplace design in the fast pick area," *OR Spectr.*, vol. 39, no. 4, pp. 945–975, Oct. 2017, doi: 10.1007/s00291-017-0479-x.
[9] S. Vanheusden, T. van Gils, K. Ramaekers, T. Cornelissens, and A. Caris, "Practical factors in order picking planning: state-of-the-art classification and review," *Int. J. Prod. Res.*, pp. 1–25, Apr. 2022, doi: 10.1080/00207543.2022.2053223.
[10] T. De Lombaert, K. Braekers, R. De Koster, and K. Ramaekers, "In pursuit of humanised order picking planning: methodological review, literature classification and input from practice," *Int. J. Prod. Res.*, pp. 1–31, Jun. 2022, doi: 10.1080/00207543.2022.2079437.
[11] E. Schneider, X. Irastorza, S. Copsey, M. Verjans, L. Eeckelaert, and V. De Broeck, "OSH in Figures: Work-related Musculoskeletal Disorders in the EU — Facts and Figures," European Agency for Safety and Health Work, Luxembourg, 2010. [Online]. Available: https://osha.europa.eu/en/publications/osh-figures-work-related-musculoskeletal-disorders-eu-facts-and-figures.
[12] M. Napolitano, "2012 warehouse/DC operations survey: Mixed signals," *Modern Materials Handling Logistics Management*, vol. 51, no. 11, pp. 48–56, 2012.
[13] E. H. Grosse, C. H. Glock, and W. P. Neumann, "Human factors in order picking system design: A content analysis," *IFAC-PapersOnLine*, vol. 28, no. 3, pp. 320–325, 2015, doi: 10.1016/j.ifacol.2015.06.101.
[14] A. J. Chambers, J. M. Haney, T. Huppert, and M. S. Redfern, "The Effect of Prolonged Walking With Intermittent Standing on Erector Spinae and Soleus Muscle Oxygenation and Discomfort.," *J. Sports Sci. Med.*, vol. 18, no. 2, pp. 337–343, Jun. 2019.
[15] Crown Equipment Corporation, "Crown QuickPick™ Remote: [Order Picking Technology]: Productivity. Motivation. Safety," *Order Picking Technology | QuickPick Remote | Crown Lift Trucks UK*, 2013. https://www.crown.com/uk/forklifts/pdfs/brochures/order-picker-quickpick-remote-brochure-GB.pdf.
[16] Toyota Material Handling, "Prolift," 2022. https://www.prolifttoyota.com/new-equipment/electric-walkie-pallet-jack/.
[17] B. Harfmann, "Carts, hand trucks indispensable in last mile delivery," *BNP Media*, 2022.
[18] Still, "Order Picker OPX 20-25 Thrillingly dynamic," 2022. https://www.still-forklift.is/trucks/new-trucks/order-pickers/opx-20-25.html.
[19] H. D. Ratliff and A. S. Rosenthal, "Order-Picking in a Rectangular Warehouse: a Solvable Case of the Traveling Salesman Problem.," *Oper. Res.*, vol. 31, no. 3, pp. 507–521, 1983, doi: 10.1287/opre.31.3.507.
[20] E. H. Grosse, C. H. Glock, and W. P. Neumann, "Human factors in order picking: a content analysis of the literature," *Int. J. Prod. Res.*, vol. 55, no. 5, pp. 1260–1276, Mar. 2017, doi: 10.1080/00207543.2016.1186296.
[21] M. Abdoli-Eramaki, J. M. Stevenson, M. J. Agnew, and A. Kamalzadeh, "Comparison of 3D dynamic virtual model to link segment model for estimation of net L4/L5 reaction moments during lifting," *Comput. Methods Biomech. Biomed. Engin.*, vol. 12, no. 2, pp. 227–237, Apr. 2009, doi: 10.1080/10255840802434233.
[22] D. B. Chaffin, G. D. Herrin, W. M. Keyserling, and A. Garg, "A method for evaluating the biomechanical stresses resulting from manual materials handling jobs," *Am. Ind. Hyg. Assoc. J.*, vol. 38, no. 12, pp. 662–675, Dec. 1977, doi: 10.1080/0002889778507678.
[23] A. Garg, D. B. Chaffin, and G. D. Herrin, "Prediction of metabolic rates for manual materials handling jobs," *Am. Ind. Hyg. Assoc. J.*, vol. 39, no. 8, pp. 661–674, Aug. 1978, doi: 10.1080/0002889778507831.
[24] R. R. Bishu, B. Donohue, and P. Murphy, "Cognitive ergonomics of a mail order filling company: Part 2 — influence of shelf coding and address information on acquisition time," *Appl. Ergon.*, vol. 23, no. 2, pp. 115–120, Apr. 1992, doi: 10.1016/0003-6870(92)90083-8.
[25] R. Kadefors and M. Forsman, "Ergonomic evaluation of complex work: a participative approach employing video–computer interaction, exemplified in a study of order picking," *Int. J. Ind. Ergon.*, vol. 25, no. 4, pp. 435–445, May 2000, doi: 10.1016/S0169-8141(99)00042-6.
[26] J. Marvel, R. Shell, and G. Weckman, "An application of heuristic algorithms for determining inventory location in a distribution warehouse," *Int. J. Ind. Eng. Theory, Appl. Pract.*, vol. 8, pp. 5–15, 2001.
[27] M. Christmansson *et al.*, "A case study of a principally new way of materials kitting—an evaluation of time

consumption and physical workload," *Int. J. Ind. Ergon.*, vol. 30, no. 1, pp. 49–65, Jul. 2002, doi: 10.1016/S0169-8141(02)00077-X.
[28] J. J. Saleem, B. M. Kleiner, and M. A. Nussbaum, "Empirical evaluation of training and a work analysis tool for participatory ergonomics," *Int. J. Ind. Ergon.*, vol. 31, no. 6, pp. 387–396, Jun. 2003, doi: 10.1016/S0169-8141(03)00024-6.
[29] M. Jorgensen, W. Marras, W. G. Allread, and C. Stuart-Buttle, "Grocery distribution centers," in *Interventions, Controls, and Applications in Occupational Ergonomics*, 2006.
[30] B. Ryan and C. M. Haslegrave, "Use of concurrent and retrospective verbal protocols to investigate workers' thoughts during a manual-handling task," *Appl. Ergon.*, vol. 38, no. 2, pp. 177–190, Mar. 2007, doi: 10.1016/j.apergo.2006.03.003.
[31] E. J. Lodree, C. D. Geiger, and X. Jiang, "Taxonomy for integrating scheduling theory and human factors: Review and research opportunities," *Int. J. Ind. Ergon.*, vol. 39, no. 1, pp. 39–51, Jan. 2009, doi: 10.1016/j.ergon.2008.05.001.
[32] C. Harris-Adamson and J.-H. Lin, "Effect of Handle Design on Pallet Jack Operations," *Ergon. Des. Q. Hum. Factors Appl.*, vol. 21, no. 2, pp. 15–21, Apr. 2013, doi: 10.1177/1064804613479122.
[33] E. H. Grosse and C. H. Glock, "An experimental investigation of learning effects in order picking systems," *J. Manuf. Technol. Manag.*, vol. 24, no. 6, pp. 850–872, Jul. 2013, doi: 10.1108/JMTM-03-2012-0036.
[34] R. Könemann, T. Bosch, I. Kingma, J. H. Van Dieën, and M. P. De Looze, "Effect of horizontal pick and place locations on shoulder kinematics," *Ergonomics*, vol. 58, no. 2, pp. 195–207, Feb. 2015, doi: 10.1080/00140139.2014.968636.
[35] E. H. Grosse, S. M. Dixon, W. P. Neumann, and C. H. Glock, "Using qualitative interviewing to examine human factors in warehouse order picking: technical note," *Int. J. Logist. Syst. Manag.*, vol. 23, no. 4, p. 499, 2016, doi: 10.1504/IJLSM.2016.075211.
[36] D. Battini, C. H. Glock, E. H. Grosse, A. Persona, and F. Sgarbossa, "Human energy expenditure in order picking storage assignment: A bi-objective method," *Comput. Ind. Eng.*, vol. 94, pp. 147–157, Apr. 2016, doi: 10.1016/j.cie.2016.01.020.
[37] O. Al Araidah, D. Dalalah, N. A. Ma', en A. A. Azeez, and M. T. Khasawneh, "A heuristic for clustering and picking small items considering safe reach of the order picker," *Eur. J. Ind. Eng.*, vol. 11, no. 2, p. 256, 2017, doi: 10.1504/EJIE.2017.083256.
[38] D. Battini, M. Calzavara, A. Persona, and F. Sgarbossa, "Additional effort estimation due to ergonomic conditions in order picking systems," *Int. J. Prod. Res.*, vol. 55, no. 10, pp. 2764–2774, May 2017, doi: 10.1080/00207543.2016.1190879.
[39] M. Calzavara, C. H. Glock, E. H. Grosse, A. Persona, and F. Sgarbossa, "Analysis of economic and ergonomic performance measures of different rack layouts in an order picking warehouse," *Comput. Ind. Eng.*, vol. 111, pp. 527–536, Sep. 2017, doi: 10.1016/j.cie.2016.07.001.
[40] R. Hanson, L. Medbo, C. Berlin, and J. Hansson, "Manual picking from flat and tilted pallet containers," *Int. J. Ind. Ergon.*, vol. 64, pp. 199–212, Mar. 2018, doi: 10.1016/j.ergon.2017.07.001.
[41] C. Nair, K. Tsiopanos, R. Martin, and G. Marshall, "Increasing Warehouse Productivity With an Ergonomic Handheld Scanner," *Ergon. Des. Q. Hum. Factors Appl.*, vol. 26, no. 3, pp. 23–31, Jul. 2018, doi: 10.1177/1064804618757281.
[42] C. H. Glock, E. H. Grosse, H. Abedinnia, and S. Emde, "An integrated model to improve ergonomic and economic performance in order picking by rotating pallets," *Eur. J. Oper. Res.*, vol. 273, no. 2, pp. 516–534, Mar. 2019, doi: 10.1016/j.ejor.2018.08.015.
[43] S. Kim, M. A. Nussbaum, and J. L. Gabbard, "Influences of augmented reality head-worn display type and user interface design on performance and usability in simulated warehouse order picking," *Appl. Ergon.*, vol. 74, pp. 186–193, Jan. 2019, doi: 10.1016/j.apergo.2018.08.026.
[44] M. Calzavara, C. H. Glock, E. H. Grosse, and F. Sgarbossa, "An integrated storage assignment method for manual order picking warehouses considering cost, workload and posture," *Int. J. Prod. Res.*, vol. 57, no. 8, pp. 2392–2408, Apr. 2019, doi: 10.1080/00207543.2018.1518609.

[45] H. Diefenbach and C. H. Glock, "Ergonomic and economic optimization of layout and item assignment of a U-shaped order picking zone," *Comput. Ind. Eng.*, vol. 138, p. 106094, Dec. 2019, doi: 10.1016/j.cie.2019.106094.
[46] B. Gajšek, G. Đukić, M. Butlewski, T. Opetuk, H. Cajner, and S. M. Kač, "The impact of the applied technology on health and productivity in manual 'picker-to-part' systems," *Work*, vol. 65, no. 3, pp. 525–536, Mar. 2020, doi: 10.3233/WOR-203107.
[47] T. Hara, Y. Li, J. Ota, and T. Arai, "Automatic risk assessment integrated with activity segmentation in the order picking process to support health management," *CIRP Ann.*, vol. 69, no. 1, pp. 17–20, 2020, doi: 10.1016/j.cirp.2020.04.011.
[48] J. A. Lee, Y. S. Chang, and W. Karwowski, "Assessment of working postures and physical loading in advanced order picking tasks: A case study of human interaction with automated warehouse goods-to-picker systems," *Work*, vol. 67, no. 4, pp. 855–866, Dec. 2020, doi: 10.3233/WOR-203337.
[49] C. M. Lind *et al.*, "Reducing postural load in order picking through a smart workwear system using real-time vibrotactile feedback," *Appl. Ergon.*, vol. 89, p. 103188, Nov. 2020, doi: 10.1016/j.apergo.2020.103188.
[50] H. Lager, A. Virgillito, and T.-P. Buchberger, "Digitalization of Logistics Work: Ergonomic Improvements Versus Work Intensification," 2021, pp. 33–53.
[51] X. Feng and X. Hu, "A Heuristic Solution Approach to Order Batching and Sequencing for Manual Picking and Packing Lines considering Fatiguing Effect," *Sci. Program.*, vol. 2021, pp. 1–17, Apr. 2021, doi: 10.1155/2021/8863391.
[52] A. Setayesh, E. H. Grosse, C. H. Glock, and W. P. Neumann, "Determining the source of human-system errors in manual order picking with respect to human factors," *Int. J. Prod. Res.*, pp. 1–23, Nov. 2021, doi: 10.1080/00207543.2021.1991022.
[53] B. Gajšek, S. Šinko, T. Kramberger, M. Butlewski, E. Özceylan, and G. Đukić, "Towards Productive and Ergonomic Order Picking: Multi-Objective Modeling Approach," *Appl. Sci.*, vol. 11, no. 9, p. 4179, May 2021, doi: 10.3390/app11094179.
[54] F. Niemann, S. Lüdtke, C. Bartelt, and M. ten Hompel, "Context-Aware Human Activity Recognition in Industrial Processes," *Sensors*, vol. 22, no. 1, p. 134, Dec. 2021, doi: 10.3390/s22010134.
[55] F. Vitolo, A. Rega, C. Di Marino, A. Pasquariello, A. Zanella, and S. Patalano, "Mobile Robots and Cobots Integration: A Preliminary Design of a Mechatronic Interface by Using MBSE Approach," *Appl. Sci.*, vol. 12, no. 1, p. 419, Jan. 2022, doi: 10.3390/app12010419.
[56] S. R. Lamooki, L. A. Cavuoto, and J. Kang, "Adjustments in Shoulder and Back Kinematics during Repetitive Palletizing Tasks," *Sensors*, vol. 22, no. 15, p. 5655, Jul. 2022, doi: 10.3390/s22155655.
[57] V. Kapou, S. T. Ponis, G. Plakas, and E. Aretoulaki, "An Innovative Layout Design and Storage Assignment Method for Manual Order Picking with Respect to Ergonomic Criteria," *Logistics*, vol. 6, no. 4, p. 83, Dec. 2022, doi: 10.3390/logistics6040083.
[58] Y. S. Zhao, M. H. Jaafar, A. S. A. Mohamed, N. Z. Azraai, and N. Amil, "Ergonomics Risk Assessment for Manual Material Handling of Warehouse Activities Involving High Shelf and Low Shelf Binning Processes: Application of Marker-Based Motion Capture," *Sustainability*, vol. 14, no. 10, p. 5767, May 2022, doi: 10.3390/su14105767.
[59] A. M. Adhaye and D. A. Jolhe, "Ergonomic assessment for designing manual material handling tasks at a food warehouse in India: A case study," *Hum. Factors Ergon. Manuf. Serv. Ind.*, Jun. 2023, doi: 10.1002/hfm.21004.
[60] R. Bezzini, L. Crosato, M. Teppati Losè, C. A. Avizzano, M. Bergamasco, and A. Filippeschi, "Closed-Chain Inverse Dynamics for the Biomechanical Analysis of Manual Material Handling Tasks through a Deep Learning Assisted Wearable Sensor Network," *Sensors*, vol. 23, no. 13, p. 5885, Jun. 2023, doi: 10.3390/s23135885.
[61] L. Schrøder Jakobsen, M. de Zee, A. Samani, K. Desbrosses, and P. Madeleine, "Biomechanical changes, acceptance, and usability of a passive shoulder exoskeleton in manual material handling. A field study," *Appl. Ergon.*, vol. 113, p. 104104, Nov. 2023, doi: 10.1016/j.apergo.2023.104104.
[62] D. R. Bassett, J. A. Vachon, A. O. Kirkland, E. T. Howley, G. E. Duncan, and K. R. Johnson, "Energy cost of stair climbing and descending on the college alumnus questionnaire," *Med. Sci. Sport. Exerc.*, vol. 29, no. 9, 1997, [Online]. Available: https://journals.lww.com/acsm-

msse/Fulltext/1997/09000/Energy_cost_of_stair_climbing_and_descending_on.19.aspx.
[63] C. E. Miller, R. A. Zemlin, A. W. Tucker, and R. A. Zemlin, "Integer Programming Formulation of Traveling Salesman Problems," *J. ACM*, vol. 7, no. 4, pp. 326–329, Oct. 1960, doi: 10.1145/321043.321046.

Contents lists available at *Dergipark*

Journal of Scientific Reports-A

journal homepage: *https://dergipark.org.tr/tr/pub/jsr-a*

E-ISSN: 2687-6167 ***Number 55, December 2023***

RESEARCH ARTICLE

Receive Date: 27.07.2023 *Accepted Date: 16.10.2023*

Investigation of low-cycle fatigue in adhesively-bonded single-lap joints

Gamze İspirlioğlu-Kara[1,*] , Adnan Özel[2]

[a*] *Ataturk University, Faculty of Engineering, Department of Mechanical Engineering, Erzurum and 25240, Turkey, ORCID: 0000-0001-9968-1739*

[b] *Erzincan Binali Yıldırım University, Faculty of Engineering, Department of Mechanical Engineering, Erzincan and 24002,Turkey, ORCID: 0000-0001-8527-3136*

Abstract

The benefits of adhesively bonded joints (ABJs), including their high strength, even stress distribution, and excellent fatigue resistance, make them a viable substitute for traditional mechanical joining techniques like bolts, rivets, welding, and soldering. In industries like aerospace and aviation where weight is a major consideration, these adhesively bonded parts are becoming increasingly significant. ABJs are preferred because they offer highly reliable connections. This work used both experimental and numerical methods to examine the low cycle fatigue of materials built as adhesively-bonded single-lap joints. It is aimed to carry out this study to expand the area of use in areas where weight is critical, such as the aerospace industry. The joints of aluminum and steel specimens were subjected to variable loads with mean failure loads lower than the failure loads obtained experimentally and the number of cycles was determined. As a result, the fatigue life of adhesively bonded single-lap stainless-steel joints was higher than that of aluminum specimens. Additionally, the fatigue life of the steel specimens was found to be greatly extended by putting glue around the joint's endpoints. The fatigue strength increased with increasing adhesive thickness based on test and investigation results. It was also found that pre-filled, ABJs increase the low cycle fatigue strength.

Keywords: Adhesive; Low-cycle fatigue; Adhesively bonded single-lap joints

* Corresponding author. Tel.: +0-553-618-29-69.
E-mail address: gamze.ispirlioglu@atauni.edu.tr
https://orcid.org/0000-0001-9968-1739

1. Introduction

Adhesives are polymeric materials that bind materials to the surface to which they are applied, preventing them from separating. Adhesives are made by combining different materials, and any kind of material can be bonded together with an adhesive. Adhesively bonded joints (ABJs) have been studied for many years. While adhesives were regarded in the early studies as linear elastic materials, the elastoplastic properties of adhesives were also considered in later studies.

ABJs perform poorly against peel stresses despite having good shear characteristics. Eccentric loading in ABJs causes peeling strains in the overlap area, which can lead to damage. Numerous research has attempted to lessen the impacts of peel stresses [1] by creating a variety of strategies, such as altering the geometry of the lap and joint [2], employing scarf joints [3], utilizing composite [4] or curved [5,6] patches in the joints, and creating an adhesive fillet [7].

Sayman et al. conducted an analytical nonlinear elastoplastic stress analysis for an adhesively attached single-acting joint in a different investigation. The impact of the bending moment was disregarded in this investigation. The finite element method (FEM) and the analytical solution were compared, and it was discovered that the outcomes were consistent. According to all of these investigations, the shear and normal stresses have a maximum value at the ends and are constant along the overlap region's center. Because of this, the high strains at the adhesive layer's ends have become increasingly significant in later research, and this phenomenon is frequently referred to as end effects [8].

The failure load of ABJs is significantly influenced by the thickness of the adhesives used in the joining process. As a result, a statistical investigation was conducted to determine how adherend thickness affected the joints' failure load [9–12].

Sawa et al.'s study [13] focused on single-lap joints (SLJs) that integrate adherents from several material kinds. Stress values were reported to be higher in materials having a low modulus of elasticity, and stress accumulation was seen to have occurred close to the interface edges. It was also determined that tension rose when adherend and adhesive thickness dropped.

Gleich et al. [14] varied the adhesive's thickness between 0.1 and 0.5 mm to examine the relationship between the maximum load the joint can support and the thickness. According to the analyses, joint strength rose as adhesive thickness increased. Nonetheless, the study emphasized that stress rises when adhesive thickness falls and vice versa.

The effect of adhesive thickness on adhesion in metal connections was examined by Xu et al. [15] using the "Cohesive Zone Model." The study's findings indicated that as adhesive thickness increases, binding strength falls.

ABJs are subjected to more than just static loads, much like any other conventional joint. Because of the influences of the environment, they are also frequently exposed to dynamic loads. Consequently, it is critical to look at fatigue behaviors. Adhesives enhance the fatigue characteristics of joints by enabling extremely light joints. ABJs are frequently utilized in engineering domains because of the many benefits they provide, the most significant of which is the improvement of fatigue behavior. Several research that looked at the fatigue performance of ABJs could be found in the literature [16–23].

Using DP460 and Al2024-T3 adhesives, Gavgali et al. conducted an experimental and numerical investigation of the static and fatigue strength of SLJs and three-step lap joints. Their investigation revealed that the connection's static and fatigue strengths were raised by the gradual overlap application. The conclusion is that the outcomes of the numerical and experimental studies corroborate one another [18].

Braga et al. compared the fatigue performance of AA2024-T3 Al-Mg-Cu alloy SLJs with ABJs formed with friction stir welding and reported that the latter had superior fatigue strength [24].

In another study, Bayramoğlu et al. investigated the impact of adhesive stresses on material thickness and overlap length using the cohesive zone model and the multilinear isotropic hardening model. The comparison of numerical data with the experimental results revealed that the cohesive zone model was more compatible. The multilinear

isotropic hardening model and the adhesive zone model differ by 7% in terms of the damage load on the adhesive and 32% in terms of displacement, respectively [25].

Hacısalihoğlu et al. examined the strength of SLJs made in the bonded material by indenting it in two and three stages with varying thicknesses and lengths. The strength of the joint was enhanced by about 33 to 40 percent by notching and recessing the joints in two or three steps [26].

The tension-tension fatigue behavior of double-lap fiber-reinforced polymer (FRP) joints joined by a ductile adhesive was experimentally studied by Liu et al. [27]. Despite the ductile adhesive's rubbery nature at both ambient and high temperatures, the investigation revealed that the joints exhibited notable sensitivity to loading rate and temperature.

Tan et al. [28] formed thick adhesive shear joints (TASJs) with Sikaflex®-265 polyurethane glue and aluminum and its alloys to investigate the impact of the transition temperature on the adhesive structure's fatigue performance. After noting that the fatigue performance of SLJs progressively declined as the temperature rose, it was determined that temperature did affect the fatigue performance of SLJs. The fatigue performance declines with increasing temperature as it approaches the adhesive's transition temperature.

Experimental research was done on the lives of AA2024-T3 aluminum alloy SLJs made with DP460 adhesive placed at five different adhesive thicknesses under various tensile fatigue loads [29–31]. The investigation showed that as adhesive thickness increased, so did the joints' static tensile strength.

In contrast to previous research published in the literature, this study uses pre-filled steel, aluminum, and steel samples with the same adhesive thickness to investigate low-cycle fatigue in SLJs. To find the load at which steel samples break, tensile tests were performed on them initially with varying adhesive thicknesses. The low-cycle values at which the steel and aluminum samples failed were then ascertained [32] by applying various percentages of the failure load, such as 50% or higher, by the ASTM standard. Ten hertz (Hz) loading rates (R = 0 were used for the fatigue tests.

2. Experimental Procedure

2.1. Material and Samples

The study was schemed by a sequential algorithm (Fig. 1) within the framework of the relevant ASTM and ISO standards. First of all, the samples were cut to the determined dimensions, and necessary surface treatments were performed. Then, the bonding of the adherents was made to form SLJs. A low-cycle fatigue test was performed on the joints. The FEM studies carried out in ANSYS were compared with the experimental test results.

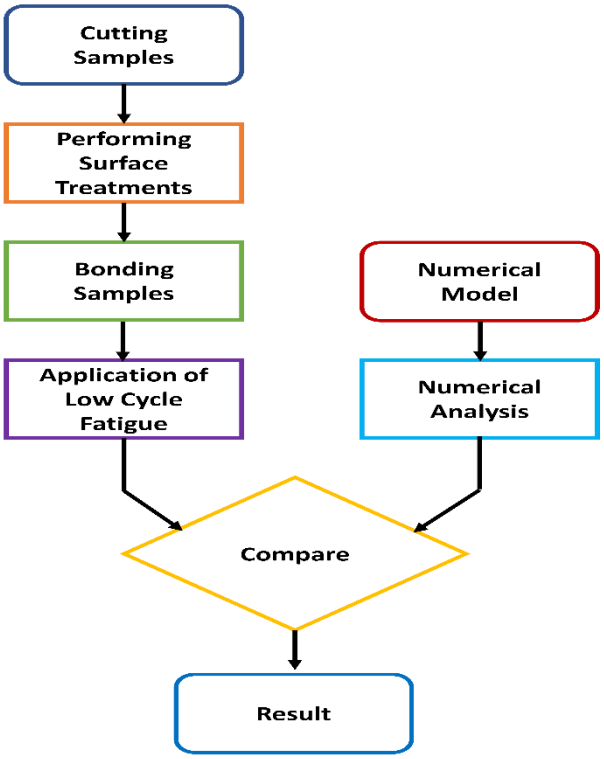

Fig. 1. General schematic of the experimental procedure followed in the study.

In this work, adherents that is, materials to be adhesively bonded were 7075-T7 aluminum alloy and AISI 304 stainless steel. The adhesive utilized in the investigation was 3M brand DP 460, a two-component, liquid epoxy structural adhesive. The joints were kept at 60°C for 120 minutes as per the manufacturer's recommended curing method, which was scrupulously followed. Table 1 displays the samples' and adhesive's mechanical characteristics [6,33].

Table 1. Mechanical properties of samples and adhesive [6,33]

Material	Modulus of Elasticity (MPa)	Poisson Ratio
Aluminum (7075-T7)	73.293	0.33
Steel (AISI 304)	180,000	0.29
Adhesive (DP 460)	2,077	0.38

Samples were cut from aluminum and steel materials in 25x100x5mm dimensions, as shown in Fig. 2(a), and necessary surface treatments were performed to prepare the samples for joining, as seen in Fig. 2(b).

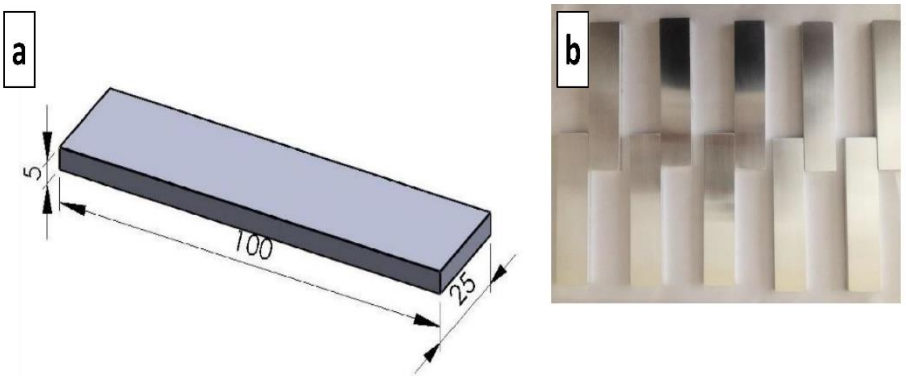

Fig. 2. (a) Sample model; (b) samples after surface preparation processes.

Regarding the strength of the adhesive union, the surfaces that need to be bonded must be properly prepared. The following procedures, in order, were part of the surface preparation process: Sanding papers with a grit of 80 to 1200 was used to deburr and sand the samples. The samples were then cleaned, rinsed, and stored in an acetone bath before being oven-dried. Fig. 2(b) displays the samples that have undergone all surface preparation procedures and are prepared for joining.

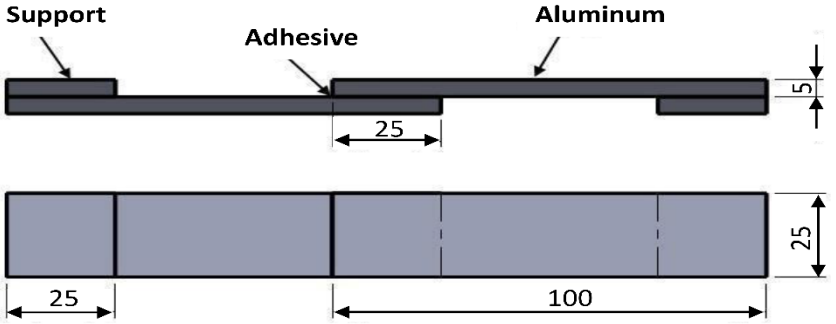

Fig. 3. Dimension and joining details of the adhesively bonded SLJs.

25x100x5mm-sized aluminum and steel samples were adhesively bonded as shown in Fig. 3, with an overlap length of 25mm, and with two pieces of 25x25x5mm-sized supports placed beside the respective ends of each adhered to make sure that the specimens are free from any eccentricity that might occur, as well as eliminating the effects of such eccentricity on the results of the tensile tests.

ISO 15166-1 standard includes issues related to the preparation of bulk samples. This standard specifies the rules to be followed in the preparation of bulk samples from one-component and two-component adhesives. By this standard, bulk samples are prepared from two-component liquid adhesive 3M™ DP 460. For this purpose, a mold consisting of two plates of a certain thickness and a frame placed between them to adjust the thickness of the adhesive layer is used. 3M™ DP 460 liquid adhesive is poured into this mold and pressure is applied using a plate on the mold to bring the adhesive to the desired thickness. After this process, the mold is placed in an oven at 60 °C for 120 minutes, and the necessary curing conditions are applied. Thus, 3M™ DP 460 bulk specimens are produced. To adjust the specimen thickness, a metal U frame with a thickness of 2 mm is prepared and placed on the lower table of the press. Silicone lubricant is sprayed onto the upper and lower tables of the press and the U frame to form

a very thin film. Thus, the adhesion of the bulk adhesive layers on the tables is prevented. The upper table of the press is pressurized until it is fully seated on the U frame and the specimens reach the desired thickness. Thus, the pressure required for the adhesive to cure is applied and the formation of air bubbles is prevented.

Two distinct adhesive thicknesses, 0.1 mm, and 0.2 mm, were tested with the steel samples in the study, while the adhesive thickness of the aluminum and pre-filled steel samples was 0.1 mm. Table 2 presents the classification of the various joints utilized in the trials.

Table 2. Joint types used in the experiment

Material	Type	Remarks
Aluminum	Type I	Aluminum bonded with 0.1mm adhesive thickness
Steel	Type II-a	Steel bonded with 0.1 mm adhesive thickness
Steel	Type II-b	Pre-filled steel bonded with 0.1 mm adhesive thickness
Steel	Type II-c	Steel bonded with 0.2 mm adhesive thickness

To prevent adhesion problems and to enable the connections to form properly, a mold made of AISI 4140 steel was used in the assembly of the joints and during the curing period, as shown in Fig. 4.

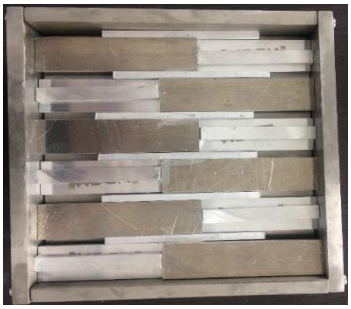

Fig. 4. Assembly of joints in the mold.

The assembly mold consisted of four parts: the lower table, the upper table, the frame, and the supports. The frame of the mold is detachable to allow the samples to be removed from the mold easily. The upper table was designed to ensure proper bonding by applying pressure onto the joints during the curing period of the adhesive. Samples were prevented from bonding to one another using intermediate supports. The upper table of the mold was sealed after the glue was applied and the adherents were joined. The mold was then placed in an oven set to 60°C for two hours to allow the adhesive to dry. The samples were taken out of the oven and let to stand at room temperature for a full day before the studies began, allowing the glue to cure.

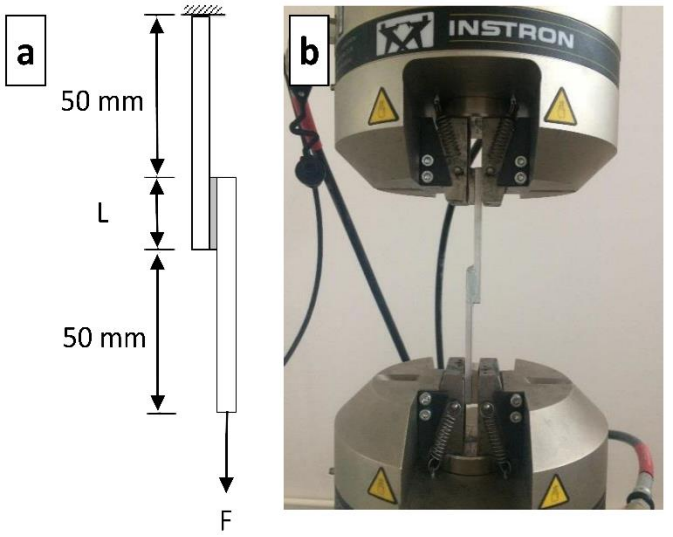

Fig. 5. (a) Boundary conditions and loads used in the tensile test and; (b) tensile loading.

Tensile testing of SLJs specimens was performed on an Instron 8801 fatigue testing system, shown in Fig. 5. All experiments were carried out at room temperature with a jaw speed of 1 mm/min until breakage.

2.2. Elastoplastic finite element analysis

Aluminum and steel joints used in the experiments, bonded with 3MTM DP460 adhesive, were modeled in 2-dimensions under tensile load using ANSYS by the Multilinear Isotropic Hardening-von Mises Plasticity (MISO) material model, assuming plane strain conditions. This was done for elastoplastic finite element analysis (FEA). The loads, boundary conditions, and sample dimensions utilized in FEA are also utilized in experimental investigations. The bonding joint was modeled in the three-dimensional analysis utilizing elements (Solid 186), which had 20 nodal points and three degrees of freedom. Bonding divides the overlay region where the operation is conducted into smaller parts, which is crucial for stress distribution.

After the tensile test, the breaking zone was examined, and the maximum load and failure modes that occurred on the samples were recorded. Boundary conditions and mesh details of the FEM applied are shown in Fig. 6.

(a)

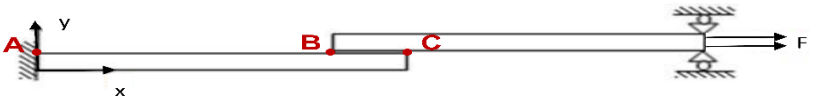

(b)

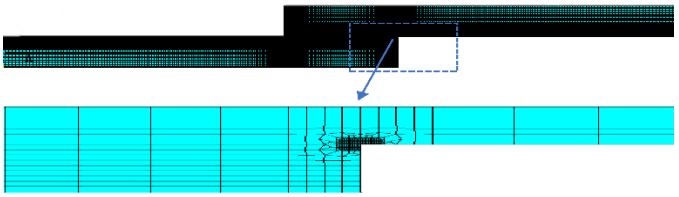

Fig. 6. (a) Boundary conditions and; (b) mesh detail of the FEM applied.

The stresses occurring in the adhesive along the BC line and in the bonded material along the AC line were considered in the analyses. The normal stresses (σ_x, σ_z), peel stresses (σ_y), shear stresses (τ_{xy}), displacements in the direction of the y-axis (U_y) and von Mises stresses along the BC line were computed and the effects of these stresses on the joint strength were investigated. Joint types, listed in Table 2, were evaluated comparatively.

3. Results and discussion

3.1. Experimental results obtained from samples subjected to tensile load

Adhesively bonded SLJs of aluminum and steel samples were subjected to the tensile test to determine the load under which they broke. Each experiment was repeated 5 times, and the average failure load was calculated and compared for each joint type [30,31]. The accuracy of the average failure load across experiments was 95% (Fig. 7). For Type-II b (0.1 mm adhesive thickness pre-filled steel) joints, very large cycle ratios were obtained for the same loading values. Therefore, they are not shown in Figure 7.

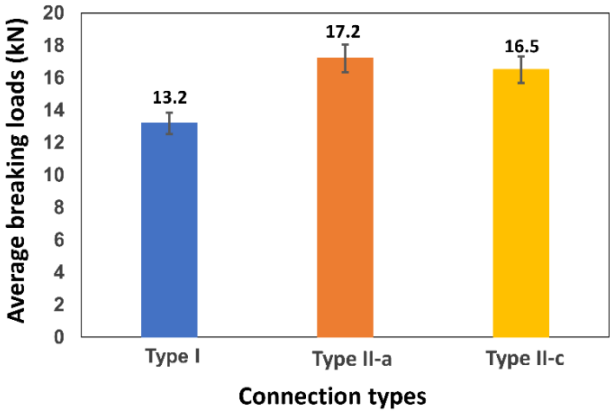

Fig. 7. Average failure loads of the samples.

3.2. Findings of the FEA

The stresses that are most effective on the strength of an adhesively-bonded SLJs are peel stress (σ_y), normal stresses (σ_x, σ_z), and shear stress (τ_{xy}).

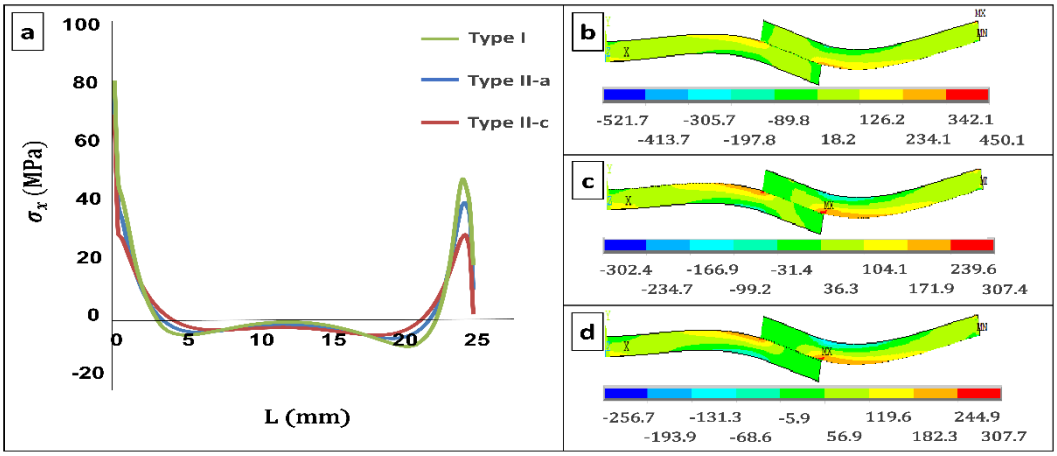

Fig. 8. (a) Distribution of the normal stress in the x-axis (σ_x) in the adhesive layer along the BC line and deformations and; (b) Type I and; c) Type II-a and; d) Type II-c.

There is a variation in the stresses at the endpoints of the link since one end has fixed support while the other end is mobile. Moment-induced peeling stresses result in a crack at the lap length's edges. Damage is caused by the crack's abrupt development toward the lap zone's core. Peel stresses created a crack at the lap length's edges, around 3 mm from the edges. As the step came to an abrupt stop, the crack grew larger. As can be seen in Figure 8, the peel stresses for the connection are compressive in the center and tensile at the overlap region's margins, approaching zero toward the center [18, 26].

In general, the stress distributions have higher values at the overlap ends, and the stresses converge close to zero from the ends towards the center when the normal stress distributions along the BC line (shown in Fig. 8) are compared in the steel and aluminum samples with varying adhesive thicknesses [31].

It was discovered that the highest stress in aluminum (Type I) at the BC line, σx, was 81 MPa. Compared to steel (Type II) stresses, this number is much higher. This explains why aluminum has a lower load capacity. Compared to the steel joint with an adhesive thickness of 0.1 mm (Type II-a), the strains at the ends of the Type II-c steel joint have a lower adhesive thickness. This outcome is in line with research findings in the literature that joints bearing heavier stresses have more adhesive thickness. As anticipated, the joint with a 0.2 mm adhesive thickness in this study was shown to be able to support the highest load [34].

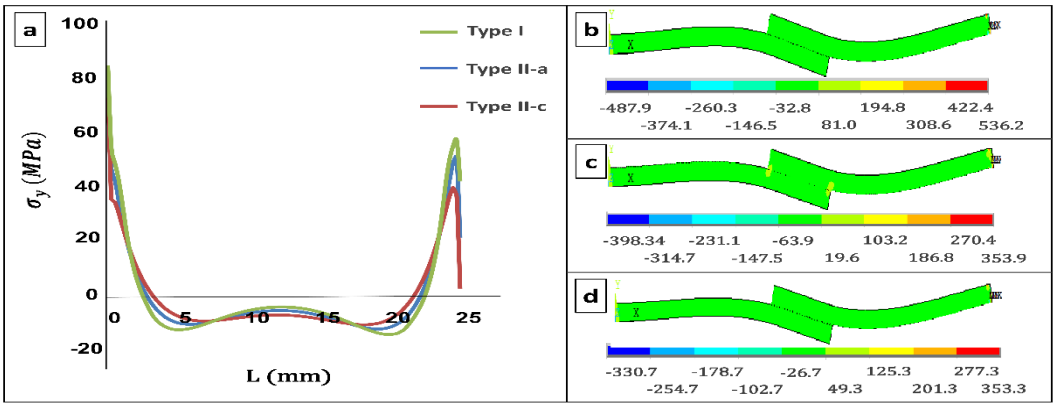

Fig. 9. (a) Distribution of the normal stress in the y-axis (σ_y) in the adhesive layer along the BC line and deformations and; (b) Type I and; c) Type II-a and; d) Type II-c.

The end locations of the joint along the BC line are where the peel stresses are at their highest. When it comes to damage occurrence, peel stress (σy) is crucial. The joint's ability to support more weight is increased when this damaging stress is reduced. When comparing the peel stress (σy) distributions shown in Figure 9, the steel sample with a 0.2 mm adhesive thickness (Type II-c) at the BC line's terminal had the lowest stress value. With an increase in adhesive thickness, the peel stress value in the steel sample drops. The joint Type II-c has the maximum load-carrying capability as a result. Conversely, in the Type I aluminum sample, the load-carrying capacity is lower than in other joints because of the peel stress [18,26].

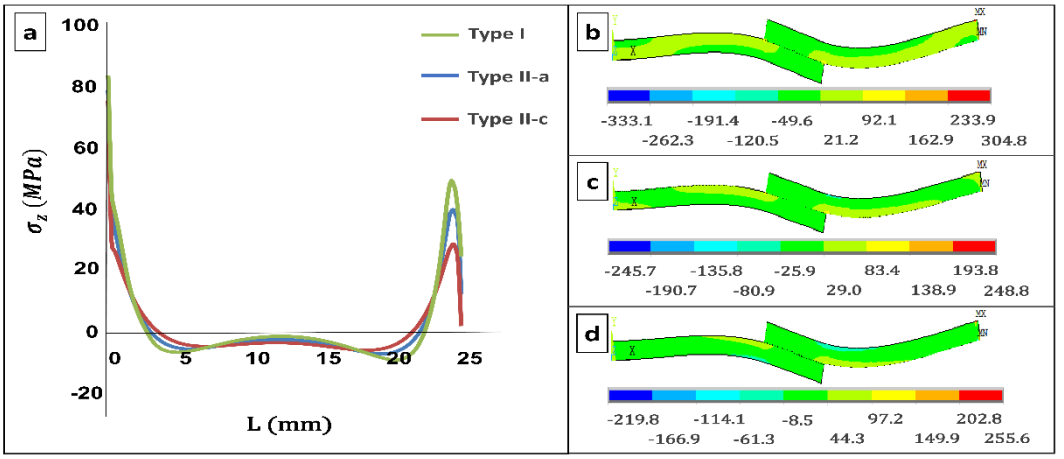

Fig. 10. (a) Distribution of the normal stress in the z-axis (σ_z) in the adhesive layer along the BC line and deformations and; (b) Type I and; c) Type II-a and; d) Type II-c.

As seen in Figure 8, the peeling stresses take values close to zero in the center and are compressive towards the center and tensile at the overlap region's boundaries. There are similarities between the stress distribution in the x-axis, σx, and the stress distribution in the z-axis, σz, as seen in Figure 10.

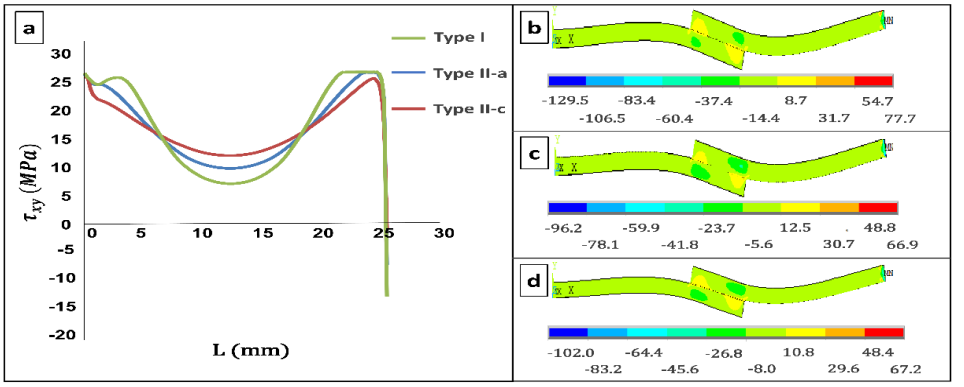

Fig. 11. (a) Distribution of z-axis (τ_{xy}) in the adhesive layer along the BC line and deformations and; (b) Type I and; c) Type II-a and; d) Type II-c.

Along line BC, shear stresses reach their maximum at the endpoints, whereas in the middle part of the line, this stress value decreases. Examining the shear stress values at point B for aluminum and steel samples, given in Fig. 11, the maximum shear stress value is determined to be around 25 MPa.

The shear stress at point C of the aluminum joint (Type I) takes a negative value of 15 MPa. When the shear stress distribution is examined, it is seen that the load-carrying capacity in the middle part of the adhesive in terms of shear is the lowest in the aluminum sample (Type I) whereas the steel joint with an adhesive thickness of 0.2 mm has the highest. This explains why the load-carrying capacities are different [34].

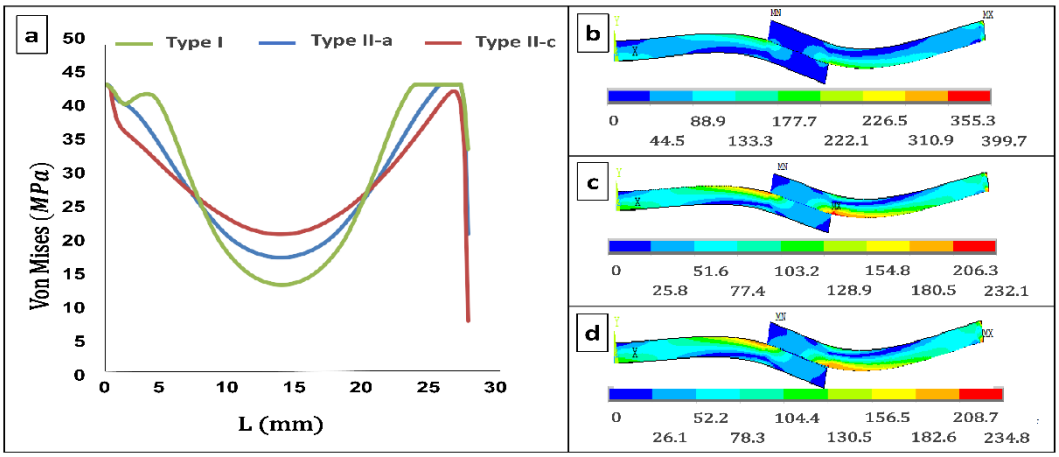

Fig. 12. (a) Distribution von Mises stresses in the adhesive layer along the BC line and deformations and; (b) Type I and; c) Type II-a and; d) Type II-c.

Examining Fig. 12, it is seen that the maximum stress value that occurred along the BC line is 45 MPa. Here, as in the shear stress distributions, the lowest load-carrying capacity occurs in the middle parts of the adhesive in the aluminum sample (Type I). The highest load-carrying capacity occurs in the steel sample with an adhesive thickness of 0.2 mm (Type II-c).

Although the stress values at the endpoints of the joints are similar, the difference in the stress distribution in the middle parts affects the load-carrying capacity. Furthermore, no plastic deformation was observed in the adherents of the SLJs subjected to tensile load. The damage initiated at the free ends of the joints and propagated until the joint failed [18,26].

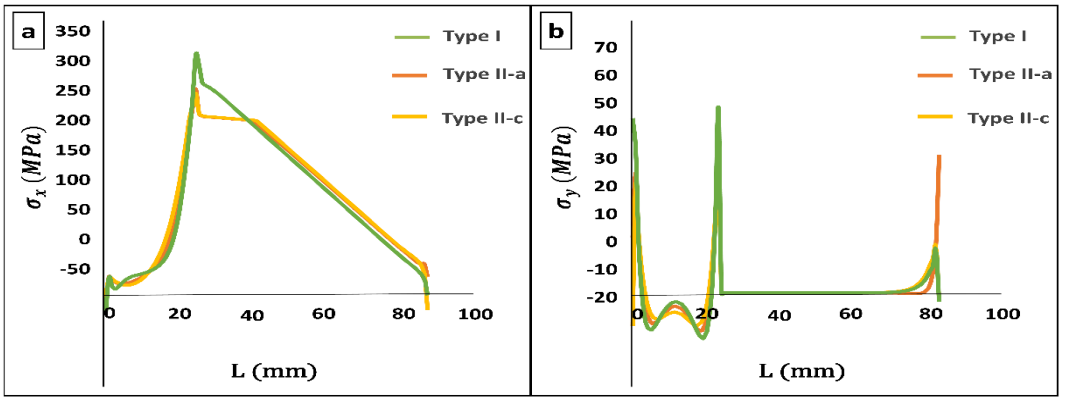

Fig. 13. Distribution of (a) Normal stress (σ_x) and; (b) Peel stress (σ_y) along the AC line.

While the distributions of normal stress (σ_x) and peel stress (σ_y) along the AC line, given in Fig. 13, generally have low values at the endpoints, the stress values increase from the ends towards the middle. Maximum stresses occur in the transition zone from the joint to the adherend.

While the maximum stress value that occurs in the aluminum sample (Type I) along the AC line is 315 MPa, this value is around 280 MPa in the steel sample (Type II). The distributions of normal stress (σ_x) in the steel joints with adhesive thicknesses of 0.1 mm (Type II-a and Type II-b) and 0.2 mm (Type II-c) are almost the same. The maximum value of the peel stress (σ_y) on the AC line that caused damage to the joint was determined to be 55 MPa. Stress accumulations caused by the discontinuities in the adhesive zone can be seen in the graphs. This is particularly evident at the endpoints. No peel stress (σ_y) occurs in regions other than the bonding zone, which is consistent with the boundary conditions [6,34,35].

No plastic deformation was observed in the materials. The damage initiated at the free ends of the joints and propagated until the joint failed.

3.3. Experimental Results Obtained from the Samples Subjected to Fatigue

The average failure loads of aluminum and steel samples were determined through tensile tests performed as per the ASTM 3166-99 standard, which requires the specimen to be subjected to high-cycle fatigue under a load that is equivalent to 50%–45% of its failure load. Since there are no requirements in the relevant standards for low-cycle fatigue testing, the experiments were carried out under 50% or more of the average failure load to examine the low-cycle fatigue behavior of the samples. This test was repeated five times for aluminum, steel, and pre-filled steel samples at each load condition. All tests were for R = 0, i.e., when the load changes from 0 to 14 kN, F_{max} = 14 kN, and F_{min} = 0, both the amplitude of the force and the average force are equal to 7 kN. The average number of cycles for Type I, Type II-a, Type II-b, and Type II-c is presented in Fig. 14 [31,35].

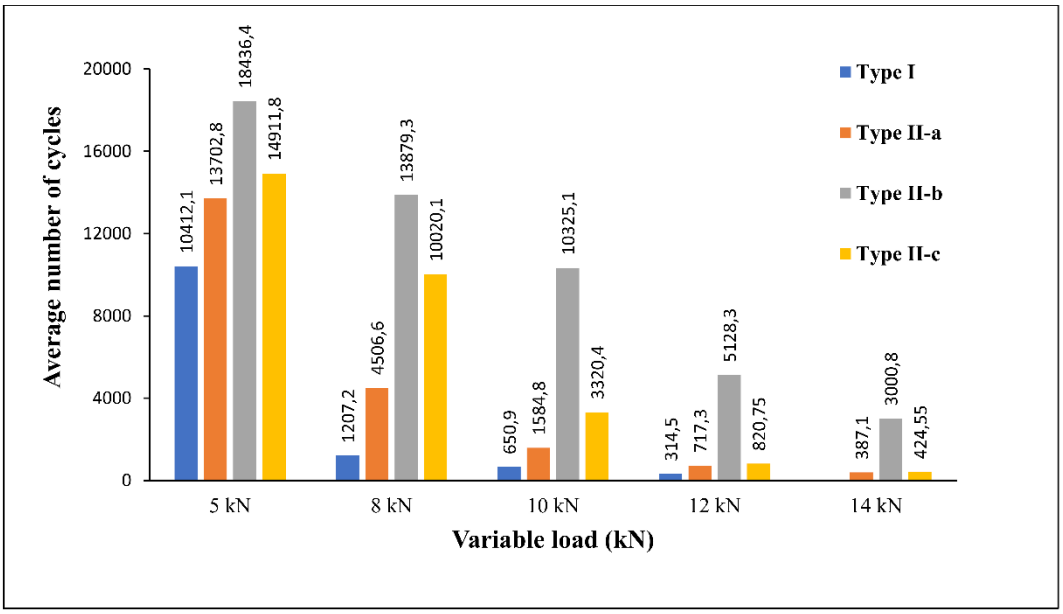

Fig. 14. Average number of cycles for Type I, Type II-a, Type II-b, and Type II-c.

In the Type-I joint, a 12 kN load corresponds to 90% of the average failure load, whereas 10 kN corresponds to 75%, 8 kN to 60%, and 5 kN to 38%. When the load was decreased from 12 kN to 10 kN, the increase in fatigue life was approximately two-folds as great, although the percentage of the change in load is approximately 15%. Likewise, when the load was decreased from 10 kN to 8 kN, where the change in the load was 20%, the increase in the number of cycles was slightly below two-folds. With the load decreased to 5 kN, which corresponds to 38% of the average failure load, the fatigue life moved into the high-cycle region.

In the Type-II joint, a 14 kN load corresponds to 81% of the average failure loads, whereas 12 kN corresponds to 75%, 10 kN to 58%, and 8 kN to 46.5%. In the Type-II-b joint, very large cycle numbers were obtained for the same load values compared to the Type-II-a joint. For example, for a 14 kN load, pre-filling with adhesive increased the number of cycles by 7.75-folds, even though all other properties of the samples were the same.

In the Type-II c joint, a 14 kN load corresponds to 85% of the average failure load, whereas 12 kN corresponds to 75%, 10 kN to 60%, and 8 kN to 49%. When the load was decreased from 14 kN to 12 kN, where the percentage of the change in load is 14%, the increase in fatigue life was approximately 1.85-folds. Likewise, when the load was decreased from 12 kN to 10 kN, the change in the load was approximately 16%, and the increase in the number of cycles was more than two-fold as great. When the load was decreased from 10 kN to 8 kN, which means the decrease in the load was 20%, the increase in the number of cycles was 2.85-folds. With the 5 kN load, on the other hand, fatigue life moved into the high-cycle region [34,35].

Even though the increase in the failure load obtained by increasing the adhesive thickness from 0.1 mm to 0.2 mm was just 4%, the increase in the number of cycles, in return, came about to be much greater and increased disproportionally as the load value decreased. For example, while the number of cycles under an 8 kN load was 4506.6 in Type II-a, it exceeded 10,000 in Type II-c under the same load.

4. Conclusions

Experimental and numerical research was done on the mechanical characteristics of SLJ configurations made of steel and aluminum samples that were subjected to tensile loads. The low-cycle fatigue testing of SLJs made of steel and aluminum, with varying adhesive thicknesses, produced the following findings:

The steel samples, which can carry a higher static load, can also withstand a higher number of cycles than the aluminum sample.

It was found that pre-filling, adhesive joints increased the low cycle fatigue strength.

The adhesive thickness was shown to affect the bonding strength in ABJs. When SLJs of steel materials with different adhesive thicknesses were compared, the fatigue strength was found to have increased with the adhesive thickness.

Furthermore, the surfaces of the failure zones in the joints were examined, and the failures were identified to be, generally, of cohesive and special cohesive failure modes.

Acknowledgment

This research has been supported by Erzincan Binali Yıldırım University and Atatürk University. The authors would like to express their gratitude to the respective institutions for funding this project.

References

[1] da Silva LFM, Adams RD. Techniques to reduce the peel stresses in adhesive joints with composites. Int J Adhes Adhes 2007;27:227–35. https://doi.org/10.1016/J.IJADHADH.2006.04.001.

[2] Gültekin K, Akpinar S, Özel A. The effect of the adherend width on the strength of adhesively bonded single-lap joint: Experimental and numerical analysis. Compos Part B Eng 2014;60:736–45. https://doi.org/10.1016/J.COMPOSITESB.2014.01.022.

[3] Adin H. The effect of angle on the strain of scarf lap joints subjected to tensile loads. Appl Math Model 2012;36:2858–67. https://doi.org/10.1016/J.APM.2011.09.079.

[4] Akpinar S. The effect of composite patches on the failure of adhesively-bonded joints under bending moment. Appl Compos Mater 2013;20:1289–304. https://doi.org/10.1007/S10443-013-9335-6/FIGURES/16.

[5] Zhao X, Adams RD, Da Silva LFM. Single lap joints with rounded adherend corners: Experimental results and strength prediction. J Adhes Sci Technol 2011;25:837–56. https://doi.org/10.1163/016942410X520880.

[6] Akpinar S. Effects of Different Curvature Patches on the Strength of Double-Strap Adhesive Joints. Http://DxDoiOrg/101080/002184642013769098 2013;89:937–47. https://doi.org/10.1080/00218464.2013.769098.

[7] Doru MO, Özel A, Akpinar S, Aydin MD. Effect of the Spew Fillet on Adhesively Bonded Single-Lap Joint Subjected to Tensile Loading: Experimental and 3-D Non-Linear Stress Analysis. Http://DxDoiOrg/101080/002184642013777900 2013;90:195–209. https://doi.org/10.1080/00218464.2013.777900.

[8] Sayman O, Ozen M, Korkmaz B. Elasto-plastic stress distributions in adhesively bonded double lap joints. Mater Des 2013;45:31–5.

[9] El Zaroug M, Kadioglu F, Demiral M, Saad D. Experimental and numerical investigation into strength of bolted, bonded and hybrid single lap joints: Effects of adherend material type and thickness. Int J Adhes Adhes 2018;87:130–41. https://doi.org/10.1016/J.IJADHADH.2018.10.006.

[10] Khoramishad H, Akhavan-Safar A, Ayatollahi MR, Da Silva LFM. Predicting static strength in adhesively bonded single lap joints using a critical distance based method: Substrate thickness and overlap length effects. Http://DxDoiOrg/101177/1464420716666427 2016;231:237–46. https://doi.org/10.1177/1464420716666427.

[11] Karachalios EF, Adams RD, Da Silva LFM. The behaviour of single lap joints under bending loading. Http://DxDoiOrg/101080/016942432012761926 2013;27:1811–27. https://doi.org/10.1080/01694243.2012.761926.

[12] Katnam KB, Crocombe AD, Khoramishad H, Ashcroft IA. Load Ratio Effect on the Fatigue Behaviour of Adhesively Bonded Joints: An Enhanced Damage Model. Http://DxDoiOrg/101080/00218460903462632 2010;86:257–72. https://doi.org/10.1080/00218460903462632.

[13] Sawa T, Liu J, Nakano K, Tanaka J. A two-dimensional stress analysis of single-lap adhesive joints of dissimilar adherends subjected to tensile loads. Http://DxDoiOrg/101163/156856100742104 2012;14:43–66. https://doi.org/10.1163/156856100742104.

[14] Gleich DM, Van Tooren MJL, Beukers A. Analysis and evaluation of bondline thickness effects on failure load in adhesively bonded structures. Http://DxDoiOrg/101163/156856101317035503 2012;15:1091–101. https://doi.org/10.1163/156856101317035503.

[15] Xu W, Wei Y. Influence of adhesive thickness on local interface fracture and overall strength of metallic adhesive bonding structures. Int J Adhes Adhes 2013;40:158–67. https://doi.org/10.1016/J.IJADHADH.2012.07.012.

[16] Pascoe JA, Zavatta N, Troiani E, Alderliesten RC. The effect of bond-line thickness on fatigue crack growth rate in adhesively bonded joints. Eng Fract Mech 2020;229:106959. https://doi.org/10.1016/J.ENGFRACMECH.2020.106959.

[17] Sahin R, Akpinar S. The effects of adherend thickness on the fatigue strength of adhesively bonded single-lap joints. Int J Adhes Adhes 2021;107. https://doi.org/10.1016/J.IJADHADH.2021.102845.
[18] Gavgali E, Sahin R, Akpinar S. An investigation of the fatigue performance of adhesively bonded step-lap joints: An experimental and numerical analysis. Int J Adhes Adhes 2021;104:102736. https://doi.org/10.1016/J.IJADHADH.2020.102736.
[19] Mariam M, Afendi M, Abdul Majid MS, Ridzuan MJM, Gibson AG. Tensile and fatigue properties of single lap joints of aluminium alloy/glass fibre reinforced composites fabricated with different joining methods. Compos Struct 2018;200:647–58. https://doi.org/10.1016/J.COMPSTRUCT.2018.06.003.
[20] Liu Y, Lemanski S, Zhang X, Ayre D, Nezhad HY. A finite element study of fatigue crack propagation in single lap bonded joint with process-induced disbond. Int J Adhes Adhes 2018;87:164–72. https://doi.org/10.1016/J.IJADHADH.2018.10.005.
[21] Saraç İ, Adin H, Temiz Ş. Experimental determination of the static and fatigue strength of the adhesive joints bonded by epoxy adhesive including different particles. Compos Part B Eng 2018;155:92–103. https://doi.org/10.1016/J.COMPOSITESB.2018.08.006.
[22] Takiguchi M, Yoshida F. Effects of Loading Speed and Shear Prestrain on Adhesive Fatigue Strength in Single-Lap Joint. Key Eng Mater 2007;340–341:1479–84. https://doi.org/10.4028/WWW.SCIENTIFIC.NET/KEM.340-341.1479.
[23] Yang QD, Shim DJ, Spearing SM. A cohesive zone model for low cycle fatigue life prediction of solder joints. Microelectron Eng 2004;75:85–95. https://doi.org/10.1016/J.MEE.2003.11.009.
[24] Braga DFO, Maciel R, Bergmann L, da Silva LFM, Infante V, dos Santos JF, et al. Fatigue performance of hybrid overlap friction stir welding and adhesive bonding of an Al- Mg- Cu alloy. Fatigue Fract Eng Mater Struct 2019;42:1262–70.
[25] Bayramoglu S, Akpinar S, Çalık A. Numerical analysis of elasto-plastic adhesively single step lap joints with cohesive zone models and its experimental verification. J Mech Sci Technol 2021;35:641–9.
[26] Hacısalihoglu İ, Akpinar S. The effect of stepped notches and recesses on joint strength in adhesive bonded joints: Experimental and numerical analysis. Theor Appl Fract Mech 2022;119:103364.
[27] Liu L, Wang X, Wu Z, Keller T. Tension-tension fatigue behavior of ductile adhesively-bonded FRP joints. Compos Struct 2021;268:113925. https://doi.org/10.1016/J.COMPSTRUCT.2021.113925.
[28] Tan W, Na J, Wang G, Xu Q, Shen H, Mu W. The effects of service temperature on the fatigue behavior of a polyurethane adhesive joint. Int J Adhes Adhes 2021;107:102819. https://doi.org/10.1016/J.IJADHADH.2021.102819.
[29] Sahin R, Akpinar S. The effects of adherend thickness on the fatigue strength of adhesively bonded single-lap joints. Int J Adhes Adhes 2021;107:102845.
[30] Akpinar S, Sahin R. The fracture load analysis of different material thickness in adhesively bonded joints subjected to fully reversed bending fatigue load. Theor Appl Fract Mech 2021;114:102984. https://doi.org/10.1016/J.TAFMEC.2021.102984.
[31] Sahin R, Akpinar S. The effects of adherend thickness on the fatigue strength of adhesively bonded single-lap joints. Int J Adhes Adhes 2021;107:102845. https://doi.org/10.1016/J.IJADHADH.2021.102845.
[32] ASTM. D3166–99. Standard Test Method for Fatigue Properties of Adhesives in Shear by Tension Loading (2012) Google Scholar n.d.
[33] Demir K, Bayramoglu S, Akpinar S. The fracture load analysis of different support patches in adhesively bonded single-lap joints. Theor Appl Fract Mech 2020;108:102653. https://doi.org/10.1016/J.TAFMEC.2020.102653.
[34] Gültekin K, Akpinar S, Özel A. The effect of moment and flexural rigidity of adherend on the strength of adhesively bonded single lap joints. J Adhes 2015;91:637–50.
[35] Akpinar S. Effects of Different Curvature Patches on the Strength of Double-Strap Adhesive Joints. Http://DxDoiOrg/101080/002184642013769098 2013;89:937–47. https://doi.org/10.1080/00218464.2013.769098.

Contents lists available at *Dergipark*

Journal of Scientific Reports-A

journal homepage: *https://dergipark.org.tr/tr/pub/jsr-a*

E-ISSN: 2687-6167 ***Number 55, December 2023***

RESEARCH ARTICLE

Receive Date: 02.12.2023 ***Accepted Date: 31.12.2023***

Synthesis and characterization of polymer-derived nanocrystal SiOC powders via high temperature XRD method

Sait Altun[1]*, Hasan Göçmez[2]

[1]*Kütahya Dumlupınar University, Advanced Technologies Center (İLTEM),ORCID: 0000-0003-3085-1351*

[2]*Kütahya Dumlupınar Üniversity, Faculty of Engineering, Department of Metalurgical and Materials Engineering, Kütahya,ORCID: 0000-0003-3748-0311*

Abstract

In the study, polymer-derived SiOC powders was synthesized by sol-gel method. The resulting composites consists of β-SiO_2, SiC and free carbon. Tetraethylorthosilicate (TEOS) and Polydimethylsiloxane (PDMS) were selected as starting materials to obtain organic-inorganic structure. After the gelling process, the powders were heat treated at 1100°C in Argon medium to obtain the desired phases. Scanning Electron Microscopy (SEM), Differential Thermal Analysis (DTA) and Fourier Transform Infrared Spectroscopy (FT-IR) analyses were used for characterization. In addition, instant phase changes were determined by high-temperature XRD in powders subjected to heat treatment up to 1500 °C in a helium environment. The effect of temperatures on the transformation in SiOC synthesis, the transformation temperatures of α-cristobalite to β-cristobalite were sharply determined and the SiC formation temperature was revealed. The effect of temperature on crystal size was also obtained as a result of the study.

Keywords: Polymer Derived Ceramics, SiOC, PDMS, High Temperature XRD

1. Introduction

Polymer derived ceramics (PDCs) are predominantly covalently bonded advanced ceramics that can be processed at relatively low temperatures such as 1000-1500 °C. The PDCs are obtained via polymer cross-linking and then a pyrolis process in inert atmosphere. This is the process called polymer to ceramic conversion[1]. There are very large number of varieties of PDCs such as, SiC[2], SiOC[3], SiCN[4], SiBN[5] have been successfully synthesized using preceramic polymers as raw material.

PDCs are versatile material so they enable many applications such as sensors [6-7], coatings [8], high temperature structure material [9-10].

SiOC (black glass) is one of the most attractive materials in terms of optical, electrical and magnetic properties in recent years [11]. The high compositional stability and oxidation resistance and the superior properties in terms of mechanical and thermal properties are among the other features that make the usability of this material [12-14].

Silicon oxycarbide is called the structure in which silicones bond simultaneously with C and O atoms in the structure. This tetrahedral bond structure is usually define as [CxSiO4-x](x=1,2,3). The addition of carbon in silicate glass allows a coordination

[1] Corresponding author.
E-mail address: sait.altun@dpu.edu.tr

number of 4 to be obtained as a result of its replacement with oxygen, which has coordination number of 2. This increase in the number of bond per anion is expected to strengthen the chemical structure of glass lattice and also expected to improve thermal and mechanical properties. The sol-gel process enables the low-temperature synthesis of silicon oxycarbide glasses without problems such as oxidation during degradation and melting. What makes this process possible is the use of polymeric materials with Si-C bonds as starting materials [15].

The first findings about SiOC date back to 1989. Porte L. and Sarte A. investigated the effects of the reinforcement of silicon carbide materials in composite materials on high temperature behavior. The result of that study, the behavior of oxygen atoms was examiden by XPS analysis and a small amount of SiO_2 phase was observed in the fiber material. In addition, the SiOC structure, which appears be more abundant, was also determined[16].

In the study examining the pyrolysis steps of 400-1000°C, Babonneu et al. stated that the gel was stable at 400°C, decomposition started between 400-600°C and Si-O, Si-C bonds started to form, methyl groups were decomposed at 600-800°C and Si-C bonds were formed at 1000 C [17].

Chi. et al. reported that using TEOS and methyltrimethyloxysilane (MTMS), the powder color turned black after the pyrolysis process in Argon medium at 1200°C, and proposed that crystalline phases were formed after 5 hours of heat treatment in Ar medium at 1450°C, and these phases were β-SiC and Cristobalite [18].

The aim of this study is to produce SiOC powders using PDMS/TEOS by the sol-gel method and to observe the phase changes instantly from 1100 to1500 °C by using high temperature XRD.

2. Experimental Procedure

2.1. Synthesis of TEOS/PDMS Organic-Inorganic Hybrid Material

TEOS and PDMS were selected as the starting material for the Sol-Gel Method. Isopropyl alcohol (iPrOH) was used as the solvent of these two materials, nitric acid (NHO_3) as the catalyst and purified water as the hydrolysis agent. TEOS and PDMS were determined as 60% TEOS and 40% PDMS by weight and the teos/iPrOH/H_2O/HNO_3 molar ratio was adjusted in 5 different compositions as (1) 1:6: 3: 0.3 (25 °C), (2) 1: 6: 3: 0.6 (25 °C), (3) 1: 6: 3: 0.6 (50 °C), (4) 1:12: 3: 0.3 (25 °C), (5) 1: 15: 3:0.3 (25 °C) and duration of gelling time were controlled. The composition with the fastest gelation time was composition 3.

Composition 3 was used for the process referred to as organic-inorganic hybrid powder preparation. Two different solutions were prepared in two different beakers. (a) in the first beaker, half of the amount of TEOS, PDMS and total iPrOH to be used; (b) in the second beaker, the remaining iPrOH, H_2O and HNO_3 were mixed until they were homogeneous solutions. Then, container b was slowly added to container a and continued to be stirred till it was homogeneous. The solution, which gelled at 50 °C in about 120 minutes, was left to dry until the weight loss was over.

Table 1. Gelation temperatures and times of the used composition.

Composition	Gelling Time	Gelling Temperature
1	1 day	25 °C
2	300 minutes	25 °C
3	120 minutes	50 °C
4	240 minutes	25 °C
5	240 minutes	25 °C

2.2. Preparation and sintering of SiOC powders

The hybrid material obtained was subjected to burning for 60 minutes at a heating rate of 5 C/min at 300 °C. This process has been carried out to avoid the free carbon content that may occur in the body. The light yellow brittle gel agate obtained was ground in the mortar until it passed completely under a 63 μm sieve. This hybrid material will be called raw powder in the article and all the heat treatments will be carried out on this raw material.

I. The hybrid material obtained was subjected to heat treatment in Argon medium for 120 minutes at 1100 °C.

II. The hybrid material was subjected to heat treatment in helium environment with a high-temperature XRD of 25 °C, 1100 ° C, and after this temperature, an XRD pattern was determined every 50 °C with a heating rate of 5 °C/min.

III. The hybrid material was subjected to heat treatment in a helium environment with a heating rate of 5 ° C/min with its high-temperature XRD at 25 °C, 600 °C, after 120 minutes at 600 °C, 1000 °C, 1050 °C, 1100 °C, after 120 minutes at 1100 °C, and then right after this temperature XRD pattern was obtained every 50 °C.

Table 2. Heat treatment of organic-inorganic hybrid material.

Heat Treatment Steps	Precursor	Heat treatment temperature	Holding time	Heating Rate	Ambient Atmosphere
I	Composition 3	1100 °C	2hours at 600 °C and 2 hours at 1100 °C	5 °C /minutes	Argon
II	Composition 3	1500 °C	No holding	5 °C /minutes	Helium
III	Composition 3	1500 °C	2hours at 600 °C and 2 hours at 1100 °C	5 °C /minutes	Helium

2.3. Characterization processes

According to the high-temperature XRD results, it was determined that the SiO_2 and SiC phases in regime (iii) were more prominent, and the raw material of this sample was selected in the preheating analysis. XRD analysis was performed to determine the temperature-dependent phase transformations and crystal sizes of the powders. SEM (FE-SEM Fei Nanonova 650) and EDS analyses were conducted to examine the morphology of the raw and heat-treated material with chemical analysis. DTA-TG (STA 409 PC) analysis was executed to determine possible reaction temperatures and weight loss. FT-IR analysis was performed to determine the bond structures in glassy regions.

3. Results

According to Figure 1, in the FTIR analysis of the raw powder, Si-O bonds at 559 $^{cm-1}$ and 699 cm-1, C≡CH bonds at 455 cm^{-1}, CO-OH bonds at 1402 cm^{-1} and C-CH_3 bonds at 2962 $cm^{-1}$are observed [19]. Si-C bonds are seen at 787 cm^{-1} and 853 cm^{-1} wavelengths, Si-O-Si at 1008 $cm^{-1}$and Si-CH_3 bonds at 1258 cm^{-1} [20]. In the sample obtained after high-temperature XRD, Si-O-Si bonds at 1085 cm^{-1} and Si-C bonds at 668 $cm^{-1}$and 792 cm^{-1} are clearly seen in the structure [21,22]. In addition, in the C-H and CH_3 bonds in the structure were reduced.

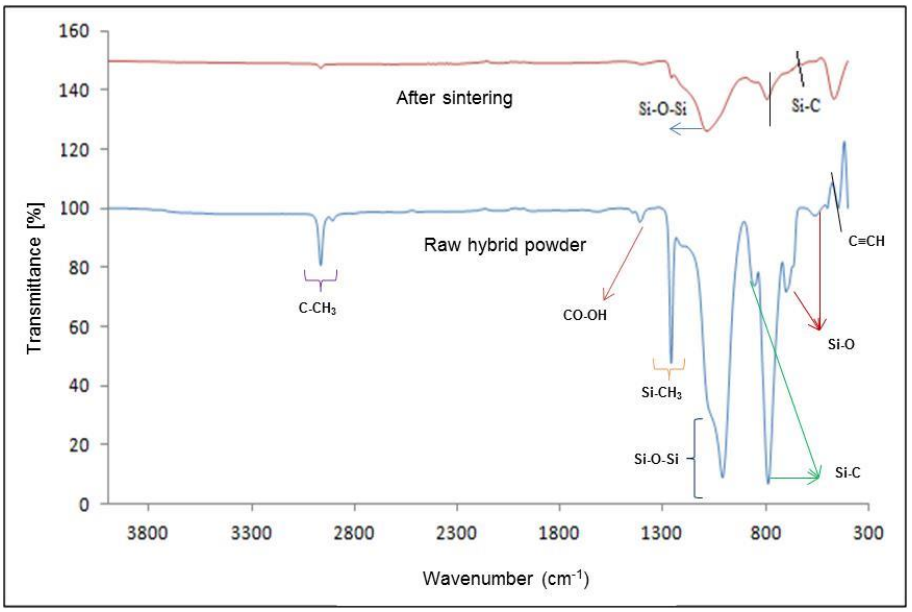

Fig. 1. FT-IR analysis of hybrid powder after raw and heat treatment.

In the phase analysis determination performed before and after the heat treatment, it was observed that the raw state of the produced organic-inorganic hybrid powder was amorphous according to the XRD result, and no crystalline structure peak was formed. The peaks seen in the XRD pattern are derived from the platinum substrate used for the high-temperature XRD (Figure 2.). The diffraction peaks corresponding to α-crystobalite (Highscore: 98-016-2245), β-crystabolite(Highscore:98-016-2666) and SiC (Highscore: 98-018-2362) (Figure 4 and Figure 5.).

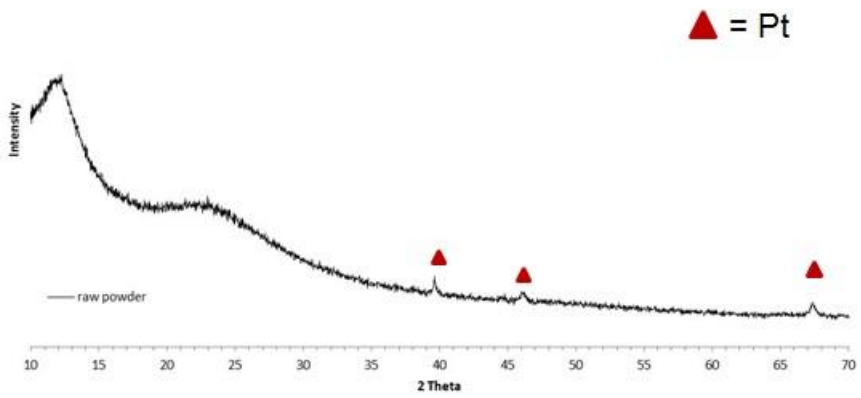

Fig. 2. XRD pattern of raw hybrid material.

The raw powder obtained was subjected to a pyrolysis process in an argon environment at 1100 °C for 2 hours at the first stage. It was observed that the obtained structure preserved its amorphous structure while the α-crystalloid phase started to form (Figure 3.).

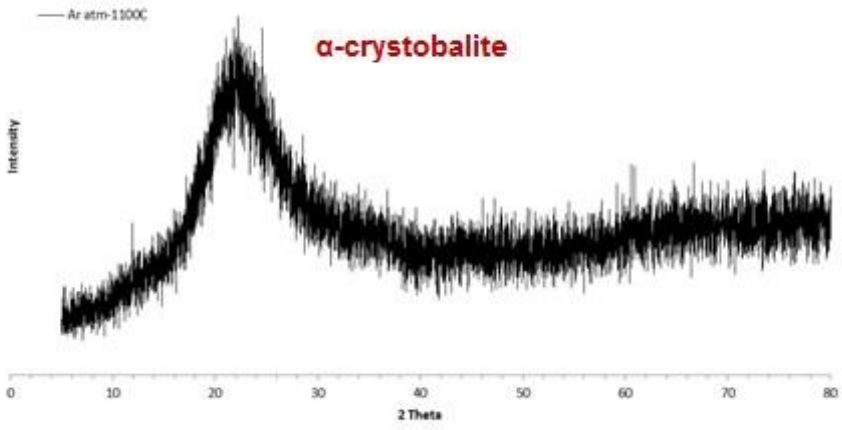

Fig. 3. XRD graph of the sample subjected to pyrolysis at 1100 °C in Ar medium.

For the high-temperature XRD analysis to observe phase transformations, heat treatment steps up to 1500 °C were carried out at annealing and pyrolysis critical temperatures (600 °C and 1100 °C) without waiting certain time and holding for 2 hours at both temperatures (Figure 4 and Figure 5).

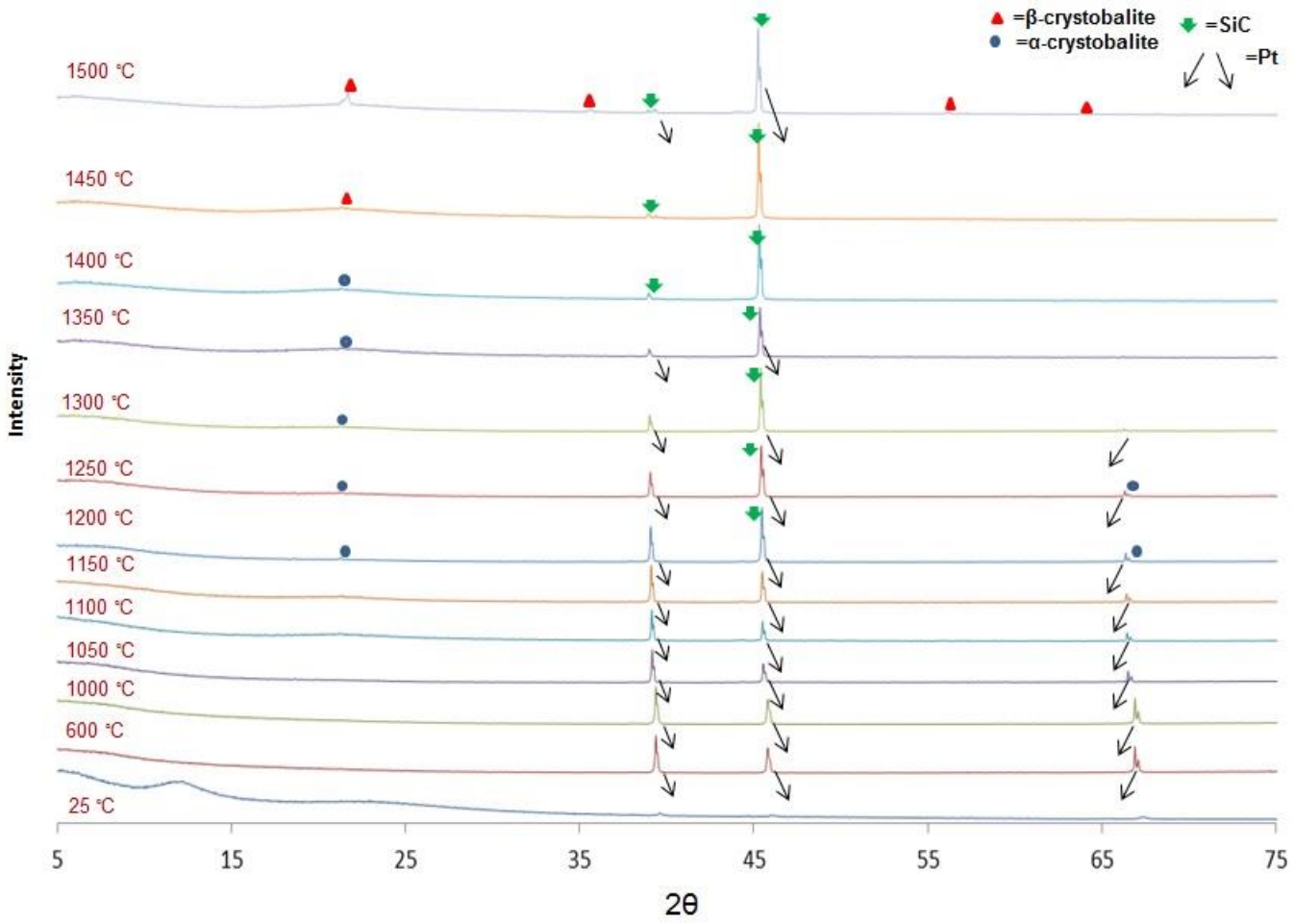

Fig. 4. High temperature XRD patterns (no holding time at annealing and pyrolysis temperature)

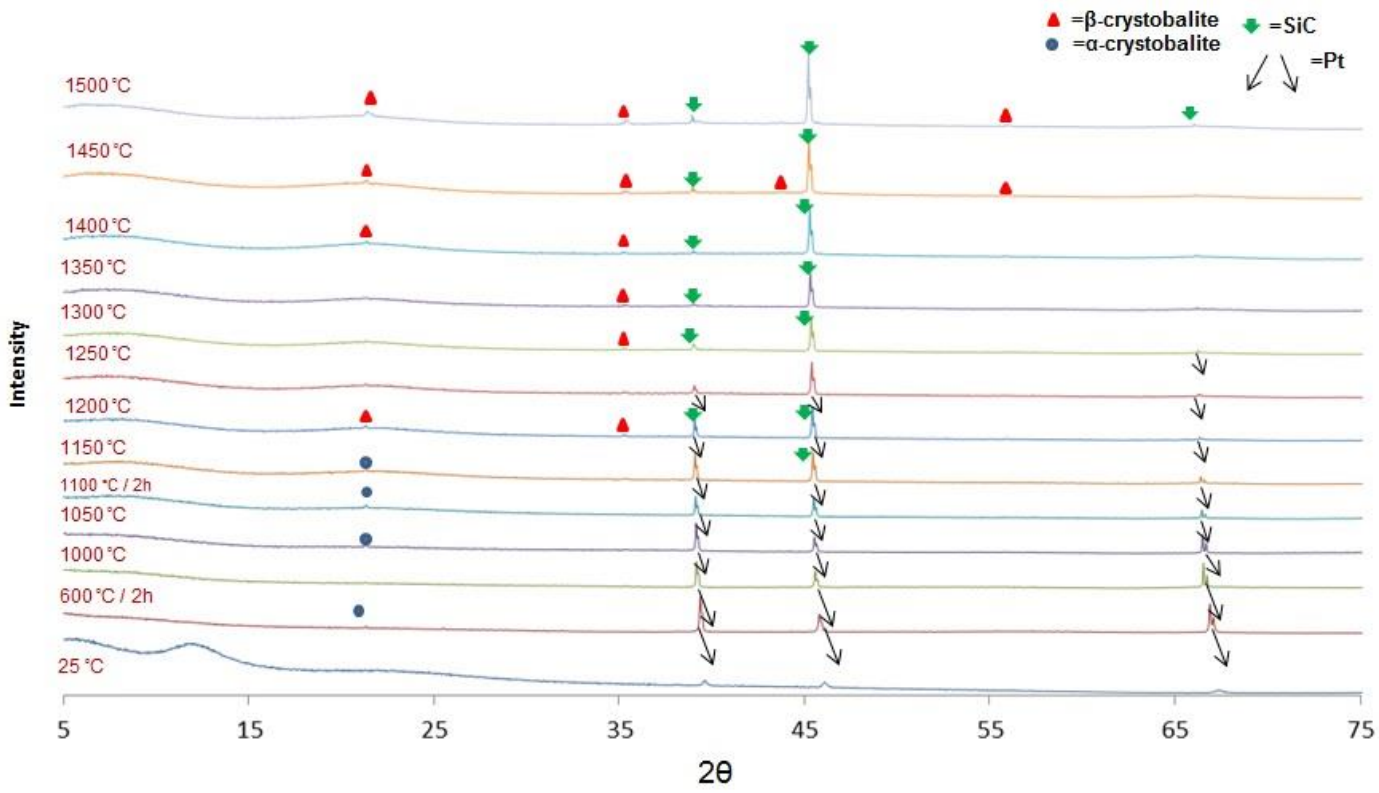

Fig. 5. High-temperature XRD patterns (Sample holding for 2 hours at annealing and pyrolysis temperature)

According to Figure 4, it was observed that α-cristobalite peaks were formed at 1200 °C- 1400 °C, and the structure transformed into the β-cristobalite phase after 1450 °C. In addition, it was detected that SiC peaks started to form in the structure around1250, then this phase was clarified at above 1450 °C.

According to Figure 5, it was observed that there is an α-crystalloid phase in the structure starting from 600 °C. It turns into a β-crystalloid phase at 1200 °C, the phase disappears with the increase in temperature, and it occurs again at 1400-1450 °C. For the SiC phase, it was perceived that the first peaks started to be seen at 1150-1200 °C, but became clear at 1450 °C and were completely found at 1500 °C.

According to both Figure 4 and Figure 5, İt's seen that ther is no SiC peak in the structure up to 1100 °C. In Figure 4, it was observed that SiC peaks were formed at 1200 °C and these peaks become more pronounced as the temperature increases. In Figure 5, it was seen that the SiC formation temperature decreased to 1150 °C. It can be said that holding at critical temperatures during the heat treatment reduces SiC formation to lower temperatures.

As a result of the heat treatment, it was observed that the initial amorphous structure turned into a crystal structure as the temperature increased, but the amorphous separation in the structure remained in the system. The crystal sizes of the SiO_2 and SiC phases, which are among the crystalline structures formed, are given in Table 3 and Table 4.

Table 3. Crystal size change of the sample at annealing and pyrolysis temperature without holding times.

Temperature (°C)	SiO_2(nm)	SiC(nm)
1000	-	-
1050	-	-
1100	30.3	-
1150	65.3	-
1200	65.4	-
1250	46.9	-
1300	30.3	-
1350	47	-
1400	65.3	-
1450	65.3	226
1500	82.4	454

Table 4. Crystal size change of the sample at annealing and pyrolysis temperature with 2 hours holding times.

Temperature (°C)	SiO_2(nm)	SiC(nm)
1000	-	-
1050	-	-
1100	218	-
1150	114	-
1200	218.2	-
1250	218.5	-
1300	-	-
1350	11.1	-
1400	65.3	-
1450	114	69
1500	218.2	120

According to the results obtained, the increase in heat treatment time led to the formation of SiC crystals in larger sizes. Depending on the temperature, crystal size growth is also seen in the results as expected.

The prepared hybrid material was subjected to DTA-TG analysis in such a way that annealing and pyrolysis temperatures up to 1500 °C were kept for 2 hours in Argon medium (Figure 6.).

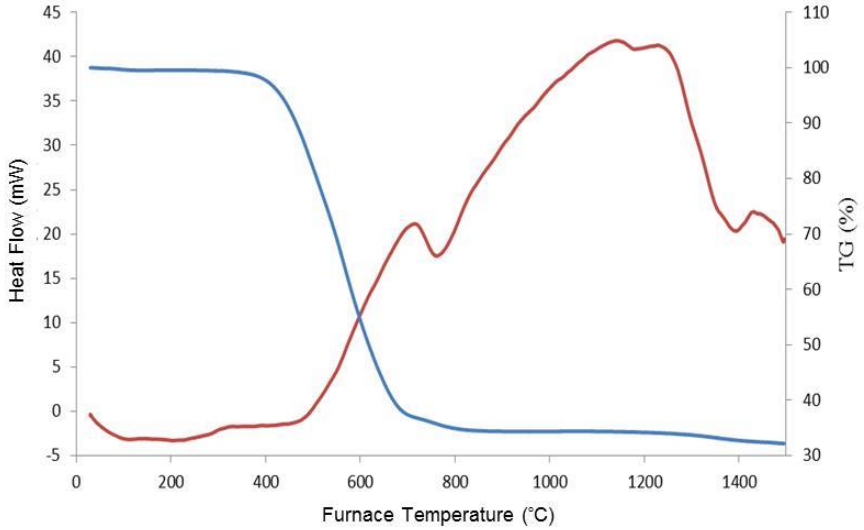

Fig. 6. DTA-TG analysis of hybrid powder up to 1500 °C

According to the results of the analysis, it was observed that weight loss occurred due to decomposition reactions between 400-800 °C. It was supported by the XRD result that the exothermic reaction at 1100 °C is the SiO_2 formation reaction and the exothermic reaction at 1400 °C is the SiC phase formation reaction.

According to the SEM analysis performed on the raw powder, it is seen that the structure is completely amorphous. EDX analysis was performed to determine the elemental constitution in the structure (Figure 7, Figure 8 and Table 3).

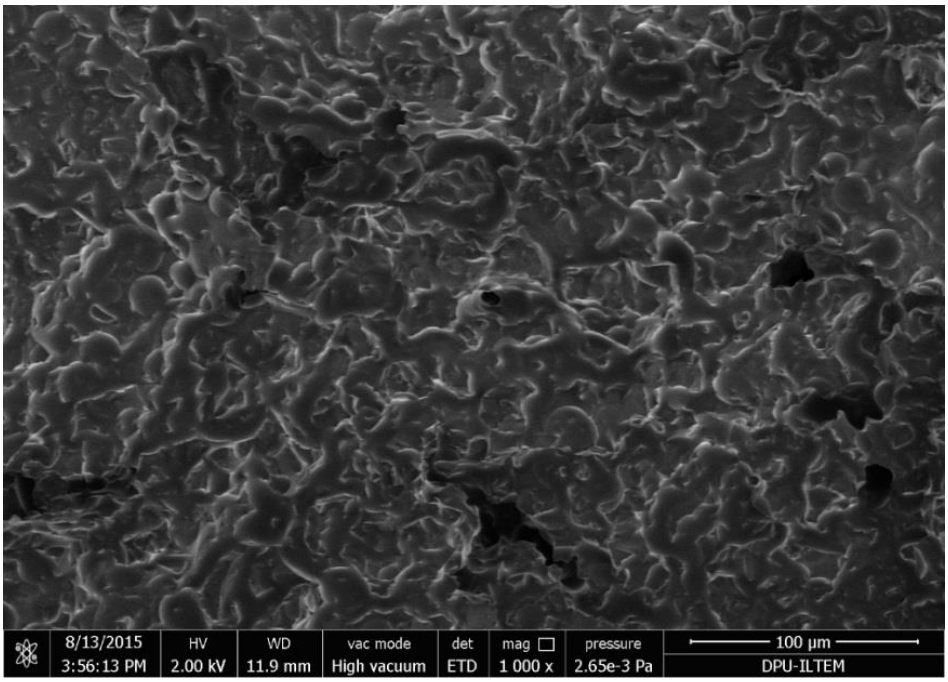

Fig. 7. SEM image of raw powder.

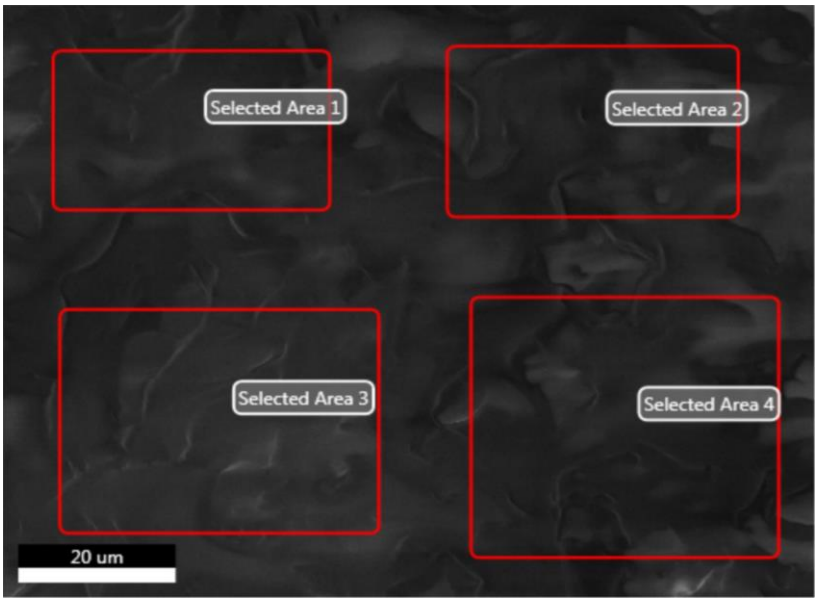

Fig. 8. EDX analysis of raw powder.

Table 3. Average EDX analysis of raw powder.

Element	By Weight (%)	atomic
Si	35.7	21.3
O	21.3	21.3
C	41.3	57.4

The SEM results of the sample subjected to heat treatment with high-temperature XRD are given in Figure 9.

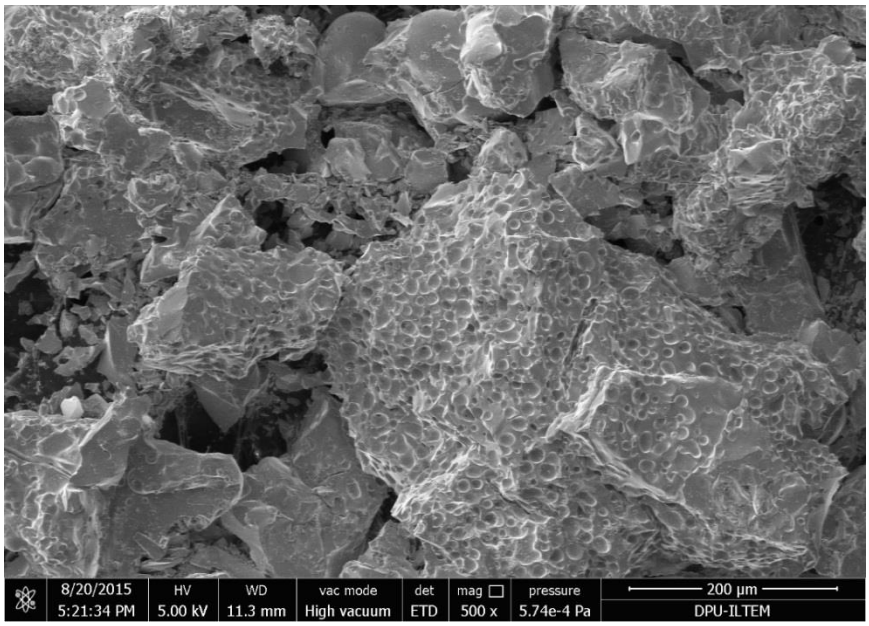
8/20/2015
5:21:34 PM
HV
5.00 kV
WD
11.3 mm
vac mode
High vacuum
det
ETD
mag
500 x
pressure
5.74e-4 Pa
200 µm
DPU-ILTEM

(a)

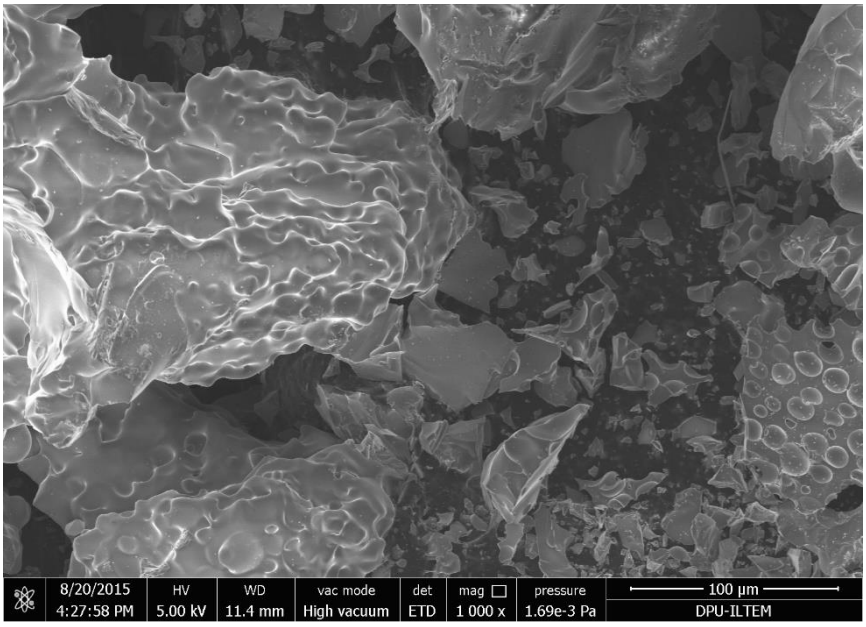
8/20/2015
4:27:58 PM
HV
5.00 kV
WD
11.4 mm
vac mode
High vacuum
det
ETD
mag
1 000 x
pressure
1.69e-3 Pa
100 µm
DPU-ILTEM

(b)

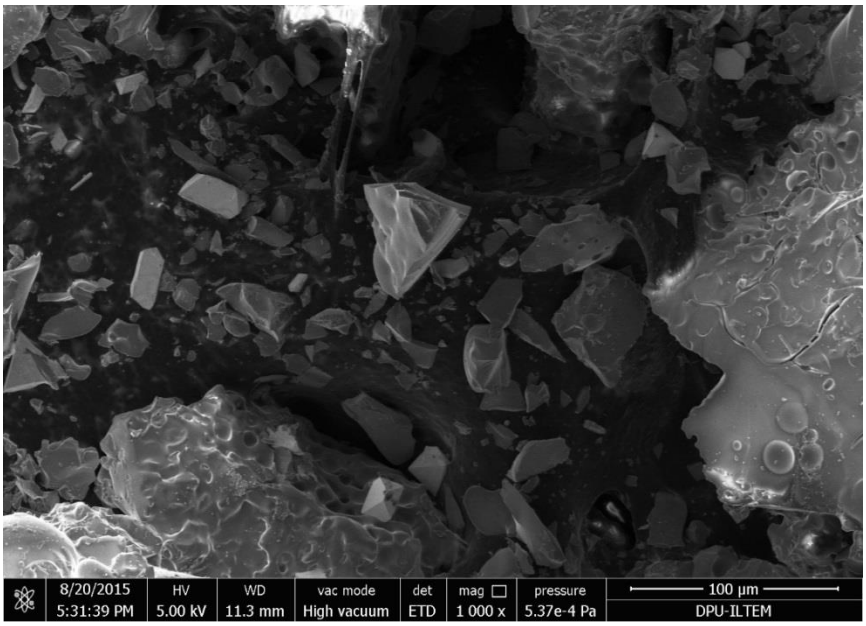

(c)

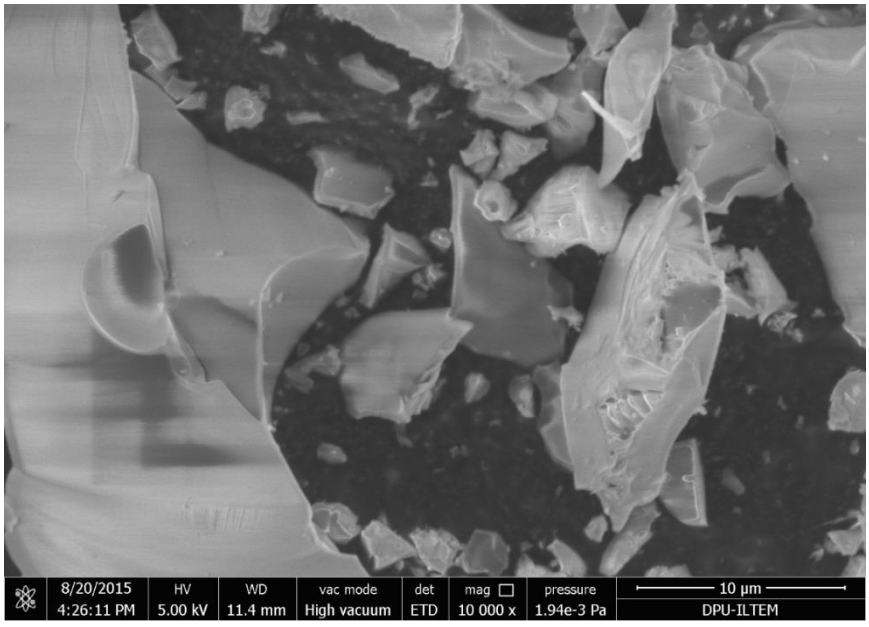

(d)

Fig. 9. SEM analysis of sample heat treated with high-temperature XRD (Sample holding for 2 hours at annealing(600 °C) and pyrolysis(1100 °C) temperature) a) 500X, b) 1000X, c) 5000X d) 10000X.

The amorphous composition in the morphology with the presence of crystalline structure were observed at the same time, and it was determined that porous structures were also present (Figure 9). As expected in the heat-treated sample, the decrease of C and O atoms was also revealed according to the EDX analysis (Figure 10 and Table 4.) [23].

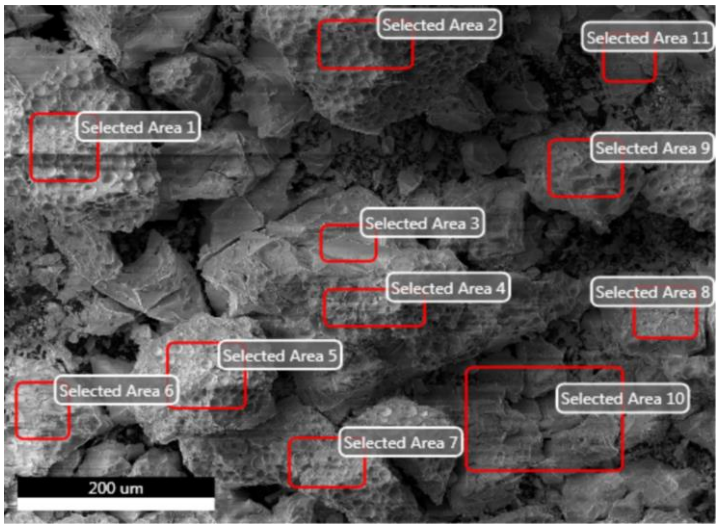

Fig. 10. EDX image of the heat-treated sample.

Table 4. Average EDX analysis of the heat-treated sample.

Element	By Weight (%)	atomic
Si	38,4	25,62
O	55,5	64.9
C	6	9,35

4. Conclusions

It has been observed that the polymer-derived sol gel method is a successful method for SiOC production. In particular, High temperature XRD was of great benefit to see how the structure changes with temperature. In the compositions prepared for organic-inorganic hybrid powder synthesis, it was observed that only increasing the solvent ratio had no effect on gelation. While the hybrid structure, which is the raw material of SiOC powder, is completely amorphous at room temperature it's seen from XRD and SEM result that the structure turns into a crystalline structure at 1500 °C. In this composition where the crystalline and amorphous structures coexist FT-IR analysis was used to investigate the bond structures and Si-O-Si and Si-C bonds were determined. It has been determined that the sintering regime has an effect on the microstructure, and it has been revealed that it has profound effects on phase formations and crystal size. Phase conversion reaction temperatures were determined in the base of XRD and DTA analysis results. The differences in the C and O atoms between the raw sample and the heat-treated sample were determined by EDX analysis.

Acknowledgment

This study is derived from the author's master's thesis on the Synthesis and Characterization of Polymer Derived Nanocrystalline SiOC Powders. We would like to thank Kütahya Dumlupınar University Advanced Technologies Center and analysis supervisors for their great help in carrying out the analyses used in experimental studies.

References

[1] L, Jıngjie., D, Qingwen., Y, C., Giuntini, D., & R. Riedel., (2023). Preparation of polymer-derived SiOC-Cu ceramic composites and their tribological performance, Journal of the European Ceramic Society, (in-press article).
[2] Y. J. Shim., S. H. Joo., H. J. Lee., K. W. Cho., & Y. J. Joo., (2023). The effect of temperature and atmospheric-pressure on mechanical and electrical properties of polymer-derived SiC fibers. Oper Ceramics, 15, 100431.
[3] G. J. Leonel., X. Guo., G. Singh., & A. Navrotsky., (2023). Chemistry, structure and thermodynamic stabilization of SiOC polymer derived ceramics made from commercial precursor. Open Ceramics, 15, 100402.
[4] K. Liu., W. Peng., D. Han., Y. Liang., B. Fan., H. Lu., H. Wang., H. Xu., R. Zhang., & G. Shao., (2023) Enhanced piezoresistivity of polymer-derived SiCN ceramics by regulating divinilybenzene-induced free carbon. Ceramics International, 49, 2296-2301.
[5] Y. Liu., K. Chen., F. Dong., S. Peng., Y. Cui., C. Zhang., K. Han., M. Yu., & H. Zhang., (2018). Effects of hydrolis of precursor on the structure and properties of polymer-derived SiBN ceramic fibers. Ceramics International, 44, 10199-10203.

[6] Z, C., X, Chen., X, Li., & G, S., (2023). Thin-film temperature sensor made from polymer-derived ceramics based on laser pyrolis. Sensors and Actuators: A. Physical, 350, 114144.
[7] Q, Yan., S, Chen., H, Shi., X, Wang., S, Meng., & J, Li., (2023). Fabrication of polymer-derived SiBCN ceramic temperature sensor with excellent sensing performance. Journal of the European Ceramic Society, 43, 7373-7380.
[8] X, Zhang., y, Zhang., L, Gou., B, Liu., Y, Wang., H, Li., H, Li., & J, Sun., (2024). Ablation resistance of ZrC coating modified by polymer-derived SiHfOC ceramic microspheres at ultrahigh temperature. Journal of Materials Science & Technology, 182, 119-131.
[9] Z, Li., & Y, Wang., (2017). Preparation of polymer-derived graphene-like carbon-silicon carbide nanocomposites as electromagnetic interference shielding material for high temperature applications. Journal of Alloys and Compounds, 709, 313-321.
[10] Y, Lu., Y, Sun., T, Zhang., F, Chen., L, Ye., & T, Zhao., (2019). Polymer-derived Ta_4HfC_5 nanoscale ultrahigh-temperature ceramics: Synthesis, microstructure and properties. Journal of the European Ceramic Society, 39, 205-211.
[11] M. A. Mazo, A. Nistal, A.C. Caballero, F. Rubio, J. Rubio, J.L. Oteo, (2013), Influence of processing conditions in TEOS/PDMS derived silicon oxycarbide materials. Part 1: Microstructure and properties Journal of the European Ceramic Society33,1195-1205.
[12] A. Klonczynski, R. Riedel, G. Mera and R. Hauser, (2006), " Silicon-Based Polymer-Derived Ceramics: Synthesis Properties and Applications-A Review, Journal of the Ceramic Society of Japan 114 (6), 425-444.
[13] P. Colombo, (2010), " Polymer-Derived Ceramics: 40 Years of Research and Innovation in Advanced Ceramics' ', Journal of American Ceramic Society, 93 (7), 1805-1837
[14] E. Bernardo, L. Fiocco, G. Parcianello, E. Storti, P. Colombo, (2014), "Advanced Ceramics from Preceramic Plymers Modified at the Nanoscale: A Review" Materials, 7, 1927-1956
[15] H. Zhang, C. G. Pantano, A. K. Singh, (1999), Silicon Oxycarbide Glasses, Journal of Sol-Gel Science and Technology, 14, 7-25
[16] Porte, L. & Sarte, A. (1989), Evidence for a silicon oxycarbide phase in the Nicalon silicon carbide fibre: Journal of Materials Science cilt 24 s.271–275.
[17] F. Babonneau, L. Bois and J. Livage, (1992), Silicon oxycarbides via sol-gel route: characterization of the pyrolysis process Journal of Non-Crystalline Solids 147-148, 280-284
[18] F. K. Chi, (1983) " Carbon-Containing Monolithic Glasses via the Sol-Gel Process' 'Ceram. Eng. Sci. Proc. 4, 704-717
[19] J. Rumble, (Ed.). (2017). CRC handbook of chemistry and physics.
[20] Y-L. Li, D. Su, H-J. An, X. Liu, F. Hou, J-Y. Li, X. Fu, (2010), Pyrolytic transformation of liquid precursors to shaped bulk ceramics, Journal of European Ceramic Society, 30, 1503-1511
[21] X. Wang, J. Qian, C. He, A. Shui, B. Du, (2023), The sutructural evolutions and enhanced thermal stability of Al cation-modified silicon oxycarbide ceramics, Journal of Sol-Gel Science and Technology, 106, 616-625
[22] D-S. Ruan, Y-L. Li, L. Wang, D. Su, F. Hou, (2010), Fabrication of silicon oxycarbide fibers from alkoxide solutions along the sol-gel process, Journal of Sol-Gel Science and Technology, 56, 184-190
[23] H, Tang., K, Wang., K, Ren., & Y, Wang., (2023). Microstructural evolation and microwave transmission/absorption transition in polymer-derived SiOC ceramics. Ceramics International, 49, 20406-20418.

Contents lists available at *Dergipark*

Journal of Scientific Reports-A

journal homepage: *https://dergipark.org.tr/tr/pub/jsr-a*

E-ISSN: 2687-6167 ***Number 55, December 2023***

RESEARCH ARTICLE

Receive Date: 26.10.2023 *Accepted Date: 15.11.2023*

Numerical Analysis for Investigation of Hydraulic Fracturing Potential of the Rockfill Dam

Sadettin Topçu[1]*,Evren Seyrek[2]

[1]*Assist.Prof.Dr., Kütahya Dumlupinar University, Kutahya Voc. School of Technical Sciences, Kutahya, Turkey, ORCID: 0000-0003-1306-2502*
[2]*Assoc.Prof.Dr., Kutahya Dumlupinar University, Civil Engineering Department, Kutahya, Turkey, ORCID: 0000-0003-4373-6723*

Abstract

Embankment dams may collapse because of internal erosion that develops in the crack developed in the upstream-downstream direction by hydraulic fracturing. It is known in the literature that many dams collapsed due to hydraulic fracturing. The hydraulic fracturing mechanism is defined as the propagation of an existing crack on the upstream face of the clay core under hydrostatic stresses or the formation of a new crack in low-stress zones by hydrostatic stress. The variety of materials and materials' mechanical properties generally affect the hydraulic fracturing potential. This study examined the effect of the deformation parameters (Elasticity modulus and Poisson ratio) of the impermeable curtain-function clay core material on the hydraulic fracturing potential. Normal Stress and Mohr-Coulomb methods were used to determine the hydraulic fracturing potential. The principal stress values required for these two methods were determined for the maximum cross-section of the clay-core rockfill type Çınarcık Dam by the finite element method. While the hydraulic fracturing potential is negligibly affected by the change of deformation parameters in the Normal Stress method, this effect is clearly seen in the Mohr-Coulomb method.

Keywords: Embankment dam; rockfill dam; hydraulic fracturing; Elasticity modulus; Poisson ratio.

1. Introduction

The concept of hydraulic fracturing is a complex problem that arises in embankment dams and a helpful process used to extract underground energy sources. Hydraulic fracturing (hydrofracking or hydrofracturing) is the technique

* Corresponding author. Tel.: +90-274-4436200
E-mail address: sadettin.topcu@dpu.edu.tr
http://dx.doi.org/10.1016/j.cviu.2017.00.000.

of injecting water and chemicals into the bedrock formation at high pressure through a typical well to create new cracks or to increase the size and connectivity of existing cracks to extract gas and oil from the formation [1]. The most general description of hydraulic fracturing for embankment dams is the growth of existing cracks in low-stress zones on the upstream surface with the impact of the hydrostatic pressure in the reservoir or the formation of a new crack with the same effect [2,3]. Hydraulic fracturing can theoretically occur in homogeneous earth-fill dams but is more likely to occur in zoned earth-fill dams when materials have different deformation and permeability characteristics [4]. Accordingly, it is an issue that threatens dam safety by causing internal erosion with the formation of transverse and horizontal cracks in the upstream-downstream direction, especially in clay-core rockfill dams [5,6]. Balderhead, Hyttejuvet, Viddalstavn, Teton, and Yard's Creek Dams are world-renowned for observing hydraulic fracturing [7].

As mentioned above, stress conditions in the environment where the failure occurs are crucial for hydraulic fracturing. Hydraulic fracturing potential also increases where transverse, longitudinal, and local arching occurs in embankment dams [8]. Because the elasticity modulus of the clay core in clay core rockfill dams is less than that of the rock utilized in the shell, the clay core will want to settle more due to the loads coming from above. For this case, vertical loads are transmitted to the shell, and transverse arching occurs. This leads to a vertical stress reduction, particularly in the portion of the clay core close to the shell. Longitudinal arching is another type caused by stress transfer to the abutments in dams constructed in narrow valleys. On the other hand, local arching occurs at the contact surface of the outlet conduit and spillway with the embankment. In addition, low-stress zones may occur due to irregularities, discontinuities, and differential settlements that will develop from surfaces with a stepped profile on the abutment [9,10]. If the dam foundation has compressible alluvial soil, transverse cracks may develop due to low-stress zones resulting from differential settlements [11]. Tension zones may occur when arching and differential settlements occur, and tension cracks may develop [12].

There are different failure approaches in the literature for the mechanism of hydraulic fracturing, defined as failure due to hydrostatic pressure in dams. The cracks expanded under shear failure [13-15] and under tensile failure [3,16-19], as well as cases where both shear and tensile failure occur together [20-22], are also available. There are also conflicting approaches regarding the presence or absence of pre-existing fractures in the embankments for hydraulic fracturing development. Therefore, two critical conditions for hydraulic fracturing initiation come to the fore. These are the low-stress zones formed due to arching and differential settlements that facilitate the development of hydraulic fracturing and the state of the existing cracks occurring due to the same factors [23]. According to Wang [24], hydraulic fracturing development requires rapid impounding, unsaturated core soil with low permeability and an upstream-downstream crack.

The method for determining the hydrostatic pressure that causes hydraulic fracturing is divided into three categories: empirical methods based on field or laboratory experiments [3,14,25], a theoretical model based on the progression of the circular cylindrical cavity under triaxial stress conditions [26], and the conceptual model based on fracture mechanics theories [27]. In addition, the hydraulic fracturing potential can be estimated by Nobari et al., [17] known as the normal stress criterion. Knowing the stress conditions developed in embankment dams for the normal stress criterion approach and empirical and theoretical models in estimating the hydraulic fracturing potential is necessary. For this reason, 2D or 3D numerical analyses must be performed for embankment dams when evaluating the hydraulic failure potential.

In recent years, hydraulic fracturing has been widely evaluated through studies based on finite element method numerical analysis [28,29]. For dams where hydraulic fracturing is observed, hydraulic fracturing is provided by numerical analysis [30-32].

In this paper, finite element analyses were performed to obtain the effect of the clay cores' deformation parameters on the behaviour of hydraulic fracturing of a clay-core rockfill dam. Numerical analyses containing 18 different combinations of Elasticity modulus and Poisson ratio of clay core were used to calculate the principal stress values required to determine hydraulic fracturing potential. After the analyses, it was seen that the result based on

the Mohr-Coulomb criterion was affected by the clay core deformation parameters; in the normal stress criterion, this effect was determined to be negligible.

2. Material and method

In this paper, the cross section of the Çınarcık Dam, located in Bursa, the fourth largest city in Turkey, was used to investigate the influence of the deformation parameters (E,ν) of the clay material used as an impervious core on the hydraulic fracturing potential. Çınarcık Dam was built on the Orhaneli stream and has a height of 125. m from the thalweg. It is located south of the Marmara Region at the coordinates of 40.01611°N and 28.77389°E (Fig. 1). It was operated in 2002 as a clay-core rockfill dam for drinking water, agricultural irrigation, and energy production. In the granular filter design of Çınarcık Dam, a crack-stopper filter arranged in the form of sand-gravel-rock rubble from fine to coarse material was used. Crack-stopper filters are recommended to prevent collapse due to internal erosion, especially in cracks formed in the upstream-downstream direction that may develop due to seismic ground movements [33].

Fig. 1. Location of Çınarcık Dam.

Normal stress and the Mohr-Coulomb criterion were used to determine the hydraulic fracturing potential within the scope of the study. The maximum cross-section of Çınarcık Dam is illustrated in Fig. 2.

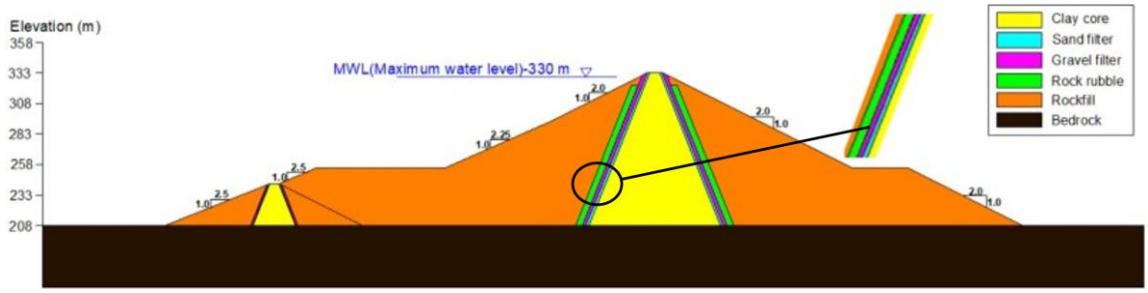

Fig. 2. Maximum cross-section of Çınarcık Dam.

2.1. The Normal Stress Criterion (Nobari et al. [17])

The normal stress criterion (NSC) compares the major principal stresses occurring on the upstream face of the clay core with the hydrostatic stresses acting on this face. When calculating the hydrostatic stresses, the maximum water level is considered the origin point. If the factor of safety (FS) is calculated when the maximum principal stresses (σ_1) at any level are in proportion to the hydrostatic stress (P_h) resulting from the reservoir water level is less than 1, hydraulic fracturing potential can be mentioned (Eq.1).

$$FS = \frac{\sigma_1}{P_h} \tag{1}$$

In the normal stress criterion, the walls of the cracks formed by the action of hydrostatic stresses are assumed to be in the horizontal plane. In this method, based on the principle of tensile failure, the tensile strength of clay soils is conservatively considered to be 0.

2.2. Mohr-Coulomb Criterion (Yanagisawa and Panah [15])

According to the Mohr-Coulomb criterion (MCC), it is stated that the planes where hydraulic fracturing occurs are shear failure planes based on total stress. In this method, hydrostatic stresses (P_f) that cause hydraulic fracturing, undrained shear strength parameters of clay soils (ϕ_u: undrained internal friction angle, c_u: undrained interception of cohesion), and major (σ_1) and minor (σ_3) principal stresses are considered. It is calculated as shown in Eq.2. When the calculated hydrostatic stresses (P_f) are in proportion to the reservoir-derived hydrostatic stresses (P_h) acting on the upstream face, the factor of safety obtained with FS= P_f/P_h is less than 1. Then, it is accepted that hydraulic fracturing will occur in the shear plane.

$$P_f = (1.5\sigma_3 - 0.5\sigma_1) \times \left(1 + \sin\phi_u\right) + 2c_u.\cos\phi_u \tag{2}$$

Undrained shear strength parameters must be considered realistically for this method to determine the hydraulic fracturing potential accurately.

3. Numerical Analysis

Geostudio 2018/R2 program was used for the principal stress values required to determine hydraulic fracturing potential using the methods described above. The analyses were carried out under two-dimensional plain strain conditions. The finite element method was applied as the calculation method. Analyzes were carried out in 18 different combinations to investigate the change in hydraulic fracturing potential if the clay core material had different deformation parameters (Table 1). These combinations include six different elasticity modulus (15000, 20000, 25000, 30000, 35000 and 40000 kPa) and three Poisson ratio (0.35, 0.40 and 0.45) values of core material. Material properties of foundation, shell, and transition zones were kept constant.

Table 1. Deformation parameters considered for clay core material.

Model No	Elasticity Modulus, E (kPa)	Poisson ratio, ν	Model No	Elasticity Modulus, E (kPa)	Poisson ratio, ν
1	15000	0.35	10	30000	0.35
2	15000	0.40	11	30000	0.40

3	15000	0.45	12	30000	0.45
4	20000	0.35	13	35000	0.35
5	20000	0.40	14	35000	0.40
6	20000	0.45	15	35000	0.45
7	25000	0.35	16	40000	0.35
8	25000	0.40	17	40000	0.40
9	25000	0.45	18	40000	0.45

The design parameters of the materials in the foundation, shell, and transition zones in the embankment dam cross-section were taken from the literature to reflect their characteristic values. These material zones are defined by the linear-elastic material model (Table 2). The Mohr-Coulomb material model was chosen for the clay core. Literature was adhered to for undrained shear strength parameters, and reasonable values were taken (c_u=75 kPa; ϕ_u=10^o).

Table 2. Design parameters of materials in foundation, shell, and transition zones.

Material	Elasticity Modulus, E (kPa)	Poisson ratio, ν	Unit weight (kN/m^3)
Bedrock	20x10^6	0.15	16.0
Rockfill	20x10^4	0.25	20.0
Rock rubble	50x10^3	0.28	19.5
Gravel Filter	40x10^3	0.30	19.0
Sand Filter	30x10^3	0.30	19.0

The maximum cross section of Çınarcık Dam was transformed into a geometric model consisting of 1498 nodes and 1440 quads&triangles elements in numerical analysis (Fig. 3). The geometric model defines boundary conditions around the bedrock, excluding the reservoir and downstream sides. While the base of the bedrock is limited to displacement in both directions, the sides of the bedrock are limited to displacement only in the horizontal direction.

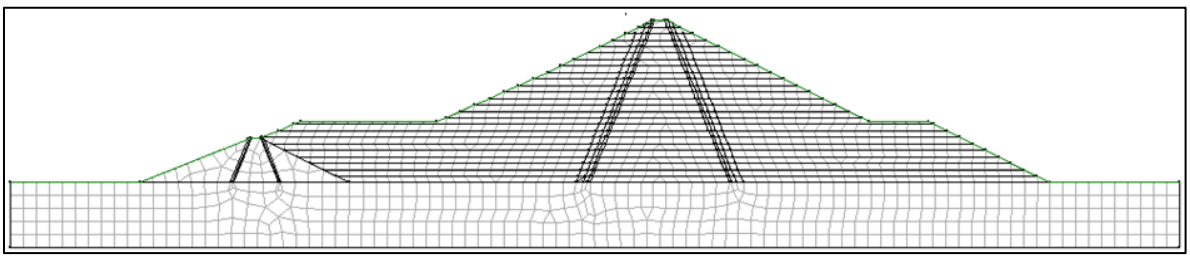

Fig. 3. Geometric model for maximum cross-section of Çınarcık Dam.

The numerical analysis considered the stress-deformation behaviour observed during the embankment dam construction. For this purpose, the analysis stages were carried out as follows:

- Modeling the stress conditions in the underlying bedrock.
- Complete modeling of the upstream cofferdam.
- Creation of stresses by modeling the main dam fill in 25 layers step by step.
- Water retention in the reservoir in 3 stages and modeling of hydrostatic stresses.

In addition, at each reservoir impounding stage, buoyancy forces are applied to the materials in the shell and transition zones below the reservoir water level by calculating the submerged unit weights. At each stage, the analysis is continued by reducing the elasticity modules by half for the shell and transition zone materials.

4. Analyses Results

4.1. Stress and Deformation

Several analyses, including 18 combinations given in Table 1, were carried out for the determination of stresses and deformations in the body of Çınarcık Dam. To not exceed the page limit, all combinations' stress and deformation contours are not given; the contours of Model 18 are provided as an example in Fig. 4-7. As seen in Fig. 4, the maximum total stress after the water impoundment occurred at the bottom of the shell and adjacent to the corners of the core. Also, the reduction of maximum total stress in the clay core can be seen in Fig. 4.

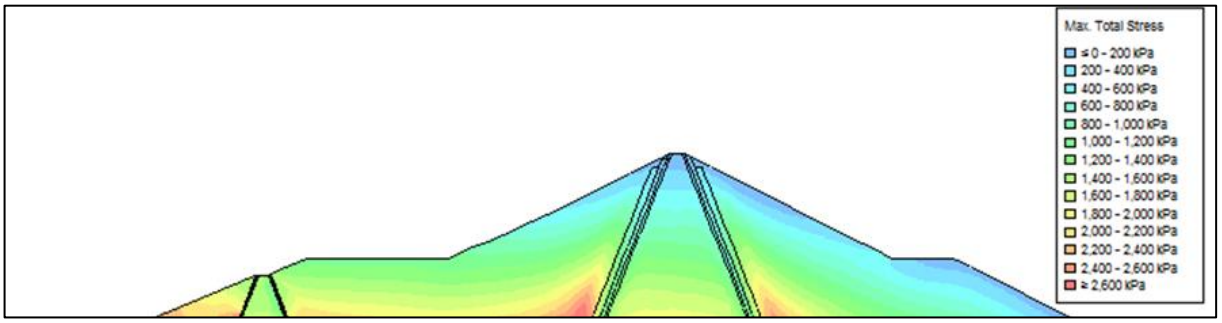

Fig. 4. Contour of the maximum total stress.

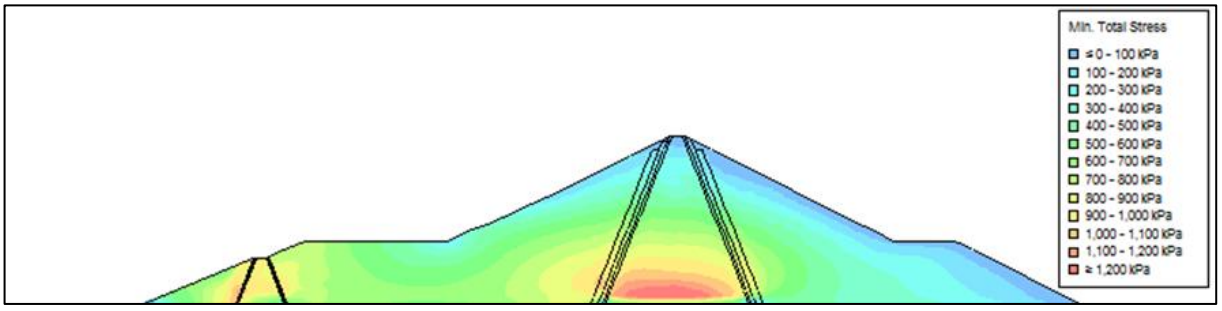

Fig. 5. Contour of the minimum total stress.

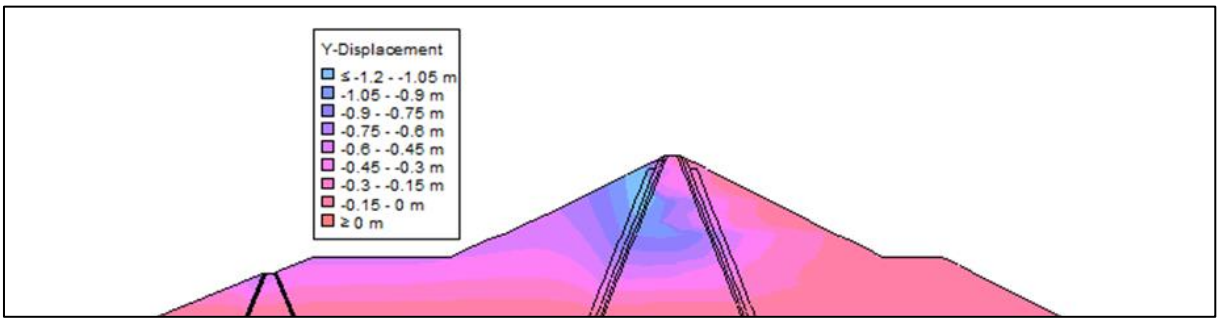

Fig. 6. Contour of the vertical deformations.

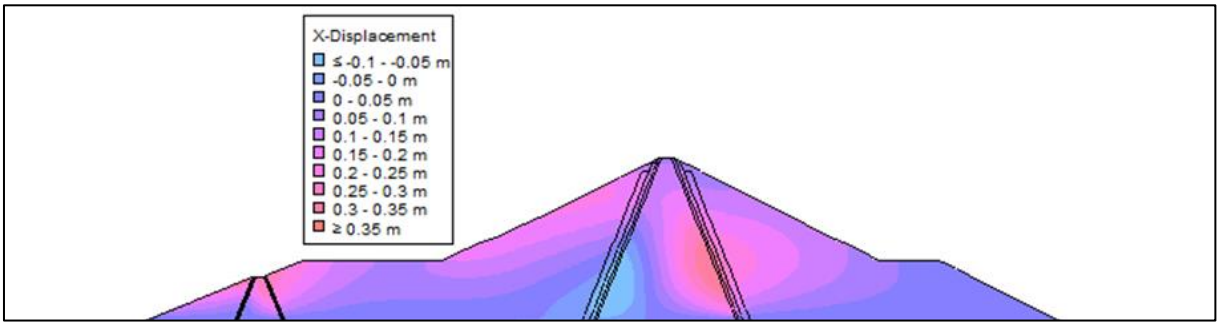

Fig. 7. Contour of the horizontal deformations.

4.2. Hydraulic Fracturing

To determine the factor of safety against hydraulic fracturing to occur on the upstream face of the clay core, major and minor principles stress values obtained from finite element analyses discussed above were used. Calculated variations of the factor of safety against hydraulic fracturing of the Çınarcık dam with depth are illustrated in Fig. 8. The graphs in the upper part of Fig. 8. were obtained according to the MCC, and the graphs in the lower part were obtained by using NSC.

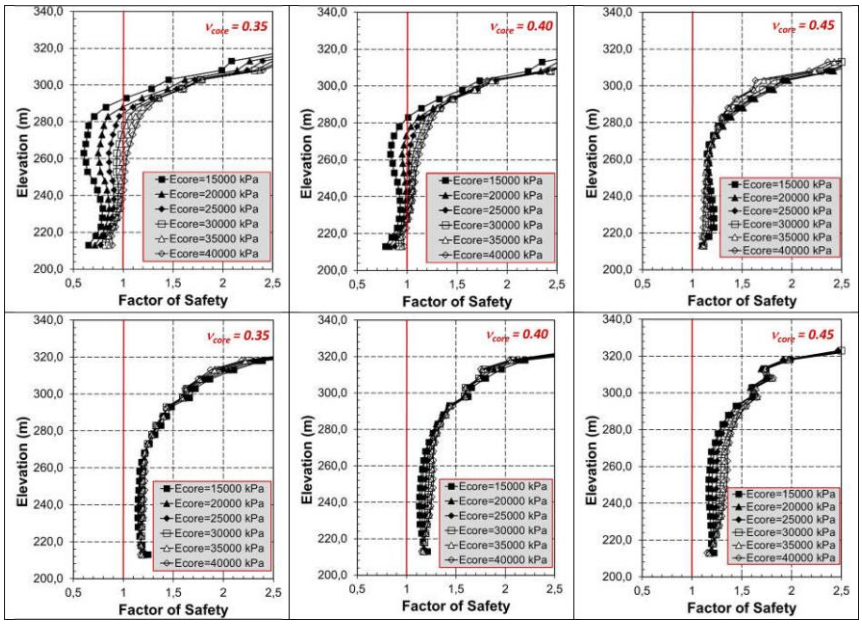

Fig. 8. Variation of a factor of safety against hydraulic fracturing with depth for constant poisson ratio values.

As can be seen in Fig. 8, there is no hydraulic potential for the selected Elasticity Modulus and Poisson ratio values for the clay core based on NSC. Contrary to NSC, in the MCC, it is understood that the factor of safety values is affected by the deformation parameter values of the clay core, especially at the middle and lower levels of the dam. In the MCC, the factor of safety values also increases with the increment of the elasticity modulus and Poisson ratio. But this increase is not noteworthy for the case where the Poisson ratio is 0.45.

To more clearly interpret the variation of the factor of safety values based on the MCC and NSC method, Fig. 9 and Fig. 10 were illustrated, respectively. According to Fig. 9, in cases where the elasticity modulus is 15000 kPa, 20000 kPa, and 25000 kPa, rising the Poisson ratio from 0.35 to 0.45 increases the F.S. values. In comparison, this increase remains limited when the elasticity modulus is 30000 kPa, 35000 kPa, and 40000 kPa. Another important point in Fig. 9 is that with the increase in the elasticity modulus, the zone of the hydraulic fracturing potential becomes smaller, and hydraulic fracturing is expected to occur, especially in the lower part of the dam. When the factor of safety values calculated based on NSC was investigated, it was seen that there was no hydraulic fracturing potential.

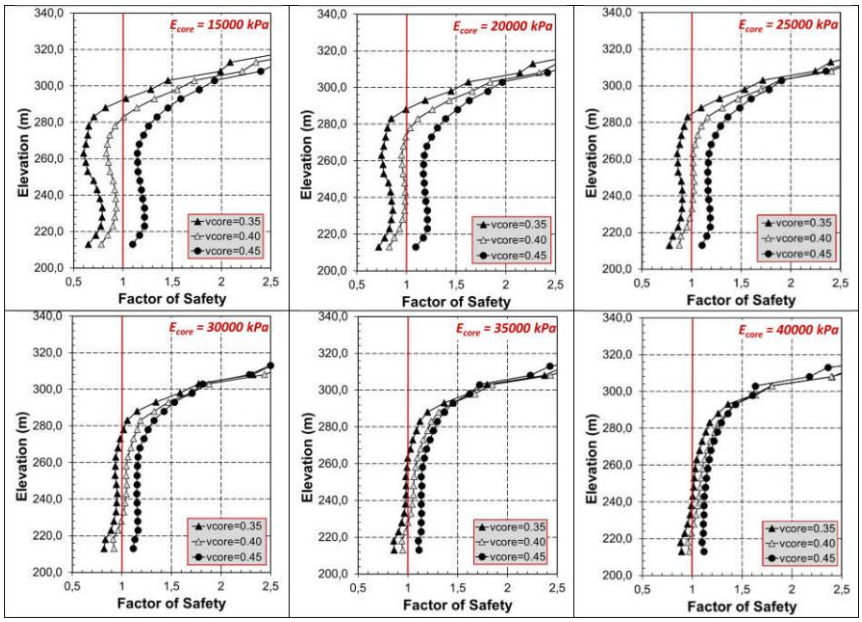

Fig. 9. Variation of the factor of safety against hydraulic fracturing with depth for constant elasticity modulus values by using MCC.

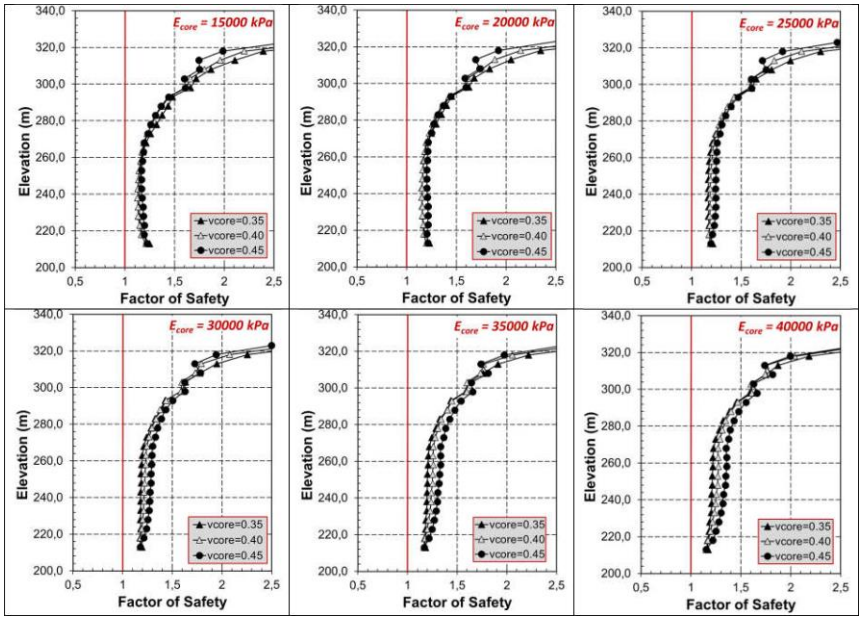

Fig. 10. Variation of the factor of safety against hydraulic fracturing with depth for constant poisson ratio values by using NSC.

Minimum values of the factor of safety for 18 different combinations and the location of the point corresponding to this value are given in Table 3. According to the MCC method, the minimum factor of safety values varies

between 0.603 and 1.113. In the same method, the points having minimum factor of safety values are located between 0.040 and 0.080 of the z/H value except for Model 1 (E=15000 kPa and ν=0.30). This difference can be explained by the fact that Model 1 has the smallest Elasticity Modulus and Poisson ratio in the clay-core among 18 different combinations. It should be stated that minimum value of the factor of safety are also obtained for Model 1. For the NSC method, the factor of safety values is greater than 1.0 in 18 different combinations.

Table 3. Minimum factor of safety values and corresponding location as depth (z/H).

Model No	MCC*		NSC**		Model No	MCC		NSC	
	FS_{min}	z/H***	FS_{min}	z/H		FS_{min}	z/H	FS_{min}	z/H
1	0.603	0.440	1.143	0.240	10	0.821	0.040	1.176	0.080
2	0.780	0.040	1.128	0.240	11	0.911	0.080	1.174	0.040
3	1.098	0.040	1.153	0.040	12	1.113	0.040	1.178	0.040
4	0.719	0.040	1.154	0.240	13	0.857	0.080	1.173	0.080
5	0.827	0.040	1.153	0.240	14	0.939	0.080	1.163	0.040
6	1.092	0.040	1.176	0.040	15	1.105	0.080	1.167	0.040
7	0.775	0.040	1.167	0.280	16	0.885	0.080	1.167	0.080
8	0.877	0.040	1.176	0.080	17	0.956	0.080	1.151	0.040
9	1.106	0.040	1.193	0.040	18	1.097	0.080	1.152	0.040

* MCC: Mohr-Coulomb Criterion

** NSC: Normal Stress Criterion

*** z: Height from dam foundation (m) H: Dam height (m)

5. Conclusions

This paper investigated the influence of deformation characteristics of clay core on the behaviour of hydraulic fracturing of a rockfill dam. For this purpose, eighteen combinations including six elasticity modulus values and three Poisson ratio values were established. It should be stated the geometry and other zones of the dam was kept just to see the effect of clay core material in the series of numerical analysis. Numerical analysis shows that:

- According to the MCC method, the minimum factor of safety values varies between 0.603 and 1.113.
- The factor of safety values is greater than 1.0 in the NSC method for all combinations.
- The factor of safety values is affected by the Elasticity Modulus and Poisson ratio values of the clay core, especially at the middle and lower levels of the dam for the MCC method.
- The factor of safety values also increases with the increment of the Poisson ratio and elasticity modulus. But, this increase is not noteworthy for the case where the Poisson ratio is 0.45.
- The zone of the hydraulic fracturing potential becomes smaller and hydraulic fracturing is expected to occur especially in the lower part of the dam with the increase in the elasticity modulus in the MCC method.

Results given above show that, hydraulic fracturing potential is closely related deformation characteristics of clay core. It is not possible to claim that this is the only effect. In the future, when more detailed studies including variations in the properties of the transition zone and shell material with the variations in the clay core parameters will be performed, results will be guiding the professionals working on dam engineering.

Acknowledgements

This research received no specific grants from any funding agency in public, commercial or non-profit sectors.

References

[1] United States Geological Survey (USGS). "Hydraulic Fracturing." usgs.gov. https://www.usgs.gov/mission-areas/waterresources/science/hydraulicfracturing#:~:text=Hydraulic%20fracturing%20(informally%20known%20as,bedrock%20formation%20via%20a%20well (accessed November, 2, 2023).
[2] S. Topçu, "Kil çekirdekli kaya dolgu barajlarda hidrolik çatlama potansiyelinin tahmin edilmesi," DSİ Teknik Bülten, 125, 1-7, 2017, https://dsiteknikbulteni.dsi.gov.tr/.
[3] G.W. Jaworski, J.M. Duncan, H.B. Seed, "Laboratory study of hydraulic fracturing," Journal of the Geotechnical Engineering Division, 107(6): pp. 713–732, 1981, https://doi.org/10.1061/AJGEB6.0001147.
[4] J.L. Sherard, "Embankment dam cracking," in: *Embankment-Dam Engineering (Casagrande Volume)*, R.C. Hirschfeld and S.J. Poulos, Eds. New York, USA: John Wiley, 1973, pp. 324–328.
[5] R. Fell, M, Foster, R. Davidson, J. Cyganiewicz, G. Sills, N. Vroman, "A Unified method for estimating probabilities of failure of embankment dams by internal erosion and piping," The University of New South Wales, Sydney, Australia, UNICIV Report R-446, 10–8, 2009.
[6] USBR, "Internal erosion risks for embankments and foundations," U.S. Bureau of Reclamation, Denver, CO, Technical Report IV-4, 2019, https://www.usbr.gov/damsafety/risk/BestPractices/Chapters/D6-InternalErosionRisksForEmbankmentsAndFoundationsWithAppendices.pdf.
[7] K.Y. Lo, K. Kaniaru, "Hydraulic fracture in earth and rock-fill dams," Canadian Geotechnical Journal, 27, pp. 496- 506, 1990, https://doi.org/10.1139/t90-064.
[8] M.M. Rezaei, B. Salehi, "The effect of changing the geometry and compaction degree on arching of earth dams," in Geo-Frontiers 2011: Advances in Geotechnical Engineering, 2011, pp. 3207- 3216, https://doi.org/10.1061/41165(397)328.
[9] H.N. Bui, R. Fell, C. Song, "Two and three dimensional numerical modeling of the potential for cracking of embankment dams during construction," The University of New South Wales, Sydney, Australia, UNICIV Report R-426, 2009, https://vm.civeng.unsw.edu.au/uniciv/R-426.pdf.
[10] K. He, C. Song, R. Fell, "Assessing potential cracking zones in embankment dams," in 23rd Australasian Conference on the Mechanics of Structures and Materials (ACMSM23), 2014, vol. II, Byron Bay, NSW, 9-12 December, Southern Cross University, Lismore, NSW, pp.721–726, https://espace.library.uq.edu.au/records/search?page=1&pageSize=20&sortBy=score&sortDirection=Desc&searchQueryParams%5Ball%5D=Proceedings+of+the+23rd+Australasian+Conference+on+the+Mechanics+of+Structures+and+Materials+(ACMSM23).
[11] K. Narita, "Design and construction of embankment dams." Department of Civil Engineering, Aichi Institute of Technology, 2000, https://aitech.ac.jp/~narita/tembankmentdam1.pdf.
[12] H. Tosun, S. Topçu "Toprak dolgu barajlarda hidrolik çatlama," Uluslararası Katılımlı IV. Ulusal Baraj Güvenliği Sempozyumu, Elazığ, Türkiye, s.519-530, 2014, https://www.barajguvenligi.com/yayin/584/4-ulusal-baraj-guvenligi-sempozyumu-2014.
[13] P.R. Vaughan, "The use of hydraulic fracture tests to detect crack formation in embankment dam cores," Department of Civil Engineering, Imperial College, UK, Interim Report, 1971.
[14] A. Mori, M. Tamura, "Hydrofracturing pressure of cohesive soils," Soils and Foundations, 27 (1), pp. 14–22, 1987, https://doi.org/10.3208/sandf1972.27.14.
[15] E. Yanagisawa, A.K. Panah, "Two dimensional study of hydraulic fracturing criteria in cohesive soils," Soils and Foundations, 34, pp. 1–9, 1994, https://doi.org/10.3208/sandf1972.34.1.
[16] I. Torblaa, B. Kjoernsli, "Leakage through horizontal cracks in the core of Hyttejuvet Dam," Norwegian Geotechnical Institute Publication, Issue 80, pp. 39-47, 1968, https://trid.trb.org/view/122553.

[17] E. Nobari, K.L. Lee, J.M. Duncan, "Hydraulic fracturing in zoned earth and rockfill dams: a report of an investigation," California Univ Berkeley Coll of Engineering, USA, DTIC Document, 1973, https://erdc-library.erdc.dren.mil/jspui/handle/11681/20528.
[18] S. Nishimura, H. Shimizu, "A study of the measurement of fracture toughness in cohesive soil —relationship between the size of initial crack and diameter of specimen," Paddy and Water Environment, 2: pp. 27–32, 2004, https://doi.org/10.1007/s10333-004-0036-5.
[19] S. Nishimura, "Occurrence of extensile cracks in cohesive soils due to compression," Soils and Foundations, 45, pp. 1–8, 2005, https://doi.org/10.3208/sandf.45.3_1.
[20] J.J. Wang, J.G. Zhu, C.F. Chiu, H.J. Chai, "Experimental study on fracture behaviour of a silty clay," Geotechnical Testing Journal, 30, pp. 303–311, 2007, DOI: 10.1520/GTJ100715.
[21] J.J. Wang, H.P. Zhang, M.J. Zhao, X. Lin, "Mechanisms of hydraulic fracturing in cohesive soil," Water Science and Engineering, 2, pp. 95–102, 2009, https://doi.org/10.3882/j.issn.1674-2370.2009.04.009.
[22] J.J. Wang, Y.X. Liu, "Hydraulic fracturing in a cubic soil specimen," Soil Mechanics and Foundation Engineering, 47, pp. 136–142, 2010, https://doi.org/10.1007/s11204-010-9101-9.
[23] D.Q. Tran, S. Nishimura, M. Senge, T. Nishiyama, "Risk of embankment dam failure from viewpoint of hydraulic fracturing: Statistics, mechanism, and measures," Reviews in Agricultural Science, 8, pp. 216-229, 2020, https://doi.org/10.7831/ras.8.0_216.
[24] J.J. Wang, "Hydraulic fracturing in earth-rock fill dams," John Wiley & Sons, 2014.
[25] A. Ghanbari, S.S. Rad, "Development of an Empirical Criterion for Predicting the Hydraulic Fracturing in the Core of Earth Dams," Acta Geotechnica,10(2), pp. 243–254. 2015, https://doi.org/10.1007/s11440-013-0263-2.
[26] A.K. Panah, E. Yanagisawa, "Laboratory studies on hydraulic fracturing criteria in soil," Soils and Foundations 29(4), pp. 14–22, 1989, https://doi.org/10.3208/sandf1972.29.4_14.
[27] L.C. Murdoch, "Hydraulic fracturing of soil during laboratory experiments, part 1 methods and observations," Geotechnique 43(2), pp. 255–266, 1993, https://doi.org/10.1680/geot.1993.43.2.255.
[28] Z. Liu, C. Wang, "The analysis of stress, deformation and arch effect of the Lianghekou earth-rockfill dam," Indian Geotech J 46(1), pp. 77–84, 2016, https://doi.org/10.1007/s40098-015-0154-6.
[29] P. Talukdar, A. Dey, "Finite element analysis for identifying locations of cracking and hydraulic fracturing in homogeneous earthen dams," International Journal of Geo-Engineering, 12(1), pp. 1-26, 2021, https://doi.org/10.1186/s40703-020-00139-8.
[30] D.Q. Tran, S. Nishimura, M. Senge, T. Nishiyama, "Research on cause of dam failure from viewpoint of hydraulic fracturing–case study of a dam failure in Vietnam," GEOMATE Journal, 14(41), pp. 86-94, 2018, https://geomatejournal.com/geomate.
[31] S.K. Razavi, B.M. Hajialilue, A. Dabaghian, "Investigation into the internal erosion and local settlement of Esfarayen Earth-Fill Dam," Journal of Geotechnical and Geoenvironmental Engineering, 146(4), 4020006–4020013, 2020, https://doi.org/10.1061/(ASCE)GT.1943-5606.0002216.
[32] M. Salari, A. Akhtarpour, A. Ekramifard, "Hydraulic fracturing: a main cause of initiating internal erosion in a high earth-rock fill dam," International Journal of Geotechnical Engineering, 15(2), pp. 207-219, 2021, https://doi.org/10.1080/19386362.2018.1500122.
[33] USBR, "Design standard no. 13-Embankment dams, protective filters," U.S. Department of Interior Bureau of Reclamation, p.1-191, 2011, https://www.usbr.gov/tsc/techreferences/designstandards-datacollectionguides/finalds-pdfs/DS13-5.pdf.

Contents lists available at *Dergipark*

Journal of Scientific Reports-A

journal homepage: *https://dergipark.org.tr/tr/pub/jsr-a*

E-ISSN: 2687-6167 ***Number 55, December 2023***

RESEARCH ARTICLE

Receive Date: 02.09.2023 *Accepted Date: 21.11.2023*

Determination of mechanical performance of boric acid filled polypropylene based polymer composites

Hüseyin Ünal[1]*, Salih Hakan Yetgin[2], Sinan Köse[3]

[1]* *Sakarya University of Applied Sciences, Faculty of Technology, Metallurgy and Materials Eng. Department, 54050, Sakarya, Türkiye, ORCID: 0000-0003-0521-6647*

[2] *Tarsus University, Faculty of Engineering, Department of Mechanical Engineering, 33400, Mersin, Türkiye, ORCID: 0000-0002-6068-9204*

[3] *Tarsus University, Vocatıonal School Of Technıcal Sciences at Mersin Tarsus Organized Industrial Zone, Department of Machinery and Metal Technologies, 33100, Mersin, Türkiye, ORCID: 0000-0002-6224-3388*

Abstract

Polypropylene (PP) polymer, which is one of the indispensable materials of our daily life and stands out with its lightness, low cost and chemical resistance properties in the industry, was used. In industrial applications where the properties of polymers without additives are not sufficient, composite materials are produced by adding some additives to the polymer. In this experimental study, the mechanical properties of composites produced by adding boric acid (BA) to PP polymer at 5 wt.% (PP/5BA), 10 wt.% (PP/10BA) and 15 wt.% (PP/15BA) ratios were investigated. the effect of both BA filler and optimum BA filler ratio on mechanical properties were investigated. In the production of PP/BA composites, granules were first produced in an industrial twin screw extruder. Then, PP/BA composite tensile and impact test specimens were moulded on a conventional injection moulding machine. As a result, it was observed that the tensile modulus, tensile and yield strength of the composite materials decreased with increasing boric acid filler content in PP polymer. Depending on the boric acid filler content, the tensile strength decreased by an average of 18.3% and the breaking strength decreased by 14.8%. The lowest tensile modulus was obtained with a value of 2713 MPa at 10wt.% boric acid filler addition. The impact strength increased slightly at 5 wt.% boric acid filler addition and decreased at 10wt.% and 15wt.% boric acid filler addition.

Keywords: Polypropylene; boric asit; mechanical properties; composite

* Corresponding author. Tel.: +90 264 295 6490
E-mail address: unal@sakarya.edu.tr

.

1. Introduction

Nowadays, polymer-based composite materials (PCMs) are widely used in different industrial applications due to their high mechanical properties, low density and ease of industrial production. Polypropylene (PP) polymer is a semi-crystalline thermoplastic polymer and is one of the most promising and widely used polymers for the production of structural PCMs. Polypropylene (PP) is one of the important thermoplastic materials with low density (0.90 g/cm^3), easy processability, high strength, excellent chemical resistance, high thermal stability and low cost/price. Due to these properties, PP polymer is used in many industrial areas such as the automotive industry, health sector, food sector, construction sector and space sector [1]. In order to produce polymer composites, some additives are added to the polymer main matrix and the desired properties are tried to be obtained. These additives can sometimes be macro-sized minerals such as talc, calcite, kaolin, glass balls, titanium dioxide, copper powders, and sometimes nano-sized clays or metal powders. One of these additives is boric acid additive. Boric acid (H_3BO_3 or $B(OH)_3$), also called boracic acid or orthoboric acid, is obtained by the reaction of white powdered colemanite ore with sulfuric acid or borax with a mineral acid. Boric acid is used in the production of single-filament glass fibre (textile type glass fibre). BA which is used as a binder in ceramics, increases fracture and scratch resistance against physical impacts and improves chemical resistance. One of the most important properties of BA is the basic form of borate-based flame retardants used to reduce the degree of ignition of combustible materials. In addition to its uses in nuclear energy, medical sector, anti-bacterial and cleaning purposes, it is a good lubricant for metal and ceramic surfaces and plays an important role in controlling the coefficient of friction [2].

PCMs with different fibre (glass, carbon, aramid) and particle additions are produced for improve properties (mechanical/thermal) of polymers, which have a wide range of applications in industry and daily life. There are lots of studies in the literature in which the properties of fibre and particle filled polymer materials are determined and investigated [3], [4], [5]. In recent years, studies on the production and properties of BA-added composites with different polymer types have been intensified. Cheewawuttipong et al [6] reported the addition of boron nitride (BN) to PP polymer increases thermal conductivity, storage modulus and loss modulus. It was stated that the degree of crystallisation of PP polymer increased with increasing amount of BN. Visakh et al [7] reported that the 50% decomposition temperature (T_{50}%) increased, and the non-flammability property improved in epoxy composites filled with BA at different rates (1-10 wt.%). Celiker et al [8] characterized the mechanical and thermal properties of BA and paper mill sludge filled polyester. In their study, the highest flexural strength (21.83MPa) was obtained when 5 wt.% paper mill sludge and 3 wt.% BA were used. It was also stated that the thermal conductivity coefficient of polyester composites decreased with the addition of BA and paper mill sludge. Pehlivanlı [9, 10] examined the thermal conductivity values of PP composites produced by addition of BA (between 0.5-2.5 wt.%) in the form of particles with low thermal conductivity to PP polymer. As a result of the study, it was stated that the addition of BA decreased the heat conductivity coefficient of PP polymer. Özdemir et al [11] examined surface and mechanical behaviors of poly(methyl methacrylate) (PMMA) composites with borax, BA and colemanite addition. The highest flexural strength was obtained in 3 wt.% borax group and 1 wt.% colemanite group. Morover, the highest impact strength value was recorded in the 1 wt.% colemanite group, the difference between the 1 wt.% colemanite group and the control group was statistically significant. Cavdar et al [12] examined the effect of boron-based flame retardants (BbFRs)/high density polyethylene (HDPE) composites with impregnated spruce wood powder (WF). As a result of the study, it was reported that borax filled samples showed better mechanical properties than boric acid filled samples. A 19% improvement in the modulus of elasticity was observed at 40% fibre loading compared to control specimens. In their study, it was stated that borax in particular has the potential to be used as a flame retardant in wood plastic composites. Kırbas et al [13] examined the microstructure and physical properties of BA filled rigid polyurethane (PU). In their study, 5 wt.%, 10 wt.% and 15 wt.% BA was added to PU polymer material

by weight. With the addition of BA, it was determined that there was a 57.2% decrease in thermal conductivity and 67.8% decrease in density compared to PU material. It was also observed that BA addition supported the formation of the cell structure of the polyurethane polymer. Awada et al [14] used BA filler in their study to improve the homogeneity and mechanical properties of cellulose fibres and polyvinyl alcohol (PVOH) based composite. The effect of BA on the mechanical properties of cellulose fibres under different pH values was investigated. The presence of BA under alkaline conditions further improved the mechanical properties of cellulose fibres. Aydın et al [15] investigated the tribological and mechanical properties of BA filled unidirectional glass fiber and carbon fiber added polyester composites. As a result, the wear resistance increased between 5% and 50%, tensile strength improved up to 32% depending on the amount of BA filler.

As can be seen in the literature, while there are studies examining mechanical, thermal and conductivity properties of boric acid filled polymer-based composites, there are a limited number of studies using polypropylene polymer as a matrix, where light weight, high chemical resistance and cheapness are prioritized in the industry. In this study, polypropylene based polymer composites filled with boric acid at different ratios (5-10-15 wt.%) were produced. The mechanical behavior of these composites was analyzed and optimum BA filler ratio was determined. With the results obtained, it is aimed to shed light on the literature about the usability of PP/BA composites in the industry.

2. Material and method

Boric acid filler material with a particle size of 150 μm for composite production was obtained from ETI Bank A.S./Turkey without surface treatment. The polymer main matrix material Polypropylene is a medium molecular weight PP homopolymer with a density of 0.905 g/cm^3, a melting temperature of 163 ^{o}C, a hardness of 94 HRR and a melt flow index value of 4.7 g/10 min, supplied from Petkim/Turkey with the code MH-418. The test specimens were first extruded in granule form and then injection moulded to produce PP-based composites filled with H_3BO_3 at different ratios (i.e. 5-10-15 wt.%). The temperature distribution during the extrusion process was set as 205-230 ^{o}C. Screw speed was set as 80 rpm. Injection heater temperatures were set at 200-230 ^{o}C from the feed unit to the head. No mould heater was used in the mould and the approximate mould temperature was around 40 ^{o}C.

Tensile tests have been made in a Zwick Roell Z-020 machine under climate-controlled room temperature, 50% humidity conditions and a tensile speed of 5 mm/min with ASTM D638 standard. Tensile strength, yield strength, yield strength, modulus of elasticity and elongation values of the material were determined as a result of the tensile test. At least five tensile test specimens were used for each polymer composite material composition in tensile tests. The arithmetic average of each five specimens was taken and the average values were given in the strength, modulus of elasticity and % elongation graphs. For the tensile test specimens, the average margin of error in the tensile and yield strength graphs was found to be between 2-4%, while the elastic modulus and impact strength were found to be between 2-5%.

Impact tests have been made in Zwick B5113 impact machine under climate controlled room temperature and 50% humidity conditions with ASTM D256 standard. The impact test specimens were printed in 4x10x80 mm3 dimensions in an injection moulding machine in accordance with ASTM standard. Then, a V-notch was made in the center of the 10 mm part of the specimens with a depth of 2 mm at an angle of 45^o. Izod impact test method was used for impact tests. In the experiments, the impact energy of the specimens was determined in joules and the izod impact strength value was automatically determined by the device by dividing the value obtained by the remaining area of the specimen after the notch. At least five test specimens were used for each material composition in the experiments and the arithmetic average of the five specimen values was taken and the average values were given in the graphs. The average margin of error in the graphs for impact test specimens was determined to be between 2-4%.

3. Results and discussion

The change in the modulus of elasticity of unfilled PP polymer and PP polymer composites filled with BA at different ratios depending on the amount of boric acid filler shows in Figure 1. As seen in the figure, while the modulus of elasticity of unfilled PP polymer was around 3173 MPa, a decrease in the modulus of elasticity was observed with the increase in the BA filler ratio. This decrease was 6.6% at 5 wt.% BA addition, 16.9% at 10 wt.% BA additions and 15.8% at 15 wt.% BA addition. The lowest modulus of elasticity was obtained with a value of 2713 MPa at 10% BA addition. It is thought that the reason for the possible decrease in the elasticity modulus is due to the release of water vapour due to the heat generated during the injection process and the formation of a porous structure in the polymer. Nazarenko et al. [16] also stated that BA releases water in the endothermic reaction during heating from 70 to 350 °C.

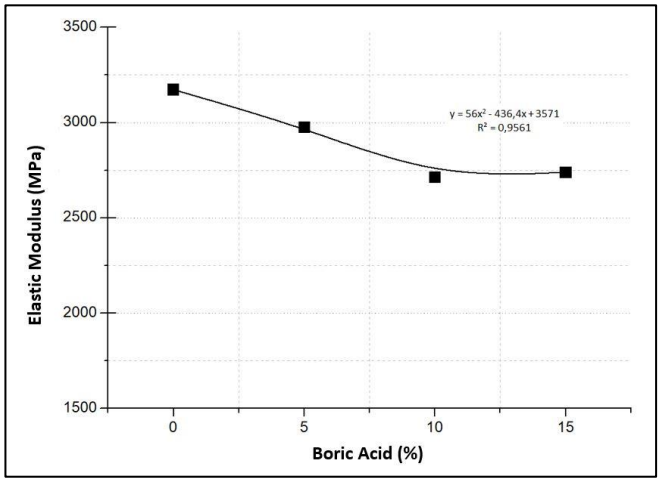

Fig. 1. Variation of elastic modulus of unfilled PP and PP composites containing BA at different ratios according to BA filler ratio.

Figure 2 shows the variation of tensile and yield strength of PP/5BA, PP/10BA and PP/15BA composites with unfilled PP polymer depending on BA filler ratio. As can be seen in the figure, yield and tensile strength of the composites decreased with the incensement in the BA filler ratio added to the PP polymer. The tensile strength of unfilled PP polymer was 35.4 MPa, it decreased by 4.23% to 33.9 MPa with 5 wt.% BA addition, by 16.9% to 30.2 MPa with 10 wt.% BA addition and by 11.8% to 31.6 MPa with 15 wt.% BA addition. Similarly, the tensile strength of the unfilled PP polymer was determined as 35.2 MPa. When 5%, 10% and 15% BA fillers were added to the unfilled PP polymer base matrix, the tensile strength values decreased by approximately 7.5%, 19.3% and 17.6%, respectively, and values of 32.7 MPa, 29.5 MPa and 29.9 MPa were obtained, respectively. As explained in the modulus of elasticity, the reason for the possible decrease in tensile strength and breaking strength can be explained by the formation of water vapour caused by the heat generated during injection moulding and boric acid filler. The water vapour formed during injection moulding will form a porous structure within the polypropylene polymer sample. This will cause the strength values of the composite to decrease. In previous studies, it has been explained that the strength increase in composite materials is related to the quality of the interfacial bond that allows stress transfer from polymer to filler element. Improvement of the interfacial bond generally results in improved strength values. Moisture/water vapour present in the composite structure may cause deterioration of the interfacial bond quality and thus decrease the composite strength [17] [18] [19]. Uygunoglu et al. [20] stated that high particle volume causes pore formation in mixtures and therefore compressive strength decreases. As is known, filler/matrix interfacial bond significantly affects the mechanical properties of polymer composites. A strong interfacial bond between the filler and the matrix increases the mechanical properties of the composite by providing efficient stress transfer [21]. However, a weak filler/matrix interface bonding will only give low composite strength. Ozdemir et al. [22] stated that the decrease in tensile strength was due to both lubricating effect of BA and the increase in the amount of filler in the composite.

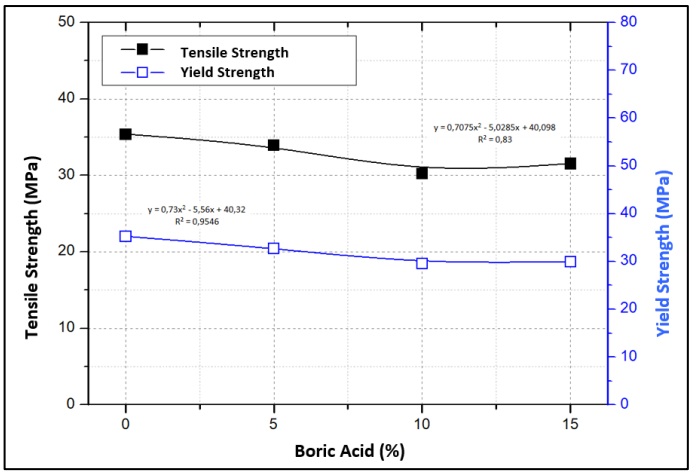

Fig. 2. Variation of tensile and yield strength of unfilled PP and PP composites containing BA at different ratios according to BA filler ratio.

Figure 3 shows the changes in % elongation and impact strength of unfilled PP polymer and PP composites filled with BA at different ratios depending on the amount of boric acid filler. As can be seen in the figure, it is observed that the elongation values change in an increasing and decreasing manner depending on the amount of BA filler. At 5 wt.% BA filler amount, the % elongation increased by 24.3%, while at 10 wt.% BA filler content it decreased by 18.7% compared to the unfilled PP polymer. At 15 wt.% BA filler content, the % elongation increased by 5.4% compared to the unfilled PP polymer. Impact strengths of the unfilled PP polymer and PP/BA composites showed a similar behavior to the elongation, i.e. increasing and decreasing. The impact strengths of unfilled PP polymer and PP/BA composites were obtained between 5.2 and 6.4 kJ/m^2. The impact strength increased by 20.7% with the addition of 5 wt.% BA while the impact strengths at high BA amounts (10 wt.%-15 wt.% BA) were obtained at the impact strength values of the unfilled PP polymer. Water vapor affects the polymer physically, chemically or in terms of plasticization and may cause bond breakage at the reinforcement/matrix interface [23, 24]. Additionally, although the decrease in the strength values of BA filled PP composites is thought to be due to the plasticization of the PP polymer phase, this contributed to almost preservation of properties such as impact strength and elongation.

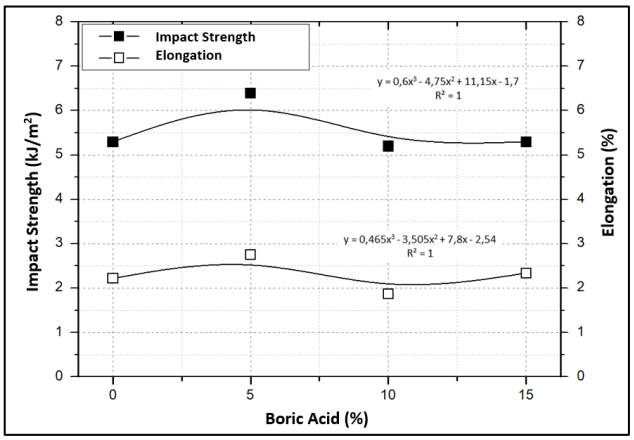

Fig. 3. Variation of % elongation and impact strength of unfilled PP and PP composites containing BA at different ratios according to BA filler ratio.

4. Conclusions

The mechanical properties of PP polymer without filler and PP composites with BA filler were investigated and the following results were obtained.

The mechanical properties of PP-based composites decreased due to the addition of BA to the PP polymer. Modulus of elasticity of PP polymer decreased depending on the BA filler ratio (5-10-15 wt.%). This decrease in the modulus of elasticity was obtained at 6.6%, 16.9% and 15.8%, respectively, depending on the BA filler rate. The addition of BA to PP polymer also decreased tensile and yield strength values of PP/BA composites. Elongation and impact strength values also showed increasing and decreasing changes depending on the amount of BA. The impact strengths of PP polymers and composites were obtained between 5.2 and 6.4 kJ/m^2. Before the BA filler is added to the polymer based materials, it must be dried in an oven at high temperatures to prevent the formation of water

and/or water vapour in the composite. It should be ensured that the interface bond between polymer base matrix and filler material is strong.

Conflict Of Interest

The author declares no conflict of interests.

Acknowledgement

This research has received no external funding.

References

[1] N. D. Sakhayana, A. D. Afanasy, P. V. Andrey, A. O. Aitalina, G. T. Aleksei, K. K. Anatoly and A. K. Aisen, "Effect of borpolymer on mechanical and structural parameters of ultra-high molecular weight polyethylene," *Nanomater.*, vol. 11, no. 12, pp. 3398, 2021, doi:org/10.3390/nano11123398.
[2] https://www.etimaden.gov.tr/storage/pages/March2019/1-borik-asit1.pdf, 01/09/2023.
[3] K. S. Dogahe, S. Akbari and M. H. Kish, "Physico-mechanical properties of poly (vinyl alcohol), poly (vinyl alcohol)/boric acid, and poly (vinyl alcohol) nanocomposites incorporated with amino-functionalized and pristine halloysite nanotubes films," *J. Appl. Polym. Sci.*, vol. 139, no. 1, pp. 51424, 2022, doi:org/10.1002/app.51424.
[4] X. Tian, Y. Sun, H. Xie, B. Shi, J. Zhong, D. Sheng and Y. Yang, "Preparation of graphene oxide/ waterborne polyurethane via boric acid cross-linked dopamine enhanced barrier and mechanical properties," *Front. Mater. Sci.*, vol. 9, pp. 1046125, 2022, doi:org/10.3389/fmats.2022.1046125.
[5] N. B. Svishcheva, P. A. Khaptakhanova, D. A. Kasatov and S. A. Uspenskii, "Preparation and study of properties of boron-containing polymer based on lactic and boric acids," *Russ. Chem. Bull.*, vol. 70, no. 9, pp. 1725-1728, 2021, doi:org/10.1007/s11172-021-3276-2.
[6] W. Cheewawuttipong, D. Fuoka, S. Tanoue, H. Uematsu and Y. Iemoto, "Thermal and mechanical properties of polypropylene/boron nitride composites," *Energy Procedia*, vol. 34, pp. 808-817, 2013, doi:org/10.1016/j.egypro.2013.06.817.
[7] P. M. Visakh, O. B. Nazarenko, Y. A. Amelkovich and T. V. Melnikova, "Thermal properties of epoxy composites filled with boric acid," *IOP Conf. Ser.: Mater. Sci. Eng.*, vol. 81, pp. 12095, 2015, doi:10.1088/1757-899X/81/1/012095.
[8] H. İ. Çeliker, A. Ç. Başbozkurt and A. Yaraş, "Mechanical and thermal properties of boric acid and paper mill sludge reinforced polyester composites," *Boron*, vol. 5, no. 4, pp. 163-169, 2020, doi:org/10.30728/boron.702466.
[9] Z. O. Pehlivanlı, "H_3BO_3/PP kompozitlerinin ısı iletim katsayılarının incelenmesi," *GU J Sci Part:C*, vol. 4, no. 3, pp. 91-96, 2016.
[10] Z. O. Pehlivanlı, "Manufacturing and characterization of polypropylene/boric acid composite," *Polym. Bull.*, vol. 78, pp. 4033–4046, 2021, doi:org/10.1007/s00289-021-03728-4.
[11] A. K. Özdemir, D. Özdemir Derya, F. Tuğut, H. Demir and H. Akın, "Effects of boron on the mechanical properties of polymethylmethacrylate denture base material," *Eur. Oral Res.*, vol. 55, no. 1, pp. 45-53, 2021, doi: 10.26650/eor.20210132
[12] A. D. Çavdar, F. Mengeloğlu and K. Karakus, "Effect of boric acid and borax on mechanical, fire and thermal properties of wood flour filled high density polyethylene composites," *Measurement*, vol. 60, pp. 6-12, 2015, doi:org/10.1016/j.measurement.2014.09.078
[13] I. Kırbas, "Improving the structural and physical properties of boric acid-doped rigid polyurethane materials," *Compos. Adv. Mater.*, vol. 30, pp. 1–7, 2021, doi:org/10.1177/263498332110108
[14] H. Awada, D. Montplaisir and C. Daneault, "The development of a composite based on cellulose fibres and polyvinyl alcohol in the presence of boric acid," *BioResources*, vol. 9, no. 2, pp. 3439-3448, 2014.

[15] T. Aydın, K.Turan and N. Y. Sarı, "Investigation of mechanical and tribological properties of boric acid reinforced composite plates," *Eur. J. Tech.*, vol. 11, no. 2, pp. 264- 269, 2021, doi:org/10.36222/ejt.923954.
[16] O. B. Nazarenko, T. V. Melnikova and P. M. Visakh, "Thermal and Mechanical Characteristics of Polymer Composites Based on Epoxy Resin, Aluminium Nanopowders and Boric Acid," *J. Phys. Conf. Ser.*, vol. 671, 012040, 2016, doi:10.1088/1742-6596/671/1/012040
[17] S. Nicole, "Influence of Moisture Absorption on Mechanical Properties of Wood Flour–Polypropylene Composites," *J. Thermoplast. Compos. Mater.*, vol. 14, pp. 421-432. 2001, doi:org/10.1106/UDKY-0403-626E-1H4P.
[18] V. Titone, A.Correnti and F. P. L. Mantia, "Effect of moisture content on the processing and mechanical properties of a biodegradable polyester," *Polymers*, vol. 13, pp. 1616, 2021, doi:org/10.3390/polym13101616.
[19] J. J. Balatinecz and B. Park, "The effects of temperature and moisture on the properties of wood-fiber thermoplastic composites," *J. Thermoplast. Compos. Mater.*, vol. 10, pp. 476–487, 1997, doi:org/10.1177/0892705797010005.
[20] T. Uygunoglu, I. Gunes and W. Brostow, "Physical and Mechanical Properties of Polymer Composites with High Content of Wastes Including Boron," *Mater. Res.*, vol. 18, no. 6, pp. 1188-1196, 2015, doi:org/10.1590/1516-1439.009815.
[21] S. Y. Fu, X. Q. Feng, B. Lauke and Y. W. Mai, "Effects of particle size, particle/matrix interface adhesionand particle loading on mechanical propertiesof particulate-polymer composites," *Compos. B. Eng.*, vol. 39, no. 6, pp. 933-961, 2008, doi:org/10.1016/j.compositesb.2008.01.002.
[22] T. Ozdemir, I. K. Akbay, H. Uzun and I. A. Reyhancan, "Neutron shielding of EPDM rubber with boric acid: Mechanical, thermal properties and neutron absorption tests," *Prog. Nucl. Energy*, vol. 89, pp. 102 -109, 2016, doi:org/10.1016/j.pnucene.2016.02.007.
[23] B. C. Ray, "Temperature effect during humid ageing on interfaces of glass and carbon fibers reinforced epoxy composites," *J. Colloid Interface Sci.*, vol. 298, no: 1, pp. 111–117, 2006, doi:org/10.1016/j.jcis.2005.12.023.
[24] C. J. Tsenoglou, S. Pavlidou and C. D. Papaspyrides, "Evaluation of interfacial relaxation due to water absorption in fiber–polymer composites," *Compos Sci Technol*., vol. 66, no. 15, pp. 2855–2864, 2006, doi.org/10.1016/j.compscitech.2006.02.022.

Contents lists available at *Dergipark*

Journal of Scientific Reports-A

journal homepage: *https://dergipark.org.tr/tr/pub/jsr-a*

E-ISSN: 2687-6167 ***Number 55, December 2023***

RESEARCH ARTICLE

Receive Date: 02.10.2023 *Accepted Date: 21.12.2023*

Positioning analysis of the lift force sensor in subsonic wind tunnel test chamber design and its effect on naca0015 airfoil

Samet Giray Tunca[1]*,Mustafa Arif Özgür[2]

[1]*Kütahya Dumlupınar University, Kütahya Evliya Çelebi Campus, Kütahya,43000, Türkiye, ORCID: 0000-0002-7632-8745*
[2]*Kütahya Dumlupınar University, Kütahya Evliya Çelebi Campus, Kütahya,43000, Türkiye, ORCID: 0000-0001-5877-4293*

Abstract

In this study, analysis was carried out by placing the force sensor in different positions in the subsonic wind tunnel test room. NACA0015 profile was used as the airfoil. The model used in the open system subsonic wind tunnel with a 50x50 cm test chamber was manufactured by 3D printing method. Lift force (CL) measurements were studied at Reynolds number (Re) values of 60000, 80000 and 100000. Measurements were analyzed in one-degree increments of the angle of attack, starting from 0^0. The force device is positioned in 4 different ways around the test room. Efficient results could not be obtained in 3 of the connection attempts. The reason why the results are not efficient is that the fasteners are incompatible with the airfoil, force device and system. The incompatibility of the fasteners caused vibration and a negative situation in the airfoil. There is a slope in the connection made from the side. As a result of the slope, the airfoil has deteriorated.
It was observed that the measurements made by positioning the force device inside the test chamber were compatible with the literature. The resulting graph shows an approach to the literature. Although it is graphically compatible, it should be noted that there is a deviation of approximately 10% in the data. Connection stiffness is gaining importance. It has been observed that stall begins at angles of approximately 10^0 and 11^0 degrees.
Improvements can be made for all connections and fasteners for the location of the force device.

Keywords: Wind tunnel, stall, airfoil, lift coefficient, Reynolds number

* Corresponding author. Tel.: 0 274 443 71 00
E-mail address: sgiray.tunca@dpu.edu.tr
http://dx.doi.org/10.1016/j.cviu.2017.00.000

1. Introduction

Experimental aerodynamic measurements are made using wind tunnels. There are many studies conducted with wind tunnels in the literature. The work to be done must comply with the characteristics of the wind tunnel. At the same time aerodynamic measurements are made to determine the characteristic structures of airfoils. These measurements are used to optimize the structure of the airfoil. Lift coefficient values are taken into consideration to examine the condition of the airfoil during takeoff, flight and landing. The airfoil is evaluated by making comparisons with studies performed at different angles. In the literature, there are many studies examining airfoil and making aerodynamic measurements.

Aeroacoustic measurements were made on two NACA 0012 airfoil sections with different chord length and sharp trailing edge in the Laminar Wind Tunnel (LWT) of the University of Stuttgart [1].

Regarding wind tunnel manufacturing studies, a small, two-dimensional, high-speed cryogenic wind tunnel was built at the Japanese National Defense Academy (NDA) in 1985. R4 airfoil test results in the NDA cryogenic wind tunnel were compared to those of NASA TM-85739 [2].

In the study by Bottasso C.L. et al. on wind tunnel modeling, it was stated that the existing experimental facility, which expands the classical scope of the models, enables various applications from aerodynamics to aeroelasticity and control [3].

Power coefficient and torque coefficient parameters were examined for the disc-shaped wind rotor used in a small-scale wind turbine. Data were obtained by numerical simulation and wind tunnel testing. It was simulated with different turbulence models in the range of Re numbers 6.8×10^4–1.70×10^5 [4].

Göv I. The study by et al. was based on the NACA 4412 airfoil. Changes have been made to the NACA 4412 profile to provide higher aerodynamic performance at 0-23 degree angles of attack during flight. Two more different airfoil profiles (NACA 4412_1 and NACA 4412_2) were obtained. The aerodynamic performances of these two profiles and the original NACA 4412 profile were compared. In these analyses, lift coefficient, drag coefficient and flow separation performance parameters were examined. At the end of the study, it was determined that it was appropriate to use the NACA 4412 airfoil between 0^0 and 12^0, the NACA 4412_2 airfoil between 12^0 and 17^0, and the NACA 4412_1 airfoil after 17^0 angle of attack in order to achieve maximum aerodynamic efficiency [5].

In the research of Du G. et al., airfoil lift, drag and lift-drag ratios were studied with numerical simulation analysis and their variables were analyzed in different parameters of NACA airfoils [6].

Rubel R.I. et al. used a symmetrical airfoil profile (NACA 0015) in their study. This airfoil is used in many applications such as aircraft submarine winglets, rotary and some fixed wings. In the study, NACA 0015 was examined numerically and experimentally in the range of 0^0 - 18^0. The aim of the study is to find the deviation and validity of the aerodynamic properties of the NACA 0015 airfoil for experimental and numerical method [7].

The vortex structure of the NACA 0018 airfoil was examined at 2.5×10^4 number and angles of attack of 10^0 and 20^0 by Gim O. and Lee G. Velocity profiles were obtained [8].

In wind tunnel tests, the vibration of the NACA0015 airfoil in the range of $18x10^4$ and $57x10^4$ Reynolds number was investigated. As a result of this research, flow visualization was realized [9].

A comparison was made between the performance of the symmetrical airfoil NACA-0012 and the asymmetric airfoil NACA-2410. The relationship between CL and CD has been explained. It can be seen that the lift and drag coefficient of NACA-0012 is higher than that of NACA-2410 [10].

Wind tunnel tests were performed on the NACA 0012 two-dimensional airfoil. The measurements taken referred to the pressure distribution on an airfoil and airfoil coefficients using six-component balance between 0^0 and 18^0 degrees angle of attack, and investigations at small angles of attack [11].

A set of 15 different corona actuators with triangular tips on their anodes were examined by mounting them on the leading edge of the NACA 0015 airfoil. Aerodynamic forces on the airfoil are measured over a wide range of angles of attack for different airflow velocities in the wind tunnel. The performance of the actuators was evaluated through various parameters, including critical and average lift increase, resistance reduction and power saving effectiveness [12].

Angular airfoil were tested in a subsonic wind tunnel at numbers lower than $2x10^4$ Reynolds number. CL and CD

tests of the NACA0012 airfoil were compared with thin and curved structures. It has been determined that the most ideal airfoil at Reynolds numbers up to $7x10^4$ is a circular structure with 5 percent. This structure provided the highest CL-CD figures across all turbulence levels [13].

New data have been obtained for the NACA-0012 airfoil at low Reynolds numbers for the analysis of vertical axis wind turbines (VAWTs). The double-slat tolerant tunnel has the best performance based on the similarity of results for the airfoils. However, post-stall force peaks are significantly lower than in conventional tunneling [14].

The lift coefficient of a NACA 0015 airfoil with and without a Gurney airfoil was examined in a wind tunnel with $Re = 2.0 \times 10^5$. The Gurney wing provided a significant and relatively constant increase in lift throughout the linear range of the CL versus α curve [15].

It was determined that the results obtained in the study conducted by Kaya M. coincide with the results of wind tunnel experiments carried out by many research units such as NACA [16]. Miklosevic studied aerodynamic force calculations in a low-speed wind tunnel at Reynolds numbers between 505,000 and 520,000 and angles of attack varying between -2˚ and 20˚ [17].

H. Hamdani and M. Sun's study with the NACA 0012 airfoil shows that at low Reynolds numbers, the instantaneous acceleration of the airfoil from one speed to another causes large aerodynamic forces to arise [18].

Kazemi examined the aerodynamic performances of the airfoil they produced numerically and experimentally. They stated that the lift/drag ratio increased approximately 2.9 times compared to the NACA0021 airfoil, which they accepted as the basis for the profile structure they produced [19].

In their study, Tanürün H. E., Ata İ., Yaşam M. E. and Acır A compared the experimental results of the aerodynamic performance of the NACA0018 airfoil with two newly designed airfoil. In the aerodynamic experimental results of the newly designed AR1 and AR2 airfoil, an improvement of 0.41% and 2.71% in CL values was achieved [20].

In our study, the ambient temperature was 20^0C, the kinematic viscosity of the air was accepted as $1.5111\ e^{-5}$ m^2/s, and the airfoil chord length was 0.15 m. Tests were carried out at Re numbers of 6×10^4, 8×10^4 and 10×10^4.

The location of the force measurement system is important in experimental studies. However, the connection of the airfoil and the force device is important for the accuracy of the data obtained. In our study, experiments were carried out with different methods to determine the position of the force system. Among these methods, there are also experiments in which the connection between the airfoil and the force device varies. The results obtained will be considered as a reference for future experiments in the subsonic wind tunnel. There is a metal flat piece between the sensor in the force device and the airfoil. For this reason, it has been determined that the force device should be on the airfoil axis.

2. Experimental studies and evaluation

There is an open system subsonic wind tunnel in Kütahya Dumlupınar University Mechanical Engineering Laboratory (Fig. 1.). The test compartment where the airfoil to be tested is placed is 50x50 cm. In our study, buoyancy measurements were obtained from many different locations and with different connection methods.

Fig.1. Subsonic Wind Tunnel

NACA0015 airfoil was used in lift force measurements made with the wind tunnel force balancing system. The airfoil and fasteners were manufactured on a 3D printer. Due to vibration, metal fasteners were also tested in the measurements.

To manufacture the airfoil, printing parameters were determined as 220^0 nozzle temperature, 60 degree table temperature and 0,2 mm layer thickness. The material used is pla filament. For airfoil printing, the ratio of airfoil length and chord length is accepted as 1/1. The airfoil mass was manufactured as 348,21 g, volume as 341379,35 mm^3 and surface area as 54582 mm^2.

The connection elements between the force device and the airfoil are important for the accuracy of the data in the experiments. In order for the fasteners to be connected rigidly, the airfoil section must be of a certain thickness. Therefore the chord length measurement is 150 mm. was determined as.

Lift force values were taken in the wind tunnel test chamber. The studies were carried out at speeds of 6, 8 and 10 m/s, in increments of 1^0 between 0^0 - 14^0 degrees. The chord length of the NACA0015 airfoil used in the tests is 150 mm. The area where the lift force acts is the lower part of the airfoil surface. The lift coefficient was obtained along with the speed and density values.

2.1. Mathematical model

Terms used in aerodynamic studies have mathematical equivalents. The terms used in the calculations made in our study were obtained with these mathematical formulas.

- The term subsonic is expressed in Mach number. In fluid mechanics, Mach number is the ratio of the speed of a moving mass to the speed of sound under the conditions in which the mass exists. V (m/s) refers to the speed of the mass in motion, and c (m/s) refers to the speed of sound.

$$Ma = {}^{V}/_{c} \tag{1}$$

V (m/s) refers to the speed of the mass in motion, and c (m/s) refers to the speed of sound. Situations where the Mach number is less than 0.8 are called subsonic.

- The buoyant force acts on the object perpendicular to the flow.

$$FL = CL\frac{1}{2}\rho AV^2 \tag{2}$$

CL is the dimensionless drag force coefficient, ρ (kg/m^3) is the density of the air, A (m^2) is the area of influence of the wind on the airfoil, and V (m/s) is the wind speed.

- In fluid mechanics, Reynolds number (Re) is the ratio of a fluid's inertial forces (v,d) to viscosity forces (μ/ρ). In our study, tests were conducted at three different Reynolds numbers.

$$Re = \frac{(v.d.\rho)}{\mu} \tag{3}$$

- Stall is a term used in aerodynamics. When stall occurs, the lift acting on the airfoils suddenly and unexpectedly decreases or disappears completely. The aerodynamic angle at which the maximum lift coefficient is reached or dropped below is called the "stall angle". As a result of the separation of the air flow on the airfoil surfaces or the flow becoming turbulent, the amount of lift that the airfoils can produce decreases. While the airfoils normally operate aerodynamically at a certain angle, when this angle is exceeded or approached with sudden changes, the air flow becomes irregular and lift decreases.

2.2. Force sensor connection from the rear area of the airfoil

In the first connection method, the device is positioned at the rear of the NACA0015 airfoil with a connecting rod coming from the rear region of the airfoil. The airfoil is manufactured as shown in figure 2. The measurement results are as seen in Figure-3. There is no stall in the measurement results. The fact that no stall is observed with such a measurement method is due to the fact that the connection part in the back region affects the force values. As seen in figure-3, lift force values are constantly increasing. Measurements were tested at different angles by making a connection in the back area, but the result did not change. Although the angle mechanism part was positioned close and far from the rear section, the increase in lifting force could not be prevented and no stall was observed.

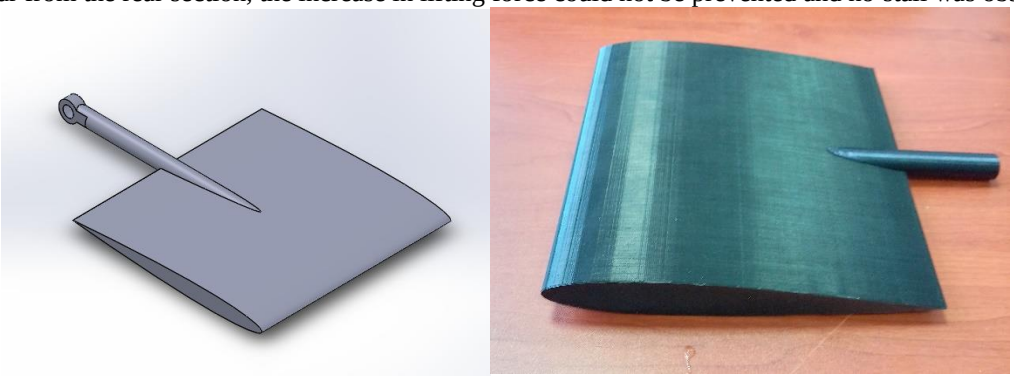

Fig. 2. Airfoil and connection used in the measurement made from the rear area of the airfoil

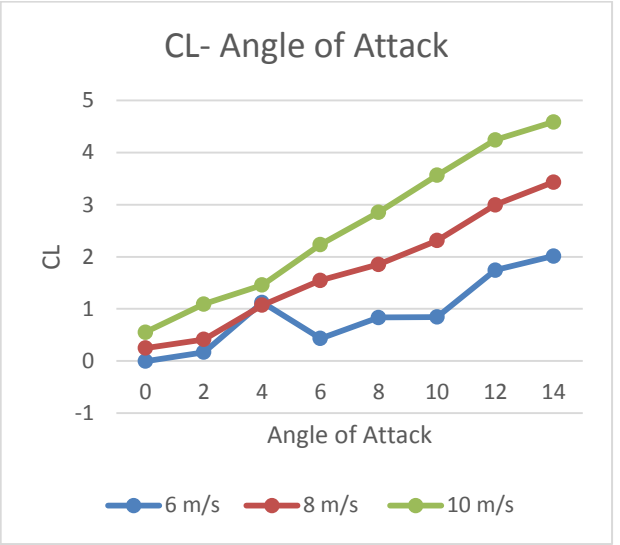

Fig. 3. NACA0015 airfoil lift coefficient (CL) and angle of attack graph (*Force Sensor Connection from the Rear Area of the Airfoil)*

Experiments were carried out with rear connection as the first method in Figure 3. The increase in the distance between the sensor airfoil is the reason for the high distribution of moment arm values created by these formations. The 6 x 10^4 Re view CL maximum value increased to 2, the 8 x 10^4 Re view CL maximum value increased to 3,43 and the 10 x 10^4 Re view CL maximum value increased to 4,588. These values do not match the literature. The blocking effect of speed and openness is observed. The airfoil is not exposed to stall and there is a continuous increase in CL values.

2.3. Force sensor connection at the bottom outside of the test chamber

As the second connection method, the device was placed under the test chamber. The device was placed on the same axis as the airfoil but outside the test chamber to avoid causing any different effects on the flow. There are 2 - 90^0 turns in the connection between the device and the airfoils. However, with the positioning, the distance between the airfoil and the device was extended and negative situations were encountered in load transfer. The buoyancy data obtained are very low compared to literature data. With this connection type, no stall was observed. As in the first connection method, the connection was made on the same axis from the back region. It has become clear that the connections applied to the airfoil in this way have an effect on preventing stall. The data obtained from the connections made to the airfoil from the rear area to the force device are not positive.

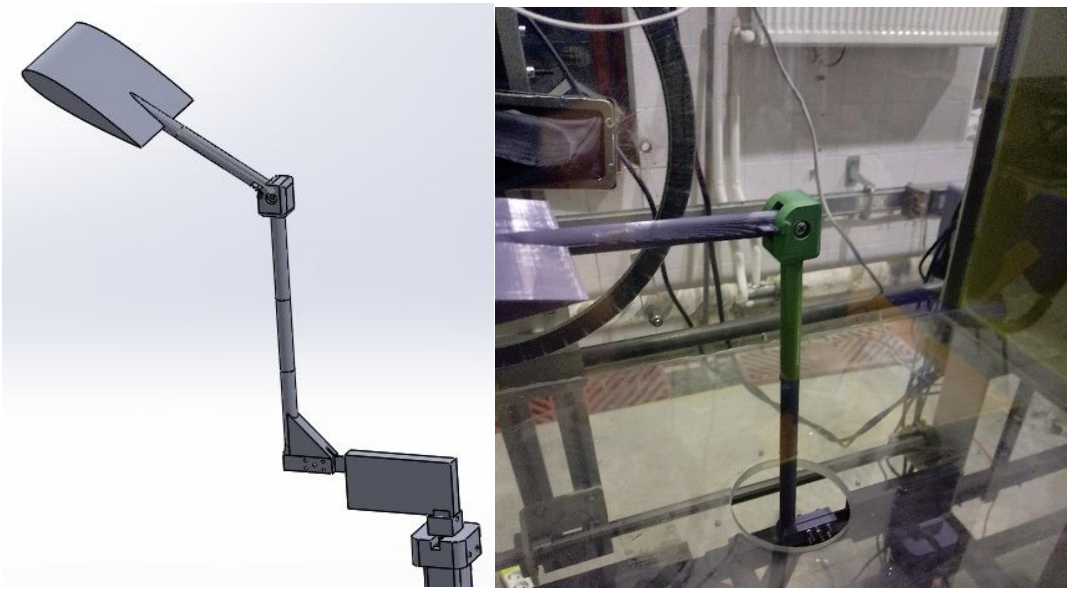

Fig. 4. Airfoil and connection used in the measurement made from the rear area of the airfoil outside the test room

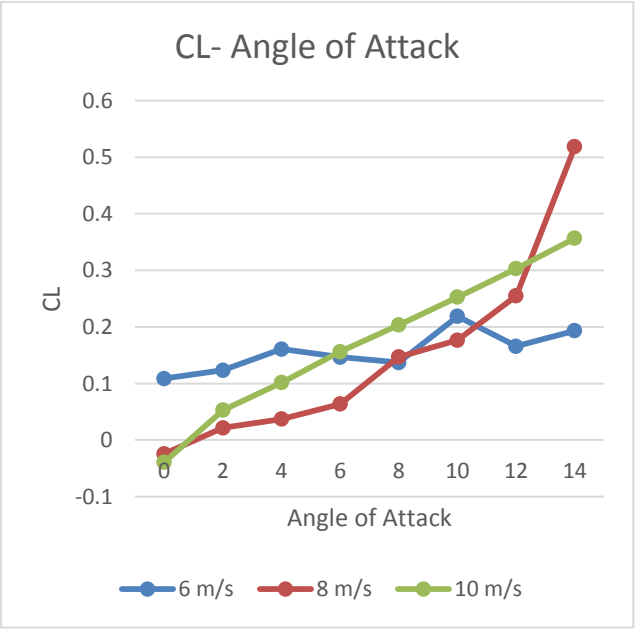

Fig. 5. NACA0015 airfoil lift coefficient (CL) and angle of attack graph (*Force Sensor Connection at the Bottom Outside of the Test Chamber)*

In the method shown in Figure 4, the force device is positioned very far from the airfoil. As seen in Figure 5, the data obtained is very low. In measurements where the Re number was 8 x 10^4, the maximum CL value was found to be 0,5186. There is no consistency between measurements made with the same method at 3 different Re numbers.

The 90^0 rotations and distance between the force device and the airfoil caused losses in force values. Likewise, it

has been determined that this method has high vibration.

2.4. Force sensor connection from side of test chamber

In this method, the device is positioned on the outer side of the test chamber and a connection is made from the side surface of the airfoil. Since the connection was one-sided, the requested data could not be obtained. As seen in Figure 6, in the connection made, the force acting on the airfoil created a force in the opposite direction on the flat iron, which is the device sensor connection element. In addition, since it is a one-sided connection, the slope and vibration have increased meaninglessly. As a result, no data could be obtained from this connection.

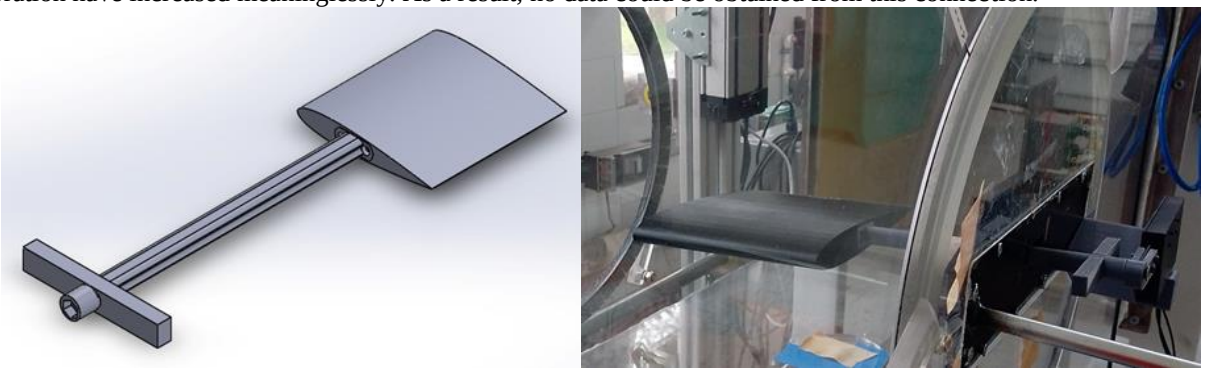

Fig. 6. Airfoil and connection used in the measurement made from the side area of the airfoil

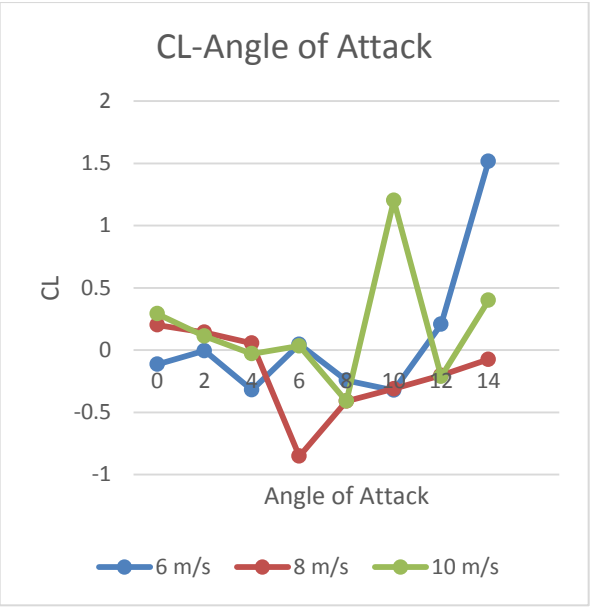

Fig.7. NACA0015 airfoil lift coefficient (CL) and angle of attack graph (Force Sensor Connection from Side of Test Chamber)

As a result of the experiments, the data in Figure 7 was obtained. Due to the one-sided connection, the wind

speed affecting the angled wing profile created a downward force at the connection point with the force device. This force has no continuity. Some of the measurements were negative and some were positive. In the data obtained, the maximum value of CL increased up to 1,5. However, the CL minimum value was between -0,5 and -1. As a result, it has been determined that this method is not a suitable method for comparing experimental data with the literature.

2.5. Force sensor connection at the bottom of the test chamber

In the last method applied in this study, the force device was fixed to the inner floor of the test chamber. As seen in Figure 8, the airfoil device connection design has been made. A stall effect is observed in the lift coefficient values obtained with this method. Although the values overlap with literature studies, it has been determined that there are losses in buoyancy values.

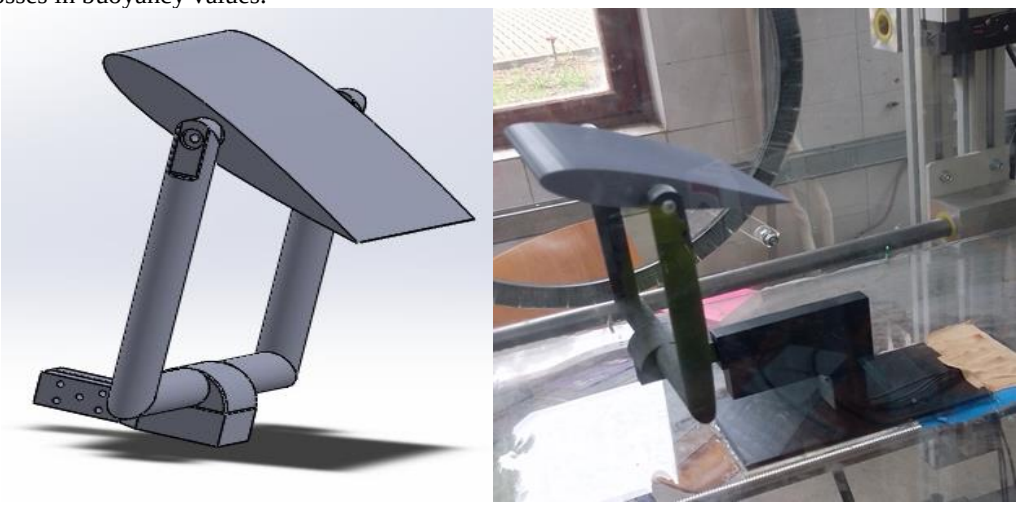

Fig. 8. Force device positioned under the airfoil, airfoil and connection

3. Results

Stall was detected in the connection made under the Naca0015 profile (Table 1.). Increases removal permanent values up to 11^0. After completing 11^0, it is seen that there is a decrease in the lifting force of the airfoil. When compared with the literature, it is revealed that there are losses in the total lifting values in Table 1. Our study has been presented to the literature as graphic curves.

Measurements were made at different speeds in the wind tunnel. It is seen that vibration has an effect on the values measured at 10 m/s speed. The result of this can be seen in the graph (Fig.9.)

In Fig. 9, lift coefficient values are given for angles of attack from 0 to 13^0 degrees. These measurements were made at speeds of 6, 8 and 10 m/s.

Table 1. Lift Coefficient (CL) values

	Vel (m/s)		
Angle of Attack	6 (m/s)	8 (m/s)	10 (m/s)
0	0,009213	0,015078	0,001254
1	0,051821	0,150776	0,016643
2	0,108962	0,156389	0,096507
3	0,159917	0,189557	0,156826
4	0,210872	0,225804	0,187386
5	0,228533	0,264769	0,184223
6	0,288234	0,304067	0,223396
7	0,31356	0,362659	0,425558
8	0,379124	0,413702	0,477638
9	0,441421	0,44204	0,528705
10	0,539058	0,579669	0,626791
11	0,544485	0,614894	0,638808
12	0,414965	0,438963	0,563353
13	0,498562	0,501032	0,45656

Table 1. shows that there is a linear increase up to 11^0 degrees, and after this degree the airfoil is subject to stall. When the studies conducted with the NACA0015 airfoil were examined, it was determined that the coefficient values we obtained were low by 10%. It is thought that this situation is caused by loads shifting to the connection points.

When the connection methods used in our study were examined, it was understood that the force sensor should be on the same axis with the airfoil at the trailing edge.

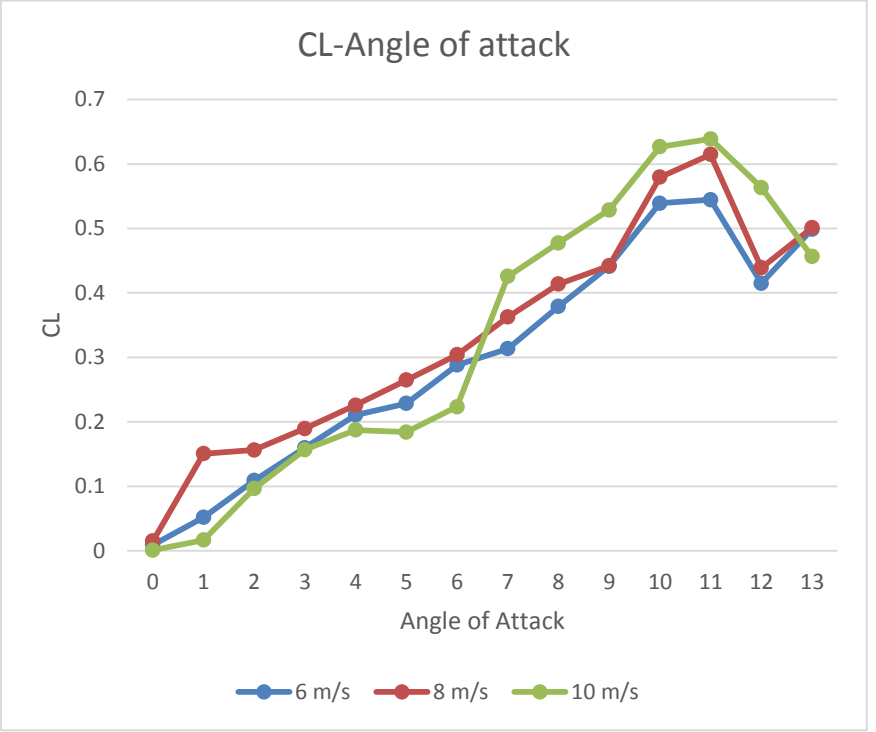

Fig. 9. NACA0015 airfoil lift coefficient (CL) and angle of attack graph

It seems that the method in heading 2.4 should be studied first for the lift coefficient values. Based on the results obtained, the studies continued and the necessity of improvement studies was determined. When the graph is examined, it is seen that there may be connection-related vibrations at 10 m/s measurements. Studies need to be done on this issue.

Güler A.A. conducted experiments with the Naca0015 airfoil at 8,6 x 10^4 Re number. He carried out his study with angle of attack increments of 2^0. It was observed that the Naca0015 airfoil entered a stall at 10^0 degrees. In the experiment, the maximum CL value was found to be 0,8 [21]. The stall angle in our study appears to be compatible with this study. Pope A. made his work in the number 23 x 10^4 Re. It has been observed that the NACA0015 airfoil enters a stall between 10^0 - 15^0 degrees [22].

It has been understood that the results of other methods other than the Figure 8 method have no equivalent in the literature.

When the studies conducted with the NACA0015 airfoil were examined, it was determined that the coefficient values we obtained were low by 10%. It is thought that this situation is caused by loads shifting to the connection points.

4. Discussions

Force losses can be eliminated with new connection designs. When the connection methods used in our study were examined, it was understood that the force sensor should be on the same axis with the airfoil at the trailing edge. Better efficiency can be achieved by changing the fasteners and system.

CL values obtained in methods other than Figure 8 are different from the literature. For this reason, these methods should not be preferred in future experiments. In some measurement results, it is seen that CL data is at negative values. Under normal conditions, the CL value should be seen as positive values in these experiments.

As the first method, experiments were carried out with a rear connection manufactured as in Figure 2. The distance between the sensor airfoil increased, and therefore the resulting moment arm caused the values to be high. In this method, as the angle increased, a blocking effect was observed on the wing. It can be seen in Figure 3 that the airfoil is not subjected to stall.

In the method shown in Figure 4, a connection is made on the rear axis. The device was taken out of the test chamber. In this method, the data obtained is low because the force device is too far away from the airfoil. There are turns in the connection system, so force losses occurred as seen in Figure 5.

In the method shown in Figure 6, the airfoil is connected to the force device from its side surface. Due to the distance between the wing and the force device, deflection was observed in the wing profile towards the opposite direction of the connection. This situation caused variability in the results. The wind speed acting on the non-rigid wing profile created a downward force value at the connection point with the force device. As seen in Figure 7, there are negative values. Force data should not be negative in the experiments performed.

Studies need to be carried out to eliminate the 10% loss in the data obtained by the method closest to the literature data. It seems that the results can be more efficient if the connection rigidity is ensured.

To create the optimum test room design, an examination should be made under headings such as materials used, fasteners and positioning.

Acknowledgements

This article benefited from the support of Kütahya Dumlupınar University Priority Area Project with project number 2021-26.

References

[1] B.Polgmann and W.Würz, Experiments in Fluids, Volume 54, article number 1556, 2013.

[2] Y.Yamaguchi, Y.Nakauchi, M.Yorozu and T.Saito, «Preliminary airfoil testing experience in the NDA cryogenic wind tunnel,» %1 içinde *"ICIASF '91"., International Congress on Instrumentation in Aerospace Simulation Facilities*, Rockville USA, 1991.

[3] C. L. Bottasso, F. Campagnolo and V. Petrovic, *Wind tunnel testing of scaled wind turbine models: Beyond aerodynamics,* cilt Volume 127, Journal of Wind Engineering and Industrial Aerodynamics, 2014, pp. 11-28.

[4] Z. X. et.al, *Experimental and numerical investigation on aerodynamic performance of a novel disc-shaped wind rotor for the small-scale wind türbine,* cilt Volume 175, Energy Conversion and Management, 2018, pp. 173-191.

[5] İ. Göv, M. H. Doğru and Ü. Korkmaz, *Uçuş esnasında değiştirilebilir kanat profili kullanarak NACA 4412'nin aerodinamik performansının artırılması,* cilt 34, Ankara: Gazi Üniversitesi Mühendislik Mimarlık Fakültesi Dergisi, 2019, pp. 1109-1125.

[6] G.-M. Du, J.-H. Chou and P.-K. Huang, *Application of Taguchi experimental method in the optimal design of the NACA cascades wing,* Taiwan, Puli: 2016 International Conference on System Science and Engineering (ICSSE), 2016.

[7] R. I. Rubel, M. Uddin, M. Islam and M. Rokunuzzaman, *Numerical and Experimental Investigation of Aerodynamics Characteristics of NACA 0015 Aerofoil,* cilt Vol.2, International Journal of Engineering Technologies, 2016, pp. 132-142.

[8] O.-S. Gim and G.-W. Lee, *Flow characteristics and tip vortex formation around a NACA 0018 foil with anendplate,* cilt Vol.60, Ocean Engineering, 2013, pp. 28-38.

[9] P. Sidlof, V. Vlcek and M. Stepan, *Experimental investigation of flow-induced vibration of a pitch–plunge NACA 0015 airfoil under deep dynamic stall,* cilt Vol.67, Journal of Fluids and Structures, 2016, pp. 48-59.

[10] S. Sarjito, *Studı Karakterıstık Aırfoıl Naca 2410 Dan Naca 0012pada Berbagaı Varıası Angle Of Attack,* Media Mesin Majalah Teknik Mesin, 2010.

[11] Michos A., Bergeles G. and Athanassiadis N., *Aerodynamic Characteristics of NACA 0012 Airfoil in Relation to Wind Generators,* cilt 7:4, United Kingdom: Wind Engineering, 1984, pp. 247-262.

[12] M. Belan and F. Messanelli, *Wind tunnel testing of multi-tip corona actuators on a symmetric airfoil,* cilt Vol.85, Journal of Electrostatics, 2017, pp. 23-34.

[13] E.V.Laitone, *Wind tunnel tests of wings at Reynolds numbers below 70 000,* cilt Vol.23, Experiments in Fluids, 1997, pp. 405-409.

[14] J.M.Rainbird, J.Peiro and J.M.R.Graham, *Blockage-tolerant wind tunnel measurements for a NACA 0012 at high angles of attack,* cilt Vol.145, Journal of Wind Engineering and Industrial Aerodynamics, 2015, pp. 2019-218.

[15] D.R.Troolin, E.K.Longmire and W.T.Lai, *Time resolved PIV analysis of flow over a NACA 0015 airfoil with Gurney flap,* cilt Vol.41,

Experiments in Fluids, 2006, pp. 241-254.
[16] M. Kaya, *Aırfoıl Yapının Yakın Çevresindeki Hız Ve Basınç Dağılımının Hesaplamalı Akışkanlar Dinamiği Yöntemi İle İncelenmesi,* Cilt %1 / %24-1, Erzincan: Erzincan Üniversitesi Fen Bilimleri Enstitüsü Dergisi, 2014, pp. 59-69.
[17] D. Miklosovic, M. Murray, L. Howle and F. Fish, *Leading-edge tubercles delay stall on humpback whale (Megaptera novaeangliae) flippers,* Cilt %1 / %216-5, Physics of Fluids, 2004, pp. L39-43.
[18] H. Hamdani and M. Sun, *Aerodynamic Forces and Flow Structures of an Airfoil in Some Unsteady Motions at Small Reynolds Number,* cilt Vol.145, Acta Mechanica, 2000, pp. 173-187.
[19] S. A. Kazemi, M. Nili-Ahmadabadi, A. Sedaghat and M. Saghafian, *Aerodynamic performance of a circulating airfoil section for Magnus systems via numerical simulation and flow visualization,* cilt Vol.104, Energy, 2016, pp. 1-15.
[20] H. E. Tanürün, İ. Ata, M. E. Canlı and A. Acır , *Farklı açıklık oranlarındaki NACA-0018 rüzgâr türbini kanat modeli performansının sayısal ve deneysel incelenmesi,* cilt 23, Politeknik Dergisi, 2020, pp. 371-381.
[21] A. A. Güler, *Naca0015 Model Uçak Kanadi Etrafindaki Akişin Plazma Aktüatör İle Aktif Kontrolünde Sinyal Modülasyonunun Deneysel İncelenmesi,* Niğde Ömer Halisdemir Üniversitesi Fen Bilimleri Enstitüsü, 2013.
[22] A. Pope, *The forces and moments over an NACA 0015 airfoil,* cilt Vol.58, Georgia Institue of Technology, Published in: Aero Digest, 1949.

Contents lists available at *Dergipark*

Journal of Scientific Reports-A

journal homepage: *https://dergipark.org.tr/tr/pub/jsr-a*

E-ISSN: 2687-6167 ***Number 55, December 2023***

RESEARCH ARTICLE

Receive Date: 29.11.2023 *Accepted Date: 28.12.2023*

Investigation of the effects of electric vehicle charging stations and solar energy integration on grid performance

Kadir Olcay[1,*], Nurettin Çetinkaya[2]

[1]*Dumlupınar Vocational School, Kutahya Dumlupınar University, 43100, Kütahya, Turkey, ORCID: 0000-0001-7918-6482*
[2]*Department of Electrical and Electronic Engineering, Konya Technical University, 42250, Konya, Turkey, ORCID: 0000-0002-6111-7769*

Abstract

In this study, the negative effects of electric vehicle charging stations, whose use has rapidly increased all over the world in the last few years, on the electricity network were analyzed. The charging station was purchased and installed in a suitable area. Measurements taken using the energy analyzer at this charging station were examined. An electrical network model has been prepared. IEEE 6-bus power test system data was used for this model. The model was built using Electrical Transient Analyzer Program (ETAP). In addition to the existing loads on the electricity grid, the loads that will occur with the increase in electric vehicle charging stations have also been added. In this case, this electrical network was analyzed using the Newton-Raphson load flow algorithm with the existing load data of the generators, buses and data of the added charging station loads in the IEEE 6-bus test system network. Considering that one thousand additional charging stations come as load for each load bus, 22 MW load was added. In order to reduce the power losses detected here, grid-connected solar power plants have been proposed. By adding these power plants, it is aimed to reduce the negative effects of the load increase caused by electric vehicle charging stations. For the case of adding solar power plants (SPP), the results were examined by making load flow and it was shown that the network losses decreased. As a result of the study, as a result of adding electric vehicle charging station loads (EVCS) to each load bus in addition to the existing loads, active power loss doubled and reactive power loss reached more than three times. In the buses with the recommended consumption, these losses, which increased with the energy production by load solar power plants, decreased by more than half.

Keywords: Electric Vehicles, Load Flow, Solar Power Plants, Charging Stations, Power Loss, Newton-Raphson Load Flow.

1. Introduction

Due to the limited lifespan of fossil fuels and their harmful effects such as greenhouse gases, the interest in electric vehicles (EV) in the automotive industry as an alternative fuel has been rapidly increasing in recent years [1,2]. For this reason, electric vehicles and their components have become an important research topic [3]. Reducing

greenhouse gas effects and using EVs that will have positive effects on climate change increases the incentives in this field. Because today, climate change is one of the leading situations that negatively affect living life [4,5,6]. It is thought that increasing EV use will significantly reduce these negative effects. Because when we look at the causes of carbon dioxide emissions in Europe, the automotive industry ranks second in terms of causing greenhouse gases when the sectors are compared [7]. For these reasons, EV technology, which can benefit from the energy production of alternative energy sources, is supported by governments due to its high efficiency, not causing CO_2 emissions and its positive contributions to energy sustainability, and their numbers are increasing day by day. [8,9,10]. In addition to the benefits of using electrical energy in electric vehicles, it also causes some problems. Especially negative situations that may arise on the electricity grid restrict the increase in the number of EVs. It is stated in academic studies that EV sales will constitute approximately 20% of total vehicle sales [11]. These vehicles, which consume electrical energy, will cause increased losses in the network, sudden load changes, changes in demand profiles, decreased energy quality as a result of harmonic distortions, shortened lifespans of transformers and conductors, network voltage losses and a significant decrease in network efficiency [12-15]. The resulting network effects will also increase the probability of failure. This is a situation that threatens energy supply demand.

This rapid promote in EVs shows that the number of electric vehicle charging stations (EVCS) will also increase [8,16]. These increases raise the infrastructure deficiency in the network. Therefore, understanding the effects of electric vehicle charging stations on energy networks and minimizing these effects has become an important research area. Olcay et al. [2] suggested the use of solar power plants to reduce the effects of electric vehicles on greenhouse gas emissions. In the study, a solar power plant (SPP) model was built in open parking lots and the emission effects of different vehicle brands were examined by EV charging with the resulting system. In addition, the emissions and SPPs caused by EVs according to the production raw material of the energy provided by the grid and their reduction amounts are shown here. In another study, the effects of EV charging in a 240-bus distribution network were investigated. An hourly demand profile data for EVs has been created. Along with this profile, the demand profile of the 240-bus distribution network was evaluated together. As a result, the degradation of energy demands arising from EV charging is shown. To reduce this degradation, three different charging scenarios have been proposed [11]. In another study, SPP was designed for EVs. In the study, the power plant was modeled and efficient use of space was aimed. Additionally, the use of a wind turbine and photovoltaic panels has been compared for EVCSs [17]. In another study, daily load curves were created using user feedback data to ensure power distribution optimization of EV charging in the electrical grid and a double-layer optimization strategy was created [18]. Other studies in the literature have examined the regulation of EV network usage times according to energy sales prices [19-21]. In another study that proposed an internet of things (IoT)-based system for EV users, EVCS usage optimization was created in multi-storey car parks. The created IoT system encourages EV users to charge during periods when the electricity grid load is less. In addition, the aim of the study is to direct EVs to charge by using solar energy in the afternoon, when solar energy is intense and the electricity grid load is less [22]. Himabindu et al. [23] proposes an alternative energy source EVCS system. The economic evaluation of this system and its improvement effect in terms of greenhouse gas emissions have been demonstrated. The effects of EVCS on the electricity grid also vary depending on their location. In a study conducted in this context, the criteria that determine EVCS locations in a certain geography were shown and optimum locations were determined [24]. In another study, it was studied to activate EVCS and smart photovoltaic inverters simultaneously to prevent or reduce the negative effects of EVCS such as voltage deviation, power losses and voltage imbalance. Pareto dominance based differential evolution algorithm is proposed and implemented to solve this optimization equation. The study results show that the electricity grid performance will raise significantly [25]. In another study, distributed generation was added to the distribution system to reduce the electrical grid power loss that would be increased by the EVCS effect [26]. Sigma Ray et al. [27], EVCS optimum location problem was created for different operators. Different objective functions were created by considering distribution system operators, charging station operators and EV user approaches. Different optimization techniques are discussed and the effects of EV-generated loads on the distribution network

are analyzed. Since EV charging and discharging schedules change the effects of EVCS on the electricity grid, studies have been conducted on various optimization techniques [28-30].

In this comprehensive study, the negative effects of electric vehicle charging stations on energy networks are analyzed in detail and innovative solution suggestions are offered. A charging station was installed in a suitable location and measurements taken using the energy analyzer were meticulously examined. For the electrical network model, a model was created using the ETAP (Electrical Transient Analyzer Program) program using IEEE 6-bus power test system data.

In addition to the existing loads, the analysis was also made to include the additional loads caused by electric vehicle charging stations. In this context, network analysis was carried out by combining the data of generators, buses, existing load data and added charging station loads in the electrical network using the Newton-Raphson load flow algorithm.

The main goal of this study is to reduce the detected power losses and optimize the performance of the energy grid. In this regard, it is recommended to add grid-connected solar power plants and a solution is offered to reduce the negative effects of the load increase caused by electric vehicle charging stations of these power plants. By examining the results of the load flow analysis for the addition of solar power plants (SPPs) in addition to electric vehicle charging stations, it is shown that network losses are reduced. In addition, using EVCS and SPP together, that is, charging EVs with energy produced by SPP, will provide a sustainable system [31-33].

This study contributes to the sustainable integration of electric vehicles and aims to improve grid performance. The proposed solutions offer a forward-looking approach to counter the growing importance of electric vehicles in our energy landscape, in line with the goals of smart grid development and sustainable energy management.

2. Materials and methods

In this section, the steps and methods of the study are explained. The network model is introduced in Section 2.1. Test Network model details are given. In Section 2.2, the infrastructure work for EVCS implementation and data collection is explained. In the last part, section 2.3, the load flow analysis performed with ETAP is shown.

2.1. IEEE 6 bus power grid test system information

IEEE 6 Bus power test system was used to analyze EVCS network effects. IEEE 6 bus power system is a standard test system used in power systems analysis, control and protection studies in the field of electrical engineering. This grid represents part of the American Electric Grid. This system is used as a reference model for power systems analyses, voltage drop calculations, short circuit analyses, frequency response evaluations and other power systems engineering applications. It is used to examine the energy flow between different buses and to evaluate the performance of each component in the system.

The 6-bus test model used in this study was created in the ETAP program. In this study, in the 6-bus network system, bus number 1 is the swing bus, buses 2 and 3 are voltage-controlled buses, and buses 4, 5 and 6 are the load buses. A single line diagram of the test system is shown in Figure 1.

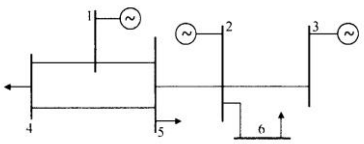

Fig. 1. IEEE 6-bus power test system.

While creating a network model, the values of production and loads are shown in Table 1.

Table 1. IEEE 6-bus test system load values (pu).

Bus number	Bus type	Bus voltage	P_{gen}	Q_{gen}	P_{load}	Q_{load}
1	Swing	1,05+j0	-	-	0	0
2	Generator	1	1,2	0,5	0	0
3	Generator	1	1,2	0,5	0	0
4	Load	-	-	-	0,7	0,7
5	Load	-	-	-	0,7	0,7
6	Load	-	-	-	0,7	0,7

While creating the model, the values of the lines between the buses were also determined. These data are shown in Table 2.

Table 2. IEEE 6-bus test system load values (pu).

Branch number	Branches		R	X	B
1	1	2	0,1	0,2	0,04
2	1	4	0,05	0,2	0,04
3	1	5	0,08	0,3	0,06
4	2	3	0,05	0,25	0,06
5	2	4	0,05	0,1	0,02
6	2	5	0,1	0,3	0,04
7	2	6	0,07	0,2	0,05
8	3	5	0,12	0,26	0,05
9	3	6	0,02	0,1	0,02
10	4	5	0,2	0,4	0,08
11	5	6	0,1	0,3	0,06

Using the data in Table 1 and Table 2, the nominal equivalent circuit of the electrical network system here was created. Equivalent circuits are created and these circuit models vary depending on the length of the transmission lines and the type of analysis to be performed. For short transmission lines, the capacitive reactance between the phase conductors and the ground and the leakage resistance here are neglected. However, since the model here is evaluated in the medium and long lines class, nominal equivalent circuits have been created. "π (pi) nominal" and "T nominal" circuits are used when creating equivalent circuits of transmission lines. These concepts represent two different approaches used in mathematical modeling and analysis of transmission lines. Pi nominal circuit will be used for the load flow analysis. This model includes inductance, capacitance, resistance and conductance values in the transmission line. These values are generally based on values measured at nominal frequency. The main reason for using this model is to evaluate power systems that are generally operated at nominal frequency (such as 50 Hz or 60 Hz) in load flow analysis. The π nominal circuit generally gives accurate results in load flow analysis and is widely used to evaluate operating conditions. The values in Table 1 and Table 2 are given per-unit. It was used in this way in the model. "Per Unit" (pu) is a unit of normalization used to compare a measurement or value to a standard reference value. It is widely used in electrical engineering and energy systems. This normalization makes it easier to compare and analyze values of different magnitudes. The expression "Per Unit" represents a ratio in which

a value is expressed as divided by a specific reference value (base value). Information on these base values is needed to obtain the real values in the system. S_{load} 100 MVA, V_{base} 230 kV and Z_{base} 529 ohms were used as base values.

2.2. EVCS field application and analysis

In the implementation phase of the study, a 22 kW AC type 3-phase charging station was used. The reason why the 22-kW station was chosen is that it is the EVCS type preferred by EV users and many commercial EVCS entrepreneurs. When industry research is done, it costs approximately 5% of the price of 120 kW DC EVCS. Since its power is much lower than DC types, it is also widely used in residences. It is much easier for 22 kW devices to integrate into existing electrical infrastructures. In addition, due to its lower price and ease of connection to existing infrastructures, their numbers are increasing much faster and becoming a collective burden. According to October data for commercially used ones, the number of AC EVCS in Turkey is approximately 3 times more than DC type

Fig. 2. Electric vehicle charging station panel assembly visual.

ones. When those that are not used commercially are added, it becomes a huge burden. Current, voltage and harmonic analysis measurement data are taken from this charging station. The infrastructure and installation works carried out for this purpose are explained in this section. First of all, a separate panel content was designed so that the charging station can receive energy from the existing electrical system and targeted measurements can be made. The point where this panel will receive energy from the existing electrical system was determined and the energy was received from the existing electrical panel through the overcurrent circuit breaker protection element, and the energy supply to the charging station panel was made with a 4x10 mm² copper cable. In addition, the protection grounding of the electric vehicle charging station panel was made with a 10 mm² single-core copper cable and connected to the existing grounding system. Energy intake from the existing electrical system and installation of the electric vehicle charging station panel are shown in Figure 2.

After the installation of the sheet metal panel and the installation of the power line from the existing system, the interior design of this panel was started. One 40/5 A current transformer for each electrical phase and three current transformers in total were used in the panel energy input. The current information that the charging station will draw

from these current transformers will be transferred to the energy analyzer. For this purpose, the connection between current transformers and energy analyzer is also made. The conductors passing through the current transformers are connected to the main input switch of the panel. With this switch, overcurrent protection is provided and the conductors are protected. From here, energy distribution was made within the panel and the energy analyzer was mounted to the relevant connection points on the energy analyzer using three single-phase circuit

breakers for electricity supply. Three-phase leakage current protection switch connections were made with the output taken from the panel input switch. In this way, user protection is provided against any leakage current fed from this panel or that may occur on the metal parts of the panel. The residual current protection switch cuts off the energy by opening the circuit at 30 mA level. In-panel installation is shown in Figure 3.

Electric vehicle charging station current, voltage and harmonic measurements will be provided through the energy analyzer mounted on the panel. The energy analyzer has RS485 communication connection and Ethernet connection. Instant remote monitoring of the data will be done using an ethernet connection. For this, an internet

Fig. 3. Electric vehicle charging station in-panel installation visual.

connection was made as seen in Figure 4. CAT6 cable was installed to connect the output from the relevant port of the energy analyzer to the free port of the data switch in the existing infrastructure. The energy analyzer connection is seen in Figure 4.

Fig. 4. Energy analyzer installation visual on the panel.

After these stages, the charging station energy cable was selected and an underground cable channel was opened from the energy receiving point to the charging station installation point. In this channel, energy cables were pulled through the plastic pipe and brought to the vehicle charging station installation point. A 4-core 10 mm² energy cable was pulled through the pipe and a connection was made between the charging station and the electrical panel from which it receives energy. In this way, the charging station power line installation has been completed. Following this

process, the metal body of the charging station was assembled and a 22 kW AC type 2-socket charging station was installed on this body. The installed charging station is seen in Figure 5.

Fig. 5. Installation image of 22 kW AC type 2-socket charging station.

2.3. Load flow analysis with ETAP

Electrical energy is of vital importance in every field in today's world. Therefore, the safety, efficiency and performance of electrical systems must be constantly monitored and analyzed. These systems may contain complex and dynamic variables due to their structure. At this point, ETAP program is a software that provides the opportunity to analyse and optimize electrical energy systems.

In this section, load flow analysis was performed with the Newton-Raphson method by adding the EVCS loads of the IEEE 6-bus power test system modelled in the ETAP program. As a result of the analysis, active power and reactive power losses in the lines were determined. Afterwards, active power and reactive power losses were reduced by connecting SPP to the production buses in the system. The most suitable production bus has also been determined.

There are many load flow analysis methods. It can be said that the most used ones are the Fast Decoupled method, Gauss-Seidel method and Newton-Raphson method. Studies in the literature [34] show that losses increase as the number of iterations of the Gauss-Seidel method increases. In the Fast Decoupled method, as the number of buses increases, it causes no results to be found in the calculation. The most appropriate results are obtained with the Newton Raphson method. For this reason, it was preferred as the load analysis method of this study.

First of all, the IEEE 6 bus power test system was modelled in the ETAP program. The model is shown in Figure 6.

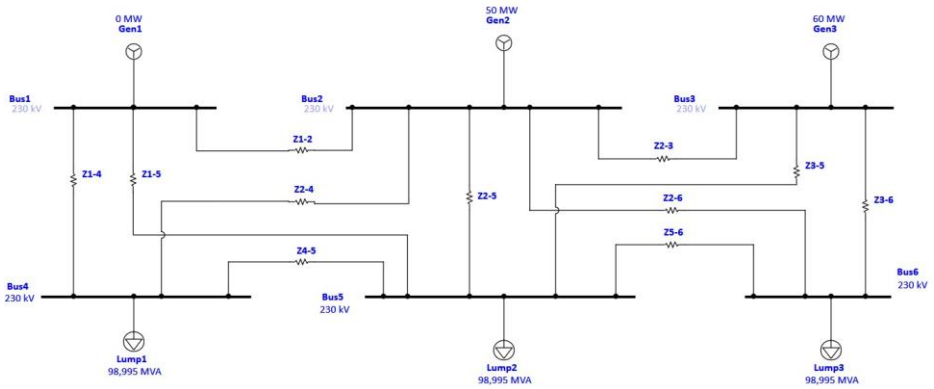

Fig. 6. Installation image of 22 kW AC type 2-socket charging station.

In this model, it was made with existing loads, lines and productions. It represents an existing grid system. The effects of electric vehicle charging stations (EVCS) to be integrated into existing systems on the network will be analysed through this model. This study will especially focus on power losses. Losses in the current system were determined by the Newton-Raphson load flow method. Afterwards, EVCSs were added to the load buses in the IEEE 6 bus network model. The added EVCS features are explained in section 2.2 and shown in Figure 5. It is considered that 1000 units of 22 kW AC type 2 charging stations are added to each load bus, individually and commercially. EVCS network effect is made according to the peak load scenario that will occur if all devices operate at the same time. The model with EVCS loads added is shown in Figure 7.

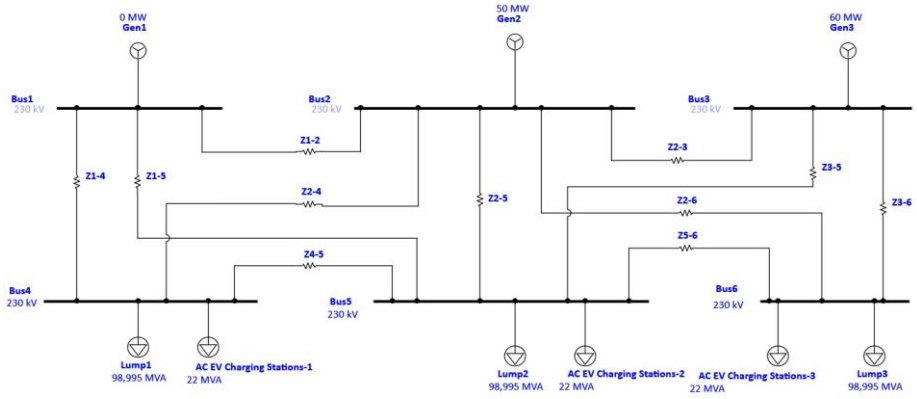

Fig. 7. ETAP model with IEEE 6 bus EVCS loads.

In order to reduce the impact of electric vehicles on the grid and ensure energy supply security, SPPs as well as EVCS consumption have been added to the system as distributed generation resources. The network model with SPPs added is shown in Figure 8.

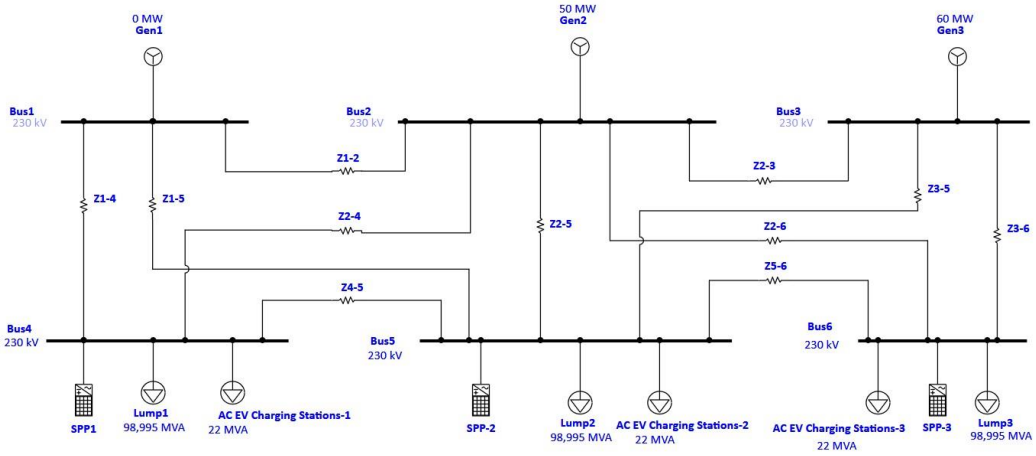

Fig. 8. IEEE 6 bus EVCS loads and SPP ETAP model.

3. Conclusion

The increase in the number of EVCS is predicted to be 1.5 million and 2.5 million in our country, according to different scenarios as medium growth and high growth. This situation will cause a significant infrastructure problem and negative effects for existing electricity grid systems. In this study, a real EVCS field installation was made and the values were read through the energy analyzer. It has been observed that no harmonics that will affect the network for AC devices occur due to EVCS energy consumption during charging. From this point on, focusing on other problems, their collective impact as a load on the network was investigated and a network model was created for this. The created network model consists of generators, existing transmission lines and existing loads. Relevant values are given in this study.

4. Results and discussion

First, load flow analysis was performed with the IEEE 6 bus power system model and data shown in Figure 6. The results are seen in Table 3.

As seen in Table 3, line losses in the current system show 23,832 kW active power loss and 34,450 kVAr reactive power loss. These losses are high for existing systems due to their own loads. As shown in Figure 7, load flow was made with these powers to analyze the line losses that would occur in the system with the addition of EVCS-sourced loads. The results are seen in Table 4.

As can be seen from the results in Table 4, by adding EVCS loads to the 4th bus, 5th bus and 6th bus in addition to the existing loads, line losses more than double. As a result of the analysis, 46,427 kW active power loss and 110,763 kVAr reactive power loss occurred.

Table 3. IEEE 6 bus Newton-Raphson load flow analysis line losses results.

Branch ID	From-to bus flow		To from bus flow		Loses		% Bus voltage	
	MW	MVAr	MW	MVAr	kW	kVAr	From	To
Z1-2	85,443	22,753	-77,539	-10,305	7.904,3	12.267,9	100	87,8
Z1-4	80,813	60,551	-75,592	-43,091	5.221,7	17.460,1	100	84,5
Z1-5	67,576	47,535	-61,880	-31,146	5.696,2	16.388,8	100	81,1
Z2-3	21,385	0,359	-21,083	-3,381	301,4	-3.022,4	87,8	86
Z2-4	4,206	26,220	-3,722	-26,735	484,3	-515,1	87,8	84,5
Z2-5	13,187	13,787	-12,657	-15,050	530,7	-1.263,1	87,8	81,1
Z2-6	38,760	22,117	-36,870	-20,222	1.890,4	1.895,3	87,8	79,5
Z3-5	-1,492	15,282	1,972	-17,734	479,8	-2.452,6	86	81,1
Z3-6	22,375	50,713	-21,721	-47,816	853,8	2.897,4	86	79,5
Z4-5	9,314	-0,174	-9,050	-4,782	263,3	-4.956,1	84,5	81,1
Z5-6	11,615	-1,288	-11,409	-1,963	206	-3.250,2	81,1	79,5

Table 4. IEEE 6 bus EVCS loads Newton-Raphson analysis line losses results.

Branch ID	From-to bus flow		To from bus flow		Loses		% Bus voltage	
	MW	MVAr	MW	MVAr	kW	kVAr	From	To
Z1-2	118,764	44,197	-102,525	-15,037	16.239	29.160,3	100	81,2
Z1-4	111,137	88,759	-100,843	-50,808	10.294	37.950,5	100	78,3
Z1-5	92,526	73,016	-81,055	-34,600	11.471	38.416,3	100	73,1
Z2-3	28,812	4,317	-28,152	-4,815	660	-498	81,2	77,9
Z2-4	4,145	20,484	-3,792	-21,052	352,3	-567,7	81,2	78,3
Z2-5	17,922	14,991	-17,031	-14,703	891,2	287,6	81,2	73,1
Z2-6	51,645	27,423	-47,914	-19,644	3.731	7.778,7	81,2	70,3
Z3-5	-2,685	14,457	3,203	-16,187	518	-1.729,5	77,9	73,1
Z3-6	30,837	52,972	-29,578	-47,779	1.258,8	5.192,7	77,9	70,3
Z4-5	12,635	1,860	-12,054	-5,287	581,3	-3.427,2	78,3	73,1
Z5-6	14,936	0,777	-14,508	-2,577	428,3	-1.800,1	73,1	70,3

These losses pose a serious problem for existing network infrastructures. These losses will cause energy loss in energy transmission and distribution lines, resulting in a decrease in energy efficiency. It may result in increased costs for consumers and companies as it will require more energy production, transmission and distribution. In addition, increasing line losses will increase voltage drops and reduce energy quality, creating the possibility of damaging devices in the system. It causes voltage regulation problems. It will cause electrical devices such as transmission lines and transformers to overheat, shortening their material life. Furthermore, it will increase the need for maintenance and the potential for failure. Excessive losses in electrical energy production and transmission can increase environmental impacts. In particular, increased consumption of fuels used for energy production and increased energy losses may increase environmental impacts. In order to reduce all these problems and support

sustainable energy, SPPs with a power of 22 MW were added to the 4th load bus, 5th load bus and 6th bus against EVCS consumption. To see the effect of this situation on line losses, load flow analysis was performed using the Newton-Raphson method and the results are shown in Table 5.

Table 5. IEEE 6 bus EVCS loads and Newton-Raphson analysis line losses results in SPP network.

Branch ID	From-to bus flow		To from bus flow		Loses		% Bus voltage	
	MW	MVAr	MW	MVAr	kW	kVAr	From	To
Z1-2	88,714	24,176	-80,159	-10,586	8,555	13.589,4	100	87,2
Z1-4	83,895	62,807	-78,276	-43,739	5,619	19.067,3	100	83,9
Z1-5	70,117	49,547	-63,975	-31,454	6,142	18.093,2	100	80,4
Z2-3	22,157	0,68	-21,829	-3,503	328,5	-2.823,4	87,2	85,3
Z2-4	4,225	25,720	-3,753	-26,240	472,7	-520	87,2	83,9
Z2-5	13,678	13,865	-13,120	-15,008	557,2	-1.142,8	87,2	80,4
Z2-6	40,099	22,500	-38,071	-20,158	2.027,7	2.341,9	87,2	78,7
Z3-5	-1,617	15,216	2,100	-17,607	482,7	-2.390,3	85,3	80,4
Z3-6	23,446	50,900	-22,562	-47,832	883,4	3.068,9	85,3	78,7
Z4-5	9,646	-0,021	-9,359	-4,811	286,3	-4.832,2	83,9	80,4
Z5-6	11,972	-1,120	-11,750	-2,011	222,7	-3.131,2	80,4	78,7

As can be seen from the results, the effects of EVCS-induced overloads on the network are quite large. The proposed addition of SPP to reduce line loss increases to the network has yielded beneficial results. Active power losses decreased by approximately 21 MW, falling to 25,577 kW. Reactive power losses decreased by approximately 70 MW, falling to 41,321 kW. As can be seen from the results, it is a useful method to reduce the effects of EVCS on existing networks. In addition, electricity generation from solar energy makes great environmental contributions since it does not cause carbon emissions. Using SPPs as distributed generation plants with EVCS also provides other advantages. These power plants will contribute to keeping the voltage stable by regulating voltage fluctuations at the points where they will be connected to the grid. In addition, having production close to consumption points, as in this study, is also an advantage and reduces line losses. It can diversify energy supply and increase energy security by locating power sources in various locations. Renewable resources such as solar panels, wind turbines or hydroelectric power plants can be used more effectively through distributed generation plants.

It should be noted that care should be taken when determining the connection points of distributed power plants. It is important that the network capacity is sufficient. Since these power plants will be connected to the grid above a certain voltage level, the grid voltage level should be analyzed when selecting connection points. Network topology, environmental and social impacts must be taken into account. Short circuit analyses, power flow analysis, voltage drop, reactive power balance, frequency, transformers and transmission lines, protection and coordination analyzes should be performed.

Acknowledgements

This research is supported by Konya Technical University Coordinatorship of Scientific Research Projects (Project number: 231102009).

References

[1] M. Moradijoz, M. Parsa Moghaddam, M.R. Haghifam, E. Alishahi, A multi-objective optimization problem for allocating parking lots in a distribution network, International Journal of Electrical Power & Energy Systems, Volume 46, 2013, Pages 115-122, ISSN 0142-0615, https://doi.org/10.1016/j.ijepes.2012.10.041.

[2] K. Olcay and N. Cetinkaya, Solar Power Plant Suggestion for Charging Electric Vehicles and The Effects of the System on The Electric Network and CO2 Emission, 2021 IEEE 2nd KhPI Week on Advanced Technology (KhPIWeek), pp. 249-254, 2021, doi: 10.1109/KhPIWeek53812.2021.9570056.

[3] Nathan Parker, Hanna L. Breetz, Deborah Salon, Matthew Wigginton Conway, Jeffrey Williams, Maxx Patterson, who saves money buying electric vehicles? Heterogeneity in total cost of ownership, Transportation Research Part D: Transport and Environment", Volume 96, 102893, ISSN 1361-9209, 2021, https://doi.org/10.1016/j.trd.2021.102893.

[4] Fan Xiaochao, et al. High voltage gain DC/DC converter using coupled inductor and VM techniques IEEE Access, 8, pp. 131975-131987, 2020, doi: 10.1109/ACCESS.2020.3002902.

[5] Ye Haixiong, et al. "High step-up interleaved dc/dc converter with high efficiency", Energy Sources A, pp. 1-20, 2020, https://doi.org/10.1080/15567036.2020.1716111.

[6] Hamian Melika, et al. A framework to expedite joint energy-reserve payment cost minimization using a custom-designed method based on mixed integer genetic algorithm Eng. Appl. Artif. Intell., pp. 203-212, 72 (2018), https://doi.org/10.1016/j.engappai.2018.03.022.

[7] Serradilla, J.; Wardle, J.; Blythe, P.; Gibbon, "J. An evidence-based approach for investment in rapid-charging infrastructure", Energy Policy, 106, 514–524, 2017, https://doi.org/10.1016/j.enpol.2017.04.007.

[8] Olcay, K.; Çetinkaya, "N. Analysis of the Electric Vehicle Charging Stations Effects on the Electricity Network with Artificial Neural Network" Energies, 16, 1282, 2023, https://doi.org/10.3390/en16031282

[9] W. Xifan, S. Chengcheng, W. Xiuli and Du Chao, "Overview of EV Charging Load and Dispatching Control Strategy", Journal of China Electrical Engineering, vol. 33, no. 01, pp. 1-10, 2013.

[10] J. Zhenya and H. Xueliang, "Plug-in electric vehicle charging infrastructure deployment of China towards 2020: policies methodologies and challenges", Renewable and Sustainable Energy Reviews, vol. 90, pp. 710-727, 2018, https://doi.org/10.1016/j.rser.2018.04.011.

[11] D. Khandelwal, S. Painuli, S. Bhowmick and R. Saha, "A Comparison of Practical Electric Vehicle Charging Policies to Improve the Performance of Power Distribution Systems", *2023 International Conference on Recent Advances in Electrical, Electronics & Digital Healthcare Technologies (REEDCON)*, New Delhi, India, pp. 7-12, 2023, doi: 10.1109/REEDCON57544.2023.10151097.

[12] L. Pieltain Fernández, T.G.S. Román, R. Cossent, C.M. Domingo and P. Frías, "Assessment of the Impact of plug-in electric vehicles on distribution networks", IEEE Transactions on Power Systems, vol. 26, no. 1, pp. 206-213, 2011, doi: 10.1109/TPWRS.2010.2049133.

[13] S. Painuli, M. S. Rawat and D. R. Rayudu, "A Comprehensive Review on Electric Vehicles Operation Development and Grid Stability", 2018 International Conference on Power Energy Environment and Intelligent Control (PEEIC), pp. 807-814, 2018, doi: 10.1109/PEEIC.2018.8665643.

[14] A. Aljanad and A. Mohamed, "Harmonic Impact of Plug-In Hybrid Electric Vehicle on Electric Distribution System", Model. Simul. Eng., pp. 1-7, Aug. 2016, https://doi.org/10.1155/2016/5968943.

[15] M. K. Gray and W. G. Morsi, "Power Quality Assessment in Distribution Systems Embedded With Plug-In Hybrid and Battery Electric Vehicles", IEEE Trans. Power Syst., vol. 30, no. 2, pp. 663-671, Mar. 2015, doi: 10.1109/TPWRS.2014.2332058.

[16] Fareed Ahmad, Atif Iqbal, Imtiaz Ashraf, Mousa Marzband, Irfan khan, "Optimal location of electric vehicle charging station and its impact on distribution network: A review", Energy Reports, Volume 8, Pages 2314-2333, 2022, ISSN 2352-4847, https://doi.org/10.1016/j.egyr.2022.01.180.

[17] K. Mohammed, H. K. Wolde and S. M. S. Alarefi, "Optimal Space Utilisation for Solar Powered EV Charging Station", 2020 6th IEEE International Energy Conference (ENERGYCon), Gammarth, Tunisia, 2020, pp. 562-567, doi: 10.1109/ENERGYCon48941.2020.9236538.

[18] W. Ruan, X. Yu, W. Liu, Z. Liu, Y. Yu and C. Wu, "Optimal Charging Strategy for EVs in Microgrid Considering Customer Urgency", 2020 12th IEEE PES Asia-Pacific Power and Energy Engineering Conference (APPEEC), Nanjing, China, 2020, pp. 1-5, doi: 10.1109/APPEEC48164.2020.9220439.

[19] S. Haifeng and L. Zhirui, "Orderly Charging Control Method for Residential Quarters of Household EVs Based on Peak-valley Electricity Price", Power Automation Equipment, vol. 35, no. 06, pp. 17-22, 2015.

[20] Y. Cao, S Tang, C Li et al., "An Optimized EV Charging Model Considering TOU Price and SOC Curve", IEEE Transactions on Smart Grid, vol. 3, no. 01, pp. 388-393, 2012, doi: 10.1109/TSG.2011.2159630.

[21] S. Xiaoming, W. Wong, S. Su, J. Jiuchun, X. Lijie and He Xuanhu, "Orderly Charging Control Strategy Design for EVs Based on Time-of-Use Electricity Price", vol. 37, no. 01, pp. 191-195, 2013.

[22] B. Kulkarni, D. Patil and R. G. Suryavanshi, "IOT Based PV assisted EV Charging Station for Confronting Duck Curve", International Conference on Computational Techniques, Electronics and Mechanical Systems (CTEMS), Belgaum, India, 2018, pp. 36-39, 2018, doi: 10.1109/CTEMS.2018.8769145.

[23] Himabindu N., Santoshkumar Hampannavar, Deepa B., Omowunmi Mary Longe, Swapna Mansani, Vahini Komanapalli, "Assessment of microgrid integrated biogas–photovoltaic powered Electric Vehicle Charging Station (EVCS) for sustainable future", Energy Reports, Volume 9, Supplement 12, Pages 139-143, 2023, ISSN 2352-4847, https://doi.org/10.1016/j.egyr.2023.09.098.

[24] Ömer Kaya, Ahmet Tortum, Kadir Diler Alemdar, M. Yasin Çodur, "Site selection for EVCS in Istanbul by GIS and multi-criteria decision-making", Transportation Research Part D: Transport and Environment, Volume 80, 102271, 2020, ISSN 1361-9209, https://doi.org/10.1016/j.trd.2020.102271.

[25] Khalil Gholami, Shahram Karimi, Amjad Anvari-Moghaddam, "Multi-objective Stochastic Planning of Electric Vehicle Charging Stations in Unbalanced Distribution Networks Supported by Smart Photovoltaic Inverters", Sustainable Cities and Society, Volume 84, 104029, ISSN 2210-6707, 2022, https://doi.org/10.1016/j.scs.2022.104029.

[26] J.J. Jamian, M.W. Mustafa, H. Mokhlis, M.A. Baharudin, "Minimization of Power Losses in Distribution System via Sequential Placement of Distributed Generation and Charging Station", Arab J. Sci. Eng., 39 (4), pp. 3023-3031, 2014, https://doi.org/10.1007/s13369-013-0922-5.

[27] Sigma Ray, Kumari Kasturi, Samarjit Patnaik, Manas Ranjan Nayak, "Review of electric vehicles integration impacts in distribution networks: Placement, charging/discharging strategies, objectives and optimisation models", Journal of Energy Storage, Volume 72, Part D, 108672, 2023, ISSN 2352-152X, https://doi.org/10.1016/j.est.2023.108672.

[28] Hussain Shareef, Md Mainul Islam, Azah Mohamed, "A review of the stage-of-the-art charging technologies, placement methodologies, and impacts of electric vehicles", Renew. Sust. Energ. Rev., pp. 403-420, 2016, https://doi.org/10.1016/j.rser.2016.06.033.

[29] Fareed Ahmad, et al. "Placement and capacity of ev charging stations by considering uncertainties with energy management strategies", IEEE Trans. Ind. Appl., 59 pp. 3865-3874, 2023, doi: 10.1109/TIA.2023.3253817.

[30] Muhammad Amjad, et al. "A review of EVs charging: from the perspective of energy optimization, optimization approaches, and charging techniques", Transp. Res. Part D: Transp. Environ., 62 (2018), pp. 386-417, https://doi.org/10.1016/j.trd.2018.03.006.

[31] X. Liang and E. Tanyi, "Charging electric cars from solar energy", 2016.

[32] P. Bauer, Y. Zhou, J. Doppler and N. Stembridge, "Charging of electric vehicles and impact on the grid," 13th Mechatronika, Trencianske Teplice, Slovakia, 2010, pp. 121-127, 2010.

[33] C. T. Ma, System planning of grid-connected electric vehicle charging stations and key technologies: A review", Energies, vol. 12, no. 21, 2019, https://doi.org/10.3390/en12214201.

[34] Yesilbudak M, Ermiş S, Bayındır R ,"Farklı Bara Sayısına Sahip Güç Sistemlerinde Yük Akışı Analiz Metotlarının Karşılaştırılması", Gazi Üniversitesi Fen Bilimleri Dergisi Part C: Tasarım ve Teknoloji, 5(3), 237 – 246, 2017.